

**Pattern formation
with a conservation law**

David Mark Winterbottom, MMath.

Thesis submitted to The University of Nottingham
for the degree of Doctor of Philosophy

November 2005

In loving memory of my mother.

Abstract

THE EVOLUTION OF many pattern-forming systems is strongly influenced by the presence of a conserved quantity. Diverse physical phenomena such as magnetoconvection, rotating fluid convection, binary fluid convection, vibrated granular and fluid layers, filament dynamics and sandbank formation, all possess a conservation law which plays a central role in their nonlinear dynamics. In this thesis, this influence of a conserved quantity is examined through analyses of three distinct pattern-formation problems.

Firstly, the consequences of conservation of mass are investigated in a phenomenological model of a vibrated granular layer. A new weakly nonlinear analysis is performed that reveals the existence of modulational instabilities for patterns composed of either stripes and squares. The nonlinear evolution of these instabilities is numerically studied and a plethora of patterns and localised arrangements are exhibited.

The second component of this work concerns an oscillatory bifurcation in the presence of a conserved quantity. Building upon existing theory for the corresponding stationary bifurcation, universal amplitude equations are constructed through symmetry and asymptotic considerations. Subsequently, the stability properties of travelling and standing waves are found to be significantly altered and new modulational instabilities are uncovered. Numerical simulations reveal that, in the presence of a conserved quantity, travelling and standing waves lose stability to spatially localised patterns, either coherent, time-periodic or chaotic.

Finally, wave-like behaviour of large-scale modes is examined through an analysis of a model for Faraday waves, that has been modified to account for finite fluid depth. Several approaches to the weakly nonlinear analysis are considered and two sets of amplitude equations are derived that account for the unusual wave-like behaviour of large-scale modes. Numerical simulations reveal amplitude-modulated and localised patterns away from the small-amplitude, weak-viscosity limit.

Acknowledgements

Primarily, I would like to pay tribute to the invaluable contribution of my supervisors, Paul Matthews and Steve Cox. Without their skilful guidance, insightful commentary and impressive depth of knowledge, this thesis would not have been possible.

I would like also to thank my family, and especially Katy, for their support and encouragement over the years.

Finally, I am grateful to the Engineering and Physical Sciences Research Council who provided the financial support for this work.

Contents

1	Introduction	1
1.1	Pattern formation	1
1.2	Theoretical approaches	2
1.2.1	Pattern-forming bifurcations	3
1.2.2	Amplitude equations	5
1.2.3	Weakly nonlinear analysis	7
1.2.4	Symmetry considerations	10
1.3	Stationary pattern formation	10
1.4	Oscillatory pattern formation	13
1.4.1	The complex Ginzburg–Landau equation	14
1.4.2	Coupled, complex Ginzburg–Landau equations	17
1.5	Pattern formation with a conservation law	20
1.5.1	One-dimensional behaviour	21
1.5.2	Two-dimensional behaviour	25
1.6	Structure of thesis	29
2	A vibrated granular layer	31
2.1	Introduction	31
2.1.1	Experimental background	33
2.1.2	Theoretical approaches	36
2.1.3	Structure of chapter	37
2.2	Order-parameter model	38
2.2.1	Linear analysis	39

CONTENTS

2.2.2	Large-scale modes	40
2.2.3	Previous nonlinear analysis	41
2.3	Weakly nonlinear analysis	43
2.3.1	No spatial modulation	43
2.3.2	Spatial modulation	53
2.4	Simulation results	56
2.4.1	Numerical scheme	56
2.4.2	Small-container numerical simulations	58
2.4.3	Large-container numerical simulations	59
2.5	Summary	64
3	Oscillatory pattern formation	66
3.1	Introduction	66
3.1.1	Coupled Ginzburg–Landau systems	66
3.1.2	Localisation	67
3.1.3	Structure of chapter	69
3.2	Derivation of the amplitude equations	70
3.2.1	Nongenericity	71
3.2.2	Amplitude equations	73
3.2.3	Binary fluid convection	74
3.2.4	Validity of amplitude equations	74
3.3	Travelling waves	75
3.3.1	Long-wave analysis	77
3.3.2	Eigenvalue behaviour for small-amplitude travelling waves	80
3.4	Standing waves	83
3.4.1	Long-wave analysis	85
3.4.2	Eigenvalue behaviour for small-amplitude standing waves	88
3.5	Numerically calculating stability regions	90
3.6	Simulation results	97
3.6.1	Travelling wave instabilities	98

CONTENTS

3.6.2	Standing wave instabilities	104
3.7	Behaviour for $O(1)$ group velocity	109
3.8	Summary	110
4	Faraday waves	113
4.1	Introduction	113
4.1.1	Experimental background	113
4.1.2	Theoretical approaches	115
4.1.3	Structure of chapter	119
4.2	The model	120
4.2.1	Previous results	121
4.2.2	Finite depth	122
4.2.3	Large-scale modes	125
4.3	Solutions of the linear problem	127
4.3.1	Numerically solving the linear problem	131
4.4	Nonlinear analysis I: Spatially uniform amplitudes	134
4.4.1	$O(\epsilon)$ analysis	135
4.4.2	$O(\epsilon^2)$ analysis	135
4.4.3	$O(\epsilon^3)$ analysis	138
4.4.4	Summary	141
4.5	Nonlinear analysis II: Spatial modulation	142
4.5.1	$O(\epsilon)$ analysis	143
4.5.2	$O(\epsilon^2)$ analysis	145
4.5.3	$O(\epsilon^3)$ analysis	147
4.5.4	Capillary waves	150
4.5.5	Summary	151
4.6	Nonlinear analysis III: A distinguished limit	151
4.6.1	Infinite depth	152
4.6.2	Finite depth	157
4.6.3	Summary	161

CONTENTS

4.7	Numerical simulation	162
4.7.1	Mixed capillary–gravity waves	163
4.7.2	Capillary waves	166
4.8	Summary	167
5	Conclusions	171
A	Eigenvalue theorem	175
B	Simulation code	178
C	Eigenfunction parity	181
D	Notation guide	183
	References	185

Introduction

1.1 Pattern formation

THE DIVERSITY OF patterns found in nature has attracted the attention of scientists for many years, and the study of pattern formation has developed into a thriving branch of nonlinear physics. Patterns are observed in a wide range of natural scenarios, including animal coat markings, cloud formation, ripples on flat beaches and sand dunes (figure 1.1). In the laboratory, patterns are studied in an array of convection experiments, chemically reacting media, interacting laser beams and parametrically forced layers of either fluid or granular material, amongst others (figure 1.2). Comprehensive reviews of pattern-forming applications have been provided by Cross and Hohenberg [1] as well as Stevens [2].

Pattern-forming systems belong to a class of problems where an external control parameter is used to drive the system beyond equilibrium. Typically, the system has some basic homogeneous state which, as the control parameter passes through a critical value, loses stability, giving rise to a patterned arrangement. For instance, in Rayleigh–Bénard convection, as the temperature gradient is increased, fluid ceases to transfer energy solely through conduction and begins to convect, giving rise to a patterned state of up and down flow (see figure 1.1b and Cross and Hohenberg [1]). Very close to the instability threshold, the realised pattern is often remarkably simple, consisting of spatially periodic cellular arrangements (figure 1.2b,c) or perhaps, taking a spatio-temporally periodic form, such as travelling or standing waves. These patterns are commonly punctuated with minor ‘defects’ where the basic pattern is deformed in some way, such as splitting or merging with itself. Variation of the system parameters can subsequently cause these primary pattern to undergo secondary instabilities, where a new pattern is selected. Secondary patterns are often slight modifications of

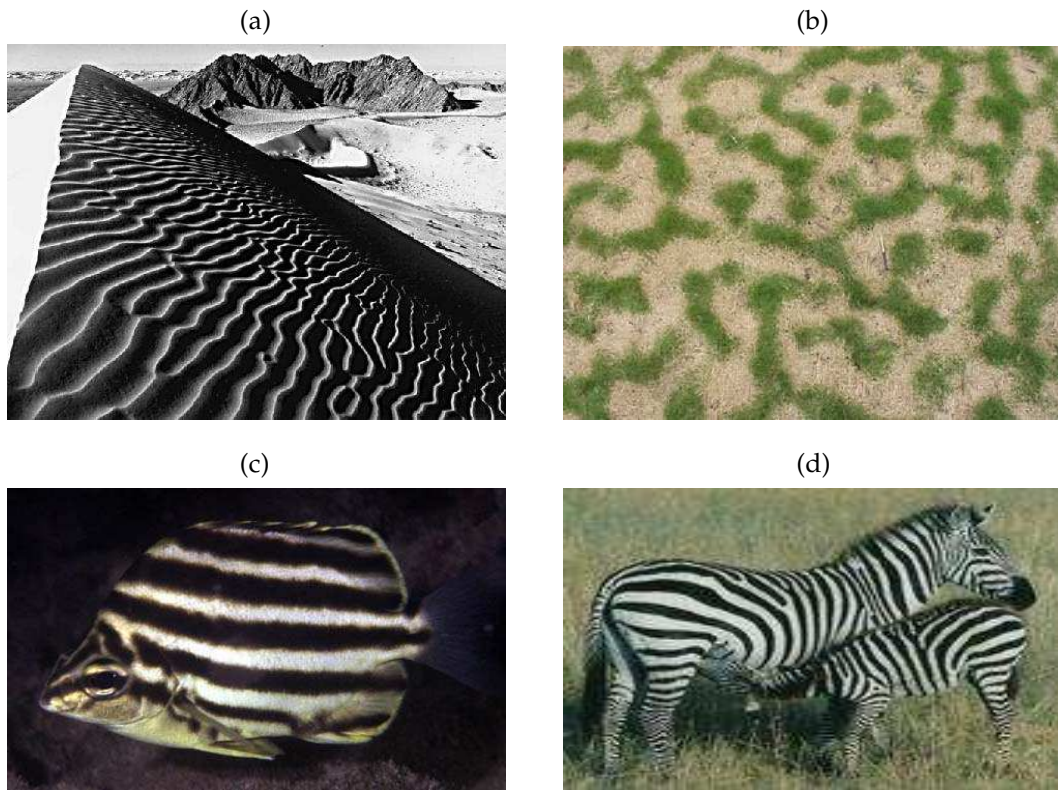


Figure 1.1: Patterns in nature: (a) sand dunes; (b) grass patterns; (c), (d) fish and animal coat markings. Many further examples can be found through a cursory internet search.

the original, and commonly feature amplitude modulation or a shift in wavenumber. Further increases to the control parameter lead to the selection of patterns of growing complexity until eventually the system descends into a chaotic or turbulent state.

Perhaps the most fascinating aspect of pattern formation is that so many disparate systems give rise to very similar near-threshold dynamics; certain behaviours appear to be universal. Indeed, it is now appreciated that many pattern-formation phenomena and instability mechanisms are *generic* in some sense and can be described by a suitable set of canonical equations. Within this framework, the appropriate description is determined primarily by the symmetries of a problem and the nature of the bifurcation at hand; the specifics of the physics play only a minor role.

1.2 Theoretical approaches

To reiterate, the study of pattern formation involves describing the slow dynamics of a system driven beyond a symmetry-breaking bifurcation or phase transition. Thus, in

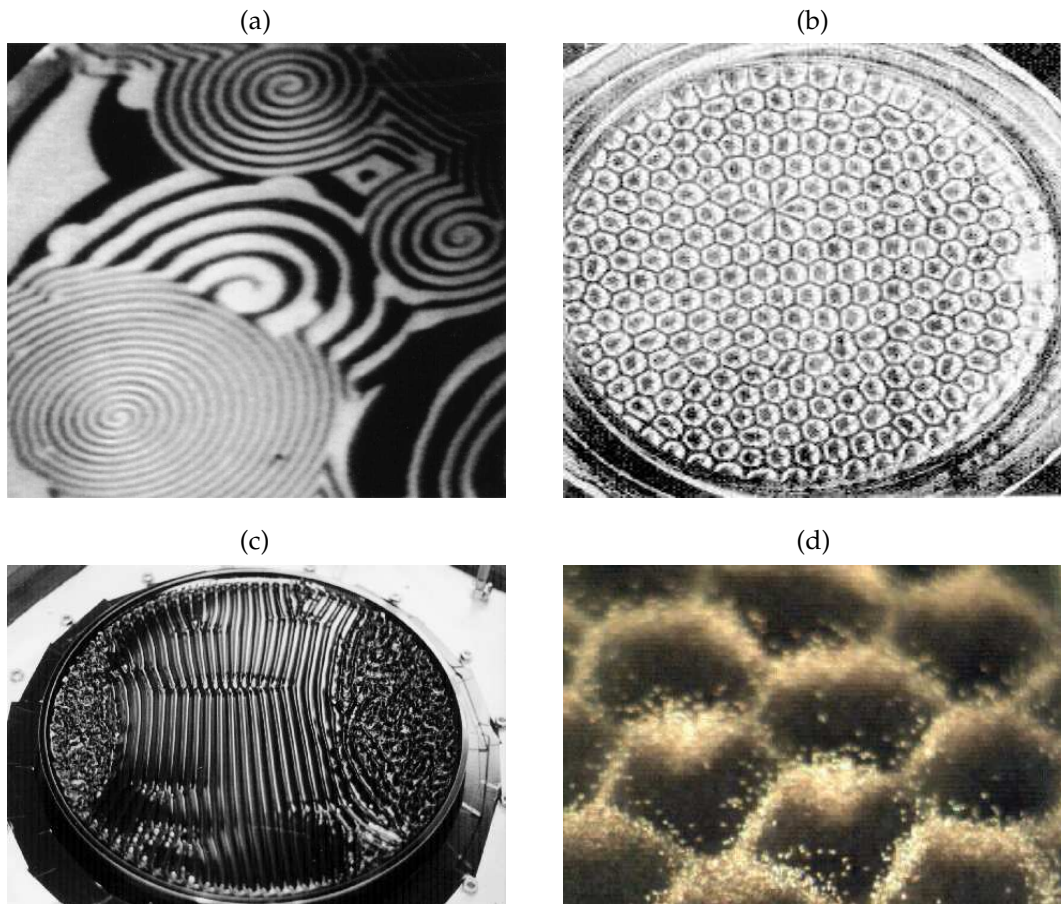


Figure 1.2: Patterns in the laboratory: (a) spatio-temporal patterns in CO-oxidation on Pt(110) [3]; (b) hexagonal Bénard convection cells arising in a layer of silicon oil heated from below [4]; (c) split domains of stripes and spatio-temporal chaos on the surface of a vibrated fluid layer (Faraday waves) [5]; (d) hexagonal patterns on the surface of a vibrated granular layer [6].

its most prevalent mathematical formulation, all pattern-formation problems identify some basic state, which loses stability as a control parameter r passes through its critical value $r = r_c$ (determined from a linear stability analysis). The theoretical challenge then lies in capturing the nonlinear dynamics of the problem slightly beyond the instability point, and examining the subsequent selection of a pattern.

1.2.1 Pattern-forming bifurcations

For typical pattern formation problems, the nature of the primary bifurcation is determined by several attributes. If we consider the linearised problem about the basic state and examine the stability of Fourier modes $e^{\lambda t + ik \cdot x}$ where k is a wavevector, then an instability corresponds to the real part of the growthrate λ first passing through zero;

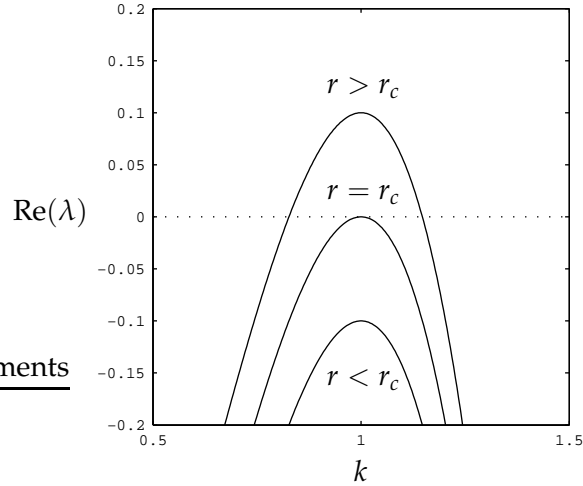


Figure 1.3: Behaviour of the growthrate $\text{Re}(\lambda)$ as a function of the perturbation wavenumber $k = |\mathbf{k}|$ for a finite-wavelength instability. The control parameter r determines whether modes are decaying ($r < r_c$), neutral ($r = r_c$) or growing ($r > r_c$). For this figure, the critical wavenumber is $k_c = 1$.

we define the corresponding r value as $r = r_c$. The critical wavenumber $|\mathbf{k}| = k_c$ for which this occurs determines whether the bifurcation is *finite-wavelength* ($k_c > 0$) or *uniform* ($k_c = 0$). Most commonly, pattern-forming bifurcations are finite-wavelength, although there are some systems such as oscillatory chemical reactions and lasers [7] where a uniform instability can arise. An illustration of the behaviour of $\text{Re}(\lambda)$ for a finite-wavelength instability is given in figure 1.3; we can see that, for $r < r_c$, all modes have $\text{Re}(\lambda) < 0$ and are therefore decaying, implying the basic state is stable, while for $r > r_c$, a narrow band of wavenumbers around k_c have slightly positive growthrates. The size of container also plays an important role in the system dynamics as it determines the spectrum of wavenumbers which are unstable. When pattern formation takes place in a spatially extended (or infinite) container, the permitted modes form a continuous spectrum, which allows modulational effects. By contrast, for pattern formation in a container of small or moderate horizontal extent, the quantisation of the wavenumber spectrum ensures that the permitted wavenumbers are well separated in wavevector space and modulation over a long lengthscale is no longer possible.

In two spatial dimensions, there often exists a degeneracy whereby the linear problem simply determines the critical wavenumber k_c but does not specify a critical wavevector or direction. In this case, all modes lying on the critical circle $|\mathbf{k}| = k_c$ are neutrally stable at onset and the linear theory does not discriminate between competing configurations. Instead, it is through the effects of boundary conditions and the nonlinear coupling and interactions between these unstable modes that the selected pattern is

determined.

The second defining attribute of a pattern-forming instability is determined by the critical wavefrequency ω_c , defined as

$$\omega_c = \text{Im}(\lambda) \Big|_{(|k|=k_c, r=r_c)} \quad (1.2.1)$$

that is, the temporal frequency of wave-modes with the critical wavenumber at threshold. If $\omega_c = 0$ then the amplitudes of modes near k_c grow or decay monotonically in time, giving a *stationary* bifurcation. By contrast, if $\omega_c \neq 0$, then each mode corresponds to a travelling wave and propagates through the system. Either way, for one- or quasi-one-dimensional systems (where only one spatial dimension is important), the solution to the full nonlinear problem for r near r_c will take the form

$$\text{physical fields} \sim A_1(X, T)e^{i\omega_c t + ik_c x} + A_2(X, T)e^{i\omega_c t - k_c x} + \text{c.c.} + \text{h.o.t.}, \quad (1.2.2)$$

where ‘c.c.’ and ‘h.o.t.’ are shorthand for complex conjugate and higher-order terms respectively (higher-order in a sense that will be explained in §1.2.2). Such a prescription for the physical fields separates the dynamics into fast- and slowly varying components: the waves $e^{i\omega_c t \pm ik_c x}$ account for the fast variation of the pattern set by the scales of the original problem, while the complex amplitudes A_1 and A_2 evolve over the slow temporal scale T and (possibly) the long spatial scale X , which are related to the measures $|r - r_c|$ and $|k - k_c|$.

The third attribute is unrelated to the linear stability problem but is determined by the amplitude of the selected stable pattern beyond threshold. If the amplitude of the pattern varies smoothly as r is increased beyond r_c then the bifurcation is *supercritical*. However, if the amplitude of the pattern jumps discontinuously as r passes through r_c then the bifurcation is *subcritical*. In this case, the nontrivial solution branch can be traced back through $r = r_c$ and can possibly lead to a hysteretic region where both the basic state and the primary pattern can be stable.

To recap, the nature of a pattern-forming instability is determined by three things: whether or not k_c and ω_c are zero and whether the amplitude of the new pattern (after saturation) grows continuously from the instability point. The appropriate descriptions for finite-wavelength, supercritical bifurcations with $\omega_c = 0$ and $\omega_c \neq 0$ in one spatial dimension are described in greater detail in §1.3 and §1.4 respectively.

1.2.2 Amplitude equations

A common procedure underpinning the theoretical analysis of pattern-forming systems is to reduce the dimension of the system by distinguishing between dynamical

cally *active* modes, which are growing or neutrally stable, and *passive* modes, which decay rapidly. This decomposition allows the near-threshold dynamics to be determined purely in terms of the active modes; the passive modes are found to be entirely dependent or ‘slaved’ to the active modes. The decomposition is determined by the linear stability of the basic state and gives rise to two qualitatively different theoretical descriptions depending on whether pattern formation is taking place in a finite or infinite container.

For pattern formation in a finite container, the spectrum of the linear operator is discrete and the distinction between active and passive modes is straightforward: the active modes are those with positive, zero, or slightly negative growth, while strongly damped modes are passive. For r very close to r_c , the amplitudes of the passive modes will relax relatively quickly to a centre manifold [8, 9] where the dynamics take place over a slow timescale. On this manifold, the evolution of the active mode amplitudes is determined by a (usually finite) set of coupled ordinary differential equations (ODEs), called *amplitude equations*. These amplitudes will be functions of a slow timescale (typically of order $(r - r_c)^{-1}$) as well as the bifurcation parameter r_{bif} , where

$$r_{\text{bif}} = \left| \frac{r - r_c}{r_c} \right|. \quad (1.2.3)$$

Such approaches were developed through the work of Landau [10] and Stuart [11] amongst others. In this situation, the passive modes are ‘slaved’ in the sense of having their amplitudes determined in terms of the amplitudes of the active modes. Thus, the passive modes play no part in selecting the near-threshold pattern; such modes will appear in the final pattern only because they are regenerated by the nonlinear interactions of the active modes [8].

If the spectrum of the linear operator is continuous, as for pattern formation in a suitably large or infinite container, the behaviour of the active modes is captured by treating the amplitudes of certain specified modes as *envelopes* of the fast-varying pattern. Like the amplitudes in a finite system, these envelopes evolve over a slow timescale but they can also modulate over a large spatial scale. In this case, the slow dynamics are determined by a set of *partial* differential equations (PDEs) known as *envelope equations* [12]. These equations describe the slow, large-scale deformations of the basic patterns and have been used extensively in the study of pattern formation. This approach of capturing the near-threshold behaviour of a system through a slowly varying envelope was pioneered by Newell and Whitehead [13] and Segel [14], who investigated the formation of stationary patterns in convection systems, and is also associated with the names Ginzburg and Landau, through their work on superconductivity [15]. For simplicity, we will henceforth use the term ‘amplitude equations’ in reference to both

amplitude and envelope equations.

Amplitude equations have become an important tool in the study of non-equilibrium pattern formation and have been successfully applied to a wide range of physical systems; many qualitative and quantitative predictions have been compared favourably with experimental data [1, 8]. Even outside their range of applicability ($r \gg r_c$), amplitude equations are often studied as general models for pattern formation phenomena as they are the simplest nontrivial models that enjoy the correct symmetries.

We now consider the two main methods through which amplitude equations are derived.

1.2.3 Weakly nonlinear analysis

In most pattern-forming systems, the governing equations of motion are nonlinear (e.g., the Navier–Stokes equations) and cannot be solved analytically. Instead, when the bifurcation is supercritical, the appropriate amplitude equations can be determined perturbatively, using the distance above threshold $|r - r_c|$ as a small parameter in a multiple scale analysis. This process, known as *weakly nonlinear analysis*, is detailed in this section.

Consider a nonlinear two-dimensional system of the form

$$\mathbf{L}u = \mathcal{N}(u, \mathbf{x}, t), \quad (1.2.4)$$

where $u(\mathbf{x}, t)$ is the field variable, $\mathbf{x} = (x, y)$ the spatial coordinates and \mathbf{L} the matrix of linear operators; the function \mathcal{N} contains the nonlinear and forcing terms. We assume that the system has a control parameter r and a uniform solution $u(\mathbf{x}, t) \equiv u_{\text{unif}}$ that loses stability at $r = r_c$. Often, this state is the zero solution $u(\mathbf{x}, t)_{\text{unif}} \equiv \mathbf{0}$, corresponding to some homogeneous state (such as the purely conductive state in Rayleigh–Bénard convection). Alternatively, the field variables can be redefined so that this is the case (i.e. the system written in terms of ‘perturbation quantities’). The essence of the weakly nonlinear method is then to employ the small quantity $|r - r_c|$ as a perturbation parameter to describe the slow evolution and modulations of the solution to the linearised problem.

We begin by specifying a near-threshold condition $r = r_c + \epsilon^m r_m$, where $\epsilon \ll 1$ and m is some integer, and expand the variables as series in the small parameter ϵ :

$$u(\mathbf{x}, t) = u_{\text{unif}} + \sum_n \epsilon^n u_n(\mathbf{x}, t). \quad (1.2.5)$$

Furthermore, in order to capture the dynamics which result just beyond a bifurcation, we introduce slow scales for temporal and spatial evolution: $T = \epsilon^p t$ and $X = \epsilon^q x, Y =$

$\epsilon^q y$. The action of the derivatives then becomes

$$\frac{\partial}{\partial t} \mapsto \frac{\partial}{\partial t} + \epsilon^p \frac{\partial}{\partial T}, \quad \frac{\partial}{\partial x} \mapsto \frac{\partial}{\partial x} + \epsilon^q \frac{\partial}{\partial X}, \quad \frac{\partial}{\partial y} \mapsto \frac{\partial}{\partial y} + \epsilon^q \frac{\partial}{\partial Y}. \quad (1.2.6)$$

In general circumstances, the slow time modulation of the basic pattern takes place over a timescale of order $(r - r_c)^{-1}$ implying $p = m$. The scale of slow spatial modulations is determined by the Taylor expansion of the growthrate λ about $k = k_c$ and is usually found to be of order $(r - r_c)^{-1/2}$ giving $q = m/2$.

After substituting (1.2.5) into (1.2.4), we then solve the problems that occur at successive orders of ϵ . The $O(1)$ problem is automatically satisfied since \mathbf{u}_0 is a solution to the full problem, but at $O(\epsilon)$, we recover a linear problem

$$\mathbf{L}\mathbf{u}_1 = \mathbf{0}, \quad (1.2.7)$$

whose general solution (which can normally be found explicitly) we write as $\mathbf{u}_1(\mathbf{x}, t) = \mathbf{u}_{\text{lin}}(\mathbf{x}, t)$. This solution will comprise components evolving over the fast scales x, y and t multiplied by amplitudes modulating slowly in space and time (cf. (1.2.2)); the evolution of these amplitudes will be determined at higher order.

At subsequent orders of ϵ , problems of the form

$$\mathbf{L}\mathbf{u}_n = \mathcal{N}_n \quad (1.2.8)$$

arise, where \mathcal{N}_n denotes the $O(\epsilon^n)$ contributions from the nonlinear, forcing and slow-derivative terms. The procedure we must follow for each of these problems is twofold. Firstly, we must ensure that the expansion (1.2.5) is asymptotic by prescribing that each \mathbf{u}_n remains bounded. This requires the imposition of *solvability conditions*, which are defined through application of the Fredholm Alternative theorem (see Grindrod [16] and Kreyszig [17] for further details of this result).

Theorem 1 (The Fredholm Alternative). *For a bounded linear operator \mathbf{L} and a problem of the form*

$$\mathbf{L}\mathbf{u} = \mathbf{f} \quad (1.2.9)$$

for some continuous \mathbf{f} , one of the following alternatives holds:

1. the inhomogeneous equation (1.2.9) has a unique solution, while the homogeneous equation $\mathbf{L}\mathbf{u} = \mathbf{0}$ has only the trivial solution $\mathbf{u} = \mathbf{0}$;
2. the homogeneous equation $\mathbf{L}\mathbf{u} = \mathbf{0}$ and the adjoint homogeneous problem, $\mathbf{L}^\dagger \mathbf{v} = \mathbf{0}$, have $n \in \mathbb{Z}^+$ linearly independent solutions. In this case, (1.2.9) has a solution if and only if

$$\langle \mathbf{f}, \mathbf{v} \rangle = 0, \quad (1.2.10)$$

for each \mathbf{v} that satisfies $\mathbf{L}^\dagger \mathbf{v} = \mathbf{0}$.

Note that the adjoint \mathbf{L}^\dagger of a linear operator \mathbf{L} is defined by the implicit relation

$$\langle \mathbf{L} \mathbf{u}, \mathbf{v} \rangle = \langle \mathbf{u}, \mathbf{L}^\dagger \mathbf{v} \rangle, \quad (1.2.11)$$

where the notation $\langle \mathbf{u}, \mathbf{v} \rangle$ refers to a inner product, given by

$$\langle \mathbf{u}, \mathbf{v} \rangle = \int_{\Omega} \mathbf{u} \cdot \mathbf{v}^* \, dx, \quad (1.2.12)$$

where Ω is the whole domain and the asterisk indicates complex conjugation.

Of course, it is the second of these alternatives that applies to weakly nonlinear analyses and solvability conditions are generated through the condition (1.2.10) which can be rewritten

$$\langle \mathcal{N}_n, \mathbf{w} \rangle = 0 \quad (1.2.13)$$

for each \mathbf{w} that solves the adjoint problem $\mathbf{L}^\dagger \mathbf{w} = \mathbf{0}$. In most problems, this condition is far simpler than it appears: for systems comprising a single PDE, the solvability conditions are usually harvested by setting the coefficients of the ‘secular’ terms (those proportional to the solutions of the linear problem) to zero. However, when a problem takes the form of a system of PDEs, the solvability conditions are somewhat more involved. We don’t explicitly outline the method for deriving solvability conditions for these situations here, rather we direct the reader to §2.3.1 and §4.4.3, where the derivation and application of solvability conditions for systems of PDEs is expounded for two different problems.

The second stage of solving a problem of the form (1.2.8) involves accounting for the nonlinearities and slow derivatives that occur at each order: the ‘nonsecular’ terms. This is simply done by introducing a planform for \mathbf{u}_n composed of the same nonsecular terms but each with an undetermined amplitude. Through substitution of this expression into (1.2.8), some manipulation allows the unspecified amplitudes of \mathbf{u}_n to be determined. Thus, the higher-order terms can be written in terms of the amplitudes of the linear solution; such modes are said to be ‘slaved’ to the linear solution.

This procedure continues at each order of ϵ up to $O(\epsilon^{m+1})$, where the solvability conditions will give rise to a set of evolution equations for the amplitudes of the linear solution.

It is worth noting that in the case of a subcritical bifurcation, the derivation (and justification) of amplitude equations is less clear. In general, higher-order nonlinearities need to be included to allow large-amplitude saturation, resulting in equations that do not scale uniformly with ϵ . Often such equations are referred to as *reconstituted amplitude equations* and comprise the combination of solvability conditions from several orders of ϵ .

1.2.4 Symmetry considerations

Aside from asymptotics, amplitude equations can be derived through an appeal to the symmetries of the underlying system [18, 19]. By retaining only terms which enjoy a specified set of symmetries subject to constraints on the asymptotic order of each term, one can derive universal amplitude equations to describe disparate systems which share the same symmetries. This method of constructing amplitude equations is applied in §3.2 in the context of deriving generic equations for oscillatory pattern formation with a conservation law. Such methods are a simple application of equivariant bifurcation theory [20], for which a large body of literature exists.

1.3 Stationary pattern formation

When the critical wavefrequency ω_c is zero at a pattern-forming bifurcation, the weakly nonlinear patterns will be stationary in space. Thus, close to the threshold of a one-dimensional, supercritical, stationary bifurcation, one can employ the ansatz

$$\text{physical fields} \sim A(X, T)e^{ik_c x} + \text{c.c.} + \text{h.o.t.}, \quad (1.3.1)$$

where A is a small complex amplitude and ‘h.o.t.’ (higher-order terms) refers to the nonlinear harmonics of the primary mode, such as terms proportional to $e^{2ik_c x}$. Now, assuming the system is invariant under the transformations

$$\text{translation:} \quad x \mapsto x + x_0, \quad (1.3.2a)$$

$$\text{reflection:} \quad x \mapsto -x, \quad (1.3.2b)$$

the generic amplitude equation for A is the real Ginzburg–Landau (RGL) equation [13, 14, 15, 21]:

$$A_T = r_2 A + A_{XX} - A|A|^2, \quad (1.3.3)$$

where $X = \epsilon x$ and $T = \epsilon^2 t$ are slow scales for space and time, and r_2 is the bifurcation parameter defined by the supercriticality condition $r = r_c + \epsilon^2 r_2$. Note that here a rescaling has been carried out to bring the coefficients of the diffusive and nonlinear terms to unity; by a further rescaling, r_2 can be scaled out; however, we choose not to do this so as to be consistent with previous literature and to avoid a control-parameter dependent scaling.

The RGL equation arises generically for a stationary, supercritical, finite-wavelength bifurcation when the system is invariant under the symmetries (1.3.2) and all modes away from $k = k_c$ have negative growth [22]. The translation symmetry (1.3.2a) prescribes the form of the cubic term and ensures the coefficients are real, while (1.3.2b)

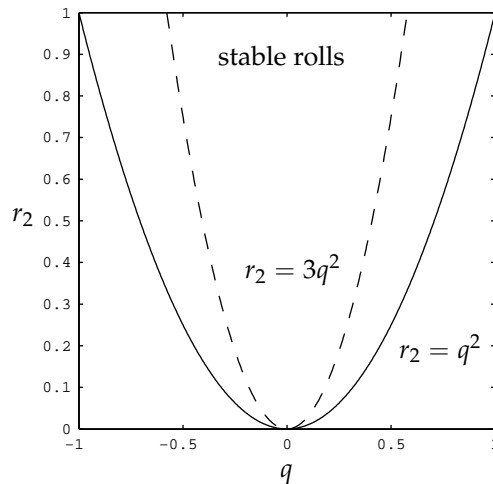


Figure 1.4: Stability diagram in (q, r_2) -space for roll solutions to the RGL equation (1.3.3). Rolls are stable inside the parabola $r_2 = 3q^2$, while outside this boundary rolls are susceptible to the Eckhaus instability (see figure 1.5 for an illustration of the behaviour of $|A|$ as a roll solution undergoes this instability).

dictates that the second-order derivative term A_{XX} arises as the lowest spatial derivative. It has been shown by Elphick et al. [23] that (1.3.3) is the normal form when an eigenvalue crosses the real axis at the origin for a finite wavenumber. The RGL equation was first derived as a long-wave amplitude equation by Newell and Whitehead [13] and by Segel [14] in the context of Rayleigh–Bénard convection. It also can be applied to Taylor–Couette flow [24, 25] and electroconvection in liquid crystals [7, 25, 26]. Despite its widespread use over the last 30 years, only recently has a rigorous justification of the equation emerged [22, 27].

The RGL equation admits ‘roll’ solutions (a term coined for convection systems) of the form $A = Qe^{iqX}$ where $Q^2 = r_2 - q^2$. These solutions describe steady periodic patterns with wavenumber near the critical value (which corresponds to $q = 0$). For $q^2 < r_2/3$, these equilibria are stable, whereas for $q^2 > r_2/3$, they are unstable to the Eckhaus instability [28, 29, 30, 31, 32]; a stability diagram for roll solutions to the RGL equation is illustrated in figure 1.4. When a solution becomes unstable to the Eckhaus instability, the value of the local wavenumber q is altered by adding or losing rolls so that a new and stable solution, lying inside the parabola $r_2 = 3q^2$, is selected. For a finite domain L , the permitted wavenumber spectrum is quantised and must take values $q = n(2\pi/L)$, where n is an integer known as the *winding number*. Figure 1.5 illustrates the Eckhaus instability for rolls with winding number 10, which gives rise to the selection of a new (and stable) roll pattern with winding number 5 (lying inside

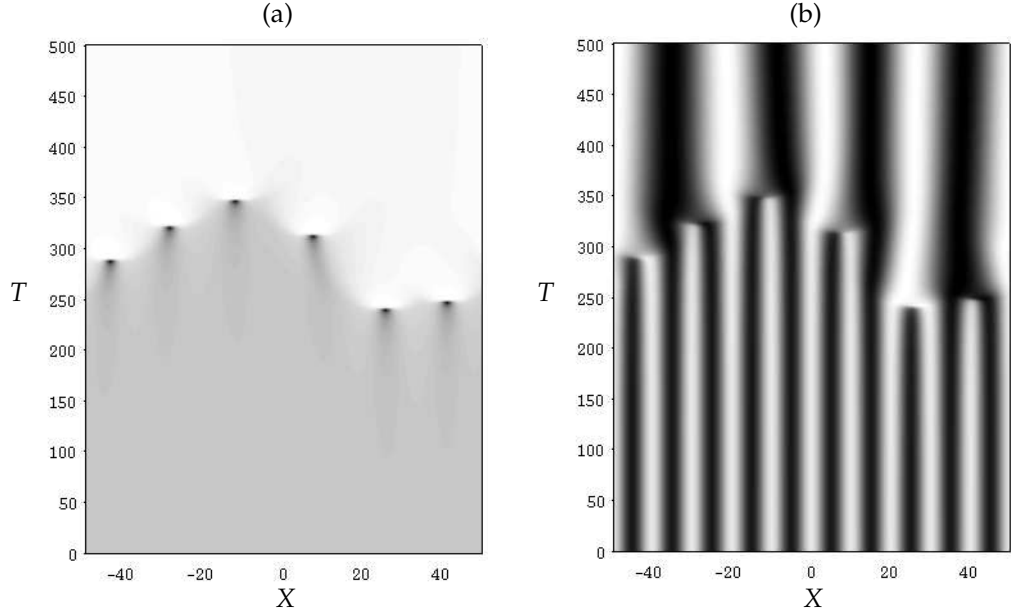


Figure 1.5: The Eckhaus instability of roll solutions to the RGL equation: surface plots of (a) $|A|$ and (b) $\text{Re}(A)$ from simulations in a domain of length $L = 100$. The initial condition was a roll of the form $\sqrt{r_2 - q^2}e^{iqX}$ with $r_2 = 1$ and $q = 20\pi/L$ perturbed by a layer of small-amplitude noise.

$r_2 = 3q^2$). This change in wavenumber is a discontinuous jump as q can only take values that fit into the container. Since q is well defined and continuous whenever $|A|$ is nonzero, these jumps occur at localised points in space and time where $|A| = 0$, where the wavenumber q is not defined. These ‘phase-slips’, which allow waves to be added or lost, are easily seen in figure 1.5(a) and the corresponding ‘slips’ in wavenumber are clearly visible in figure 1.5(b). The Eckhaus instability generalises to travelling waves as well as two-dimensional patterns [33, 34] and has been the subject of considerable attention [21, 29, 35] (see also section §1.4).

The RGL equation can be written in variational form

$$A_T = -\frac{\delta\mathcal{F}}{\delta A^*}, \quad \text{where} \quad \mathcal{F} = \int \left[-r_2|A|^2 + |A_X|^2 + \frac{1}{2}|A|^4 \right] dX, \quad (1.3.4)$$

and the asterisk denotes complex conjugation. It can then be seen that

$$\frac{d\mathcal{F}}{dt} = - \int |A_T|^2 dX < 0 \quad (1.3.5)$$

and thus \mathcal{F} is a Lyapunov functional, occupying the role of a ‘free energy’ function. Many aspects of the dynamics can then be reformulated in terms of the system relaxing to the lowest ‘free-energy’ states, the extrema of \mathcal{F} ; oscillatory solutions are not permitted. It is known that the RGL admits only two types of stable stationary solution: Eckhaus-stable rolls and a solution composed of stationary fronts [31, 36, 37]

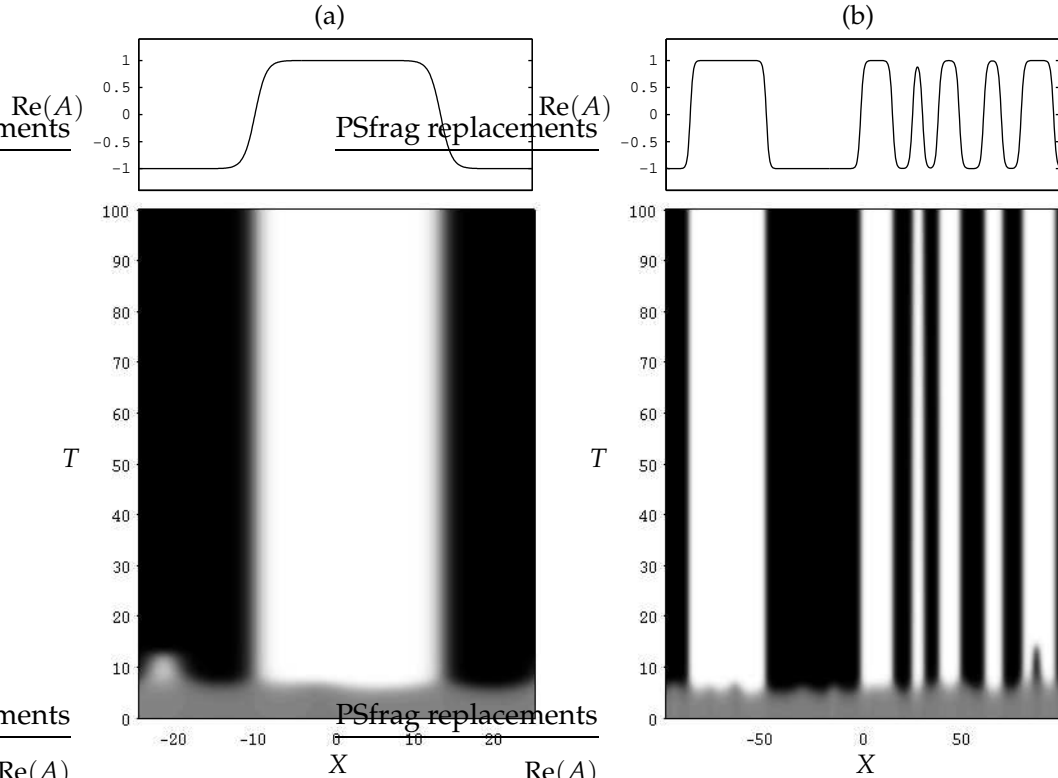


Figure 1.6: Front solutions to the RGL equation: (a) two steady fronts in a domain of length $L = 50$; (b) multiple fronts in a domain of length $L = 200$. The space-time plots show the evolution of $\text{Re}(A)$ from a initial condition of small-amplitude noise; the imaginary part of A remains zero in each case.

(figure 1.6); all quasiperiodic and homoclinic solutions are unstable [38]. This situation is substantially altered by the presence of a slow diffusive field which can facilitate the stabilisation of a wide range of patterns; we examine this topic in more detail in §3.1.

1.4 Oscillatory pattern formation

When both the critical wavenumber k_c and wavefrequency ω_c are nonzero at a pattern-forming bifurcation, the uniform state undergoes a Hopf–Turing bifurcation and the primary modes take the form of travelling waves (TWs). However, depending on the existence of a reflectional symmetry, we either need to consider a single TW or two independent counter-propagating modes. Each case demands a different amplitude system and we consider each separately now.

1.4.1 The complex Ginzburg–Landau equation

For systems without reflectional symmetry, only a single TW need be considered and the nonlinear dynamics are captured by an ansatz of the form

$$\text{physical fields} \sim A(X, T)e^{i\omega_c t + ik_c x} + \text{c.c.} + \text{h.o.t.} \quad (1.4.1)$$

Assuming the bifurcation is supercritical, the generic equation for the evolution of A is the complex Ginzburg–Landau (CGL) equation [7]:

$$A_T = r_2 A + (1 + ic_1)A_{XX} - (1 - ic_2)|A|^2 A, \quad (1.4.2)$$

where the units of length and amplitude have been chosen to set various coefficients to unity. The coefficients c_1 and c_2 characterise linear and nonlinear dispersion respectively, while r_2 is a control parameter. Depending on the values of c_1, c_2 and r_2 , a huge range of behaviours are possible [7]. Of course, the RGL equation (1.3.3) corresponds to the special case $(c_1, c_2) = (0, 0)$.

The CGL equation is one of the most celebrated equations in applied mathematics. It describes qualitatively, and often quantitatively, a vast array of phenomena including nonlinear waves, second-order phase transitions, Rayleigh–Bénard convection and superconductivity (see the ample review of Aranson and Kramer [7] and references therein). The CGL equation is the generic amplitude equation for an order parameter undergoing a continuous Hopf bifurcation on long space and timescales close to the critical point of instability, and has been the subject of a tremendous volume of analysis. In general, the group velocity of a travelling wave-packet will be nonzero and so, in the laboratory frame, the CGL equation should include an advective term sA_X (s is the group velocity). However, for an infinite domain or periodic boundary conditions, one can write the CGL equation in a frame moving with the group velocity ($x \mapsto x \pm st$), eliminating the offending term.

The CGL equation was introduced phenomenologically by Newell and Whitehead [39] in the context of Rayleigh–Bénard convection but has been derived separately by several other authors. For instance, the CGL equation was derived by Stewartson and Stuart [40] to describe the instability of Poiseuille flow, by Ermentrout [41] who studied reaction-diffusion systems and by Kuramoto [42] for chemical reactors.

The CGL equation admits travelling wave (TW) solutions of the form $Qe^{ivT+iqX}$ where

$$Q^2 = r_2 - q^2, \quad v = r_2 c_2 - (c_1 + c_2)q^2. \quad (1.4.3)$$

The stability of these solutions is determined by examining small disturbances with wavenumber l and considering the limit of small wavenumbers $l \rightarrow 0$ (or equivalently,

large wavelengths). In this limit, the stability of TWs is determined by the eigenvalue [41, 43]:

$$\lambda = -2il(c_1 + c_2) - D_{\parallel}l^2 + O(l^3), \quad (1.4.4)$$

where

$$D_{\parallel} = 1 - c_1c_2 - \frac{2q^2(1 + c_2^2)}{r_2 - q^2}. \quad (1.4.5)$$

Since the leading order component of (1.4.4) is purely imaginary, any instability is convective in nature and the stability criterion is determined at higher order. We see that TWs are unstable to long-wavelength perturbations when $D_{\parallel} < 0$ and furthermore, all TWs are unstable when the stability criterion $c_1c_2 < 1$ (often called the Newell or Benjamin–Feir criterion) is violated [12, 21, 28, 41, 44]. This instability, which has a parabolic stability boundary,

$$r_2 = \left(\frac{2(1 + c_2^2)}{1 - c_1c_2} + 1 \right) q^2, \quad (1.4.6)$$

in (q, r_2) -space, is a combination of the Eckhaus [28] (the condition $D_{\parallel} < 0$ reduces to the Eckhaus condition $q^2 > r_2/3$ when $c_1 = -c_2$) and Benjamin–Feir [21, 45] instabilities and is of a convective nature. Henceforth, we will refer to this instability as the Benjamin–Feir–Eckhaus (BFE) instability. The manifestation of this instability leads either to wavenumber reselection (cf. the Eckhaus instability of figure 1.5) [35], or a bifurcation to modulated-amplitude waves [46, 47].

Unlike the RGL equation, the CGL equation is not relaxational except for the special case of $c_1 = -c_2$ where (1.4.2) can be transformed to

$$A_T = (1 - ic_2)(A + A_{XX} - |A|^2A) \quad (1.4.7)$$

and subsequently written as

$$A_T = -(1 - ic_2) \frac{\delta \mathcal{F}}{\delta A^*}, \quad (1.4.8)$$

where \mathcal{F} is defined in (1.3.4). Additionally, in the limit of $(c_1, c_2) \rightarrow (\infty, -\infty)$, the CGL equation (after some rescaling) transforms into the nonlinear Schrödinger equation:

$$iA_T = A_{XX} \pm |A|^2A, \quad (1.4.9)$$

which is both Hamiltonian and integrable (it has known soliton solutions). Thus, the CGL equation can be thought of as a dissipative extension of the conservative nonlinear Schrödinger equation. The fact that the CGL equation reduces to a relaxational equation in one limit and a Hamiltonian equation in another is indicative of the range

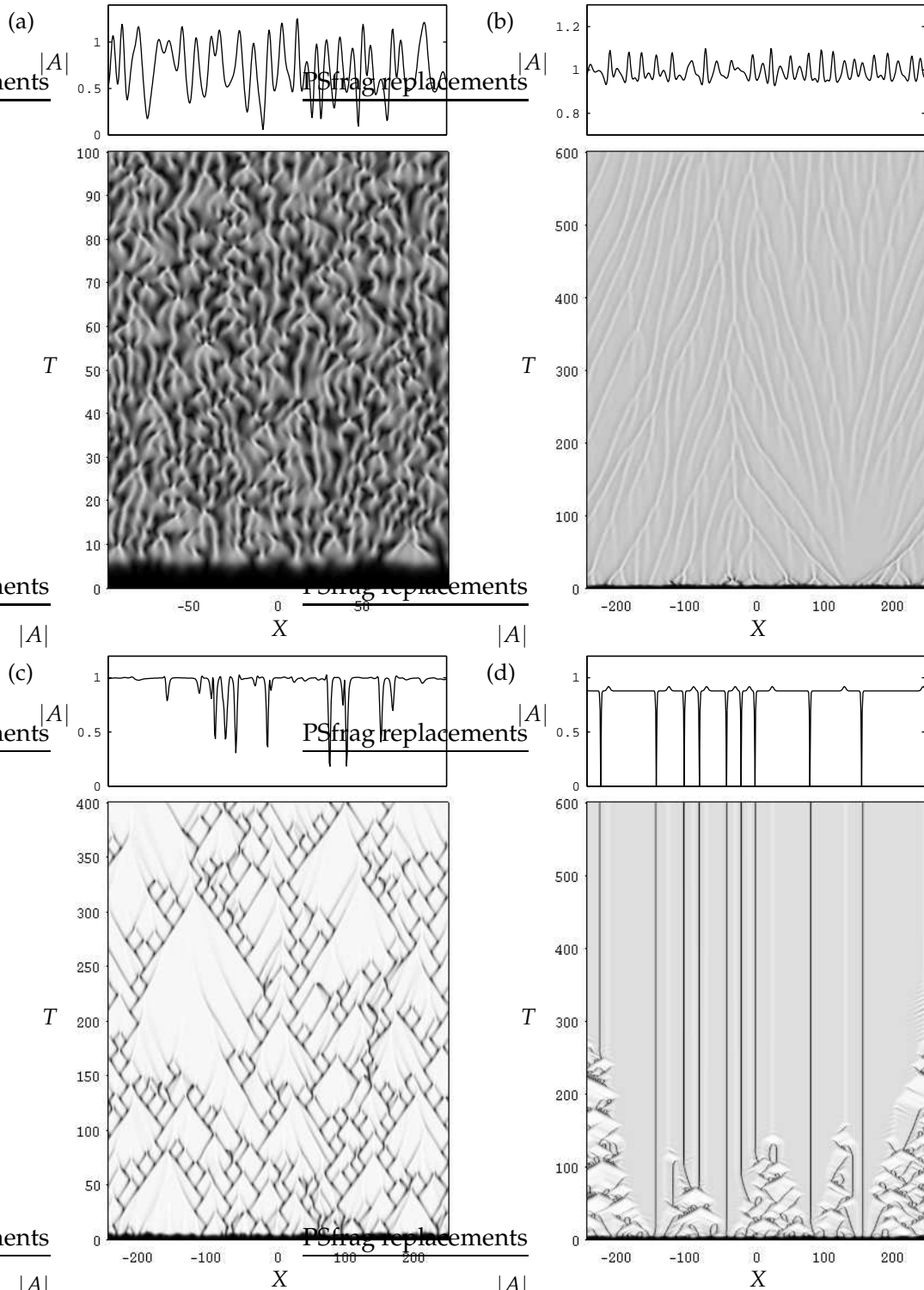


Figure 1.7: Chaotic behaviour in the CGL equation: (a) defect-mediated chaos in a container of size $L = 200$ and $(c_1, c_2) = (3, 0.67)$; (b) phase turbulence with $L = 500$ and $(c_1, c_2) = (3, 2)$; (c), (d) spatiotemporal intermittency with $L = 500$ and $(c_1, c_2) = (0.5, 1.43), (-0.75, 5.55)$ respectively.

of interesting behaviours that it can produce. Indeed, aside from travelling waves, a zoo of other solutions and behaviours in the CGL equation have been documented, featuring several different flavours of chaos (figure 1.7). Shraiman et al. [48] distinguished between two forms of turbulent behaviour found beyond the regime of stable TWs: ‘defect-mediated turbulence’, involving large amplitude fluctuations and phase slips, and ‘phase turbulence’ (similar to that seen in the Kuramoto–Sivashinsky equation [49]). The distinction between these two states is the presence of phase slips, where the winding number of the solution is allowed to change. A further behaviour, ‘spatio-temporal intermittency’, was identified by Chaté [50] in the regime where TWs are stable. This regime is characterised by linearly stable TWs separated by localised objects evolving in a complicated spatio-temporal manner. In figure 1.7(c), the objects, which correspond to dips in $|A|$ propagate and branch continuously, leaving triangular regions of TWs (in (X, T) -space). On the other hand, figure 1.7(d) illustrates a stable, stationary arrangement of shocks (localised pulses of $|A|$) and Nozaki–Bekki holes [51], where $|A|$ locally equals zero. Phase diagrams for (c_1, c_2) -space, cataloguing the regions where these various behaviours are observed, have been provided by several authors, including Shraiman et al. [48] and Chaté [50].

Nozaki–Bekki holes belong to a family of solutions known as *coherent structures* that are functions of a moving coordinate $\xi = X - cT$ for some real speed c . TWs themselves are an elementary coherent structure, but many more complicated examples exist such as shocks, sink, sources, homoclines and many others (see [7, 52] for more details). In general, steady coherent structures in one dimension satisfy three first-order ODEs for real variables and can be classified as pulses, fronts or domain boundaries [1]. A thorough examination of coherent structures in the one-dimensional CGL equation is provided by van Saarloos and Hohenberg [52], who introduce a classification system based on simple counting arguments.

1.4.2 Coupled Ginzburg–Landau equations

When a left-right reflectional symmetry is enjoyed by a pattern-forming system undergoing a supercritical Hopf bifurcation, the weakly nonlinear ansatz must include both left- and right-travelling waves:

$$\text{physical fields} \sim A_1(X, T)e^{i\omega_c t + ik_c x} + A_2(X, T)e^{i\omega_c t - ik_c x} + \text{c.c.} + \text{h.o.t.} \quad (1.4.10)$$

In the CGL equation, which describes the slow modulation of a single TW, the role of energy transport is usually eliminated by a Galilean transformation (assuming an infinite container or periodic boundary conditions). This, however, is not possible when

counter-propagating waves are considered and the appropriate set of amplitude equations is determined by the size of the rate of energy transport, measured by the linear group velocity s . When s is of the same order as the perturbation amplitudes A_1, A_2 , the appropriate amplitude equations are the complex coupled Ginzburg–Landau (CCGL) equations [53, 54, 55]:

$$A_{1T} + sA_{1X} = r_2A_1 + (1 + ic_1)A_{1XX} - (1 - ic_2)|A_1|^2A_1 - (b_3 - ic_3)|A_2|^2A_1, \quad (1.4.11a)$$

$$A_{2T} - sA_{2X} = r_2A_2 + (1 + ic_1)A_{2XX} - (1 - ic_2)|A_2|^2A_2 - (b_3 - ic_3)|A_1|^2A_2. \quad (1.4.11b)$$

In addition to the dispersion parameters c_1, c_2 shared with the CGL equation, the CCGL equations accommodate three extra coefficients s, b_3 and c_3 which characterise linear group velocity, nonlinear coupling and cross-dispersion respectively. Through variation of these five parameters, a large range of behaviours is possible giving rise to a highly complicated parameter space [56, 57, 58].

Several physical systems undergo an instability accounted for by the CCGL equations. Most prominent are convection experiments in doubly diffusive or binary fluids [59], which have shown good qualitative agreement with the CCGL equations [60, 61]. Other applications are Rayleigh–Bénard convection, Taylor–Couette instabilities between co-rotating cylinders, electroconvection in nematic liquid crystals [62] and the transverse field of high Fresnel-number lasers [1].

The CCGL equations admit two plane wave solutions, TWs matching those found in the CGL equation and standing waves (SWs):

$$\text{TWs :} \quad A_1 = \sqrt{r_2 - q^2}e^{iqX + isT}, \quad A_2 = 0; \quad (1.4.12a)$$

$$\text{SWs :} \quad A_1 = \sqrt{\frac{r_2 - q^2}{1 + b_3}}e^{ivT + iqX}, \quad A_2 = \sqrt{\frac{r_2 - q^2}{1 + b_3}}e^{ivT - iqX}. \quad (1.4.12b)$$

When the cross-coupling coefficient b_3 satisfies $b_3 > 1$, the two waves suppress each other and TWs can be stable. In this case, one only needs to consider the CGL equation; the counter-propagating mode can be discounted. On the other hand, in the case of $|b_3| < 1$, the superposition of oppositely travelling waves, in the form of SWs, becomes important. In contrast to TWs in the CGL equation, relatively little literature has been devoted to these SW solutions and their modulational instabilities. Early work, concentrating on a few special cases, was provided by Matkowsky and Volpert [43], Couillet et al. [56] and Sakaguchi [53]. In particular, the long-wave instability of SWs in the centre of the wavenumber band ($q = 0$) was analysed through phase equations [53, 56]. The first survey of the modulational behaviour away from band-centre

was provided by Riecke and Kramer [54], who identified a number of qualitatively different scenarios. The modulational stability of SWs was found to be limited by two long-wavelength destabilisation mechanisms as well as a generic, finite-wavelength instability. Firstly, a so-called *conservative-type* instability (the eigenvalues sum to zero) can take place, where a pair of eigenvalues cross from the imaginary plane to the real line, giving steady instability. In (q, r_2) -space, this is delimited by the lines $q = q_{\pm}$ where

$$q_{\pm} = -\frac{1}{2} \left(\frac{s(1 \pm b_3)}{c_1(1 \pm b_3) + (c_2 \pm c_3)} \right); \quad (1.4.13)$$

SWs can be stable either inside or outside the interval delimited by q_{\pm} . In addition, at higher order, the stability of SWs is bounded by a shifted parabola

$$r_2 = \beta_1 q + \beta_2 q^2, \quad (1.4.14)$$

where β_1 and β_2 are complicated functions of the system parameters (omitted here, see [54]). Depending on the parameters, this parabola can be convex from above or below, and SWs can be stable both inside and outside the boundary. The instability this parabola delimits is convective in nature and, despite having a much more complicated boundary, is the analogue of the Benjamin–Feir–Eckhaus instability for TWs. Thus, the dominant nonlinear behaviour beyond these secondary instability thresholds is wavenumber reselection. In contrast to the relatively simple stability regions of TWs in the CGL equation, the boundaries (1.4.13) and (1.4.14) give rise to a large number of qualitatively different stability regions for SWs (see [54, figures 3,4 and 5]).

As with the CGL equation, a host of coherent structures are supported in the CCGL equations. A detailed investigation into the role of coherent structures in the CCGL equations was reported by van Hecke et al. [55], drawing attention to the importance of sinks and sources. Cross [59] examined the CCGL equations in a finite geometry and found various nonlinear solutions such as confined and blinking states. Elsewhere, Sakaguchi [58] numerically investigated the CCGL equations, focussing on the appearance of the inversely-travelling wave component when the TWs are spatially chaotic; two-mode solutions termed ‘soliton lattices’ were observed, featuring interchanging A_1 - and A_2 -dominant regions. Further studies of the behaviour of the CCGL equations and their close relatives have been provided by Amengual and coworkers [63, 64], Malomed [65], Montagne and Hernández-García [66] and Deissler [67].

As mentioned above, one must be cautious about the range of validity of the CCGL equations. The advection terms in (1.4.11) are only formally valid near a co-dimension two point, where the linear group velocity is small at the bifurcation point. Such a bifurcation has been noted in lasers [68] as well as binary fluid mixtures [59]; however,

in other realistic TW systems, the group velocity is of order unity ($s = O(\epsilon^{-1})$) and the CCGL equations do not scale uniformly. In this case, Knobloch and De Luca [69] and Vega [70] have found the appropriate amplitude equations to be the mean-field Ginzburg–Landau (MFGL) equations:

$$A_{1T} = rA_1 + (1 + ic_1)A_{1\zeta\zeta} - (1 + ic_2)|A_1|^2 A_1 - (b_3 - ic_3)\langle |A_2|^2 \rangle A_1, \quad (1.4.15a)$$

$$A_{2T} = rA_2 + (1 + ic_1)A_{2\eta\eta} - (1 + ic_2)|A_2|^2 A_2 - (b_3 - ic_3)\langle |A_1|^2 \rangle A_2, \quad (1.4.15b)$$

where $A_1(\zeta, T)$ and $A_2(\eta, T)$ are functions of the co-moving coordinates $\zeta = x + s\tau$ and $\eta = x - s\tau$ respectively and $\langle \dots \rangle$ denotes integration over a single period in ζ or η . Physically, this corresponds to the waves propagating many times through the system on the timescale set by dispersion and diffusion, meaning waves interact only through their spatial average, giving a *nonlocal* coupling [71, 72].

The MFGL equations exhibit much simpler linear stability behaviour for SWs than the CCGL equations. However, despite their limitations, the CCGL equations remain far more popular than the MFGL equations with theoreticians. They are often taken as *model* equations, with the expectation that since they possess the correct symmetries, they will in some sense be valid at a finite distance above threshold where the diffusive and group velocity timescales may be of similar order.

1.5 Pattern formation with a conservation law

The RGL and CGL equations (and their variants) accurately describe the near-threshold dynamics of many pattern-forming systems; however, there is an important class of problems for which they are not suitable. Such systems arise when pattern formation occurs in the presence of a conservation law [1], a common component of many physical systems. Recent work by Couillet et al. [56], Fauve et al. [73] and Matthews and Cox [74, 75] has brought to light the result that a conservation law leads to a large-scale neutral mode that must be included in the asymptotic analysis. Remarkably, the presence of this mode then gives rise to a new instability mechanism that can destabilise patterns arising from the primary instability. The extension of this concept provides the central aim of this thesis and this section is devoted to expounding some of the consequences of a conservation law that have been published elsewhere. For simplicity, we follow the analysis of Matthews and Cox [74] and consider below the generic behaviour from a one-dimensional partial differential equation (PDE) with a conserved quantity; however, the results easily extend to systems of PDEs as well as higher dimensions (see Cox and Matthews [75]).

1.5.1 One-dimensional behaviour

A one-dimensional PDE for a conserved quantity $w(x, t)$ with control parameter r , must take the form

$$\frac{\partial w}{\partial t} + \frac{\partial}{\partial x} F(\partial_x, w; r) = 0, \quad (1.5.1)$$

where F is some (usually nonlinear) function of w and r , possibly incorporating further spatial differentiation. Hence, with suitable boundary conditions, integrating over the whole domain Ω yields the conservation condition

$$\frac{d}{dt} \int_{\Omega} w \, dx = 0. \quad (1.5.2)$$

We assume that (1.5.1) admits a uniform solution $w_{\text{unif}}(x, t)$ which, without loss of generality, we take to be $w_{\text{unif}}(x, t) \equiv 0$ and we assume further that w_{unif} undergoes a finite-wavelength bifurcation at $r = r_c$ with critical wavenumber $k = k_c$. It then follows that the linearised expression for $\partial w / \partial t$ about $w_{\text{unif}}(x, t)$ contains only x -derivatives. Consequently, the growthrate λ of perturbations $e^{\lambda t + ikx}$ tends to zero in the limit of small wavenumbers, $k \rightarrow 0$, indicating that large-scale modes are neutrally stable (cf. figure 1.8). It is important to note that these large-scale modes do not affect the linear stability problem, but must be included in a weakly nonlinear analysis in order to derive asymptotically consistent amplitude equations. Note that for a single PDE the large- and small-scale near-neutral modes all derive from a single branch. By contrast, in systems of PDEs, the neutral stability of long-wave modes and the finite-wavelength bifurcation can arise from different branches of eigenmodes deriving from different equations (this is the case for the model equations (2.2.1) of chapter 2).

The weakly nonlinear behaviour is dependent on the action of the reflection symmetry ($x \mapsto -x$) on the large-scale mode, for which two distinct behaviours have been identified [74]:

$$\text{'velocity-like' behaviour:} \quad x \mapsto -x \quad w \mapsto -w, \quad (1.5.3a)$$

$$\text{'density-like' behaviour:} \quad x \mapsto -x \quad w \mapsto w. \quad (1.5.3b)$$

Velocity-like behaviour arises when the system has a Galilean invariance [76] but not necessarily a conservation law, representing an alternative scenario where a neutrally stable zero mode exists. This case has been examined in detail [76, 77, 78, 79] but we draw attention to Matthews and Cox [80], who showed that the usual Ginzburg–Landau equation is replaced by

$$A_T = A + A_{XX} - ifA, \quad (1.5.4a)$$

$$f_T = \nu f_{XX} - (|A|^2)_X, \quad (1.5.4b)$$

where f is a mean mode. The strong coupling between the pattern and mean mode in these equations prevents the stabilisation of steady states and numerical simulations have revealed the near-onset dynamics to consist of small-amplitude chaos [80]. The equations (1.5.4) are also the leading-order amplitude equations for systems obeying a conservation law with velocity-like behaviour, but without Galilean invariance. However, these two descriptions match only up to quadratic order; if higher-order terms are included then differing amplitude equations are recovered.

The alternative case of density-like behaviour of the large-scale mode has received rather more attention (e.g., [74, 75, 81]), especially in the case of a stationary bifurcation [74, 75]. In this case, the linearised expression for $\partial w/\partial t$ can only contain even x -derivatives. Consequently, on large spatial scales, the leading-order linear term is the second derivative w_{xx} and so large-scale modes obey the diffusion equation. In the case of a one-dimensional, finite-wavelength bifurcation with a density-like conserved quantity, the near-onset patterns are described by an ansatz,

$$w(x, t) \sim A(X, T)e^{ik_c x} + A^*(X, T)e^{-ik_c x} + B(X, T), \quad (1.5.5)$$

where X and T are the usual rescaled forms of x and t and A and B are complex and real amplitudes respectively. For this scenario Matthews and Cox [74] derived the following set of amplitude equations:

$$A_T = A + A_{XX} - A|A|^2 - AB, \quad (1.5.6a)$$

$$B_T = \sigma B_{XX} + \mu (|A|^2)_{XX}, \quad (1.5.6b)$$

where $\sigma > 0$ so that, in the absence of A , large-scale modes relax diffusively; μ can take both positive and negative values. These equations had previously been introduced by Couillet and Iooss [82] in a different context and were also derived by Komarova and Newell [83] for an instability of sand ripples.

The system (1.5.6) admits roll solutions $A = Qe^{iqX}$, $B = 0$, where $Q^2 = 1 - q^2$, which are unstable to monotonically growing perturbations if

$$2(\mu - \sigma)Q^2 + \sigma(4q^2 - l^2) > 0, \quad (1.5.7)$$

where l is the perturbation wavenumber. Thus, the most dangerous disturbances arise in the long-wave limit $l \rightarrow 0$ and rolls are unstable when their wavenumber q satisfies

$$(3\sigma - \mu)q^2 > \sigma - \mu \quad (1.5.8)$$

with all plane waves being unstable when $\mu > \sigma$. Note that (a rescaling of) the Eckhaus criterion $q^2 > 1/3$ is recovered when the coupling between the mean and pattern

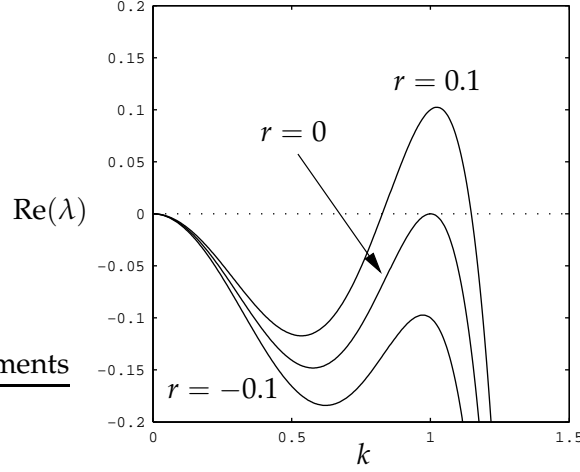


Figure 1.8: The linear growthrate λ in the DSH equation (1.5.10) as a function of the wavenumber k for $r = -0.1, 0, 0.1$.

modes is removed ($\mu = 0$). Additionally, rolls can suffer an oscillatory instability if

$$(3 + \sigma - \mu)q^2 > (1 + \sigma - \mu), \quad (1.5.9)$$

provided that $\mu(\sigma - 1) - \sigma^2 > 0$.

Beyond the stability boundaries for rolls, numerical simulations have revealed stable stationary solutions in the form of strongly amplitude-modulated and localised patterns (see figures 1.9 and 1.10). Furthermore, the envelope of these patterns has been determined through the use of Jacobi elliptic functions [74, 84].

Some care must be exercised when considering the secondary instability of a regular pattern to long-wave disturbances. This is because the cubic coefficient in the amplitude equation for these disturbances (not exhibited here) is small [74]. It is now appreciated that the bifurcation from a regular pattern to a modulated pattern is subcritical [85] (apart from the special case where A is real [74]) and one can introduce new scalings to allow the subcritical bifurcation to be captured by a single equation [85]. Further work on the nonlinear steady solutions to (1.5.6) has been reported by Norbury et al. [86] and Vega [37].

To illustrate the behaviour described above, it is instructive to consider the derivative Swift–Hohenberg (DSH) equation [74],

$$\frac{\partial w}{\partial t} = -\frac{\partial^2}{\partial x^2} \left[rw - \left(1 + \frac{\partial^2}{\partial x^2} \right)^2 w - sw^2 - w^3 \right], \quad (1.5.10)$$

which differs from the usual Swift–Hohenberg equation through the inclusion of the operator $-\partial^2/\partial x^2$, which acts on the right-hand side of (1.5.10). The DSH equation is

clearly of the form (1.5.1) and so $w(x, t)$ is conserved. Considering the linearised problem about $w(x, t) = 0$, one finds the growthrate λ of small disturbances with wavenumber k to be defined by

$$\lambda = k^2 [r - (1 - k^2)^2], \quad (1.5.11)$$

and it follows that (1.5.10) undergoes a stationary, finite-wavelength instability at $r = r_c \equiv 0$ with critical wavenumber $k = k_c \equiv 1$. As figure 1.8 illustrates, for small positive r , a narrow band of wavenumbers near $k = 1$ is unstable, while modes with $k \approx 0$ have near-neutral decay. Thus, near onset, one expects to see stationary periodic patterns (rolls) with wavenumber $k_c = 1$.

As reported by Matthews and Cox [74], a standard weakly nonlinear analysis allows amplitude equations to be derived through setting $r = \epsilon^2 r_2$ and introducing slow scales for space and time: $X = \epsilon x, T = \epsilon^2 t$. The appropriate ansatz is:

$$w(x, t) = \epsilon \left[A(X, T)e^{ix} + A^*(X, T)e^{-ix} \right] + \epsilon^2 \left[B(X, T) + C(X, T)e^{2ix} + C^*(X, T)e^{-2ix} \right] + O(\epsilon^3), \quad (1.5.12)$$

where the mean mode $B(X, T)$ has been introduced at higher order than the pattern modes to ensure a balance of terms in the amplitude equations. Substituting (1.5.12) into (1.5.10), the $O(\epsilon)$ problem is automatically satisfied (by virtue of choosing $k_c = 1$) and the $O(\epsilon^2)$ nonlinear resonance terms are balanced by specifying $C = -sA^2/9$. Subsequently, the amplitude equation for A is determined by the solvability conditions at $O(\epsilon^3)$, which amount to setting the coefficients of $e^{\pm ix}$ to zero. This yields

$$A_T = r_2 A + 4A_{XX} - (3 - 2s^2/9)|A|^2 A - 2sAB. \quad (1.5.13)$$

Thus, the bifurcation to rolls is supercritical if $s^2 < 27/2$, which we assume to be the case. In addition, the evolution equation for B follows from the terms independent of x at $O(\epsilon^4)$:

$$B_T = B_{XX} + 2s(|A|^2)_{XX}. \quad (1.5.14)$$

We can rescale (1.5.13) and (1.5.14) to the canonical form (1.5.6) where

$$\sigma = 1/4, \quad \text{and} \quad \mu = \frac{s^2}{3 - 2s^2/9}. \quad (1.5.15)$$

Hence, the condition for all rolls to be unstable ($\mu > \sigma$) becomes

$$s^2 > s_c^2 \equiv 27/38. \quad (1.5.16)$$

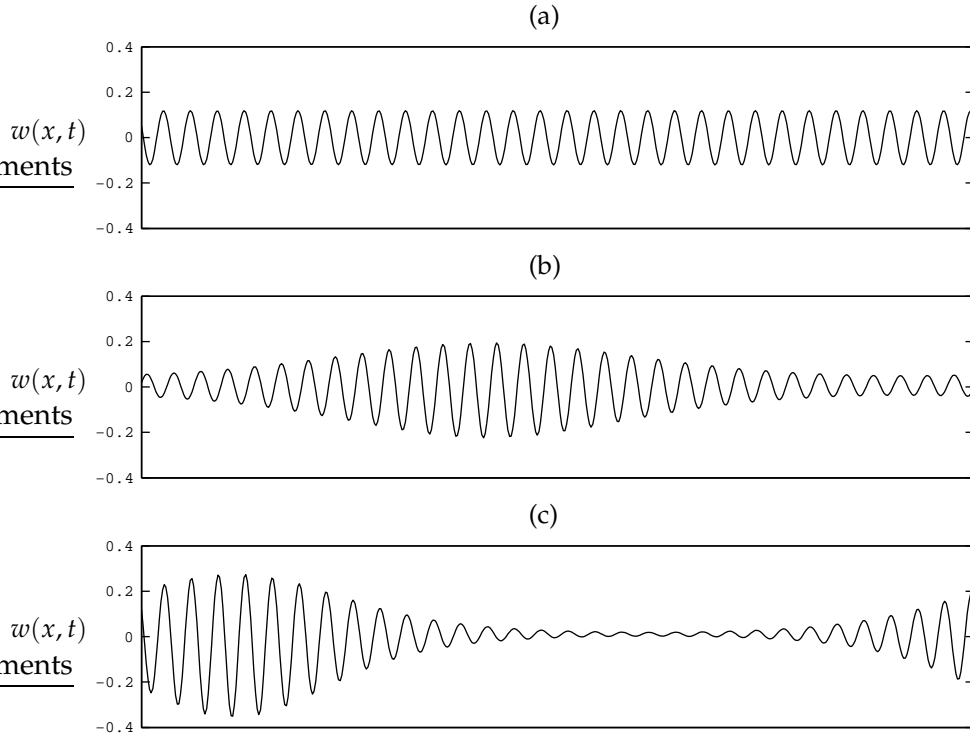


Figure 1.9: Steady states of the DSH equation (1.5.10) in a periodic domain $L = 62\pi$ with $r = 0.01$ and (a) $s = 0.9$, (b) $s = 0.95$ and (c) $s = 1.0$. For finite L , the instability condition (1.5.7) becomes $\mu > \sigma(1 + 2\pi^2/L^2)$ or $|s| > 0.9215$ [74].

Figure 1.9 illustrates the near-onset steady states of the DSH equation realised in a large container for values of s slightly larger than s_c (which is adjusted for finite-container effects). For s just above critical, steady amplitude-modulated states are found with the degree of modulation increasing as the distance from s_c increases. Indeed, steady states found far above threshold (shown in figure 1.10) take the form of localised envelopes of rolls surrounded by regions of zero amplitude. These localised pockets of nonzero amplitude can be steady or propagating with a very small speed [74]. Also, it is possible for the envelope to be ‘pinned’ to the underlying pattern.

1.5.2 Two-dimensional behaviour

Cox and Matthews [75] studied the analogous problem of a stationary bifurcation in two spatial dimensions, where a range of periodic patterns, such as stripes, squares and hexagons, are possible. In the absence of a conserved quantity, previous work has led to a ‘balloon’ of parameter values being determined [87, 88, 89], marking the boundary of the stability region of stripes. Analogous stability regions for squares and hexagons have also been reported [33, 34]. These stability regions are delimited by both

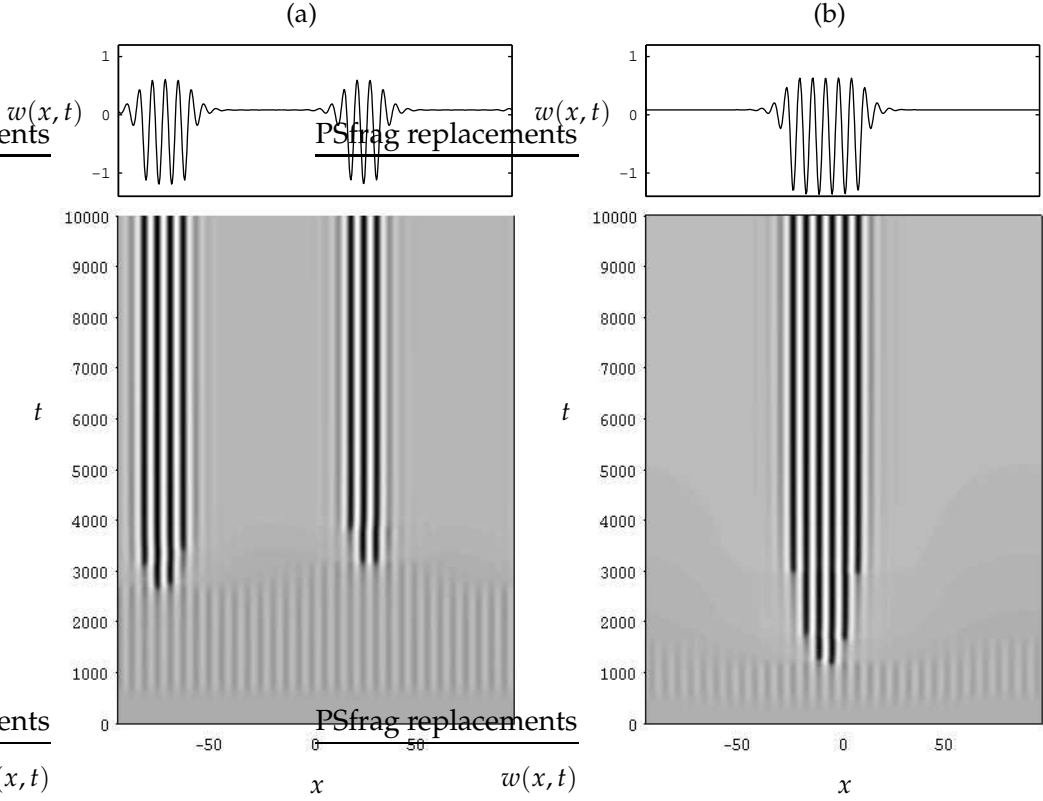


Figure 1.10: The selection and final arrangement of localised states in the DSH equation (1.5.10). The simulations took place in a periodic domain $L = 62\pi$ with $r = 0.1$ and (a) $s = 1.5$ and (b) $s = 1.6$, where the initial condition took the form of small-amplitude noise.

finite- and long-wavelength instabilities and a range of different scenarios can arise. The principal modulational instability for stripes is a two-dimensional analogue of the Eckhaus instability, where wavenumber reselection takes place, leading to a new stripe pattern. Analogues of this instability have also been found for squares and hexagons [33, 34, 90].

Given the rotational degeneracy of most pattern formation problems, a range of different amplitude equations are possible depending on the arrangement of the leading-order modes. For a planform composed of four modes at right-angles to each other together with a large-scale mode,

$$w = \epsilon \left[A_1(X, Y, T)e^{ik_c x} + A_2(X, Y, T)e^{ik_c y} + \text{c.c.} \right] + \epsilon^2 B(X, Y, T) + \text{q.t.} + O(\epsilon^3), \quad (1.5.17)$$

where ‘q.t.’ is shorthand for the other quadratic terms that appear at $O(\epsilon^2)$, and assum-

ing the system is invariant under the symmetries:

$$\text{translations:} \quad (x, y) \mapsto (x + x_0, y + y_0), \quad (1.5.18a)$$

$$\text{reflection 1:} \quad x \mapsto -x, \quad (1.5.18b)$$

$$\text{reflection 2:} \quad (x, y) \mapsto (y, x), \quad (1.5.18c)$$

the amplitude equations (in canonical form) are

$$A_{1T} = r_2 A_1 + A_{1XX} - |A_1|^2 A_1 - \beta |A_2|^2 A_1 - A_1 B, \quad (1.5.19a)$$

$$A_{2T} = r_2 A_2 + A_{2XX} - |A_2|^2 A_2 - \beta |A_1|^2 A_2 - A_2 B, \quad (1.5.19b)$$

$$B_T = \sigma \nabla^2 B + \mu_+ \nabla^2 (|A_1|^2 + |A_2|^2) + \mu_- (\partial_X^2 - \partial_Y^2) (|A_1|^2 - |A_2|^2). \quad (1.5.19c)$$

These equations admit the solutions:

$$\text{stripes 1:} \quad A_1 = \sqrt{r_2 - q^2} e^{iqX}, \quad A_2 = 0, \quad B = 0; \quad (1.5.20a)$$

$$\text{stripes 2:} \quad A_1 = 0, \quad A_2 = \sqrt{r_2 - q^2} e^{iqY}, \quad B = 0; \quad (1.5.20b)$$

$$\text{squares:} \quad A_1 = \sqrt{\frac{r_2 - q^2}{1 + \beta}} e^{iqX}, \quad A_2 = \sqrt{\frac{r_2 - q^2}{1 + \beta}} e^{iqY}, \quad B = 0. \quad (1.5.20c)$$

Analogous to the one-dimensional analysis, new modulational instabilities are found for each pattern. For stripes, considering only one-dimensional disturbances, one recovers the instability criterion

$$(3\sigma - \mu_+)q^2 > r_2(\sigma - \mu_+), \quad (1.5.21)$$

matching the form of (1.5.8) for one-dimensional pattern formation. Again, all stripes are destabilised when $\mu_+ > \sigma$. With two-dimensional (or transverse) disturbances, one finds the usual zigzag instability for stripes with $q < 0$ and also a new modulational instability when

$$\mu_+ - \mu_- > \sigma. \quad (1.5.22)$$

In the absence of a conservation law, the stability region of square patterns is delimited by several long-wave instabilities, such as the zigzag instability and two analogues of the Eckhaus instability [34]. However, analysing the stability of square patterns in (1.5.19) reveals a new instability mechanism, which implies that for

$$\mu_+ > \frac{1}{2}(1 + \beta)\sigma, \quad (1.5.23)$$

all square patterns are unstable (see Cox and Matthews [75] for more details).

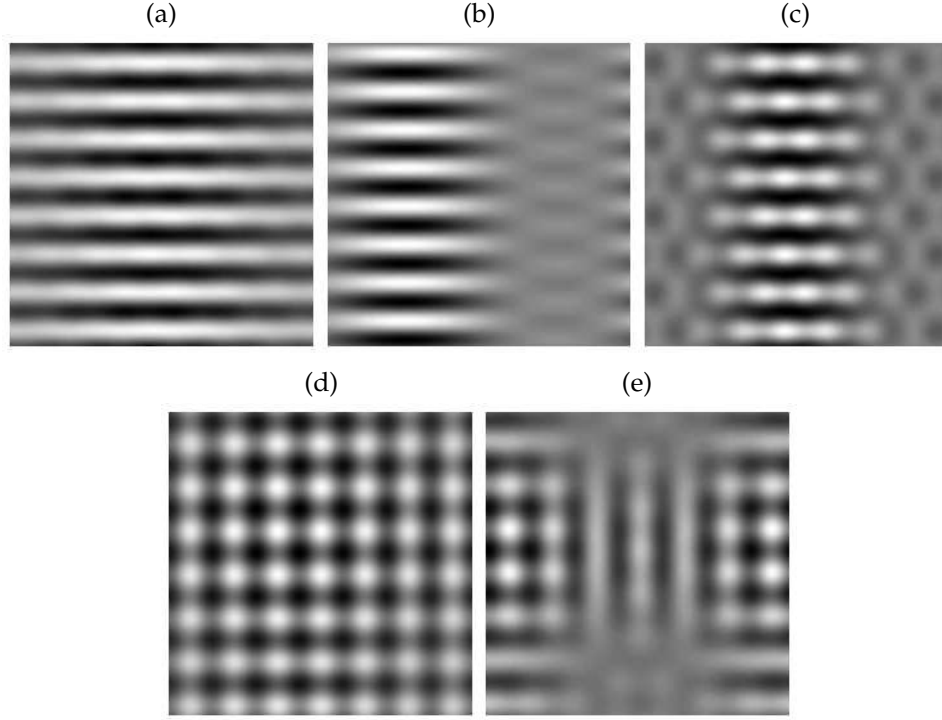


Figure 1.11: Steady states in the 2D DSH equation (1.5.24): (a), (b) and (c) are the realised states beyond the transverse instability of stripes in a box of side lengths 49 and 50.3, while (d) and (e) are the steady states in a box of length 44. All figures were generated with $p = 3.3, s = 2.2$ as well as (a) $(r, u) = (0.001, -1)$; (b) $(r, u) = (0.001, -0.8)$; (c) $(r, u) = (0.001, -0.5)$; (d) $(r, u) = (0.003, 0.4)$ and (e) $(r, u) = (0.001, -0.5)$.

Again, this behaviour is neatly illustrated through simulation of an example equation: in this case, a two-dimensional extension of the DSH equation

$$\frac{\partial w}{\partial t} = -\nabla^2 [rw - (1 + \nabla^2)^2 w - pw\nabla^2 w - q|\nabla w|^2 - sw^2 - w^3] + u\nabla \cdot (\nabla^2 w \nabla w), \quad (1.5.24)$$

where p, q, r, s and u are the parameters; it is straightforward to derive the amplitude equations (1.5.19) from (1.5.24) [75]. We see in figure 1.11 various amplitude-modulated states found in the unstable parameter regimes. Subfigures (a), (b) and (c) illustrate modulated stripe patterns found in a slightly off-square container with side lengths 49 and 50.3. These values are chosen so as to ensure rolls are preferred; there exists a curious degeneracy in the 2D DSH equation whereby the condition for the transverse instability of stripes coincides with the condition for stripes to be unstable to squares so that in a perfectly square box, the modulational instability of rolls cannot take place. A similar phenomenon is also found in the model equations considered in chapter 2. Subfigures (a) and (b) illustrate the patterned arrangements selected by the transverse

instability of stripes, with increasing degrees of modulation, while in (c) a tertiary instability leads to the weak appearance of a hexagonal pattern. Subfigures (d) and (e) illustrate modulated square patterns found in a square container of sidelength $L = 44$.

Amplitude equations incorporating a neutral large-scale mode have been successfully applied to several physical systems with a conserved quantity. To date, this has included rotating convection [91], magnetoconvection [91, 92], thin films [93], Faraday waves [94] and sand ripples [83]. A new application of the existing theory is detailed in chapter 2, where a model of a vibrated granular layer is examined.

1.6 Structure of thesis

The primary objective of this thesis is to examine the role of a conservation law in pattern formation problems, under various formulations. This examination comprises a new application of the existing two-dimensional results of Cox and Matthews [75] as well as two new studies, where the previous theory cannot be applied and we provide the necessary extension. In all cases, analytical work is complemented with the results of extensive numerical simulation.

We begin in chapter 2, with a (re-)examination of a phenomenological model for a vibrated granular layer. This model, first proposed by Aranson and Tsimring [6, 95], has previously been investigated through the techniques of weakly nonlinear analysis. However, the dynamical effects of conservation of mass, which is preserved by the model equations, were neglected as spatial variation was not considered. We present a new weakly nonlinear analysis of the model equations that fully accounts for the neutrally stable large-scale mode. This enables the amplitude equations (1.5.6) of Matthews and Cox [74] to be derived and gives rise to new and interesting results regarding the stability of the primary cellular patterns.

The amplitude equations (1.5.6) are constructed for the generic case of a stationary one-dimensional bifurcation where a conservation law is present. A natural extension, which is pursued in chapter 3, is to examine the analogous problem but with an oscillatory bifurcation. Through simple symmetry considerations, the appropriate amplitude equations are constructed and the modulational stability results for travelling and standing waves are presented. For both forms of solution, the standard long-wave results are altered and new instabilities are induced by the conserved quantity. The nonlinear development of these instabilities is subsequently examined by means of a numerical integration of the amplitude equations. Previously unseen amplitude-modulated and localised coherent structures are observed, stabilised by the presence

of the conserved quantity.

In the analysis of chapter 3, the behaviour of the conserved quantity is assumed to lead to diffusive relaxation at leading order. However, this need not necessarily be the case: several alternative behaviours are possible. In chapter 4, we analyse an alternative form of large-scale mode through the examination of a quasi-potential model for the occurrence of Faraday waves, reported by Zhang and Viñals [96]. Several weakly non-linear analyses are performed, each corresponding to a different choice of scalings in the model equations. The resulting amplitude equations are then investigated through numerical simulations.

Finally, the main results of this thesis are summarised in chapter 5. Note that table D.1 of appendix D contains a guide to the notation of each chapter, for quick reference.

Pattern formation in a model of a vibrated granular layer

2.1 Introduction

A GRANULAR MEDIUM, consisting of a body of dry, cohesionless particles can display a panoply of exotic behaviours, of which few are thoroughly understood. Phenomena such as size segregation, density waves, convective transport have been recorded, for review see Jaeger et al. [97], Rajchenbach [98], Kadanoff [99] and Aranson and Tsimring [100]. The root cause of the difficulty in constructing accurate models lies in the extremely complicated rheology of granular media. To date, there is no generally accepted theoretical description, rather, a plethora of different models and approaches has been suggested, often incorporating contradictory or inconsistent concepts. The obstacles to deriving theoretical models are numerous and challenging. For instance, collisions between granular particles are highly dissipative and so the results of equilibrium theory are not directly applicable. Also, dissipation can lead to the appearance of large gradients and shocks, making the application of continuum models questionable. Granular materials settle rapidly under the Earth's gravitational field and, in the absence of forcing, will occupy metastable or 'frozen' states. Thus, to ensure motion of the granular material, energy must be injected externally into the system. It is now appreciated that the statistical properties of a granular medium, and thus the appropriate modelling approaches, are strongly dependent on the nature of this forcing [101, 102].

Perhaps the most fascinating behaviour of the medium is the appearance of long-range coherent patterns and localised structures in vertically vibrated granular layers [103, 104, 105, 106]. When a thin layer of granular material (with a layer depth of as little as 5 particles) is subject to vertical oscillation $z(t) = \mathcal{A} \sin(2\pi ft)$ (see figure 2.1), a

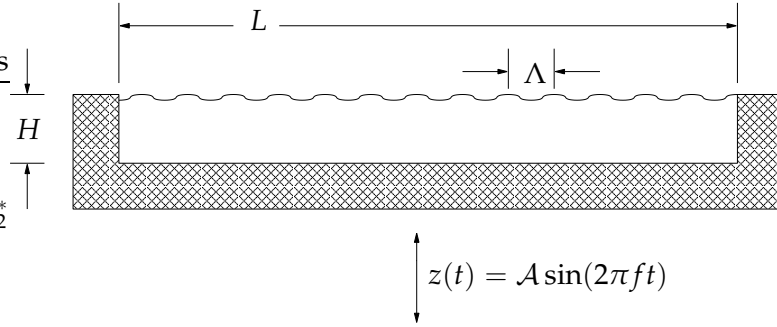


Figure 2.1: The experimental setup for examining vibrated granular layers. A rigid container filled with granular material of mean depth H and horizontal dimension L is filled with granular material. The container is then subject to periodic vertical acceleration $z(t)$. Subsequently, as some critical acceleration threshold is breached, standing waves of wavelength Λ appear on the surface.

rich array of standing wave patterns, similar to those seen in the Faraday experiment [107, 108, 109], can be observed. These patterns oscillate with half the frequency of the forcing, indicating the subharmonic resonance characteristic of a parametric instability. Depending on the interplay of the driving frequency f and the dimensionless acceleration,

$$\Gamma = 4\pi^2 f^2 \mathcal{A}/g, \quad (2.1.1)$$

(g is the acceleration due to gravity), surface patterns such as stripes, squares and hexagons can be observed (figure 2.2) [103, 104, 105]. Such behaviours were identified some two hundred years ago by Chladni [110] and Faraday [111], but interest has been revived recently through work by Douady et al. [112] and Fauve et al. [73]. This renaissance culminated in the discovery of highly localised excitations termed ‘oscillons’ (figure 2.3) by Umbanhowar et al. [106].

In this chapter, we consider a highly simplified model of pattern formation in a vibrated granular layer, taking the form of a parametric Ginzburg–Landau equation coupled to a conservation law for the granular material. A weakly nonlinear analysis of this model has already been performed [6]; however, spatial modulation was not included and the full influence of the conservation law was neglected. In this chapter, we re-examine the same model but incorporate spatial modulation, which means a large-scale mode is neutrally stable and needs to be included in the amplitude description.

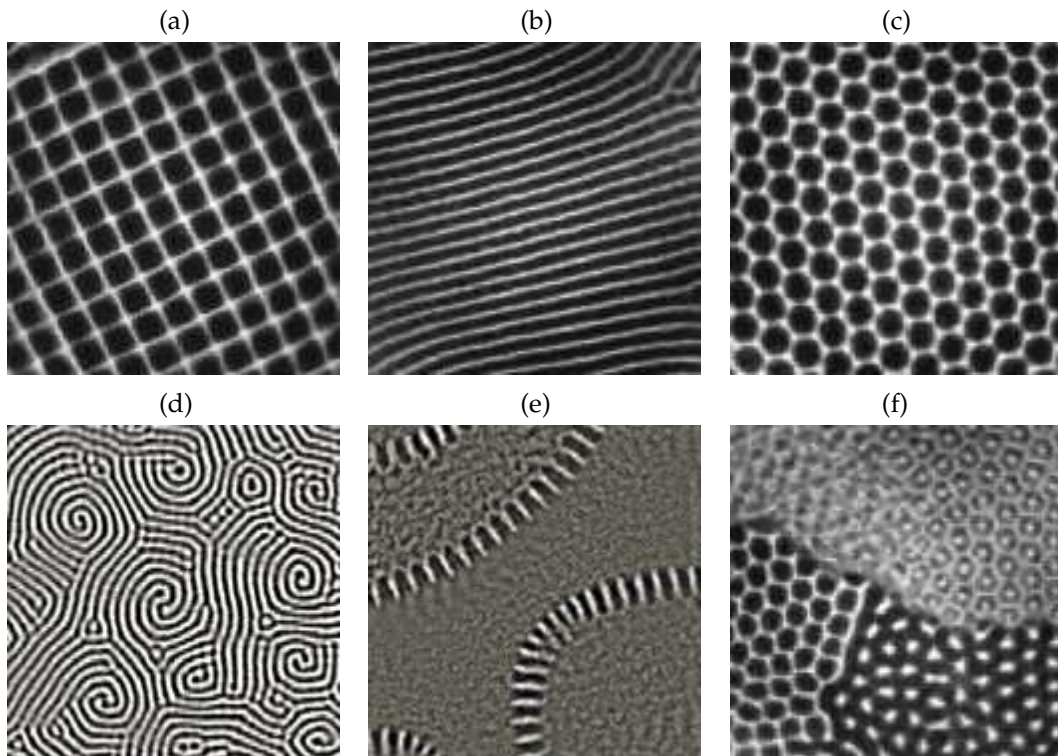


Figure 2.2: Patterns observed experimentally in vibrated granular layers: (a) squares, (b) stripes, (c) hexagons, (d) labyrinth patterns, (e) interfaces, (f) mixed domain patterns. All experiments were performed in a circular container but have been cropped for this figure. Images (a), (b), (c), (f) are from [113] while (d) and (e) are from [114].

2.1.1 Experimental background

The experimental setup for the study of standing waves in vibrated granular layers is illustrated in figure 2.1. In general, the granular medium is composed of identical spheres made of bronze, lead or glass; the sphere diameter can be anywhere between 0.1mm and 3mm. A typical ‘thin’ layer would be between 5 and 30 particles deep and the container is usually of length/radius around 15cm. This layer is then energised by precise vertical vibration, through an electromagnetic shaker mounted underneath.

Depending on the experimental conditions, a profusion of phenomena can occur (see Jaeger et al. [97]). In general, these phenomena are caused by the presence of surrounding gas as well as sidewall driving, and are highly dependent on the container geometry. Thus, in the study of standing wave patterns, the container is usually evacuated to a low Torr value so that the volumetric effects of gas are negligible and heaping is prevented [115]. Experimentalists have reported that transition thresholds and pattern organisation take on clearer definition as the ratio of container size to pattern

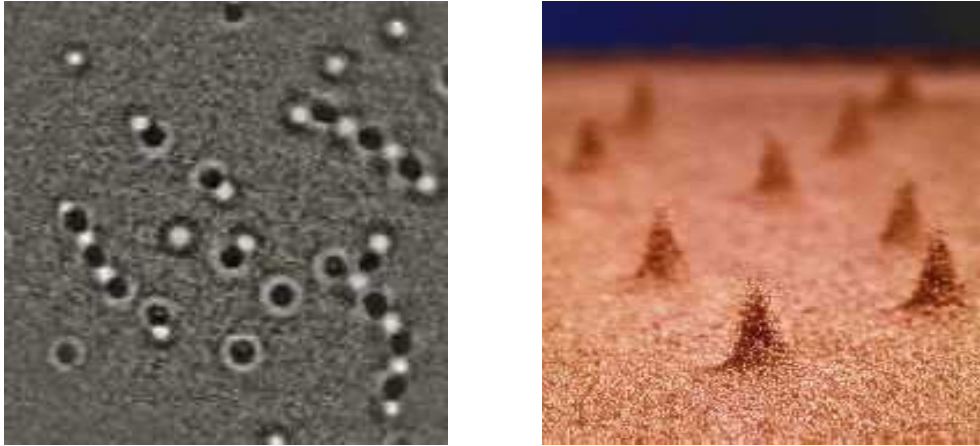


Figure 2.3: Oscillons observed in vibrated granular layers [113, 118].

wavelength is increased, indicating that the dynamics of these surface patterns are not determined by gas or sidewall effects [104]. Neglecting boundary effects, the form of granular motion is dependent on the ratio H/d where H is the mean depth of the granular layer and d is the particle diameter. For $H/d \gg 1$, steady convective motion is found [116], while for moderate H/d , a parametric instability to subharmonic standing waves occurs. It is with these standing wave patterns that we shall concern ourselves.

Slightly above an instability to standing waves, the realised pattern is determined by the interplay of driving frequency f and acceleration Γ of the forcing plate [103, 104]. At $\Gamma = 1$, the granular layer begins to separate from the driving plate as the downward acceleration of the plate exceeds gravity. Subsequently, irrespective of the driving frequency, standing waves appear at $\Gamma \approx 2.4$, where either subharmonic stripes or squares are found [103, 105]; below this threshold, the granular layer remains flat. At frequencies below some threshold $f < f^*$ (under certain experimental conditions, $f^* \approx 40\text{Hz}$ [103]), a subcritical transition to regular square patterns (figure 2.2a) is observed, while for $f > f^*$, stripes (figure 2.2b) are selected [103] and the transition is supercritical. It has been noted that the threshold frequency for stripes and squares is dependent on $d^{-1/2}$ and that the wavelength of the cellular pattern scales linearly with the layer depth [101]. Similar to roll patterns in convection experiments [87, 88, 89], stripe patterns have been observed to undergo secondary instabilities, including the skew-varicose and cross-roll instabilities [117].

At higher accelerations ($\Gamma > 3.7$), squares and stripes become unstable and hexagons appear instead [119]. At higher Γ still, the layer begins to collide with the plate on every other oscillation of the forcing and the flat state is recovered. This regime is generally identified with so-called ‘interface’ or ‘kink’ patterns, which are composed of

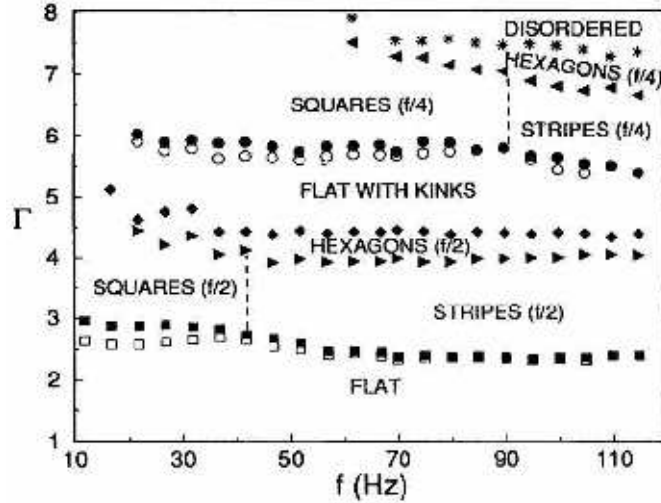


Figure 2.4: Phase diagram for the various pattern regimes in vibrated granular layers. (See [104] for further details of the experimental setup that this diagram corresponds to.)

domain-like arrangements of flat layers oscillating with opposite phase and separated by either smooth or ‘decorated’ interfaces (figure 2.2e) [120]. Further increases in Γ lead to the emergence of quarter-harmonic ($f/4$) patterns [104] in the form of stripes, squares or hexagons. Finally, for very large Γ , phase bubbles have been observed to spontaneously nucleate before patterns descend into spatiotemporal chaos in the form of moving labyrinth kinks [121]. A phase diagram for a particular experimental setup is exhibited in figure 2.4; alternative diagrams have been provided by Bizon et al. [119], Umbanhowar et al. [106] and Moon et al. [121].

Considerable excitement has surrounded the discovery of oscillons by Umbanhowar et al. [106]. These are found in a hysteretic region of the primary instability, where both the flat layer and some disturbance pattern can be stable, and in an intermediate frequency range where square and stripes compete. Oscillons are small circularly symmetric pulses, surrounded by a homogeneous granular surface, which oscillate subharmonically (figure 2.3). They can occur either individually or bound together, with adjacent excitations oscillating out of phase, in chains or lattices. In general, oscillons do not propagate, rather they drift slowly and randomly [106]. Also, oscillons do not form spontaneously from a uniform layer; instead, they are produced by generating a stable pattern of stripes or squares and decreasing Γ back through the primary instability value. Interestingly, localised oscillon-like objects have been observed in vibrated layers of non-Newtonian fluids [122].

Undoubtedly, there are remarkable similarities between the observed behaviours in

vibrated granular layers and the Faraday experiment (see chapter 4). As such, the theoretical approaches developed for modelling Faraday waves have often been used as a foundation for the study of granular patterns. However, there are several qualitative differences between fluids and granular materials, such as strong dissipation and a lack of surface tension in the latter, which cause the primary instabilities to differ in two key ways:

- In fluids, the primary bifurcation is generally supercritical, whereas in granular layers, the instability can be hysteretic, with patterns disappearing at a lower plate acceleration than where they first appeared [103, 104].
- High-speed photography has revealed that the motion of the granular material takes place in two distinct stages [104, 123]. First, the driving plate accelerates upwards to strike the granular bed. At the point of impact, the pattern is at its sharpest but subsequently, the particles scatter. Next, the plate moves downwards with acceleration faster than gravity, causing the granular bed to separate from the plate, where inter-particle collisions lead to the reformation of a patterned state. Such a behaviour is not possible in vibrated fluid layers as the fluid must stay in contact with the driving plate. The identification of this behaviour has motivated several stroboscopic treatments of granular pattern formation (e.g., [124, 125]), where the granular arrangement is considered only at discrete instants in time.

2.1.2 Theoretical approaches

There exist many obstacles to the construction of accurate and general models of patterns in vibrated granular layers, the principal one being the extremely complicated rheology of the medium. Unlike fluid dynamics, the size of the particle is large compared with the length scale over which the flow varies, which makes the application of a continuum description questionable. Thus, there is no analogue of the Navier–Stokes equations to be used as a starting point for a model derivation and, in the attempt to capture the rich variety of experimentally observed phenomena, many different theoretical models have been proposed; see Aranson and Tsimring [100] for a comprehensive review.

A common approach has been to simulate a large number of interacting particles in a two- [123, 126] or three-dimensional [117, 119, 127] gravitational field where the particles interact through dissipative binary collisions, preserving linear and angular momentum. Without incorporating friction, only a supercritical bifurcation to stripes can

occur [128], but with friction, an accurate reproduction of experimental patterns, with the important omission of oscillons, was reported [119].

In addition, several semi-continuum models and mappings have been proposed [124, 125, 129, 130, 131, 132]. These often comprise a model for a field variable which treats space continuously but time discontinuously by either dictating a bounce condition [124] or a time mapping [129, 130]; in other cases, both time and space are treated discretely [131, 132]. Such models have reproduced oscillons [124, 125, 131] as well as many other cellular patterns observed experimentally.

Whilst a generally accepted continuum description for all granular systems does not exist, there is evidence that, for certain parameter regimes (particularly, near the primary instability), a continuum model is appropriate [101, 117]. Several authors have used quasi-two-dimensional hydrodynamic models [125, 133, 134, 135, 136] to model the motion of granular layers; a common technique is to partition the model into separate equations of motion for the free flight time and the collision with the plate [125, 135]. In this chapter, we concern ourselves with one of the first continuum models proposed, a phenomenological model reported by Aranson and Tsimring [6, 95], comprising a parametric Ginzburg–Landau equation coupled to a conservation law for the granular material. This coupled model describes pattern formation near the threshold of the primary bifurcation, and admits stripes, squares and oscillons as solutions, in good qualitative correspondence with experiment for a model of such simplicity. This model also provides an accurate description of patterns at high accelerations such as hexagons and interfaces [137]. In this regime, the slow dynamics associated with the conservation law can be dispensed with, and the dynamics can be described by a single parametric Ginzburg–Landau equation. A more detailed discussion of this coupled model is reserved for §2.2.

2.1.3 Structure of chapter

Whilst many of the observed experimental patterns have been theoretically accounted for in various models, a rigorously derived and widely accepted description of granular motion does not currently exist. Thus, there is no accepted starting point for deriving a model of pattern formation in a vibrated granular layer. In this chapter, we choose to (re-)examine a phenomenological model proposed by Aranson and Tsimring [6, 95]. A previous investigation of this model [6] failed to take into account the dynamical effect of the conservation of mass by ignoring spatial modulation. This chapter details a new weakly nonlinear analysis of the model equations, which leads to the derivation of the amplitude equations (1.5.19) for two-dimensional pattern formation with a

conservation law [138], which allow existing stability results to be applied.

In §2.2, the phenomenological model is reviewed and previous results summarised; a new weakly nonlinear analysis is then performed in §2.3. The case of no spatial modulation is considered first, which gives rise to several interesting results regarding the model equations. Next, spatial modulation is included allowing the full dynamical implications of a conservation law to be examined. The results of these analyses are then complemented with numerical simulations in §2.4. Finally, conclusions are presented in §2.5.

2.2 Order-parameter model

Our starting point is the phenomenological model [6, 95]

$$\psi_t = \gamma\psi^* - (1 - i\omega)\psi + (1 + ib)\nabla^2\psi - |\psi|^2\psi - \rho\psi, \quad (2.2.1a)$$

$$\rho_t = \beta\nabla^2\rho + \alpha\nabla \cdot (\rho\nabla|\psi|^2), \quad (2.2.1b)$$

where the order parameter $\psi(x, y, t)$ characterises the complex amplitude of the subharmonic pattern (so that the disturbance to the planar layer surface is $h = \psi \exp\{i\pi ft\} + \text{c.c.}$), while $\rho(x, y, t)$ is the local mass of the granular layer per unit area.

Equation (2.2.1a) is a parametric version of the Ginzburg–Landau equation, where the term $\gamma\psi^*$ provides the parametric driving required for standing waves to become excited and the control parameter γ is the normalised amplitude of the parametric forcing. The coefficient b characterises the ratio of dispersion to diffusion while ω characterises the frequency of driving. It is possible to derive the linear terms of this equation from a dispersion relation for parametrically driven granular waves, expanded near the frequency ω and corresponding wavenumber k [6]. The nonlinear term $|\psi|^2\psi$ is introduced phenomenologically to account for the saturation of oscillations through inelastic collisions, while the term $\rho\psi$ characterises the coupling between the order parameter and the local granular density. Equation (2.2.1a), with no coupling to the mean-field $\rho(x, y, t)$, has been studied previously as a model for a vibrated fluid layer [139, 140] as well as for the large- Γ regime of a vibrated granular layer [137, 141], where ρ is assumed to be slaved to ψ .

Equation (2.2.1b) describes the conservation of mass in the granular layer; the distributive mechanisms are a diffusive flux ($\alpha - \nabla\rho$) and a flux $\propto -\rho\nabla|\psi|^2$ corresponding to particles ‘escaping’ from regions of large fluctuation. The coefficient α will always be positive, indicating that particles are driven out of these regions, rather than being drawn in. The mass diffusion constant β is also positive and is expected to be pro-

portional to the energy of the plate vibrations and should increase with the driving frequency f [6]. It is this rapid diffusive smoothing which allows the role of ρ to be discounted in investigations of the high-acceleration regime of a vibrated granular layer [137, 141]. The model equations (2.2.1) bear a noticeable resemblance to the amplitude equations (1.5.6) for a stationary bifurcation in the presence of a conservation law. Indeed, it is shown in §2.3.2 that the amplitude equation (1.5.6) can be derived from this model.

2.2.1 Linear analysis

Let us consider the linear stability of the uniform solution $\psi = 0, \rho = \rho_0$ which corresponds to a flat homogeneous layer—we shall see later that ρ_0 is an important parameter in the system's behaviour. We examine perturbations to this solution of the form:

$$\psi = \chi\psi_1(x, y, t), \quad (2.2.2a)$$

$$\rho = \rho_0 + \chi\rho_1(x, y, t), \quad (2.2.2b)$$

where χ is a small book-keeping parameter. Collecting $O(\chi)$ terms, we find the linear problem:

$$\mathbf{L} \begin{pmatrix} \psi_1 \\ \rho_1 \end{pmatrix} = \begin{pmatrix} 0 \\ 0 \end{pmatrix}, \quad (2.2.3)$$

where the operator \mathbf{L} is defined by

$$\mathbf{L} \begin{pmatrix} \psi_1 \\ \rho_1 \end{pmatrix} \equiv \begin{pmatrix} -\psi_{1t} + \gamma\psi_1^* - (1 - i\omega)\psi_1 + (1 + ib)\nabla^2\psi_1 - \rho_0\psi_1 \\ \beta\nabla^2\rho_1 \end{pmatrix}. \quad (2.2.4)$$

We see that ρ_1 decouples from ψ_1 and perturbations $e^{\sigma t + ikx}$ decay with $\sigma = -\beta k^2$. This allows us to neglect ρ_1 in this instance; however, the near-neutral growth of large-scale modes ($k \rightarrow 0$) in the ρ equation will be important in §2.3.2, where spatial modulation is considered. We make the substitution

$$\psi_1 = P_1(t)e^{ikx} + P_2^*(t)e^{-ikx}, \quad (2.2.5)$$

(the conjugation of P_2 is to simplify the analysis) into (2.2.3) to yield two evolution equations, resonant along $e^{\pm ikx}$:

$$P_{1t} = \gamma P_2 - [1 - i\omega + ibk^2 + \rho_0 + k^2] P_1, \quad (2.2.6a)$$

$$P_{2t} = \gamma P_1 - [1 + i\omega - ibk^2 + \rho_0 + k^2] P_2. \quad (2.2.6b)$$

Now, looking for solutions proportional to $e^{\sigma t}$ gives rise to the characteristic polynomial

$$\sigma^2 + 2(1 + k^2 + \rho_0)\sigma + (1 + k^2 + \rho_0)^2 + (\omega - bk^2)^2 - \gamma_c^2 = 0, \quad (2.2.7)$$

which leads to the neutral curve (where $\sigma = 0$),

$$\gamma_c^2 = (1 + k^2 + \rho_0)^2 + (\omega - bk^2)^2. \quad (2.2.8)$$

Differentiating the right-hand side of (2.2.8) with respect to k , we find the critical wave-number k_c satisfies

$$k_c^2 = \frac{\omega b - 1 - \rho_0}{1 + b^2}, \quad (2.2.9)$$

which gives the threshold condition

$$\gamma_c^2 = \frac{(\omega + b(1 + \rho_0))^2}{1 + b^2}. \quad (2.2.10)$$

However, we see from (2.2.9) that a finite-wavelength instability requires $\omega b - 1 - \rho_0 > 0$. In the alternative case of $\omega b - 1 - \rho_0 \leq 0$, spatially uniform perturbations with $k_c = 0$ are the first to become unstable; the threshold condition in this case is found by substituting $k = 0$ into (2.2.8) to give

$$\gamma_c^2 = (1 + \rho_0)^2 + \omega^2. \quad (2.2.11)$$

Figure 2.5 illustrates the neutral curve (2.2.8) for various values of ρ_0 , where we see the transition between a finite-wavelength and uniform instability. It is clear that the threshold of the primary instability γ_c rises with the unforced layer depth ρ_0 . This behaviour matches experimental results [103, 104, 106] and can be attributed to the increase in internal energy dissipation in thicker layers. Note that the results of this linear analysis have been presented previously [6, 137].

For the forthcoming analysis of this chapter, we restrict our attention to the case of a finite-wavelength instability and so, henceforth, assume $\omega b - 1 - \rho_0 > 0$.

2.2.2 Large-scale modes

Since (2.2.1b) is a conservation law of the form described in §1.5, large-scale modes are neutrally stable and should be included in the nonlinear analysis. This can be seen by considering perturbations to a uniform state with $\rho = \rho_0$ proportional to $e^{\sigma t + ikx}$, which have $\sigma \propto -k^2$ in the limit of $k \rightarrow 0$. Hence, large-scale modes have almost neutral growth; the growth rates σ for various γ values are illustrated in figure 2.6. Thus, as argued by Matthews and Cox [74] and detailed in §1.5, these large-scale modes cannot be slaved to the growing modes but must be treated independently in the nonlinear analysis. These neutral modes can play a significant role in the stability behaviour of the system and, as we shall see, can lead to amplitude modulation and localisation.

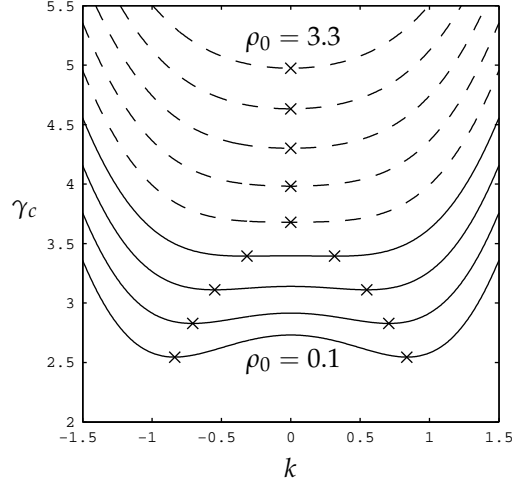


Figure 2.5: The neutral curve (2.2.8) for ρ_0 ranging between 0.1 and 3.3 in steps of 0.4; the other parameter values are $\omega = 2.5$ and $b = 1$. The solid lines correspond to scenarios where a finite-wavelength instability takes place while the dashed lines denote the occurrence of spatially uniform instability. The locations of the minima of each curve, which correspond to the realised critical wavenumber k_c , are marked with crosses.

2.2.3 Previous nonlinear analysis

In the analysis of Tsimring and Aranson [6, 95], amplitude equations for the near-onset behaviour of (2.2.1) are derived through consideration of the planform

$$\psi = [A(T) \sin k_c x + B(T) \sin k_c y] e^{i\nu} + \text{h.o.t.}, \quad (2.2.12)$$

where A and B are slowly varying real amplitudes of two orthogonal standing waves, and the phase ν is determined by the solution to the linearised problem. Crucially, it is then assumed that near threshold, the density ρ is slaved to $|\psi|^2$ and follows a ‘quasi-stationary’ solution, which is derived by setting the left-hand side of (2.2.1b) to zero and integrating to give:

$$\rho = \rho_{\text{qs}}(t) e^{-\eta|\psi|^2}, \quad (2.2.13)$$

where $\eta = \alpha/\beta$. The function $\rho_{\text{qs}}(t)$ is found through the condition of mass conservation

$$S^{-1} \int \rho \, dx dy = \rho_0 \quad (2.2.14)$$

where S is the total area of the container. This assumption corresponds to the conditions $\alpha \gg 1$ and $\beta \gg 1$, which imply that ρ evolves to its steady state on a much faster timescale than that of the standing waves solutions in the equation for ψ . Importantly,

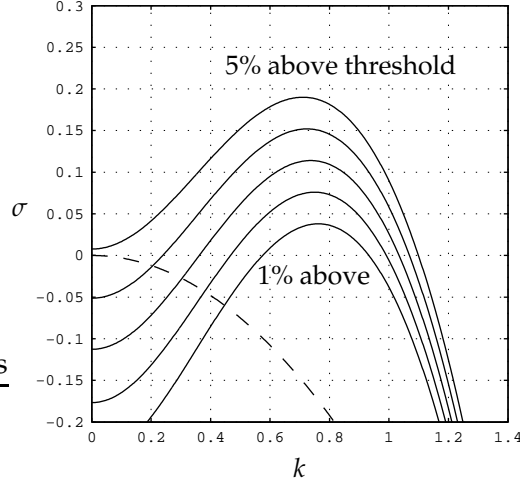


Figure 2.6: The growth rates of perturbations in the model equations (2.2.1). The amplitude term γ ranges between 1% and 5% above threshold. The growth rates of perturbations in (2.2.1a) are solid while those of (2.2.1b) are dashed; the latter are, of course, independent of γ .

this assumption does not allow the neutral stability of large-scale modes to contribute to the system dynamics. Subsequently, the amplitude equations:

$$A_T = A \left[r + \frac{1}{4}(\rho_0\eta - 3)A^2 + \frac{1}{2}(2\rho_0\eta - 3)B^2 - \frac{1}{2}\rho_0\eta^2(A^2B^2 + 2B^4) \right], \quad (2.2.15a)$$

$$B_T = B \left[r + \frac{1}{4}(\rho_0\eta - 3)B^2 + \frac{1}{2}(2\rho_0\eta - 3)A^2 - \frac{1}{2}\rho_0\eta^2(B^2A^2 + 2A^4) \right], \quad (2.2.15b)$$

are constructed, although it is not entirely clear how these equations are derived systematically since they contain both cubic and quintic terms. This suggests that these equations are *reconstituted*: they are the superposition of several solvability conditions. (The definition for the linear coefficient r is given in (2.3.13).)

Analysis of these equations shows that, near threshold, stripes are stable for $\rho_0\eta < 1$ while squares are stable when $\rho_0\eta > 1$. This is in qualitative agreement with experimental results assuming that $\rho_0\eta$ decreases with increasing frequency. Further above threshold (larger $r\eta$), stripes and squares compete and there is a bistable region where both can be stable. A phase diagram of the regions of stability of both patterns is illustrated in figure 2.7. Also on this diagram are the parameter values where oscillons have been observed through numerical simulations of the model equations (2.2.1). Note that the parameter combination $\rho_0\eta$ is later referred to as ϕ .

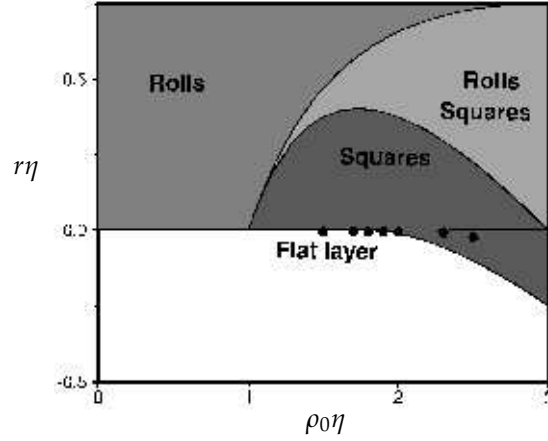


Figure 2.7: Phase diagram for square and stripe solutions to the amplitude equations (2.2.15) [6, 95]. The dots denote parameter values where oscillons have been observed.

2.3 Weakly nonlinear analysis

We consider the system (2.2.1) close to the primary bifurcation of the uniform solution, where a finite-wavelength pattern-forming instability takes place. We proceed via a weakly nonlinear framework by introducing a small parameter ϵ to allow us to set $\gamma = \gamma_c + \epsilon^2\gamma_2$; we also expand ψ and ρ about the uniform state $\psi = 0, \rho = \rho_0$ as series in the small parameter ϵ :

$$\psi = \epsilon\psi_1 + \epsilon^2\psi_2 + \epsilon^3\psi_3 + \dots, \quad (2.3.1a)$$

$$\rho = \rho_0 + \epsilon^2\rho_2 + \dots. \quad (2.3.1b)$$

Note that only even powers of ϵ appear in the expansion for ρ since the forcing in (2.2.1b) is quadratic in ψ . Making the appropriate substitutions in (2.2.1) and collecting linear terms, we recover the problem

$$\partial_t\psi_1 = \gamma_c\psi_1^* - (1 - i\omega)\psi_1 + (1 + ib)\nabla^2\psi_1 - \rho_0\psi_1. \quad (2.3.2)$$

This equation inherits from (2.2.1a) a rotational symmetry: all modes with a given wavenumber k grow at the same rate, regardless of their orientation. Thus, the modes that are realised in practice are dictated by the container geometry and nonlinear interactions.

2.3.1 No spatial modulation

We begin our analysis by examining the nonlinear descriptions of two specific and one general solution to the linear problem (2.2.3), which do not vary on a long spatial scale.

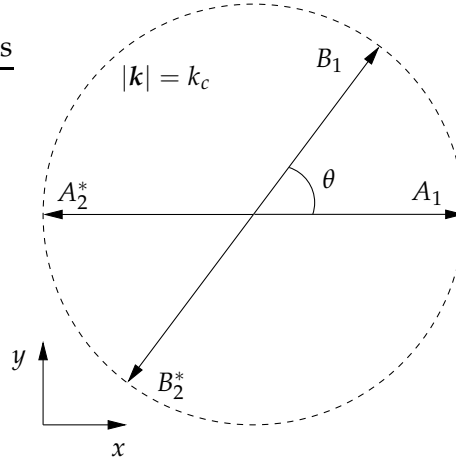


Figure 2.8: The arrangement of modes in the rhombic planform (2.3.3).

Although the dynamical consequences of the conservation of mass are missed through this analysis, it does give rise to several interesting results.

Two mode planform

Consider a two-mode rhombic ansatz (see figure 2.8),

$$\psi_1 = A_1 e^{ikx} + A_2^* e^{-ikx} + B_1 e^{ik(x \cos \theta + y \sin \theta)} + B_2^* e^{-ik(x \cos \theta + y \sin \theta)} + \text{c.c.}, \quad (2.3.3)$$

where A_1, A_2, B_1, B_2 are complex amplitudes, evolving on the slow timescale $T = \epsilon^2 t$, and θ parameterises the angle between the two modes. Substituting (2.3.3) into (2.3.2) and following an analogous procedure to that outlined in the linear analysis of §2.2.1 leads to the neutral curve

$$\gamma_c^2 = (1 + k^2 + \rho_0)^2 + (\omega - bk^2)^2, \quad (2.3.4)$$

from which the critical values k_c and γ_c (given in (2.2.9)–(2.2.11)) are readily derived. For the remainder of this analysis, we pursue the fastest-growing solution, that is, the solution with wavenumber $k = k_c$ as defined in (2.2.9). Also at this order, we recover the relationships:

$$A_2 = \left(\frac{\omega + b(1 + \rho_0)}{\gamma_c(i + b)} \right) A_1, \quad B_2 = \left(\frac{\omega + b(1 + \rho_0)}{\gamma_c(i + b)} \right) B_1, \quad (2.3.5)$$

which are important for constructing the final amplitude equations.

The $O(\epsilon^2)$ problem is

$$\mathbf{L} \begin{pmatrix} \psi_2 \\ \rho_2 \end{pmatrix} = \begin{pmatrix} 0 \\ \alpha \rho_0 \nabla^2 |\psi_1|^2 \end{pmatrix}, \quad (2.3.6)$$

where \mathbf{L} is defined in (2.2.4). To satisfy this equation, we simply set $\psi_2 = 0$ and choose ρ_2 to satisfy

$$\nabla^2 \rho_2 = -\phi \nabla^2 |\psi_1|^2, \quad (2.3.7)$$

where $\phi = \alpha\rho_0/\beta$; it is remarkable that this combination of parameters plays a critical role in the dynamics of the model equations. Indeed, the observed near-threshold patterns exhibited by the model equations (2.2.1) can be classified in terms of r and ϕ . The right-hand side of (2.3.7) is composed of purely quadratic terms and is solved by setting

$$\begin{aligned} \rho_2 = & \rho_{21} A_1 A_2 e^{2ik_c x} + \rho_{22} B_1 B_2 e^{2ik_c(x \cos \theta + y \sin \theta)} + \rho_{23} (A_1 B_2 + B_1 A_2) e^{ik_c((1+\cos \theta)x + y \sin \theta)} \\ & + \rho_{24} (A_1^* B_1 + A_2^* B_2) e^{ik_c((-1+\cos \theta)x + y \sin \theta)} + \text{c.c.} \end{aligned} \quad (2.3.8)$$

where the coefficients are given by $\rho_{21} = \rho_{22} = \rho_{23} = \rho_{24} = -\phi$.

At $O(\epsilon^3)$, we find

$$\mathbf{L} \begin{pmatrix} \psi_3 \\ \rho_3 \end{pmatrix} = \begin{pmatrix} \gamma_2 \psi_1^* - |\psi_1|^2 \psi_1 - \rho_2 \psi_1 - \psi_{1T} \\ 0 \end{pmatrix}, \quad (2.3.9)$$

and we must pay careful attention to the appropriate solvability conditions. To this end, we specify ψ_3 to take a similar form to the linear solution (2.3.3):

$$\psi_3 = C_1 e^{ik_c x} + C_2^* e^{-ik_c x} + D_1 e^{ik_c(x \cos \theta + y \sin \theta)} + D_2^* e^{ik_c(x \cos \theta + y \sin \theta)} + \text{c.t.}, \quad (2.3.10)$$

where the shorthand ‘c.t.’ stands for cubic terms which need to be included to balance the cubic harmonics (e.g., terms proportional to e^{3ix}). However, as these terms do not contribute to the amplitude equations for A_1 and B_1 , we can safely neglect them. Solvability conditions are then derived by eliminating C_1 and C_2 (or equivalently, D_1 and D_2). Note that this algorithmic approach to solvability conditions is equivalent to the more formal procedure outlined in §1.2.3. After substituting (2.3.10) into (2.3.9), collecting terms proportional to the modes $e^{\pm ik_c x}$ yields:

$$\begin{aligned} 0 = & (-1 + i\omega + ibk^2 - \rho_0 - k^2)C_1 + \gamma_c C_2 - A_{1T} + \gamma_2 A_2 - 2A_1 |B_1|^2 - 2A_1 |A_2|^2 \\ & - 2A_1 |B_2|^2 - A_1 |A_1|^2 + \phi(A_1 |A_2|^2 + A_1 |B_2|^2 + A_1 |B_1|^2 + 2A_2 B_1 B_2^*), \end{aligned} \quad (2.3.11a)$$

$$\begin{aligned} 0 = & (-1 - i\omega + ibk^2 - \rho_0 - k^2)C_2 + \gamma_c C_1 - A_{2T} + \gamma_2 A_1 - 2A_2 |B_1|^2 - 2A_2 |A_1|^2 \\ & - 2A_2 |B_2|^2 - A_2 |A_2|^2 + \phi(A_2 |A_1|^2 + A_2 |B_2|^2 + A_2 |B_1|^2 + 2A_1 B_1^* B_2), \end{aligned} \quad (2.3.11b)$$

and after eliminating C_2 from these equations, we find C_1 also disappears due to the criticality conditions (2.2.9) and (2.2.10). Setting the remaining terms equal to zero then gives the solvability condition, which takes the form of an amplitude equation for A_1 :

$$A_{1T} = rA_1 - (3 - \phi)|A_1|^2 A_1 - 2(3 - 2\phi)|B_1|^2 A_1, \quad (2.3.12)$$

where

$$r = \frac{\gamma_c \gamma_2 (1 + b^2)}{b(\omega + b(1 + \rho_0))}. \quad (2.3.13)$$

By a similar procedure involving the terms proportional to the modes $e^{\pm ik_c(x \cos \theta + y \sin \theta)}$, we can derive the corresponding equation for B_1 :

$$B_{1T} = rB_1 - (3 - \phi)|B_1|^2 B_1 - 2(3 - 2\phi)|A_1|^2 B_1. \quad (2.3.14)$$

Curiously, these equations are independent of the angle between the wavevectors θ . Generically, the behaviour for a two-mode ansatz (in the absence of a conservation law) is for the ‘cross-coupling’ cubic coefficient (here equal to $-2(3 - 2\phi)$) to tend to a fixed value (2 in the nondimensional case) as $\theta \rightarrow 0$. Here, the influence of the conservation law means this coefficient can be altered by variation of the parameter ϕ . Note that when $\phi > 3$, both nonlinear terms have a positive coefficient and saturation of the solutions will not occur. In this case, the amplitude equations must be augmented with quintic terms for solutions to saturate.

The equations (2.3.12) and (2.3.14) admit two nontrivial solutions:

- stripes (e.g., $|A_1|^2 = r/(3 - \phi)$, $B_1 = 0$);
- rectangles ($|A_1|^2 = |B_1|^2 = r/(9 - 5\phi)$);

an example of each is given in figure 2.10. To determine the stability of stripe solutions, we make the substitution

$$A_1 = \sqrt{\frac{r}{3 - \phi}} e^{iv} + \chi a_1(T), \quad B = \chi b_1(T), \quad (2.3.15)$$

where χ is a small book-keeping parameter and v is a real phase. Collecting $O(\chi)$ terms, we look for solutions $a_1, b_1 \propto e^{\Sigma T}$, which give rise to the simple eigenvalues:

$$\Sigma_1^{\text{str}} = -2r, \quad \Sigma_2^{\text{str}} = -\frac{3r(1 - \phi)}{3 - \phi}. \quad (2.3.16)$$

Thus, while $r > 0$, stripes are stable for $\phi < 1$. An analogous procedure for rhombic solutions yields the eigenvalues:

$$\Sigma_1^{\text{rho}} = -2r, \quad \Sigma_2^{\text{rho}} = \frac{6r(\phi - 1)}{9 - 5\phi}, \quad (2.3.17)$$

implying rectangles are stable when $1 < \phi < 9/5$. This picture is consistent with experimental observations, since ϕ is expected to decrease with increasing f [6].

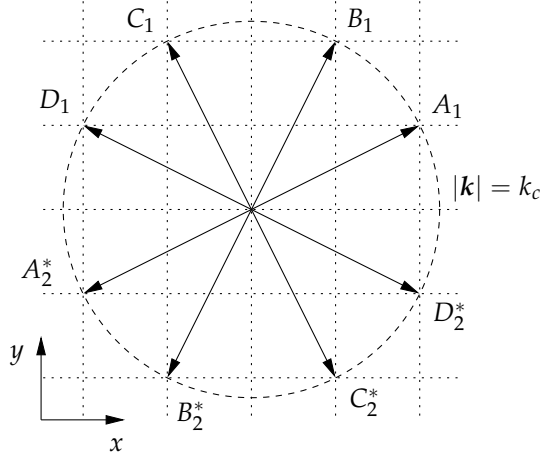


Figure 2.9: The arrangement of modes in wavenumber space for the four mode ansatz (2.3.18). The modes can be seen to lie on a spatially periodic square lattice.

Four-mode planform

Let us consider a lattice-periodic ansatz comprising four modes (see figure 2.9):

$$\begin{aligned} \psi_1 = & A_1 \exp \left\{ \frac{ik}{\sqrt{5}}(2x + y) \right\} + B_1 \exp \left\{ \frac{ik}{\sqrt{5}}(x + 2y) \right\} \\ & + C_1 \exp \left\{ \frac{ik}{\sqrt{5}}(-x + 2y) \right\} + D_1 \exp \left\{ \frac{ik}{\sqrt{5}}(-2x + y) \right\} \\ & + A_2^* \exp \left\{ \frac{-ik}{\sqrt{5}}(2x + y) \right\} + B_2^* \exp \left\{ \frac{-ik}{\sqrt{5}}(x + 2y) \right\} \\ & + C_2^* \exp \left\{ \frac{-ik}{\sqrt{5}}(-x + 2y) \right\} + D_2^* \exp \left\{ \frac{-ik}{\sqrt{5}}(-2x + y) \right\}, \end{aligned} \quad (2.3.18)$$

which can describe a wide range of spatially periodic patterns [18]. Performing an analogous weakly nonlinear expansion as for the two mode ansatz (2.3.3), we obtain the amplitude equations:

$$A_{1T} = rA_1 - (3 - \phi)|A_1|^2 A_1 - 2(3 - 2\phi)A_1 (|B_1|^2 + |C_1|^2 + |D_1|^2), \quad (2.3.19a)$$

$$B_{1T} = rB_1 - (3 - \phi)|B_1|^2 B_1 - 2(3 - 2\phi)B_1 (|A_1|^2 + |C_1|^2 + |D_1|^2), \quad (2.3.19b)$$

$$C_{1T} = rC_1 - (3 - \phi)|C_1|^2 C_1 - 2(3 - 2\phi)C_1 (|A_1|^2 + |B_1|^2 + |D_1|^2), \quad (2.3.19c)$$

$$D_{1T} = rD_1 - (3 - \phi)|D_1|^2 D_1 - 2(3 - 2\phi)D_1 (|A_1|^2 + |B_1|^2 + |C_1|^2), \quad (2.3.19d)$$

where the control parameter r is defined in (2.3.13). These equations admit several forms of steady state (see figure 2.10g,h) although only two can be stable:

- stripes (e.g., $|A_1|^2 = r/(3 - \phi)$, $B_1 = C_1 = D_1 = 0$), stable for $\phi < 1$;
- squares (e.g., $|A_1|^2 = |C_1|^2 = r/(9 - 5\phi)$, $B_1 = D_1 = 0$), always unstable;

- rectangles (e.g., $|A_1|^2 = |B_1|^2 = r/(9 - 5\phi)$, $C_1 = D_1 = 0$), always unstable;
- three-mode solutions (e.g., $|A_1|^2 = |B_1|^2 = |C_1|^2 = r/(15 - 9\phi)$, $D_1 = 0$, always unstable (this solution does not exist when higher-order terms are included in the amplitude equations);
- four-mode solutions with $|A|^2 = |B|^2 = |C|^2 = |D|^2 = r/(21 - 13\phi)$, stable when $1 < \phi < 21/13$.

Since the equations (2.3.19) are invariant under phase translations ($A \mapsto Ae^{iv}$, $v \in \mathbb{R}$), higher-order terms are required to resolve the relationships between the phases of the modes in the four-mode solutions. However, analysis of these phase relations has revealed that only two steady states can exist: ‘supersquares’ and ‘antisquares’ [18] (see (g) and (h) of figure 2.10). Numerical simulations presented in §2.4 will indicate which of these forms may be found stably in the present problem. Before leaving our examination of the unmodulated problem, we extend our analysis to patterns comprising an arbitrary number of modes.

N-mode ansatz

Let us consider a general solution to the linear problem composed of N distinct modes (and their conjugates), each lying, equally spaced, on the circle of critical wavenumbers $|\mathbf{k}| = k_c$:

$$\psi_1 = \sum_{n=0}^{2N-1} A_j(T) \exp \left\{ ik \left(x \cos \left(\frac{\pi n}{N} \right) + y \sin \left(\frac{\pi n}{N} \right) \right) \right\}. \quad (2.3.20)$$

Due to the term $\gamma\psi^*$ of (2.2.3), the conjugate term of each mode must be included and so this linear solution contains $2N$ complex amplitudes.

Now, after substituting (2.3.20) into the linear problem (2.2.3), we find problems of the form (cf. (2.2.6)):

$$0 = \gamma_c A_{j+N}^* - A_j (1 - i\omega + ibk^2 - \rho_0 - k^2), \quad (2.3.21a)$$

$$0 = \gamma_c A_j - A_{j+N}^* (1 + i\omega - ibk^2 - \rho_0 - k^2), \quad (2.3.21b)$$

for each $j = 0, \dots, N - 1$. As one might expect, eliminating either amplitude from these equations recovers the neutral curve (2.2.8) and the critical values for γ and k are then easily derived.

Collecting terms at $O(\epsilon^2)$, we find the problem (2.3.6) and so we set $\psi_2 = 0$ and choose ρ_2 to satisfy

$$\nabla^2 \rho_2 = -\phi \nabla^2 |\psi_1|^2. \quad (2.3.22)$$

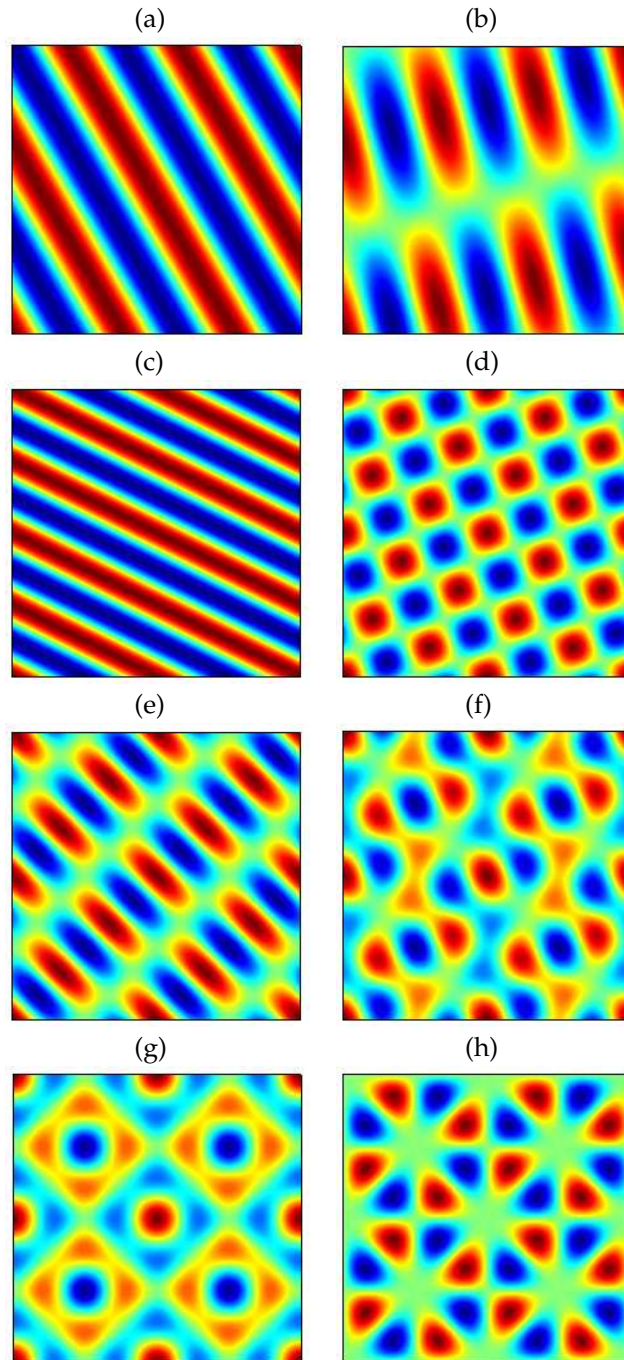


Figure 2.10: Patterns admitted by the amplitude equations (2.3.12) and (2.3.14) as well as the system (2.3.19): (a) stripes 1; (b) rectangles 1; (c) stripes 2; (d) squares; (e) rectangles 2; (f) 3-mode pattern; (g) supersquares; (h) anti-squares. Patterns (a),(b) are the solutions to (2.3.12) and (2.3.14) plotted in a box of sidelength $L = 3\Lambda_c$ (where $\Lambda_c = 2\pi/k_c$ is the critical wavelength), while (c)–(h) are the possible solutions to the system (2.3.19) plotted in a box with sidelength $L = 3\sqrt{5}\Lambda_c$. Note that these patterns are simple constructions; they are not the results of simulating the amplitude equations.

We solve this equation by setting

$$\rho_2 = -\phi \sum_{\substack{p,q=0 \\ p \neq q}}^{2N-1} A_p A_q^* \exp \left\{ ik_c x \left[\cos \left(\frac{\pi p}{N} \right) + \cos \left(\frac{\pi q}{N} \right) \right] \right. \\ \left. + ik_c y \left[\sin \left(\frac{\pi p}{N} \right) + \sin \left(\frac{\pi q}{N} \right) \right] \right\}.$$

Moving on to $O(\epsilon^3)$, we find the problem (2.3.9) and derive solvability conditions by substituting an analogue of the linear solution:

$$\psi_3 = \sum_{j=0}^{2N-1} C_j(T) \exp \left\{ ik_c \left(x \cos \frac{\pi j}{N} + y \sin \frac{\pi j}{N} \right) \right\} + \text{c.t.}, \quad (2.3.23)$$

where the cubic harmonic terms ('c.t.') can be neglected. Considering the conjugate modes C_j and C_{j+N}^* , we find

$$\gamma_c C_{j+N}^* - C_j (1 - i\omega + ibk^2 + \rho_0 + k^2) = F_j, \quad (2.3.24a)$$

$$\gamma_c C_j - C_{j+N}^* (1 + i\omega - ibk^2 + \rho_0 + k^2) = F_{j+N}, \quad (2.3.24b)$$

where

$$F_j = \gamma_2 A_{j+N}^* + \phi \left[A_j \sum_{\substack{k=0 \\ k \neq j, j+N}}^{2N-1} |A_k|^2 + A_{j+N}^* \sum_{\substack{k=0 \\ k \neq j, j+N}}^{2N-1} A_k A_{k+N} + A_j |A_{j+N}|^2 \right] \\ - A_j |A_j|^2 - 2A_j \sum_{\substack{k=0 \\ k \neq j}}^{2N-1} |A_k|^2 - A_{j+N}^* \sum_{\substack{k=0 \\ k \neq j, j+N}}^{2N-1} A_k A_{k+N} - A_{jT}, \quad (2.3.25)$$

and the subscripting within this expression is modulo $2N$. The appropriate expression for F_{j+N} can be found by making the transformation $j \mapsto j + N, \text{ mod } 2N$. Eliminating either C_j or C_{j+N}^* from (2.3.24) yields the solvability condition

$$\gamma_c F_j + (1 - i\omega + ibk^2 + \rho_0 + k^2) F_{j+N}^* = 0, \quad (2.3.26)$$

and using the relationships

$$\gamma_c A_{j+N}^* = (1 - i\omega + ibk^2 + \rho_0 + k^2) A_j \quad \text{and} \quad |A_{j+N}|^2 = |A_j|^2, \quad (2.3.27)$$

we can construct amplitude equations for each A_j :

$$A_{jT} = \left[\frac{\gamma_2 \gamma_c (1 + b^2)}{b(\omega + b(1 + \rho_0))} \right] A_j - A_j \left[(3 - \phi) |A_j|^2 + 2(3 - 2\phi) \sum_{\substack{k=0 \\ k \neq j}}^{2N-1} |A_k|^2 \right], \quad (2.3.28)$$

resulting in a set of N coupled amplitude equations. As with the amplitude equations derived from the two and four mode planforms, if $\phi > 3$, the nonlinear terms in (2.3.28) will no longer allow standing wave solutions to saturate and the primary bifurcation will be subcritical.

Steady states of the N -mode system

Amplitude equations of the form (2.3.28) admit steady states composed of $1, \dots, N$ equal-amplitude modes; however, based on the analysis of the four mode system, where only stripes and four-mode patterns can be stable, we concentrate our attention here on stripes and N -mode solutions; it is expected that all other solutions are unstable.

Stripe solutions to (2.3.28) can take N equivalent forms depending on which mode has nonzero amplitude. If the k th mode ($0 \leq k \leq N - 1$) is nonzero then stripes are given by

$$A_j = \delta_{jk} Q e^{i\theta}, \quad \theta \in \mathbb{R} \quad \text{for } j = 0, \dots, N - 1, \quad (2.3.29)$$

where the amplitude Q is defined as

$$Q^2 = \frac{r}{3 - \phi} \quad (2.3.30)$$

and

$$r = \frac{\gamma_2 \gamma_c (1 + b^2)}{b(\omega + b(1 + \rho_0))}.$$

We examine the stability of these solutions by introducing small perturbation terms:

$$A_j = \delta_{jk} (Q e^{i\theta} + \chi a_j(T)) + \chi (1 - \delta_{jk}) a_j(T) \quad \text{for } j = 0, \dots, N - 1, \quad (2.3.31)$$

where χ is the usual book-keeping parameter. After substituting into (2.3.28), and retaining only linear terms in χ , we can derive two evolution equations:

$$a_{jT} = \begin{cases} a_j [r - 3Q^2(3 - \phi)], & \text{for } j = k, \\ a_j [r - 2Q^2(3 - 2\phi)], & \text{for } j \neq k \end{cases} \quad \text{for } j = 0, \dots, N - 1, \quad (2.3.32a)$$

which leads to a Jacobian matrix of the form

$$\mathbf{J}_{\text{stripes}} = \begin{bmatrix} a & 0 & \cdots & 0 \\ 0 & b & \cdots & 0 \\ \vdots & \vdots & \ddots & \vdots \\ 0 & 0 & \cdots & b \end{bmatrix} \quad (2.3.33)$$

where

$$\begin{aligned} a &= r - 3Q^2(3 - \phi), \\ b &= r - 2Q^2(3 - 2\phi). \end{aligned}$$

Clearly, $\mathbf{J}_{\text{stripes}}$ has eigenvalues Σ of the form

$$\Sigma_1^{\text{str}} = -2r, \quad \Sigma_2^{\text{str}} = -3r \left(\frac{1-\phi}{3-\phi} \right), \quad (2.3.34)$$

and so stripes will be stable to perturbations when $\phi < 1$.

The N -mode solution to (2.3.28) has form $A_j = Qe^{i\theta_j}$, $j = 0, \dots, N-1$, where

$$Q^2 = \frac{r}{6N-3+\phi(3-4N)}. \quad (2.3.35)$$

As with the four-mode solutions of the previous section, the evolution and steady states of the phases θ_j of the solution are determined at higher order. Introducing perturbations of the form

$$A_j = Qe^{i\theta_j} + \chi a_j(T), \quad j = 0, \dots, N-1,$$

and substituting into the j th amplitude equation (2.3.28), the linear terms in χ give rise to evolution equations of the form

$$a_{jT} = ra_j - Q^2 \left[a_j(3+6N-\phi(1-4N)) + 4(3-2\phi) \sum_{\substack{k=0 \\ k \neq j}}^{N-1} a_k \right], \quad (2.3.36)$$

for $j = 0, \dots, N-1$. Constructing the appropriate Jacobian, we find $N \times N$ matrices of the form

$$\mathbf{J}_{N\text{-mode}} = \begin{bmatrix} a & b & \cdots & b \\ b & a & \cdots & b \\ \vdots & \vdots & \ddots & \vdots \\ b & b & \cdots & a \end{bmatrix} \quad (2.3.37)$$

where

$$\begin{aligned} a &= r - Q^2(3+6N-\phi(1-4N)), \\ b &= -4Q^2(3-2\phi). \end{aligned}$$

A straightforward exercise in linear algebra shows that matrices of the form (2.3.37) have eigenvalues $(N-1)b+a$ and $b-1$ with multiplicities 1 and $N-1$ respectively; this procedure is detailed in appendix A. It then follows that the solution in question has stability eigenvalues of the form

$$-6r(\phi-1)Q^2, \quad -2r. \quad (2.3.38)$$

Thus, the N mode solution will always be stable to amplitude perturbations for

$$1 < \phi < \frac{6N-3}{4N-3}. \quad (2.3.39)$$

One can see that as N increases, the width of the stability region for N -mode solutions shrinks, tending to the limiting case $1 < \phi < 3/2$.

Hence, for small containers where modulational effects do not take place, and for $1 < \phi < 3/2$, one expects the selected pattern to comprise all the critical modes which fit into the domain. This prediction is verified in §2.4 where results of simulations performed in a variety of small containers are presented. This interesting and unusual behaviour is not present in many pattern formation models and is only made possible here by the coupling to a large-scale mode.

2.3.2 Spatial modulation

The weakly nonlinear analysis of the previous section holds when the pattern spectrum consists of discrete modes whose wavenumbers are close to the critical circle $|k| = k_c$. This will generally be true for small containers where the quantisation induced by the boundary conditions ensures that the permitted wavenumbers are suitably separated. In a spatially extended domain however, mass conservation leads to the existence of slowly evolving modes of large wavelength (i.e., with wavenumber close to zero), representing adjustments of large-scale inhomogeneities in the thickness of the layer. These slowly varying modes, even though linearly damped through the diffusive term in the equation of mass conservation, must be included in any amplitude-equation description of the near-threshold dynamics of the pattern [74, 75, 83]. Previous theoretical work outlined in §1.5 has indicated the appropriate amplitude equations for a system undergoing a stationary bifurcation to a pattern (cf. (1.5.19)), and we describe below how this analysis may straightforwardly be extended to the present problem of parametric forcing.

We concentrate on mutually perpendicular modes ($\theta = \pi/2$) and consider the planform

$$\psi_1 = A_1(X, Y, T)e^{ikx} + A_2^*(X, Y, T)e^{-ikx} + B_1(X, Y, T)e^{iky} + B_2(X, Y, T)^*e^{-iky}. \quad (2.3.40)$$

As before, the evolution of the amplitudes takes place on the slow timescale $T = \epsilon^2 t$, while spatial modulations occur over the long scales given by $X = \epsilon x$ and $Y = \epsilon y$; we find A_2, B_2 are related to A_1, B_1 by (2.3.5).

At $O(\epsilon^2)$ we recover the problem

$$\mathbf{L} \begin{pmatrix} \psi_2 \\ \rho_2 \end{pmatrix} = \begin{pmatrix} 2(1 + ib)(\psi_{1xX} + \psi_{1yY}) \\ -\alpha\rho_0 \nabla^2 |\psi_1|^2 \end{pmatrix}. \quad (2.3.41)$$

where \mathbf{L} is defined in (2.2.4), and set the planforms ψ_2, ρ_2 to be

$$\psi_2 = D_1(X, Y, T)e^{ikx} + D_2(X, Y, T)^*e^{-ikx} + E_1(X, Y, T)e^{iky} + E_2(X, Y, T)^*e^{-iky}, \quad (2.3.42a)$$

$$\begin{aligned} \rho_2 = & \rho_{21}A_1A_2e^{2ikx} + \rho_{22}B_1B_2e^{2iky} \\ & + \rho_{23}(A_1B_2 + B_1A_2)e^{ik(x+y)} + \rho_{24}(A_1^*B_1 + A_2^*B_2)e^{ik(-x+y)} + \text{c.c.} + C(X, Y, T), \end{aligned} \quad (2.3.42b)$$

where $\rho_{21} = \dots = \rho_{24} = -\phi$ and $C(X, Y, T)$ is a large-scale mode. Subsequently, after substituting (2.3.42) into (2.3.41) and collecting terms proportional to $e^{\pm ikx}$ (or equivalently, $e^{\pm iky}$), we can eliminate D_1 and D_2 (E_1 and E_2) to yield the relations:

$$A_{2X} = \left(\frac{\omega + b(1 + \rho_0)}{\gamma_c(b + i)} \right) A_{1X}, \quad (2.3.43a)$$

$$B_{2Y} = \left(\frac{\omega + b(1 + \rho_0)}{\gamma_c(b + i)} \right) B_{1Y}. \quad (2.3.43b)$$

Integrating (2.3.43a) with respect to X and (2.3.43b) with respect to Y recovers the previously found relationships (2.3.5) so no further constraints are imposed. Also at this order we find the relationships

$$\gamma_c D_2 = D_1 (1 + \rho_0 + k^2 - i\omega + ibk^2) + 2k(b - i)A_{1X}, \quad (2.3.44a)$$

$$\gamma_c E_2 = E_1 (1 + \rho_0 + k^2 - i\omega + ibk^2) + 2k(b - i)B_{1Y}, \quad (2.3.44b)$$

which are important for deriving the correct form of the amplitude equations. At $O(\epsilon^3)$, amplitude equations for A_1 and B_1 are derived by applying solvability conditions. One means of doing this is to form two equations by collecting terms proportional to $e^{ik_c x}$ and $e^{-ik_c x}$ and then eliminate E_1 (or equivalently, E_2). In the resulting equation, the coefficient of E_2 (E_1) will be

$$\gamma_c^2 - (1 + k^2 + \rho_0)^2 + (\omega - bk^2)^2, \quad (2.3.45)$$

which, since k_c lies on the neutral curve (2.2.8), will be zero. The remaining terms can then be rearranged to give an amplitude equation for A_2 :

$$\begin{aligned} A_{1T} = & \left(\frac{\gamma_c \gamma_2 (1 + b^2)}{b(\omega + b(1 + \rho_0))} \right) A_1 + \left(\frac{2(1 + b^2)(b\omega - 1 - \rho_0)}{b(\omega + b + b\rho_0)} \right) A_{1XX} \\ & - (3 - \phi)|A_1|^2 A_1 - 2(3 - 2\phi)|B_1|^2 A_1 - A_1 C, \end{aligned} \quad (2.3.46)$$

where the conditions (2.2.9) and (2.2.10) have been used to simplify the coefficients. Similarly, by performing the same procedure but using the terms proportional to $e^{ik_c y}$ and $e^{-ik_c y}$, an evolution equation for B_1 can be derived:

$$\begin{aligned} B_{1T} = & \left(\frac{\gamma_c \gamma_2 (1 + b^2)}{b(\omega + b(1 + \rho_0))} \right) B_1 + \left(\frac{2(1 + b^2)(b\omega - 1 - \rho_0)}{b(\omega + b + b\rho_0)} \right) B_{1YY} \\ & - (3 - \phi)|B_1|^2 B_1 - 2(3 - 2\phi)|A_1|^2 B_1 - B_1 C. \end{aligned} \quad (2.3.47)$$

To complete the system, we only require an evolution equation for C , which can be derived by integrating the ρ component of the $O(\epsilon^4)$ terms. We find

$$C_T = \beta \nabla^2 C + 2\alpha\rho_0 \nabla^2 (|A_1|^2 + |B_1|^2), \quad (2.3.48)$$

where $\nabla^2 \equiv \partial_X^2 + \partial_Y^2$. After rescaling and dropping subscripts, we can rewrite (2.3.46), (2.3.47) and (2.3.48) as

$$A_T = rA + A_{XX} - |A|^2 A - \lambda |B|^2 A - AC, \quad (2.3.49a)$$

$$B_T = rB + B_{YY} - |B|^2 B - \lambda |A|^2 B - BC, \quad (2.3.49b)$$

$$C_T = \sigma \nabla^2 C + \mu \nabla^2 (|A|^2 + |B|^2), \quad (2.3.49c)$$

where r is defined in (2.3.13), λ is defined by

$$\lambda = 2 \left(\frac{3 - 2\phi}{3 - \phi} \right) \quad (2.3.50)$$

and

$$\sigma = \frac{\beta}{2} \left[\frac{\omega b + b^2(1 + \rho_0)}{(\omega b - 1 - \rho_0)(1 + b^2)} \right], \quad (2.3.51a)$$

$$\mu = \frac{\alpha\rho_0}{3 - \phi} \left[\frac{\omega b + b^2(1 + \rho_0)}{(\omega b - 1 - \rho_0)(1 + b^2)} \right]. \quad (2.3.51b)$$

Since the average of C over X and Y is conserved, according to (2.3.49c), we may with no loss of generality set this average to zero (by redefining γ_2 if necessary).

Solution behaviour

The amplitude equations (2.3.49) are precisely those of Cox and Matthews [75] (in the special case that their parameter $\mu_- = 0$) and so we may apply directly their modulational stability results for stripes and squares.

We first consider stripes: the system (2.3.49) admits a family of solutions of form $A = Qe^{iqx}$, $B = C = 0$, where $Q^2 = r - q^2$, corresponding to stripes of wavenumber $k_c + \epsilon q$. Of course, we recover the results of §2.3.1 regarding the stability of stripes to disturbances with exactly critical wavenumber: stripes are unstable to squares if $\lambda < 1$ (i.e., if $\phi > 1$). Analysis of the modulational stability of stripes (see §1.5.2 [75]) indicates that a new instability, leading to amplitude modulation, replaces the usual Eckhaus instability and, when $\mu > 0$, is more widespread than the case when there is no conserved mode. Indeed, all stripes may be modulationally unstable if $\mu > \sigma$, with the last stripes to succumb to the instability being those at band-centre ($q = 0$). We thus focus on the band-centre stripes. For these stripes, in terms of the original variables, the region

of modulational instability corresponds to $1 < \phi < 3$, identical to that for instability to perturbations in a perpendicular mode (i.e., instability of stripes to squares). Since we expect the timescale for the growth of perpendicular modes to be less than that for modulational modes, we do not expect to see a long-wavelength instability of stripes in simulations, except under contrived circumstances, and we expect instead to see only the transition to squares. Recall that this coincidence of stability conditions is also present in the modified two-dimensional Swift–Hohenberg model (1.5.24) considered in §1.5.2 and Cox and Matthews [75].

Squares take the form $A = B = Qe^{iqX}, C = 0$ with $Q^2 = (r - q^2)/(1 + \lambda)$ and are stable to roll-type perturbations only while $|\lambda| < 1$, i.e., $1 < \phi < 9/5$. All square patterns are found to be unstable to modulational perturbations when $2\mu > (1 + \lambda)\sigma$ [75]. This implies that squares are modulationally unstable while $\phi > 1$, again matching the roll-perturbation stability boundary. This leads to the remarkable result that all square patterns are unstable, provided the container size is suitably large, and so a stable regular square pattern can never be seen in corresponding simulations. A more detailed analysis indicates that the initial deformation of a modulationally unstable square pattern will be primarily to its amplitude if the wavenumber $k + \epsilon q$ lies near the band-centre, but to its phase otherwise [75]. Nevertheless, in a finite computational box, one would generally expect some modulation of both the amplitude and phase.

2.4 Simulation results

In this section, we numerically study the system (2.2.1) for a variety of container sizes, ϕ values and initial conditions. Our exploration is twofold: we first explore the predictions of §2.3.1 by simulating the model equations in small containers, where the permitted wavenumbers are discretely spaced, preventing the occurrence of modulational effects. Secondly, we perform simulations in large boxes where modulational effects are possible and the instabilities identified in §2.3.2 can occur.

2.4.1 Numerical scheme

We solve the model equations (2.2.1) in a square box of size L with periodic boundary conditions. We use a pseudo-spectral method to solve the partial differential equations, whereby most calculations are carried out in spectral (wavenumber) space with the exception of evaluating nonlinear and conjugate terms, which are performed in physical space (see Trefethen [142] for more details of pseudo-spectral methods). Due to the

slowly varying long-wave mode associated with a conservation law and the existence of rapidly decaying modes at high wavenumber, the system (2.2.1) is ‘stiff’, meaning it evolves over both a fast and slow timescale. Conventionally, such systems are treated using an explicit scheme with a very small time-step. However, sophisticated implicit schemes exist that can resolve the behaviour without resorting to tiny time-steps. We use an exponential time-stepping (ETD) scheme **ETD2** [138], that integrates the linear terms exactly, catering for the dynamics on both timescales. Similar schemes have been known for over forty years, are periodically rediscovered, and are currently undergoing something of a renaissance [143].

Exponential time differencing methods for systems of the form

$$u_t = cu + F(u, t), \quad (2.4.1)$$

where c is a constant and $F(u, t)$ represents nonlinear forcing terms, are derived by multiplying through by the integrating factor e^{-ct} then integrating over a single time-step, from $t = t_n$ to $t = t_{n+1} = t_n + h$, to give

$$u(t_{n+1}) = u(t_n)e^{ch} + e^{ch} \int_0^h e^{-c\tau} F(u(t_n + \tau), t_n + \tau) d\tau. \quad (2.4.2)$$

Various ETD schemes can be derived from this exact equation by employing different approximations to the integral term. The simplest scheme is **ETD1** which assumes F to be constant between $t = t_n$ and $t = t_{n+1}$, giving

$$u_{n+1} = u_n e^{ch} + F_n (e^{ch} - 1)/c, \quad (2.4.3)$$

where $u_n = u(t_n)$ and $F_n = F(u_n, t_n)$; this scheme has a truncation error of $h^2 \dot{F}/2$. Our chosen scheme uses the higher-order approximation of F :

$$F = F_n + \tau(F_n - F_{n-1})/h + O(h^2). \quad (2.4.4)$$

This gives rise to the scheme **ETD2**, given by

$$u_{n+1} = u_n e^{ch} + \left((1 + ch)e^{ch} - 1 - 2ch \right) \left(\frac{F_n}{hc^2} \right) + \left(1 + ch - e^{ch} \right) \left(\frac{F_{n-1}}{hc^2} \right), \quad (2.4.5)$$

which has local truncation error $5h^3/12\ddot{F}$. Note that in the limit of $c \rightarrow 0$, this scheme reduces to the second-order Adams–Bashforth formula

$$u_{n+1} = u_n - \frac{1}{2}F_n + \frac{3}{2}F_{n-1}. \quad (2.4.6)$$

For a typical simulation, we choose initial conditions composed of a periodic pattern or uniform state perturbed by a layer of Gaussian noise of order 10^{-4} . Subsequently,

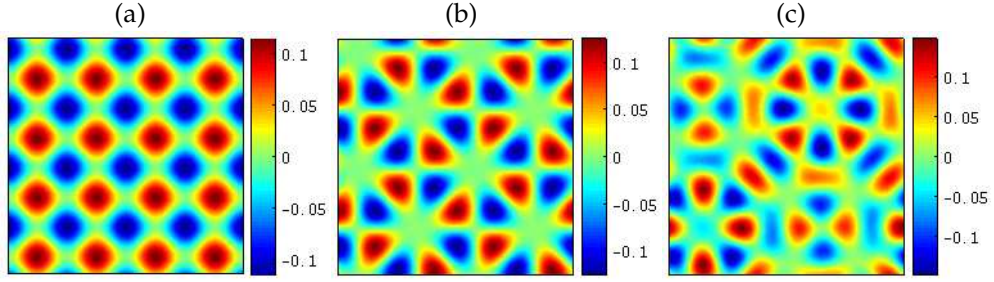


Figure 2.11: The steady states of $\text{Re}(\psi)$ for the container sizes (a) $L = 2\Lambda_c$, (b) $L = 2\sqrt{5}\Lambda_c$ and (c) $L = 5$. Each simulation was run with an initial condition of small-amplitude noise and $\phi = 1.05$, chosen so that, for each value of L , stripes are unstable.

using a time-step of $h = 0.2$ and a 128×128 grid, we are able to capture both the fast and slow dynamics of the system. Since many of the exhibited simulations are taken very close to threshold, the growth of large-scale modes and the phase relaxation of the observed pattern takes place on a very slow timescale. Typically, simulations need to be run over times $T \approx 50000$ to capture the full nonlinear development of an instability. The MATLAB code used to generate the figures of this section is discussed further in appendix B.

For §2.4.2 and §2.4.3, we prescribe the parameter values $\beta = \rho_0 = 0.3, b = 1, \omega = 2.5$, to ensure the primary instability is finite-wavelength, and use the mobility coefficient α (which effectively equals ϕ with this choice of parameters) as a control parameter. All simulations take place in a square container of size L with periodic boundary conditions.

2.4.2 Small-container numerical simulations

We begin by choosing L to be small so that only a small number of pattern wavelengths fit inside the simulation container. In such a situation, the permitted wavenumbers are well separated and modulational (‘sideband’) instabilities are not permitted.

In figure 2.11, we illustrate the realised steady states of $\text{Re}(\psi)$ for three different values of L . In figure 2.11(a), we choose $L = 2\Lambda_c$ where $\Lambda_c = 2\pi/k_c$ is the critical pattern wavelength. In this scenario, the fastest-growing modes are perpendicular to and aligned with the periodic boundaries and the leading-order pattern is of the form (2.3.3) with $\theta = \pi/2$. As predicted in §2.3.1, we find stripes to be stable for $\phi < 1$, but stable squares when $1 < \phi < 3/2$.

Alternatively, if we choose $L = n\sqrt{5}\Lambda_c, n \in \mathbb{N}$, then the dominant modes take the form

of those comprising the four-mode planform (2.3.18). (Note that n must be relatively small otherwise modulational effects will be permitted.) Again simulations support the theory: stripes are stable for $\phi < 1$ and antisquares are stable for $1 < \phi < 3/2$ (see figure 2.11b, where $\phi = 1.05$). However, the range of validity of the weakly nonlinear approximation is found to be fairly small: at 1% above threshold, antisquares are no longer realised and instead we find stripe-like patterns. Such results are in correspondence with the phase diagram of [6, 95].

Further support for the analysis of §2.3.2 is seen in figure 2.11(c), where the steady state for a container of sidelength $L = 5\Lambda_c$ is presented. In this container geometry, there are six unstable modes, of the form

$$e^{ik_c x}, e^{ik_c(4x+3y)/5}, e^{ik_c(3x+4y)/5}, e^{ik_c y}, e^{ik_c(-3x+4y)/5}, e^{ik_c(-4x+3y)/5} \quad (2.4.7)$$

and the realised pattern takes a form denoted ‘minus supersupersquares’ which can be written [19]:

$$\begin{aligned} \text{Re}(\psi) \sim & -\cos(k_c x) - \cos(k_c y) + \cos(k_c(4x + 3y)/5) \\ & + \cos(k_c(3x + 4y)/5) + \cos(k_c(-3x + 4y)/5) + \cos(k_c(-4x + 3y)/5). \end{aligned} \quad (2.4.8)$$

All the steady states of figure 2.11 support the N -mode analysis of §2.3.1, whereby the steady state arrangement when $1 < \phi < 3/2$ is composed of all the permitted modes.

2.4.3 Large-container numerical simulations

In this section, we report the results of simulations performed in a large square container, where long-wavelength modulations to the pattern can occur. Extensive simulations support the predictions of §2.3.2 regarding the modulational stability of both stripes and squares.

Figure 2.12 illustrates the evolution of a perturbed square pattern, which previous analysis had suggested was stable [6]. The figure illustrates the occurrence of a long-wave instability, which initially gives rise to amplitude modulation in the form of a large-scale square ‘superstructure’. (A limited analysis of such a superstructure [75] is consistent with the square shape observed here.) The final state reached in this example is a highly localised oscillon chain, similar to patterns previously found in a model based on the assumption of nearest-pattern interaction [131, 132], which provides some hope that the observed state is not merely an artefact of the present model. We find such localised states, composed of straight or wavy oscillon chains, widely in our simulations in intermediate to large containers with $\phi > 1$. In large containers we also commonly

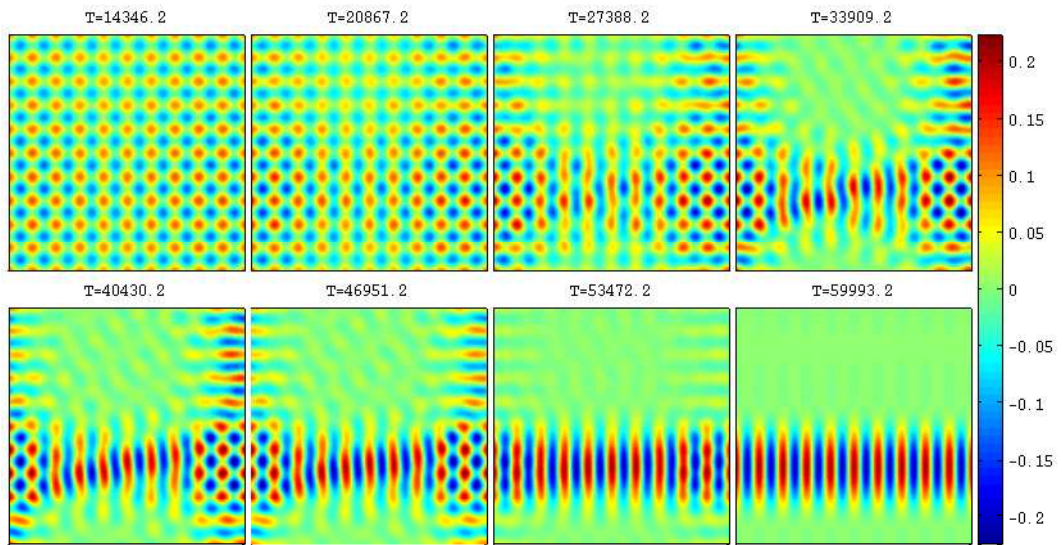


Figure 2.12: Plots of $\text{Re}(\psi)$ depicting snapshots of the long-wavelength instability of square patterns in a container of size $L = 10\Lambda_c$ and $\phi = 1.1$. The initial condition was periodic squares perturbed by small-amplitude noise and γ was set at 0.1% above its critical value.

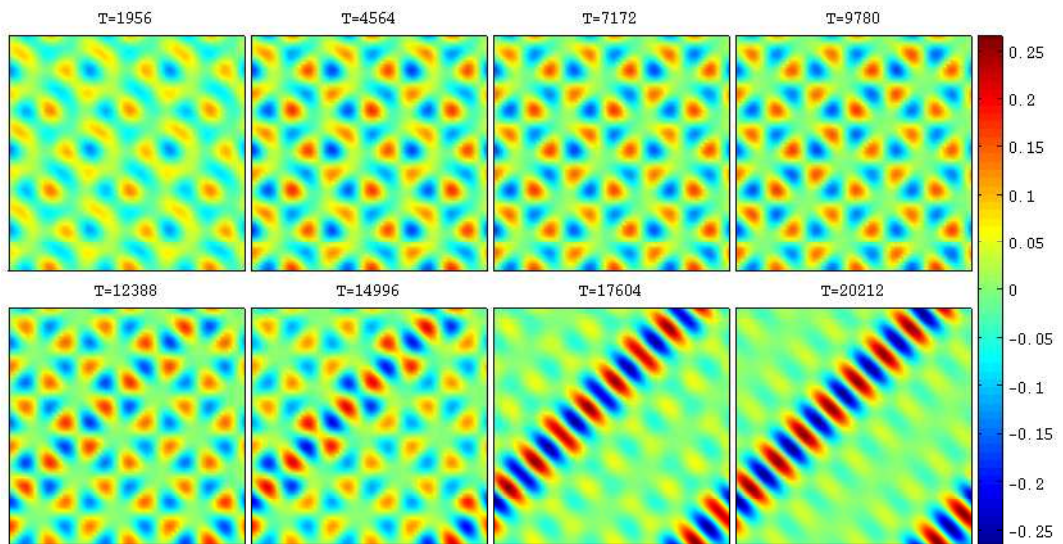


Figure 2.13: Plots of $\text{Re}(\psi)$ depicting snapshots of the long-wavelength instability of antisquare patterns in a container of size $L = 3\sqrt{5}\Lambda_c$ with $\phi = 1.1$. The initial condition was small-amplitude noise and γ was set at 0.1% above its critical value.

observe worm-like patterns [62], several of which can co-exist in any given simulation, in various orientations in different parts of the domain.

Although no corresponding analysis is currently available, an analogous modulational instability for antisquares can be seen in figure 2.13. After an initial condition of small-amplitude noise, the container size $L = 3\sqrt{5}\Lambda_c$ dictates that regular antisquares are selected in the early stages of the nonlinear evolution. However, like squares, these are also unstable to a modulational instability which leads to a one-dimensional superstructure. Subsequently, the system evolves to a single oscillon chain. These patterns are reminiscent of the ‘worm’ patterns that have been observed in electroconvection [144].

In figure 2.14, an array of different configurations are presented that illustrate the characteristic behaviours of the system. Each individual plot corresponds to a particular pair of values (ϕ, γ) and represents the realised pattern in a square container of side length $L = 100$ after 10^5 units of T . Most critically from this figure, we see that the localised patterns induced by the long-wave instability mechanism are only found very close to onset (around 0.1% above threshold); in this regime, the realised patterns are all localised oscillon chains of some sort. Slightly further above onset, the degree of localisation increases with ϕ but giving rise to a different kind of localised pattern to those observed at 0.1% above threshold. As γ increases further, stripes become the preferred pattern for the exhibited ϕ values. This preference for stripes as the distance from threshold increases compares favourably with the phase diagram of Tsimring and Aranson [6] (recalled in figure 2.7).

Further exposition of the general behaviour of the model equations is given by figure 2.15 where the results of ‘morphological’ simulations are presented. These are derived through simulations of the model equations (2.2.1) in large containers where the control parameter ϕ is varied linearly along the x axes. Such a simulation allows the realised pattern to reflect the character of a range of different scenarios and gives an approximate picture of the stability regions of various configurations. The illustrations of figure 2.15 are in qualitative agreement with figure 2.14: when very close to threshold, we see highly localised patterns, while as we move further from onset, the degree of localisation decreases until we only find stripe solutions. One drawback of these figures is the normalisation required to apply the color scheme sometimes causes patterns to disappear, as their amplitude is significantly smaller than the maximum. This is apparent in the plot at $\gamma = 1.001\gamma_c$ where the stripe patterns, which should be visible for $\phi < 1$ can barely be discerned. What this does tell us though, is that, in this regime, the amplitude of the realised pattern increases with ϕ .

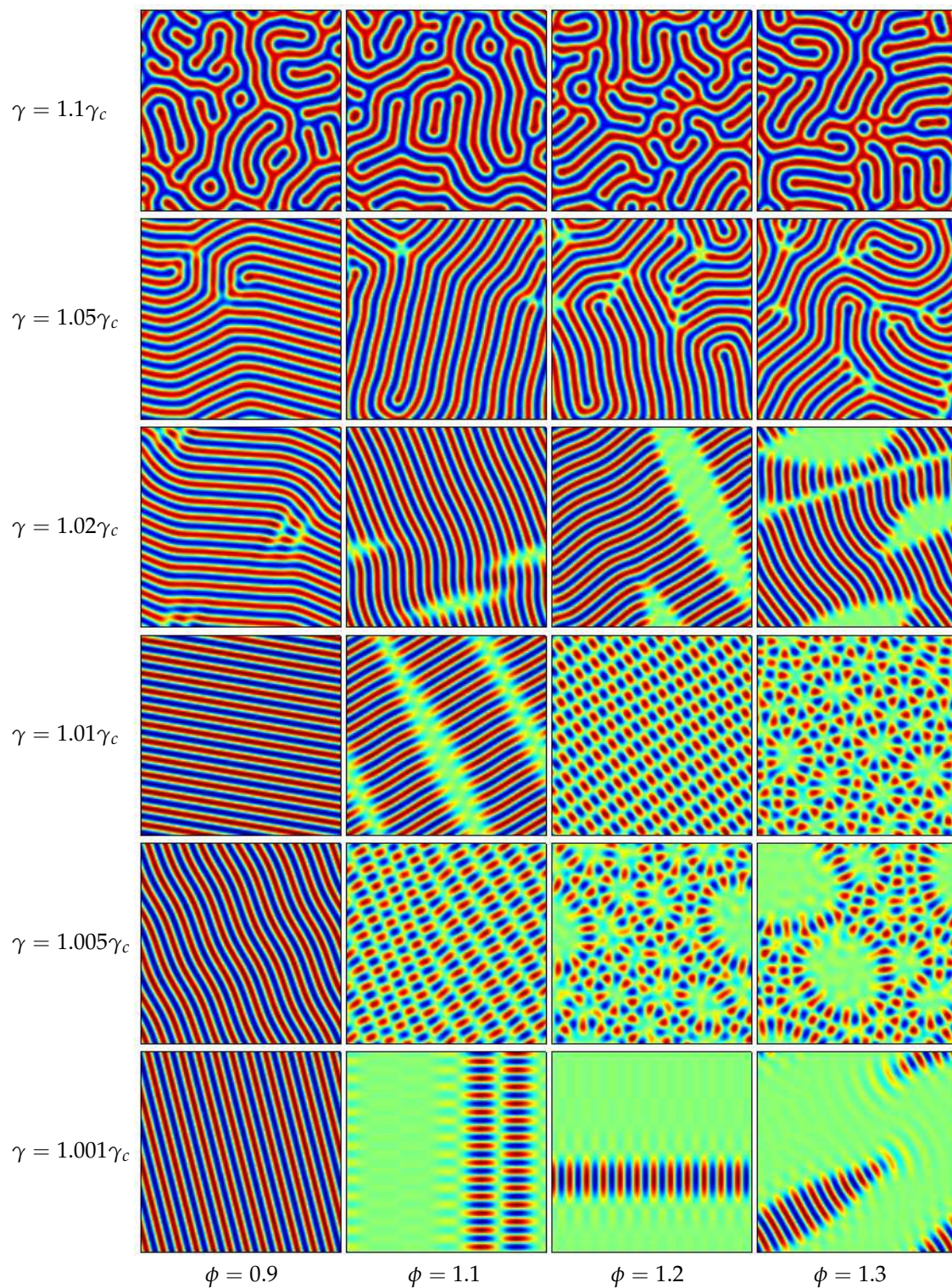


Figure 2.14: The realised states of $\text{Re}(\psi)$ from simulations in a container of size $L = 100$ after 10^6 units of T for various values of ϕ and γ . The behaviours illustrated here are characteristic of much of parameter space.

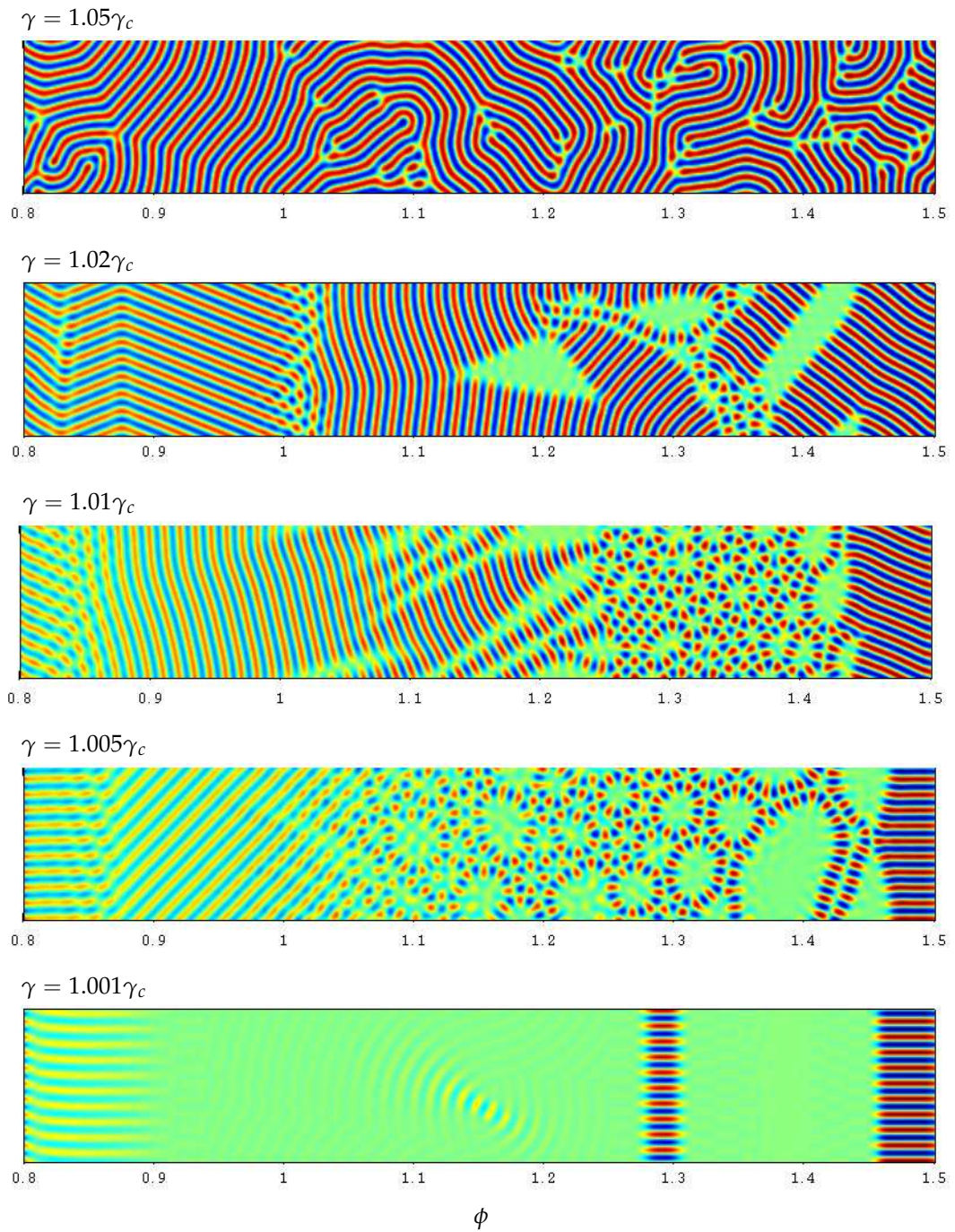


Figure 2.15: ‘Morphological’ plots: simulations of the model equations (2.2.1) in a long rectangular domain of horizontal size 487 and vertical size 81, where the control parameter ϕ varies continuously along the x -axis. Each plot corresponds to a particular near-threshold condition, where γ ranges between 0.1% and 5% above critical; ϕ aside, all other parameter values remain fixed.

2.5 Summary

The analysis presented in this chapter extends that of Tsimring and Aranson [6, 95] by allowing for spatial modulation of stripe and square patterns in their phenomenological model for pattern formation in a vertically vibrated granular layer. We have shown that either pattern may suffer a modulational instability, which is strongly influenced by the constraint of mass conservation. It turns out that stripes are effectively immune to this modulational instability because it arises only where a regular stripe pattern is already unstable to a regular pattern of squares; by contrast, squares are always susceptible.

The fact that squares are always unstable would appear to be in conflict with the experimental results, where stable square patterns are commonly observed [103]; however, this is not necessarily the case. Since the modulational instability leads to long-wavelength perturbations becoming unstable first, the instability can take place only if perturbations on a sufficiently large spatial scale can be accommodated in the container. So for finite containers, squares will generally be stable close to the stripe–square transition, but will lose stability as the driving frequency is decreased (effectively increasing ϕ). A further possible explanation for the absence of observations of the instability of squares is that the long-wavelength nature of the instability corresponds to a very slow temporal growth of the disturbance. Thus, square patterns may be observed for a significant period of time before the long-wavelength modulation manifests itself; this was certainly apparent in the numerical simulations. Extensive numerical experiments on (2.2.1) have supported all the analysis.

Since we have considered only a supercritical bifurcation from the uniform state, the usual bistability arguments [145, 146, 147] are not necessary in explaining the existence of strongly localised solutions. Rather, it is the influence of the conserved quantity that provides the localisation mechanism: particles tend to flee regions in which ψ is large, leading to an increased flux of particles and a reduction in the local density ρ . This, in turn, decreases the damping in the ψ equation (2.2.1a). The feedback loop just described enables localised structures to remain stable. In effect, a large-scale redistribution of the granular medium causes some regions to be locally ‘supercritical’ and others locally ‘subcritical’, while the system as a whole is (on average) supercritical. Many other models of a vertically vibrated granular layer include in them the principle of conservation of mass and one might expect corresponding long-wavelength effects to be applicable in a wide range of models. However, few continuous order-parameter models exist; most are of a semi-continuum or stroboscopic nature and the weakly nonlinear analysis carried out here is not immediately transferable.

Our interest in the system (2.2.1) is not exclusively in the context of vibrated granular layers; such a phenomenological model could also account for a vibrated fluid layer. In this situation, the complex order-parameter ψ corresponds to the velocity potential at the free surface [139] while ρ represents the displacement from the undisturbed fluid height (whose average value is constant). In addition, aside from its application to granular and fluid layers, the phenomenological model (2.2.1) is an interesting and unusual model of pattern formation in its own right. It is unusual in the sense that the coupling to a mean field enables the selection of cellular patterns to be determined by the parameter values rather than being solely dependent on symmetries as in other common models such as the Swift–Hohenberg equation. What makes the model (2.2.1) particularly interesting is how the coupling with a large-scale mode facilitates the near-threshold exhibition of a myriad of cellular, but predominantly localised, patterns.

Oscillatory pattern formation with a conserved quantity

3.1 Introduction

THERE ARE MANY examples of patterns whose evolution is strongly influenced by the presence of a conserved quantity in the underlying physical system; examples include magnetoconvection [84, 148], binary fluid convection [149], vibrated granular layers [6, 103] (and chapter 2), two-layer Couette flow [150] and sandbank formation [83]. As identified by Fauve [151], and later on, Matthews and Cox [74] and Barthelet and Charru [152] (see §1.5), the presence of a conserved quantity leads to the neutral stability of a real, slowly varying large-scale mode, which must be included as an independent variable in the appropriate theoretical description. The interactions between the pattern and a large-scale mode related to the conserved quantity can significantly affect the stability of regular patterns and can lead to amplitude-modulated states and localisation of the pattern, even close to onset. The influence of a conservation law on a stationary bifurcation has recently attracted considerable attention [74, 75, 82, 83, 84, 85] and is now relatively well understood; the case of an oscillatory bifurcation with a conservation law is considerably more complicated and is the subject of the present chapter. The work of this chapter has been published in Winterbottom et al. [81].

3.1.1 Coupled Ginzburg–Landau systems

In the absence of a conservation law, pattern-forming systems undergoing a Hopf (or oscillatory) bifurcation are governed by either the CGL equation (1.4.2), the CCGL equations (1.4.11), or the MFGL equations (1.4.15) depending on the existence of a reflection symmetry or otherwise and on the relative size of the group velocity. Detailed

reviews of these equations have already been presented in §1.4.

Since the conserved quantity affects the evolution of a pattern through coupling to a slowly varying, large-scale, conserved mode, its effects on the pattern share some features with other problems in which such a mode arises. Of particular physical relevance are problems with some slowly diffusing field, such as thermohaline convection at small Lewis number [153] or binary fluid convection with a suitably strong coupling between the thermal and concentration fields [149]. Motivated by these applications, the influence of a slowly evolving real-valued field on a Hopf bifurcation, where a single travelling wave is present, has been examined extensively [62, 145, 147, 154, 155, 156, 157, 158, 159]. The influence of such an additional mode is often profound and can significantly alter the stability behaviour of existing solutions [157] as well as stabilising new solutions [62, 145, 147, 155].

3.1.2 Localisation

A striking feature of many pattern-forming systems is the occurrence of localisation, or the confinement of a pattern to some small region of the container surrounded by the homogeneous state. Localised states have been observed in diverse array of physical settings with perhaps the most celebrated being vibrated granular layers, where localised excitations termed ‘oscillons’ have been observed [106] (see figure 2.3). Elsewhere localised states, either stationary or propagating have been found in binary fluid convection [149, 160, 161, 162], the Faraday experiment using a colloidal suspension [122], reaction-diffusion systems [163] and electroconvection [164, 165, 166] amongst others. Examples of localised patterns seen in binary fluid convection and electroconvection are illustrated in figure 3.1.

Commonly, localisation is attributed to a mechanism associated with bistability [145, 146, 147], whereby a uniform state as well as a patterned state are both stable for some parameter range. Such a scenario can only occur if the patterned state bifurcates subcritically from the uniform solution. The localised state is then composed of regions of both solutions, separated by fronts or interfaces [145, 147]. Localised states arising through supercritical bifurcations have also been noted in electroconvection [164, 165, 166].

It is well known that the CGL equation admits localised pulse solutions of the form [168]:

$$A = a_0 [\operatorname{sech}(kx)]^{1+i\nu_1} e^{-i\nu_2 t}, \quad (3.1.1)$$

where a_0, k, ν_1, ν_2 are all real parameters; however, this solution is always unstable. On

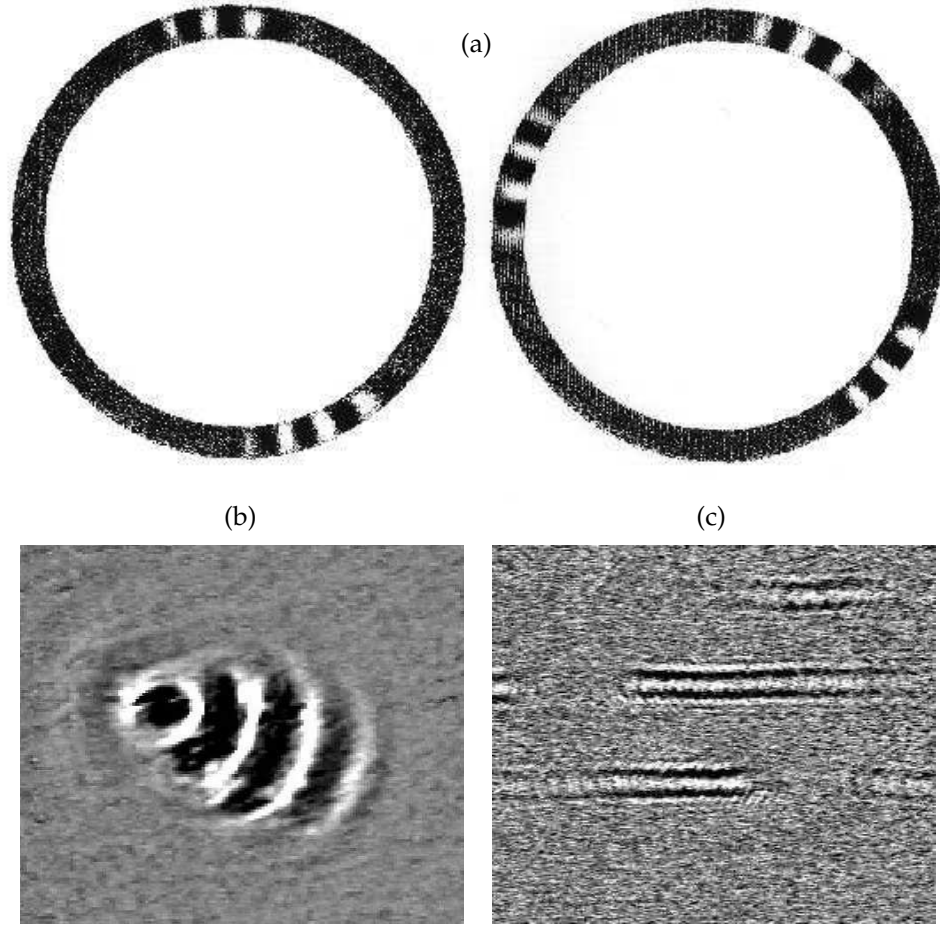


Figure 3.1: Localised patterns: (a) convection pulses in an annulus filled with a mixture of ethanol and water, heated from below [160]; (b) localised pulses (through which roll-like patterns travel) in binary fluid convection [167]; (c) worm patterns observed in electroconvection [164].

the other hand, various studies such as that of Doelman et al. [155] and Riecke [154] have shown that solitary pulse-like solutions can be stabilised by the coupling to a slow diffusive mode (see the review of Riecke [169]). More generally, stable localised solutions have been identified in coupled equations of the form [74, 145, 147, 154, 156, 170, 171]:

$$A_T = \alpha_1 A + \alpha_2 A_{XX} + \alpha_3 |A|^2 A + \alpha_4 AB + \text{h.o.t.}, \quad (3.1.2a)$$

$$B_T = \sigma B_{XX} + G(B, |A|^2; \partial_X), \quad (3.1.2b)$$

where $\alpha_1, \alpha_2, \alpha_3, \alpha_4 \in \mathbb{C}$, $\sigma > 0$ and G is some function of B , $|A|^2$ and their derivatives; ‘h.o.t.’ is the usual shorthand for higher-order terms. Generally, systems are studied where the Ginzburg–Landau equation is subcritical and thus $\text{Re}(\alpha_3) > 0$ (e.g., [155, 156, 170]). Then, for saturation to occur, one requires either $\text{Re}(\alpha_1) < 0$ or for

a term of the form $-\alpha_5|A|^4A$ to be included in the higher-order terms. Some attention has also been paid to supercritical bifurcations in the presence of a slow mode [62, 154, 171], where stable localised solutions have been identified. Systems of the form (3.1.2) with $\text{Re}(\alpha_3) < 0$ give rise to two separate instability mechanisms: the usual long-wave instability of the CGL equation that, in the absence of a diffusive field, leads to the Benjamin–Feir–Eckhaus instability (see §1.4.1), and a new instability mechanism, induced by the diffusive mode. The effect of a slowly varying mode on coupled Ginzburg–Landau equations has also been investigated by Riecke and Granzow [62] and Iima and Nishiura [172].

We show in this chapter that localisation, or at least very strong selective suppression of the pattern amplitude, can take place in supercritical systems undergoing a Hopf bifurcation due to the influence of a conservation law; no bistability is required. Some previous studies have cited a conservation law as the localisation mechanism [67, 173], but in those cases the localised pattern is embedded in a periodic pattern. Also, Charru and Barthelet [150, 152] have derived amplitude equations for a single travelling wave in the presence of a conserved quantity corresponding to interfacial waves in two-layer Couette flow. However, they used moving spatial coordinates and hence the evolution of the mean mode is determined by an advection–diffusion equation. It is also remarkable that the resulting amplitude equations are not asymptotically consistent.

3.1.3 Structure of chapter

In this chapter, we investigate the role of a conservation law on an oscillatory bifurcation. We adopt the same approach as Matthews and Cox [74], using symmetry and asymptotic concerns to derive a set of amplitude equations. Our amplitude equations comprise the CCGL equations coupled to an evolution equation for a large-scale mode, according to which large-scale perturbations to the conserved field relax diffusively, but are forced by spatial gradients in the pattern amplitude. The amplitude equations we investigate may be considered nongeneric, in that an expected leading-order coupling term is absent; however, they seem to be generic for a class of convection problems including magnetoconvection and rotating convection, and may, in principle at least, be derived from the governing equations for those problems. Subsequently, we investigate the long-wave stability of both travelling and standing waves and detail the various forms of stability region that can occur. These results are then verified and extended through numerical examination of the amplitude system.

In §3.2, we outline the construction of our amplitude system, discuss the applicability of our equations to a range of convection problems and address the question of their

nongenericity. Subsequently, in §3.3, the stability properties of travelling waves are examined and a number of modulational stability boundaries are calculated in the limit of long-wave perturbations. In §3.4, an entirely analogous investigation is carried out for standing waves, again concentrating on the appropriate long-wave stability results. In §3.5, a numerical method is employed to extend the long-wave stability regions of §3.3 and §3.4 to include instability to finite-wave perturbations. Next, in §3.6, the results of a careful investigation into the nonlinear development of each new instability of travelling and standing waves are reported. Subsequently, in §3.7, we assess the influence of energy transport in our equations by examining the case of $O(1)$ group velocity. Finally, conclusions and extensions are discussed in §3.8.

3.2 Derivation of the amplitude equations

We consider a partial differential equation (PDE), or a system of PDEs, in one space dimension, with a conserved quantity $w(x, t)$ and a uniform steady-state solution, which we may take to be $w(x, t) \equiv 0$. We suppose that the system possesses translational and reflectional symmetries. The linear stability of the trivial state is determined by considering the evolution of Fourier modes with wavenumber k in the system linearised about $w = 0$. A consequence of the presence of the conserved quantity and of the assumed symmetries is that, generically, the growthrate λ satisfies $\lambda = O(k^2)$ as $k \rightarrow 0$, where we assume that λ is real-valued in this limit. Thus, modes of the largest spatial scales are nearly neutral. Although they are all linearly damped, such modes play a significant role in the dynamics and must be included in the near-threshold amplitude description; they are not ‘slaved’ to the critical growing modes. See §1.5 for a more detailed discussion of this effect.

Let us suppose that the system possesses a control parameter r , and that it undergoes a bifurcation at $r = r_c$, so that for $r > r_c$ the trivial state becomes unstable to modes with nonzero wavenumber $k = k_c$ and nonzero frequency $\omega = \omega_c$. The weakly nonlinear patterns formed near $r = r_c$ comprise two propagating modes together with a large-scale mode:

$$w \sim \tilde{A}_1(X, T) e^{i(\omega_c t + k_c x)} + \tilde{A}_2(X, T) e^{i(\omega_c t - k_c x)} + \text{c.c.} + \tilde{C}(X, T) + \text{h.o.t.}, \quad (3.2.1)$$

where the amplitudes \tilde{A}_1, \tilde{A}_2 are complex, \tilde{C} is real and X and T are scaled, slowly varying scales for space and time, respectively.

Suitable amplitude equations for \tilde{A}_1, \tilde{A}_2 and \tilde{C} may be derived either directly from the original PDE(s), or, as done here, by imposing the relevant symmetries and retaining

only terms of correct asymptotic order. In particular, the amplitude equations inherit the following invariances under translation (in space and time):

$$x \mapsto x + x_0 : \quad \tilde{A}_1 \rightarrow \tilde{A}_1 e^{i\theta}, \quad \tilde{A}_2 \rightarrow \tilde{A}_2 e^{-i\theta}, \quad \tilde{C} \rightarrow \tilde{C}, \quad (3.2.2a)$$

$$t \mapsto t + t_0 : \quad \tilde{A}_1 \rightarrow \tilde{A}_1 e^{i\phi}, \quad \tilde{A}_2 \rightarrow \tilde{A}_2 e^{i\phi}, \quad \tilde{C} \rightarrow \tilde{C}, \quad (3.2.2b)$$

where $\theta = k_c x_0 \in \mathbb{R}$, $\phi = \omega_c t_0 \in \mathbb{R}$, and under reflection:

$$x \mapsto -x : \quad \tilde{A}_1 \rightarrow \tilde{A}_2, \quad \tilde{A}_2 \rightarrow \tilde{A}_1, \quad \tilde{C} \rightarrow \tilde{C}. \quad (3.2.3)$$

As detailed in §1.4.2, in the absence of a conserved quantity and when the group velocity is small, A_1 and A_2 are governed by the CCGL equations (1.4.11) [1, 7]. Taking the conserved quantity into account, the translational symmetry (3.2.2a) dictates that the leading-order coupling, which extends the CCGL equations, must take the form $\tilde{A}_{iT} = \dots + \text{const.} \times \tilde{A}_i \tilde{C}$. Furthermore, with regard to the evolution of \tilde{C} , the conservation law and reflectional symmetry (3.2.3) imply that \tilde{C} obeys a diffusion equation with nonlinear forcing from the propagating modes. The translation symmetries (3.2.2) force any coupling terms to include equal numbers of \tilde{A}_i and \tilde{A}_i^* (asterisks denote complex conjugation) while the leading-order term consistent with the reflectional symmetry in X is

$$\tilde{C}_T = \dots - \text{const.} \times (|\tilde{A}_1|^2 - |\tilde{A}_2|^2)_X. \quad (3.2.4)$$

This is the generic form of the coupling when \tilde{C} represents a conserved scalar quantity. However, it is not this generic coupling that is investigated in this chapter, since the applications that motivate the present work are magnetoconvection and rotating convection, where the conserved quantity is not a scalar but a *pseudoscalar*, and, furthermore, it is *gradients* of the conserved quantity that drive the pattern. These two features arise quite commonly in convection problems and change the nature of the coupling, as we now describe.

3.2.1 Nongenericity

We illustrate the vanishing of the coefficient of the term (3.2.4) by considering an equation for a conserved scalar or pseudoscalar quantity p in a cellular flow between horizontal boundaries at $z = 0, 1$, of the form

$$\frac{\partial p}{\partial t} + \nabla \cdot (\mathbf{u}p) = \kappa \nabla^2 p. \quad (3.2.5)$$

Here $\mathbf{u} = (u(x, z, t), w(x, z, t))$ is a two-dimensional velocity field satisfying periodic lateral boundary conditions $\mathbf{u}(0, z, t) = \mathbf{u}(L, z, t)$ and Dirichlet conditions on the upper

and lower surfaces: $\mathbf{u}(x, 0, t) = \mathbf{u}(x, 1, t) = 0$. The conserved quantity p satisfies periodic lateral boundary conditions $p(0, z, t) = p(L, z, t)$ and the Neumann conditions $p_z(x, 0, t) = p_z(x, 1, t) = 0$. The expression (3.2.5) is a somewhat simplified version of the corresponding equations found in binary fluid convection [154, 174], magnetoconvection [148] and rotating convection [91], and we expect it to be applicable more widely to other pattern-forming systems with a conserved scalar/pseudoscalar quantity in a cellular flow.

Let us now consider the form of the divergence term in (3.2.5), supposing that slow spatial modulations are taken into account. Using the boundary conditions given above, we see that the spatial integral of this term, which contributes to the evolution of the slowly varying component of the conserved field, is

$$\begin{aligned} \langle \nabla \cdot (\mathbf{u}p) \rangle &\equiv \int_0^L \int_0^1 \nabla \cdot (\mathbf{u}p) \, dz \, dx, \\ &= \int_0^1 [up]_0^L \, dz + \frac{dX}{dx} \int_0^L \int_0^1 \frac{\partial}{\partial X} (up) \, dz \, dx + \int_0^L [wp]_0^1 \, dx, \\ &= \frac{dX}{dx} \int_0^L \int_0^1 \frac{\partial}{\partial X} (up) \, dz \, dx. \end{aligned} \quad (3.2.6)$$

It is remarkable at this stage that the form of any nonlinear contribution depends on the action of the reflection symmetry $x \rightarrow -x$ on p . The horizontal velocity component u is reversed under the action of this symmetry ($u \mapsto -u$) and so we specify

$$u \sim f(z) \left[A_1(X, T)e^{i\omega t + ikx} - A_2(X, T)e^{i\omega t - ikx} \right] + \text{c.c.}, \quad (3.2.7)$$

where f is a complex-valued eigenfunction. In addition, if p is a scalar, it maintains its sign ($p \mapsto p$), while if it is a pseudoscalar then its sign is reversed ($p \mapsto -p$). We thus consider two different leading-order planforms for p :

$$p \sim g(z) \left[A_1(X, T)e^{i\omega t + ikx} \pm A_2(X, T)e^{i\omega t - ikx} \right] + \text{c.c.}, \quad (3.2.8)$$

where g is a complex-valued eigenfunction and $f(0) = f(1) = g'(0) = g'(1) = 0$. Here the plus and minus signs in the expression for p refer, respectively, to the scalar and pseudoscalar cases. Substituting these expressions into (3.2.6), we find

$$\frac{\omega}{2\pi L} \int_0^{2\pi/\omega} \langle \nabla \cdot (\mathbf{u}p) \rangle \, dt = \frac{dX}{dx} \int_0^1 (fg^* + f^*g) \, dz (|A_1|^2 \mp |A_2|^2)_X. \quad (3.2.9)$$

Generically, this is the term that drives the large-scale conserved mode. However, the coefficient of this coupling term vanishes if

$$\int_0^1 (fg^* + f^*g) \, dz = 0, \quad (3.2.10)$$

such as will occur quite generally when f and g have opposite parities about $z = 1/2$.

For incompressible flow, we may write u in stream-function form as $u = -\psi_z$, where ψ is determined by an expression of the form (3.2.7), but with $f(z)$ replaced by $h(z)$, where $f = -h'$. In this situation, the condition (3.2.10) becomes

$$\int_0^1 (h_z g^* + h_z^* g) dz = 0, \quad (3.2.11)$$

which is clearly the case when g and h have the *same* parity about $z = 1/2$. For magnetoconvection and rotating convection, however, the eigenfunctions for ψ and the relevant conserved quantity (here called p) have *opposite* parities about $z = 1/2$ [91, 148], and so, generically, (3.2.9) is indeed the leading-order nonlinear forcing term in the conserved-mode amplitude equation. In both these applications, the conserved quantity is a pseudoscalar, and so the coupling term is of the form

$$P_T = \cdots - \text{const.} \times (|A_1|^2 + |A_2|^2)_X, \quad (3.2.12)$$

where $P(X, T)$ is the average of p over the $O(1)$ scales x and t . In addition, in each case it is *gradients* of P that drive or suppress the pattern and hence the discussion above applies to $\tilde{C} = P_X$ (see [74, 91]). Thus the amplitude equation for \tilde{C} is of the form

$$\tilde{C}_T = \cdots - \text{const.} \times (|A_1|^2 + |A_2|^2)_{XX}. \quad (3.2.13)$$

Hence, two of the applications that motivated the present work fail to exhibit the ‘generic’ nonlinear forcing term (3.2.4); both magnetoconvection and rotating convection have instead the leading-order forcing term in (3.2.13). In this present work, we examine only this nonlinear term as the forcing term in the evolution equation for the mean-mode. The effects of ‘generic’ leading-order forcing of the form (3.2.4) remain to be examined.

A significant feature of these two convection examples is that it is possible to formulate an asymptotically consistent system of amplitude equations. By contrast, we have been unable to do so for generic coupling of the form $\tilde{A}_{1T} = \cdots - \tilde{C}\tilde{A}_1$, $\tilde{A}_{2T} = \cdots - \tilde{C}\tilde{A}_2$, $\tilde{C}_T = \cdots - \text{const.} \times (|\tilde{A}_1|^2 - |\tilde{A}_2|^2)_X$.

3.2.2 Amplitude equations

We now derive asymptotically consistent amplitude equations for \tilde{A}_1 , \tilde{A}_2 and \tilde{C} by introducing a supercriticality parameter $\epsilon \ll 1$ such that $r = r_c + \epsilon^2 r_2$ and choosing

$$\tilde{A}_1 = \epsilon A_1, \quad \tilde{A}_2 = \epsilon A_2, \quad \tilde{C} = \epsilon^2 C, \quad X = \epsilon x, \quad T = \epsilon^2 t.$$

We also set $c_g = \epsilon s$, where c_g is the physical group velocity. With these scalings, the amplitude equations (after a rescaling, if necessary, to set many coefficients to unity)

take the form

$$\begin{aligned}
 A_{1T} + sA_{1X} &= r_2 A_1 + (1 + ic_1)A_{1XX} - A_1 [(1 - ic_2)|A_1|^2 + (b_3 - ic_3)|A_2|^2] \\
 &\quad - (1 - ic_4)A_1 C,
 \end{aligned} \tag{3.2.14a}$$

$$\begin{aligned}
 A_{2T} - sA_{2X} &= r_2 A_2 + (1 + ic_1)A_{2XX} - A_2 [(1 - ic_2)|A_2|^2 + (b_3 - ic_3)|A_1|^2] \\
 &\quad - (1 - ic_4)A_2 C,
 \end{aligned} \tag{3.2.14b}$$

$$C_T = \sigma C_{XX} + \mu(|A_1|^2 + |A_2|^2)_{XX}, \tag{3.2.14c}$$

where we have assumed that, in the absence of C , the bifurcation of travelling waves is supercritical. All parameters are real and we set $\sigma > 0$ so that, in the absence of the propagating modes, long-wave modes are linearly damped. For simplicity, we shall subsequently omit the subscript on the supercriticality measure r_2 , henceforth denoting it by r , with no risk of confusion.

3.2.3 Binary fluid convection

Convection in a binary mixture provides a more subtle exhibition of large-scale modes. If zero-flux boundary conditions are applied to the concentration field at $z = 0, 1$ then this field is a conserved scalar. Furthermore, the coefficient of the generic coupling term in (3.2.4) vanishes, since the relevant eigenfunctions (g and h in (3.2.11)) do indeed have the same parity about $z = 1/2$ (see appendix C for details). Thus binary fluid convection provides a third nongeneric example of the influence of a conserved quantity.

However, a different type of large-scale mode arises when the diffusion coefficient is small. In this case, the reason for the existence of a large-scale mode is not that the mode is conserved [175]; indeed it need not be conserved for the coupling to occur. Instead the mode arises because of the correspondingly slow evolution of large-scale disturbances to the concentration field. In this case, the dominant large-scale concentration mode is that forced by the nonlinear advection term, whose parity generates the generic form of coupling, as shown in [154]. These modes have a vertical dependence $\sin 2\pi z$ and so are not of the type considered here.

3.2.4 Validity of amplitude equations

Analogous to the CCGL equations (1.4.11), the physical group velocity is assumed to be small ($c_g = \epsilon s$) to allow the advection terms (e.g., $\propto A_{1X}$) to appear at the correct asymptotic order. This assumption brings the validity of the CCGL equations into

question and has been the subject of much discussion [54, 55, 69, 71, 176, 177]. Both Knobloch and De Luca [69, 71] and Martel and Vega [176, 177] find that for finite group velocity, the appropriate equations are the MFGL equations where the interaction between the counter-propagating waves is through an averaged term. Intuitively, the averaged term is found since the group velocity is effectively infinite once the advection terms are scaled out. In other words, if we follow one mode moving with the group velocity then the other propagating mode moves by so quickly that only its average influences the slow dynamics.

For the case of $O(1)$ group velocity when a conserved quantity is present, the appropriate amplitude description is not currently known. While we remain focussed on the amplitude system (3.2.14), we address the role of finite group velocity in §3.7 by considering the limit $s \rightarrow \infty$ in the appropriate analytic results.

3.3 Travelling waves

In this section, the stability properties of travelling wave (TW) solutions to (3.2.14) are investigated. A traditional perturbation expansion is pursued with the majority of work concentrated on the long-wavelength limit, where the analysis remains tractable. The full stability problem, including disturbances of finite wavelength, is addressed in §3.5 and supports the use of the long-wave limit investigated here since many of the stability boundaries do in fact correspond to that limit.

TW solutions to (3.2.14) of wavenumber $k_c + \varepsilon q$, can take two equivalent forms:

$$A_1 = Qe^{i(vT+qX)}, \quad A_2 = C = 0; \quad (3.3.1a)$$

$$A_2 = Qe^{i(vT+qX)}, \quad A_1 = C = 0, \quad (3.3.1b)$$

where $Q^2 = r - q^2 > 0$, and

$$v = \begin{cases} rc_2 - sq - (c_1 + c_2)q^2, & \text{solution (3.3.1a);} \\ rc_2 + sq - (c_1 + c_2)q^2, & \text{solution (3.3.1b).} \end{cases}$$

Without loss of generality, we restrict attention to the TW solution (3.3.1a); analogous results for (3.3.1b) can be recovered through the transformation $s \rightarrow -s$. To analyse stability, we set

$$A_1 = [1 + a_1(X, T)] Qe^{i(vT+qX)}, \quad (3.3.2a)$$

$$A_2 = a_2(X, T), \quad (3.3.2b)$$

$$C = c(X, T), \quad (3.3.2c)$$

substitute these expressions into (3.2.14), and linearise with respect to the small perturbation terms a_1, a_2 and c . It is convenient to consider sideband instability by setting

$$a_1(X, T) = R(T)e^{ilX} + S^*(T)e^{-ilX}, \quad (3.3.3a)$$

$$a_2(X, T) = U(T)e^{ilX} + V^*(T)e^{-ilX}, \quad (3.3.3b)$$

$$c(X, T) = W(T)e^{ilX} + W^*(T)e^{-ilX}, \quad (3.3.3c)$$

where R, S, U, V, W are complex amplitudes; then we find

$$\dot{R} = (\alpha_1 + \alpha_2)R - \alpha_3 Q^2 S - \alpha_4 W, \quad (3.3.4a)$$

$$\dot{S} = (\alpha_1^* - \alpha_2^*)S - \alpha_3^* Q^2 R - \alpha_4^* W, \quad (3.3.4b)$$

$$\dot{U} = (\alpha_5 + ils)U, \quad (3.3.4c)$$

$$\dot{V} = (\alpha_5^* + ils)V, \quad (3.3.4d)$$

$$\dot{W} = -\mu Q^2 l^2 (R + S) - \sigma l^2 W, \quad (3.3.4e)$$

where

$$\alpha_1 = r - q^2 - Q^2(2 - ic_2) - l^2(1 + ic_1),$$

$$\alpha_2 = -l[2q + i(s + 2qc_1)],$$

$$\alpha_3 = 1 - ic_2,$$

$$\alpha_4 = 1 - ic_4,$$

$$\alpha_5 = r - Q^2(b_3 - ic_3) - l^2(1 + ic_1).$$

We seek solutions to the system (3.3.4) proportional to $\exp(\lambda T)$, which gives rise to five stability eigenvalues, which we consider in turn. From the decoupled (3.3.4c) and (3.3.4d), we find the eigenvalues

$$\lambda^{(1,2)} = r - Q^2(b_3 \pm ic_3) + isl - l^2(1 \pm ic_1), \quad (3.3.5)$$

which indicate that TWs are stable to these eigenvalues provided

$$r - l^2 - b_3 Q^2 < 0. \quad (3.3.6)$$

It can be seen that the most dangerous disturbances arise in the limit $l \rightarrow 0$ (i.e., perturbations with large wavelength), yielding the stability condition

$$b_3 > \frac{r}{Q^2} = \frac{r}{r - q^2} \geq 1 \quad (3.3.7)$$

and the parabolic stability boundary

$$r = \left(\frac{b_3}{b_3 - 1} \right) q^2. \quad (3.3.8)$$

Thus, as we approach the transition to standing waves (given by $b_3 = 1$), the band of stable wavevectors decreases to zero, with the band-centre solutions ($q = 0$) being the last to lose stability. It can also be seen from (3.3.3b) that the evolution of this instability leads to growth of the counter-propagating mode A_2 . One might expect this to lead in turn to the stabilisation of standing waves, but while $b_3 > 1$ standing waves cannot be stable. Numerical simulations of TW slightly outside this stability region show that, ultimately, a new TW solution develops, this time with wavenumber lying inside the stable region. This instability has also been investigated elsewhere [54, 55], where simulations have revealed chaotically evolving patches of waves. We do not examine this particular instability further, but note that it is also present in the CCGL equations [43], and does not require the presence of a conserved quantity.

Returning to the remaining modes, R , S and W , we find that (3.3.4a), (3.3.4b) and (3.3.4e) give rise to growth rates governed by a *cubic* dispersion relation of the form

$$F_{\text{TW}}(\lambda, q, r, l) \equiv \sum_{j=0}^3 \kappa_j \lambda^j = 0, \quad (3.3.9)$$

with coefficients

$$\begin{aligned} \kappa_3 &= 1, \\ \kappa_2 &= 2Q^2 + 2il(s + 2c_1q) + l^2(2 + \sigma), \\ \kappa_1 &= 2ilQ^2[2q(c_1 + c_2) + s] + l^2[2Q^2(1 - c_1c_2 + \sigma - \mu) - 4q^2(1 + c_1^2) - 4c_1qs - s^2], \\ \kappa_0 &= 2iQ^2l^3[\sigma(s + il(c_1c_2 - 1) + 2q(c_1 + c_2)) - \mu(s + il(c_1c_4 - 1) + 2q(c_1 + c_4))] \\ &\quad - \sigma l^4[s + (c_1 - i)(2q + l)][s + (c_1 + i)(2q - l)]. \end{aligned}$$

The cubic nature of (3.3.9) and its algebraically cumbersome (and complex) coefficients make the stability of TWs difficult to assess comprehensively. Thus, as is often done in the literature (e.g., [54, 74]), we turn to the long-wave limit, $l \rightarrow 0$, to afford analytical progress. Of course, by restricting our analysis to this limit, we neglect any finite-wavelength instabilities, and our conclusions are necessarily incomplete. We return to this point in §3.5, where the validity and relevance of the long-wave limit are assessed by comparison with direct numerical solutions of the full dispersion relation (3.3.9).

3.3.1 Long-wave analysis

By considering spatially homogeneous perturbations ($l = 0$), we find two degenerate zero eigenvalues ('phase modes') together with a single 'amplitude mode', corresponding to $\lambda^{(3)} = -2Q^2$. Since the last of these can never give rise to an instability, we now

investigate the phase modes, through long-wave expansions; here the leading-order terms are dictated by the long-wave balance in (3.3.9), from which we find

$$\lambda^{(4)} = l\lambda_1^{(4)} + l^2\lambda_2^{(4)} + \dots, \quad (3.3.11a)$$

$$\lambda^{(5)} = l^2\lambda_2^{(4)} + l^3\lambda_3^{(5)} + \dots. \quad (3.3.11b)$$

Substituting (3.3.11a) into (3.3.9) and collecting terms at $O(l)$, we find a purely imaginary component:

$$\lambda_1^{(4)} = -i[2q(c_1 + c_2) + s], \quad (3.3.12)$$

and so any instability from this growthrate will be convective in nature. Little else can be concluded from this term and so we must consider the higher orders in the expansion of $\lambda^{(4)}$ to obtain a stability criterion. The $O(l^2)$ component of $\lambda^{(4)}$ is

$$\lambda_2^{(4)} = c_1c_2 - 1 + \frac{2q^2(1 + c_2^2)}{r - q^2} + \frac{2q\mu(c_2 - c_4)}{2q(c_1 + c_2) + s}, \quad (3.3.13)$$

which gives rise to a generalisation of the Benjamin–Feir–Eckhaus (BFE) instability discussed in §1.4; we recover the parabolic boundary (1.4.6) when we set $\mu = 0$ in $\lambda_2^{(4)} < 0$. Also, with $\mu \neq 0$, we find the Benjamin–Feir–Newell condition $c_1c_2 < 1$ at band-centre, $q = 0$. Hence this growthrate is influenced by the conserved quantity only away from band-centre, where (3.3.13) leads to the generalised Eckhaus stability boundary

$$r = q^2 \left[\frac{2(1 + c_2^2)[2q(c_1 + c_2) + s]}{(1 - c_1c_2)[2q(c_1 + c_2) + s] - 2\mu q(c_2 - c_4)} + 1 \right]. \quad (3.3.14)$$

In contrast to the BFE instability, which is bounded by the parabola (1.4.6), the behaviour here is more subtle and has several notable properties:

- The denominator of (3.3.14) is q -dependent which leads to apparently divergent behaviour where

$$2q = \frac{s(1 - c_1c_2)}{(c_1 + c_2)(c_1c_2 - 1) + \mu(c_2 - c_4)}. \quad (3.3.15)$$

- Away from values of q satisfying (3.3.15), and generally for sufficiently large $|q|$, the stability boundary in (3.3.14) is approximately a parabola, which can be convex from either above or below, depending on the parameters of the problem. This unusual property is not found in the BFE instability but is shared with the Eckhaus instability for standing waves in the CCGL equations [54].
- The expression (3.3.13) for the growthrate itself also appears to exhibit singular behaviour, along the line

$$q = q_\infty \equiv -\frac{1}{2} \left(\frac{s}{c_1 + c_2} \right), \quad (3.3.16)$$

and along the neutral curve $r = q^2$. Such behaviour indicates that the assumed long-wave balance becomes inappropriate in these two cases, in the former because the leading-order term (3.3.12) of the expansion (3.3.11a) vanishes, and in the latter because the amplitude of the TW becomes vanishingly small ($Q = 0$). However, we can obtain useful information about the stability of TWs by observing that on either side of the line $q = q_\infty$, (3.3.13) has different signs and so, by continuity, one expects the real part of the eigenvalue to pass through zero somewhere near $q = q_\infty$ (this expectation is confirmed by numerical calculations). Henceforth, we assume that the line $q = q_\infty$ is a long-wave stability boundary although it is only an *approximation* to the exact stability threshold. A discussion of this phenomenon, which arises repeatedly in the calculations below, and an examination of the correct behaviour for small-amplitude TWs is reserved for §3.3.2.

We note that the growthrate (3.3.13) has two stability boundaries: the curve (3.3.14) where the long-wave theory predicts the real part of the eigenvalue to be zero, and (approximately) the line $q = q_\infty$, where the long-wave balance breaks down, but continuity implies that the real part passes through zero.

For the final growthrate, we substitute (3.3.11b) into (3.3.9) to find at $O(l^2)$ that

$$\lambda_2^{(5)} = \mu \left(\frac{2q(c_1 + c_4) + s}{2q(c_1 + c_2) + s} \right) - \sigma, \quad (3.3.17)$$

which gives rise to the stability boundary

$$q = q_0 \equiv -\frac{1}{2} \frac{s(\mu - \sigma)}{\mu(c_1 + c_4) - \sigma(c_1 + c_2)}. \quad (3.3.18)$$

We thus find a new instability, which necessarily requires the presence of a conserved quantity: with no coupling to a conserved mode, (3.3.17) reduces to $\lambda_2^{(5)} = -\sigma$ which cannot drive an instability. At band-centre, the stability condition $\lambda_2^{(5)} < 0$ reduces to $\mu < \sigma$ (note that this is precisely the band-centre condition for the instability of stationary roll-type solutions [74]).

Again, from (3.3.17), we find apparently singular behaviour at $q = q_\infty$. As above, the corresponding singularity in $\lambda^{(5)}$ is spurious and could be removed by a more detailed analysis of the limit $q \rightarrow q_\infty$; however, such an analysis does not seem justified here, and we content ourselves with interpreting the singularity as indicating a change in the sign of the real part of $\lambda^{(5)}$ at some point $q \approx q_\infty$. Thus we infer an (approximate) stability region in the form of a strip

$$(\min\{q_0, q_\infty\}, \max\{q_0, q_\infty\}), \quad (3.3.19)$$

with TWs stable inside or outside this strip according to the large- $|q|$ limit of (3.3.17):

$$\lim_{q \rightarrow \pm\infty} \lambda_2^{(5)} = \mu \left(\frac{c_1 + c_4}{c_1 + c_2} \right) - \sigma. \quad (3.3.20)$$

TWs are stable inside the band (3.3.19) when the expression on the right-hand side of (3.3.20) is positive, and vice versa.

Long-wave stability regions

In the absence of a conserved quantity, the stability of TWs is determined by the CCGL equations, which can only give rise to two possible long-wave stability regions, delimited by three parabolas: the neutral curve $r = q^2$, the parabola

$$r = \left[\frac{2(1 + c_2^2)}{1 - c_1 c_2} + 1 \right] q^2$$

(recalled from (3.3.14)) and (3.3.8). For $b_3 > 1$, this can lead to only two qualitatively different stability regions, depending on the relative sizes of

$$\frac{b_3}{1 - b_3} \quad \text{and} \quad \frac{2(1 + c_2)^2}{1 - c_1 c_2} + 1.$$

If the latter of these expressions is greatest (figure 3.2a) then the boundary (3.3.8) lies outside (3.3.14) and TWs are stable only within (3.3.14). Alternatively, if the former expression is greater (figure 3.2b) then TWs are stable only within (3.3.8).

In contrast, the presence of a conserved quantity introduces a wide variety of qualitatively different stability regions, due largely to the complicated behaviour of the boundary (3.3.14), which can be convex from above or below, and the fact that stable TWs can exist either inside or outside the band (3.3.19). We choose not to catalogue all possible forms of stability region, but instead illustrate four qualitatively different long-wave stability regions in figure 3.3. It can be seen from this figure that these regions are generally asymmetric about $q = 0$ and may split into two noncontiguous parts. In particular, unlike the BFE instability of TWs in the CGL equation (with no conserved quantity), the stability of TWs here is *not* determined at band-centre. We note also that, for a variety of parameter values, it is possible for all TW solutions to be unstable.

3.3.2 Eigenvalue behaviour for small-amplitude travelling waves

In this section, we explore in more detail the stability of TWs near the neutral curve $r = q^2$, where the amplitude of the TW is small. We begin by noting that, in order for the long-wave balance of the previous section to be valid, the series expansion for

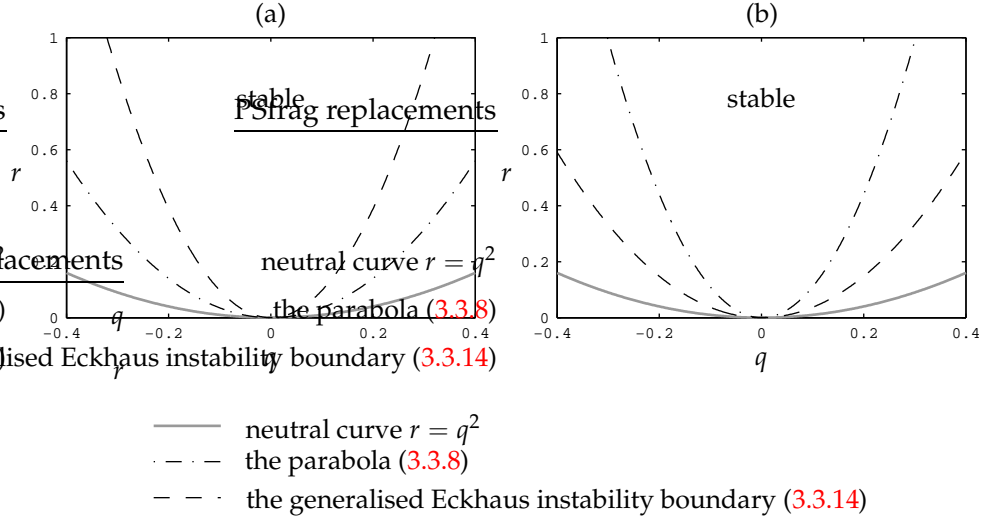


Figure 3.2: The two qualitatively different stability regions for TWs in the CCGL equations (where there is no conserved quantity); TWs are stable up to the nearest long-wave boundary. Both regions are plotted by setting $\mu = 0$ in the expressions (3.3.8) and (3.3.14) with the parameter values (a) $c_1 = 2.5, c_2 = 0.3, b_3 = 1.4$, and (b) $c_1 = 2.5, c_2 = 0.1, b_3 = 1.1$ (the values of the remaining parameter values are irrelevant). As indicated in the legend, the neutral curve $r = q^2$ is the thick grey solid line while the dashed and dot-dashed lines indicate the boundaries (3.3.14) and (3.3.8) respectively. These plotting conventions are adopted throughout the rest of this section.

each growthrate $\lambda^{(j)}$ should remain asymptotic, so that $\lambda_{n+1}^{(j)} l / \lambda_n^{(j)} \ll 1$ as $l \rightarrow 0$. While this asymptotic ordering certainly holds almost everywhere in (q, r) -space, it fails in the neighbourhood of the curves $q = q_\infty$ and $r = q^2$. As we have discussed above, the former case can be recognised as signalling a change in sign of the corresponding real part of the growthrate; the exact details of the transition are not of particular interest.

Of rather more interest is the stability of TWs in the vicinity of the neutral curve $r = q^2$. The particular significance of the neutral curve is apparent by observing, from (3.3.10), that at leading-order in l , the coefficients κ_0, κ_1 and κ_2 each carry a factor of Q^2 . Hence, for small-amplitude TWs ($0 < Q \ll 1$), one would expect a dominant balance different from that leading to (3.3.13), as indicated by the fact that this expression blows up along the neutral curve. The corresponding stability behaviour may be obtained by temporarily dispensing with the long-wave limit and setting $r = q^2 + \delta p$, where δ is a small parameter. Making the appropriate substitution in (3.3.9) and expanding λ as a

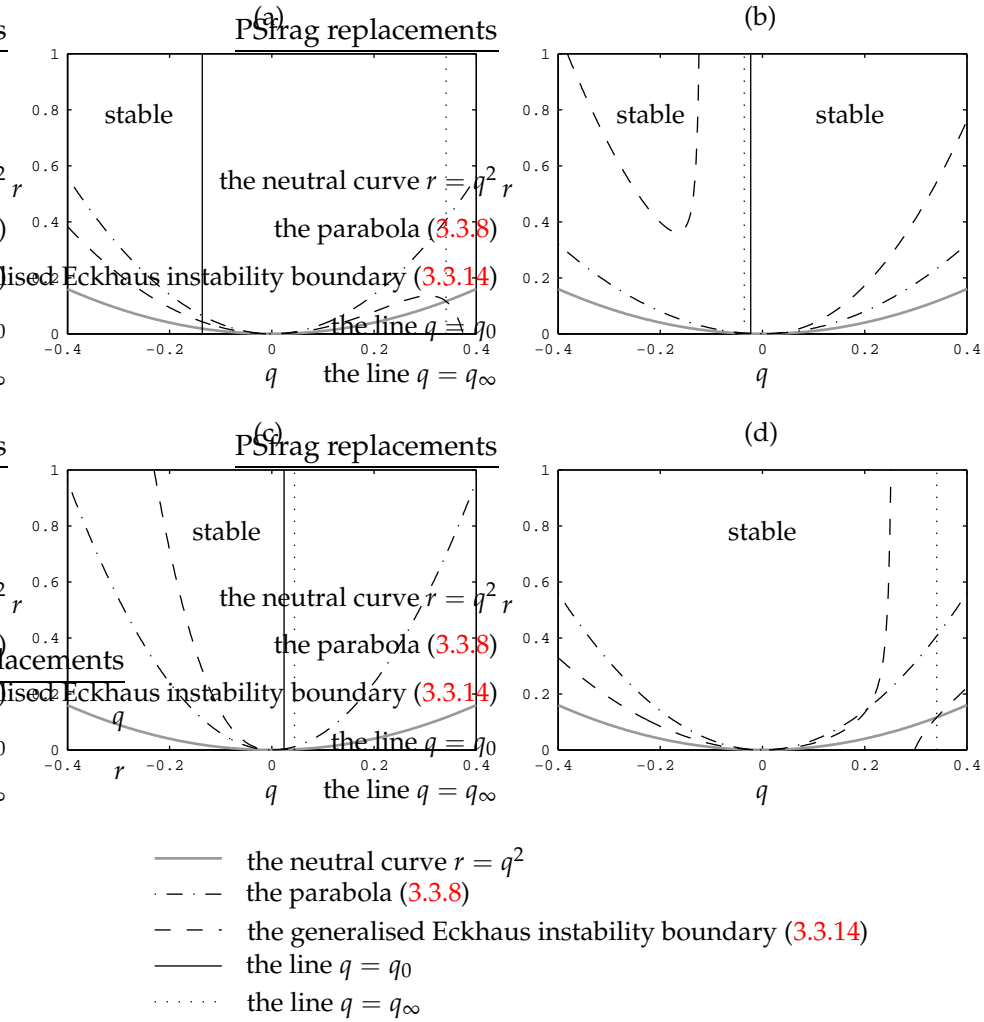


Figure 3.3: Long-wave stability regions for TWs under the parameter sets: (a) $s = 1.5, c_1 = -2.5, c_2 = 0.3, b_3 = 1.4, c_3 = 1.0, c_4 = 1.0, \sigma = 1.0, \mu = 1.1$; (b) $s = 0.1, c_1 = 1.8, c_2 = -0.4, b_3 = 2.0, c_3 = 1.0, c_4 = 1.0, \sigma = 1.0, \mu = -1.2$; (c) $s = 0.2, c_1 = -1.96, c_2 = -0.3, b_3 = 1.2, c_3 = 1.0, c_4 = 1.0, \sigma = 1.0, \mu = 0.6$; (d) $s = 1.5, c_1 = -2.5, c_2 = 0.3, b_3 = 1.4, c_3 = 1.0, c_4 = 1.0, \sigma = 1.0, \mu = -1.8$. Where indicated, TWs are stable to long-wave perturbations up to the nearest boundary.

series in δ , we find the three eigenvalues

$$\lambda^{(a)} = 2lp - l^2(1 + ic_1) - il(s + 2c_1p) + O(\delta), \quad (3.3.21a)$$

$$\lambda^{(b)} = -2lp - l^2(1 - ic_1) - il(s + 2c_1p) + O(\delta), \quad (3.3.21b)$$

$$\lambda^{(c)} = -\sigma l^2 + O(\delta), \quad (3.3.21c)$$

which have real parts $\text{Re}(\lambda^{(a,b)}) = \pm 2lp - l^2$ and $\text{Re}(\lambda^{(c)}) = -\sigma l^2$. Thus, in the vicinity of the neutral curve, TWs are unstable to finite-wavelength perturbations with wavenumber $|l| < |2p|$; the most dangerous perturbations are those with wavenumber $l = \pm p$. This can also be seen from the fact that near the neutral curve TWs have small amplitude, so the stability problem reduces to that of the original basic state, which has fastest-growing modes with zero wavenumber (i.e., spatially homogeneous modes). Thus, by considering (3.3.2a) and (3.3.3a), we see that the most unstable perturbations will have wavenumber l satisfying either $p + l = 0$ or $p - l = 0$. It is noteworthy that this finite-wavelength instability will always occur in the vicinity of the neutral curve and is independent of the presence of a conserved quantity.

3.4 Standing waves

The amplitude equations (3.2.14) admit quasi-standing wave (QSW) solutions of the form

$$A_1 = Q_1 e^{i(\nu_1 T + q_1 X)}, \quad A_2 = Q_2 e^{i(\nu_2 T - iq_2 X)}, \quad C = 0, \quad (3.4.1)$$

where

$$Q_1^2 = \frac{r(1 - b_3) - q_2^2 + b_3 q_1^2}{1 - b_3^2}, \quad Q_2^2 = \frac{r(1 - b_3) - q_1^2 + b_3 q_2^2}{1 - b_3^2},$$

$$\nu_1 = -c_1 q_1^2 - s q_1 + Q_1^2 c_2 + Q_2^2 c_3, \quad \nu_2 = -c_1 q_2^2 - s q_2 + Q_2^2 c_2 + Q_1^2 c_3.$$

Recall that the amplitudes A_1 and A_2 correspond to a leading-order planform

$$\text{physical fields} \sim A_1 e^{i(\omega_c t + ik_c x)} + A_2 e^{i(\omega_c t - ik_c x)} + \text{c.c.}, \quad (3.4.2)$$

which allow QSWs to be visualised; figure 3.4(a) illustrates an example of a QSW solution where $q_1 \neq q_2$ (arbitrary values of ω_c and k_c have been chosen for the figure). These solutions take a similar form to pure standing waves (which have $q_1 = q_2$ and are illustrated in figure 3.4b), but with a slight drift.

In this section, we concentrate on pure standing wave (SW) solutions, which take the form

$$A_1 = Q e^{i(\nu T + q X)}, \quad A_2 = Q e^{i(\nu T - q X)}, \quad C = 0, \quad (3.4.3)$$

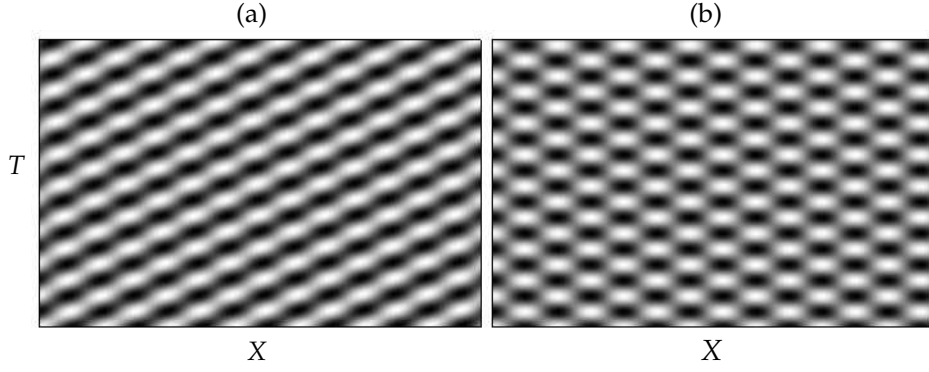


Figure 3.4: (a) Quasi-standing waves ($q_1 \neq q_2$) and (b) standing waves ($q_1 = q_2$). Both patterns are constructed from the formula (3.4.2) by choosing appropriate values of ω_c and k_c .

where

$$Q^2 = \frac{r - q^2}{1 + b_3} > 0, \quad \nu = -c_1 q^2 - sq + Q^2(c_2 + c_3). \quad (3.4.4)$$

Physically, these correspond to patterns of the form $Q \cos(\omega_m t) \cos(k_m x)$ where ω_m and k_m are slightly modified values of the critical values ω_c and k_c .

The stability analysis below is based on the following linearisation about the SW state:

$$A_1(X, T) = [1 + a_1(X, T)] Q e^{i(\nu T + qX)}, \quad (3.4.5a)$$

$$A_2(X, T) = [1 + a_2(X, T)] Q e^{i(\nu T - qX)}, \quad (3.4.5b)$$

$$C(X, T) = c(X, T), \quad (3.4.5c)$$

together with

$$a_1(X, T) = R(T)e^{ilX} + S^*(T)e^{-ilX},$$

$$a_2(X, T) = U(T)e^{ilX} + V^*(T)e^{-ilX},$$

$$c(X, T) = W(T)e^{ilX} + W^*(T)e^{-ilX},$$

where R, S, U, V, W are complex amplitudes. Making the appropriate substitutions in (3.2.14) and linearising leads us to the evolution equations:

$$\dot{R} = (\beta_1 + \beta_2)R - \beta_3 Q^2 S - \beta_4 Q^2 U - \beta_4 Q^2 V - \beta_5 W, \quad (3.4.6a)$$

$$\dot{S} = (\beta_1^* - \beta_2^*)S - \beta_3^* Q^2 R - \beta_4^* Q^2 U - \beta_4^* Q^2 V - \beta_5^* W, \quad (3.4.6b)$$

$$\dot{U} = (\beta_1 - \beta_2)U - \beta_3 Q^2 V - \beta_4 Q^2 R - \beta_4 Q^2 S - \beta_5 W, \quad (3.4.6c)$$

$$\dot{V} = (\beta_1^* + \beta_2^*)V - \beta_3^* Q^2 U - \beta_4^* Q^2 R - \beta_4^* Q^2 S - \beta_5^* W, \quad (3.4.6d)$$

$$\dot{W} = -\mu Q^2 l^2 (R + S + U + V) - \sigma l^2 W, \quad (3.4.6e)$$

where

$$\begin{aligned}\beta_1 &= r - q^2 - Q^2(2 + b_3 - ic_2) - l^2(1 + ic_1), \\ \beta_2 &= -l(2q + i(s + 2qc_1)), \\ \beta_3 &= 1 - ic_2, \\ \beta_4 &= b_3 - ic_3, \\ \beta_5 &= 1 - ic_4.\end{aligned}$$

Solutions to (3.4.6) proportional to $e^{\lambda T}$ have growthrate λ that satisfies the *quintic* dispersion relation

$$F_{SW}(\lambda, q, r, l) \equiv \sum_{i=0}^5 \kappa_i \lambda^i = 0, \quad (3.4.7)$$

where $\kappa_5 = 1$, but the remaining coefficients $\kappa_0, \dots, \kappa_4$ are complicated functions of the system parameters (not given explicitly here). As in §3.3, the order of the dispersion relation (3.4.7) means that the long-wave limit is appropriate to allow analytical progress. The relevance of this simplification is confirmed in §3.5 where the full stability problem is solved numerically, and we shall see that at least some part of the stability boundary for SWs corresponds to long-wave perturbations.

3.4.1 Long-wave analysis

Momentarily ignoring modulational instability, we set $l = 0$ in (3.4.7) to find three phase modes (with $\lambda = 0$) as well as two amplitude-driven growthrates

$$\lambda^{(1,2)} = -2(1 \pm b_3)Q^2. \quad (3.4.8)$$

Thus, the condition $-1 < b_3 < 1$ is required for amplitude stability; together with (3.3.8), this implies that stable TWs and SWs cannot coexist. After considering the small- l balance in the dispersion relation, we expand the eigenvalues corresponding to the phase modes as

$$\lambda^{(3,4)} = l\lambda_1^{(3,4)} + l^2\lambda_2^{(3,4)} + \dots, \quad (3.4.9a)$$

$$\lambda^{(5)} = l^2\lambda_2^{(5)} + l^3\lambda_3^{(5)} + \dots. \quad (3.4.9b)$$

Substituting (3.4.9a) into (3.4.7) and collecting terms at $O(l)$, we find

$$\left(\lambda_1^{(3,4)}\right)^2 = -\frac{\eta_+ \eta_-}{1 - b_3^2}, \quad (3.4.10)$$

where

$$\eta_{\pm} = s(1 \pm b_3) + 2q[c_1(1 \pm b_3) + (c_2 \pm c_3)].$$

When $\eta_+\eta_- < 0$, SWs are monotonically unstable since $\lambda_1^{(3)}$ and $\lambda_1^{(4)}$ (which then take real values) have opposing signs. In the case $\eta_+\eta_- > 0$, stability is determined at higher order since $\lambda_1^{(3)}$ and $\lambda_1^{(4)}$ are purely imaginary. Note that this is always the case for band-centre ($q = 0$) SWs, where $(\lambda_1^{(3,4)})^2 = -s^2 < 0$. The boundaries for the transition of $\lambda_1^{(3,4)}$ from real to imaginary occur when $\eta_+\eta_- = 0$, that is, along the lines $q = q_+$ and $q = q_-$ where

$$q_{\pm} = -\frac{1}{2} \left(\frac{s(1 \pm b_3)}{c_1(1 \pm b_3) + (c_2 \pm c_3)} \right); \quad (3.4.11)$$

these values of q_{\pm} are unchanged from the equivalent boundaries for the CCGL equations (1.4.13) [53, 54]. SWs are unstable inside the band

$$(\min\{q_-, q_+\}, \max\{q_-, q_+\}) \quad (3.4.12)$$

when q_{\pm} have the same sign, and unstable outside when q_{\pm} have different signs. Riecke and Kramer [54] also note that, as in a conservative system, $\lambda_1^{(3)} + \lambda_1^{(4)} = 0$, meaning that monotonic stability is impossible at this order. The apparent intersection of $q = q_{\pm}$ with the neutral curve is illusory; it is an indication that a new balance of leading-order long-wave terms is required there (such as found earlier for TWs). Following an analogous argument to that for TWs in §3.3.2, SWs cannot be stable near the neutral curve; the correct dynamical description for the regime of small Q is detailed in §3.4.2.

In the case $\eta_+\eta_- > 0$, stability is determined at $O(I^2)$, where we find the unwieldy eigenvalue

$$\lambda_2^{(3,4)} = \frac{\gamma_3 q^3 + \gamma_2 q^2 + \gamma_{1a} q - r(\gamma_{1b} q + \gamma_0)}{(r - q^2)(1 - b_3)^2(1 + b_3) [(2c_1 q + s)(1 + b_3) + 2q(c_2 + c_3)]}, \quad (3.4.13)$$

where

$$\begin{aligned} \gamma_0 &= s(1 - b_3^2)(1 - b_3^2 - c_1 c_2 + c_1 c_3 b_3), \\ \gamma_{1a} &= 2b_3 s^2(1 + b_3)(c_2 b_3 - c_3), \\ \gamma_{1b} &= 2(1 - b_3)(c_1(1 + b_3) + c_2 + c_3)(1 - b_3^2 - c_1 c_2 + c_1 c_3 b_3) \\ &\quad + 2\mu(1 - b_3)^2(c_4(1 + b_3) - c_2 - c_3), \\ \gamma_2 &= s(2c_2^2 + 3 + c_1 c_2 + 2c_3^2 + (2 + 2c_2^2 - 4c_2 c_3 - 7c_1 c_3 - 6c_3^2)b_3 \\ &\quad - (4 + 8c_1 c_3 - 4c_2^2 - 4c_2 c_3 - 9c_1 c_2)b_3^2 - (2 + c_1 c_3 - 8c_1 c_2)b_3^3 + b_3^4), \\ \gamma_3 &= 2(c_1(1 + b_3) + c_2 + c_3)(3 - c_1 c_2 - 2c_3^2 - (1 + 3c_1 c_3 - c_1 c_2)b_3 \\ &\quad - (3 + c_1 c_3 - 4c_1 c_2)b_3^2 + b_3^3). \end{aligned}$$

The influence of the conserved quantity is now apparent through the presence of the coupling parameter μ in γ_{1b} . However, at band-centre the stability condition $\lambda_2^{(3,4)} < 0$

reduces to

$$c_1 c_2 - 1 < c_1 c_3 b_3 (1 - b_3), \quad (3.4.14)$$

which is the same as that for the CCGL equations [54, 56], independent of μ . Thus, as with the growthrate (3.3.13), the influence of the conserved quantity is felt only away from band-centre. As (3.4.13) is real-valued, it determines the boundary of long-wave instability:

$$r = \frac{\gamma_3 q^3 + \gamma_2 q^2 + \gamma_{1a} q}{\gamma_{1b} q + \gamma_0}, \quad (3.4.15)$$

which, when $\mu = 0$, reduces to the generalised Eckhaus parabola for SWs found by Riecke and Kramer [54] (henceforth, the ERK instability of SWs). However, when $\mu \neq 0$ this boundary has complicated behaviour, similar to the analogous boundary (3.3.14) for TWs; in this case, the apparent divergence of (3.4.15) takes place at $q = -\gamma_0/\gamma_{1b}$. Away from this point, (3.4.15) is well approximated by a parabola

$$r \approx \left(\frac{\gamma_3}{\gamma_{1b}} \right) q^2 + \left(\frac{\gamma_2 \gamma_{1b} - \gamma_0 \gamma_3}{\gamma_{1b}^2} \right) q + \left(\frac{\gamma_{1a} \gamma_{1b}^2 - \gamma_{1a} \gamma_2 \gamma_0 + \gamma_3 \gamma_0^2}{\gamma_{1b}^3} \right), \quad (3.4.16)$$

which can be convex from above or below, depending on the sign of α_3/α_{1b} . Once again, we observe apparently singular behaviour of (3.4.13) at the boundary of its validity, $q = q_+$, as well as along the neutral curve, but we do not attempt to resolve these here.

We now consider the remaining growthrate $\lambda^{(5)}$, which has leading-order component

$$\lambda_2^{(5)} = \frac{2\mu(s + 2q(c_1 + c_4))}{(s + 2c_1 q)(1 + b_3) + 2q(c_2 + c_3)} - \sigma, \quad (3.4.17)$$

yielding the steady instability boundary $q = q_0$, where

$$q_0 = -\frac{1}{2} \left[\frac{s(2\mu - \sigma(1 + b_3))}{2\mu(c_1 + c_4) - \sigma(c_1(1 + b_3) + c_2 + c_3)} \right]. \quad (3.4.18)$$

As with (3.3.17) for TWs, the growthrate (3.4.17) signals a new type of instability for SWs, reliant upon the presence of a conserved quantity. The growthrate reduces to $\lambda_2^{(5)} = -\sigma$ when the coupling to the conserved quantity is removed ($\mu = 0$), and so no instability is possible in that case. At band-centre the stability condition $\lambda_2^{(5)} < 0$ reduces to

$$\frac{2\mu}{1 + b_3} - \sigma < 0, \quad (3.4.19)$$

which is precisely the condition for squares to be stable in a two-dimensional pattern-forming system with stationary pattern onset and a conserved quantity [75]. The amplitude equations in that case, describing the competition between two orthogonal sets of one-dimensional patterns, are a special case of (3.2.14), and it is noteworthy that the additional parameters present in (3.2.14) do not arise in (3.4.19).

As with TWs, the apparent divergence of the growthrate at $q = q_+$ suggests the presence of a stability boundary near this line, and so we choose to denote the corresponding stability boundaries as (approximately) the strip

$$(\min\{q_0, q_+\}, \max\{q_0, q_+\}). \quad (3.4.20)$$

SWs can be stable either inside or outside this band, depending on the large- $|q|$ limit of (3.4.17):

$$\lim_{q \rightarrow \pm\infty} \lambda_2^{(5)} = \frac{2\mu(c_1 + c_4)}{c_1(1 + b_3) + c_2 + c_3} - \sigma. \quad (3.4.21)$$

SWs are stable inside the band when (3.4.21) is positive and vice versa.

Long-wave stability regions

In the CCGL equations in the absence of a conserved quantity, the possible long-wave stability regions for SWs are bounded by the neutral curve $r = q^2$, the vertical lines $q = q_{\pm}$ and a shifted parabola [54]—found by setting $\mu = 0$ in (3.4.15). With these boundaries alone, a great range of qualitatively different stability regions is possible, since SWs can be unstable inside or outside the strip (3.3.8) and the parabola (which can be convex from above or below). As with TWs, this already complicated situation is extended considerably by the presence of a conserved quantity. The boundary for the analogue of the Eckhaus instability can now take many forms and a new stability band is introduced by the growthrate (3.4.17). Thus, an even larger range of scenarios can arise for SWs than for TWs, which we do not attempt to catalogue here. Instead, four examples of the possible stability regions are illustrated in figure 3.5. As with TWs, it is found that stability regions are generically asymmetric about $q = 0$, can split into noncontiguous parts, or, most importantly, disappear altogether, so that no SWs are stable.

3.4.2 Eigenvalue behaviour for small-amplitude standing waves

The intersection of the lines $q = q_{\pm}$ with the neutral curve indicates that, as for TWs, the long-wave analysis must be revisited for small-amplitude SWs. Thus, as in §3.3.2, we remove the restriction to small l and instead set $r = q^2 + \delta p$ with $0 < \delta \ll 1$. Then from the dispersion relation (3.4.7) we obtain the following expansions of the various growthrates λ as series in δ :

$$\lambda^{(a,b)} = 2pl - (1 \pm ic_1)l^2 \pm (s + 2pc_1)il + O(\delta), \quad (3.4.22a)$$

$$\lambda^{(c,d)} = -2pl - (1 \mp ic_1)l^2 \pm (s + 2pc_1)il + O(\delta), \quad (3.4.22b)$$

$$\lambda^{(e)} = -\sigma l^2 + O(\delta). \quad (3.4.22c)$$

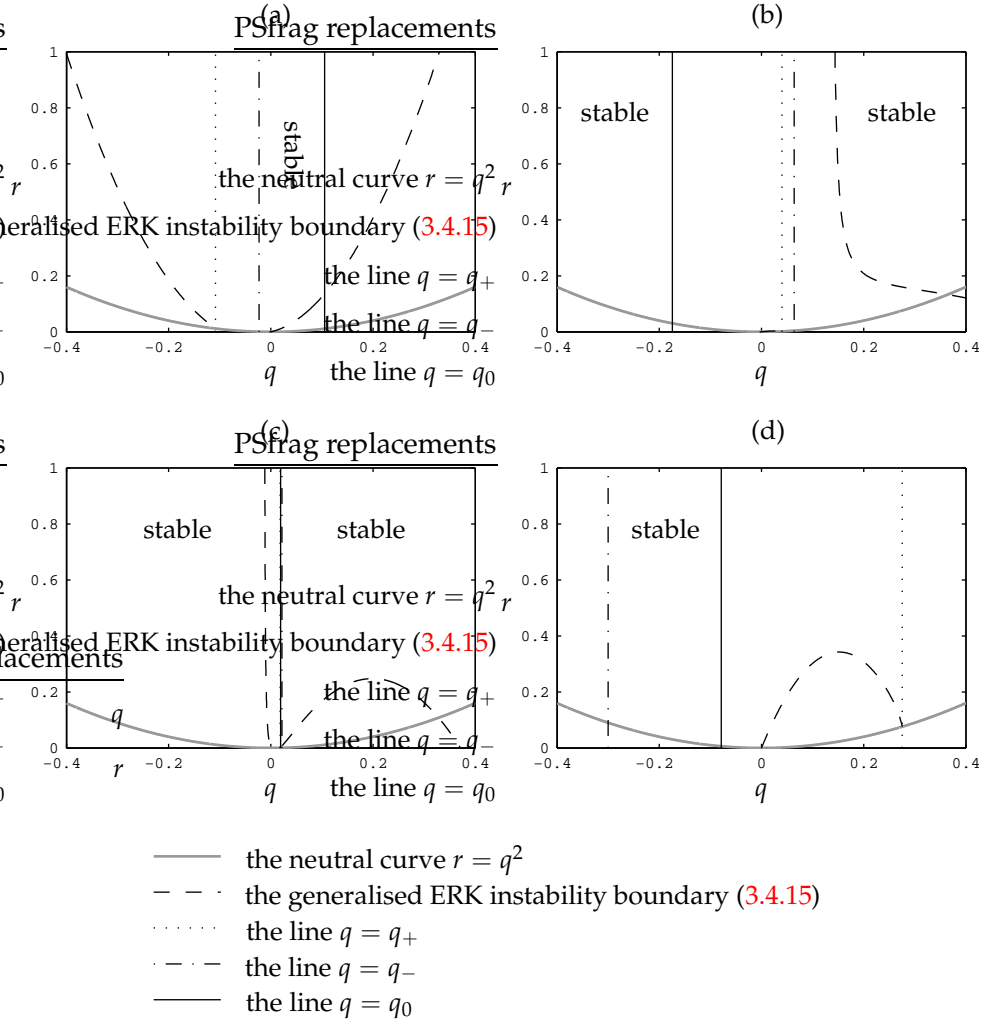


Figure 3.5: Long-wave stability regions for SWs under the parameter sets: (a) $s = 0.1, c_1 = 0.4, c_2 = 0.4, b_3 = 0.6, c_3 = -0.3, c_4 = 1.0, \sigma = 1.0, \mu = 0.4$; (b) $s = 0.2, c_1 = 0.4, c_2 = 0.4, b_3 = 0.5, c_3 = -0.5, c_4 = 1.0, \sigma = 1.0, \mu = 1.5$; (c) $s = 0.2, c_1 = -4.85, c_2 = -0.3, b_3 = 0.2, c_3 = -0.5, c_4 = 1, \sigma = 1.0, \mu = -0.1$; (d) $s = 1.5, c_1 = -2.5, c_2 = 0.3, b_3 = 0.8, c_3 = -0.7, c_4 = 1.0, \sigma = 1.0, \mu = 1.0$. Within the indicated regions, SWs are stable to long-wave perturbations up to the nearest boundaries.

The leading-order real parts are $\text{Re}(\lambda^{(1,2)}) = 2pl - l^2$, $\text{Re}(\lambda^{(3,4)}) = -2pl - l^2$, and $\text{Re}(\lambda^{(5)}) = -\sigma l^2$ and so in the vicinity of the neutral curve SWs are always unstable.

3.5 Numerically calculating stability regions

In §3.3.1 and §3.4.1, analytical progress was made possible through expanding the growthrates of perturbations to pure TW and SW states in the limit of large perturbation wavelength. Of course, such analysis does not capture instability to finite-wavelength perturbations, and so only a partial picture is obtained of the stability regions. Indeed, in §3.3.2 and §3.4.2 it was shown that the fastest-growing perturbations can have finite wavelengths. We now examine the validity and relevance of the long-wave limit by numerically calculating the complete stability regions for both TWs and SWs.

In order to determine complete stability regions, we numerically solve the appropriate dispersion relation, holding all the parameters in the amplitude equations (3.2.14) fixed, apart from r . In this setting, both TWs and SWs are two-parameter solutions, defined by the pair (q, r) . For each of these pairs, we define

$$\mathcal{S}(q, r) = \max_{l \in \mathbb{R}} \left[\{\text{Re}(\lambda) : \lambda \in \mathbb{C}, F(\lambda, q, r, l) = 0\} \right], \quad (3.5.1)$$

where F is the appropriate dispersion relation for perturbations of wavenumber l and growthrate λ ; $\mathcal{S}(q, r)$ is the maximum possible growthrate of any disturbance to the underlying solution. We now distinguish between two stability phenomena. A solution is said to be *neutrally stable* if $\mathcal{S}(q, r) = 0$, while the same solution is *marginally stable* if $\mathcal{S}(q, r) = 0$ and $\mathcal{S}(q, r)$ changes sign at (q, r) .

For the calculation of the full stability regions, the appropriate dispersion relation is solved for a range of perturbation wavenumbers l over a grid in (q, r) -space to find $\mathcal{S}(q, r)$. Subsequently, a bisection method is applied to the intervals where $\mathcal{S}(q, r)$ changes sign, to locate accurately the marginal stability boundary. Since the dispersion relations depend on r, q and l , finding the stability boundaries of a solution is essentially a three-dimensional problem that gives results to be plotted over two dimensions.

Figures 3.6 and 3.7 illustrate the full stability regions for the same parameter sets used for figures 3.3 and 3.5 respectively. It can be seen that, for both TWs and SWs, the long-wave boundaries (hollow squares) remain relevant in each example, in the sense that at least some part of the boundary of each stability region corresponds to a long-wave instability. While short-wave instabilities (solid squares) are important in completing

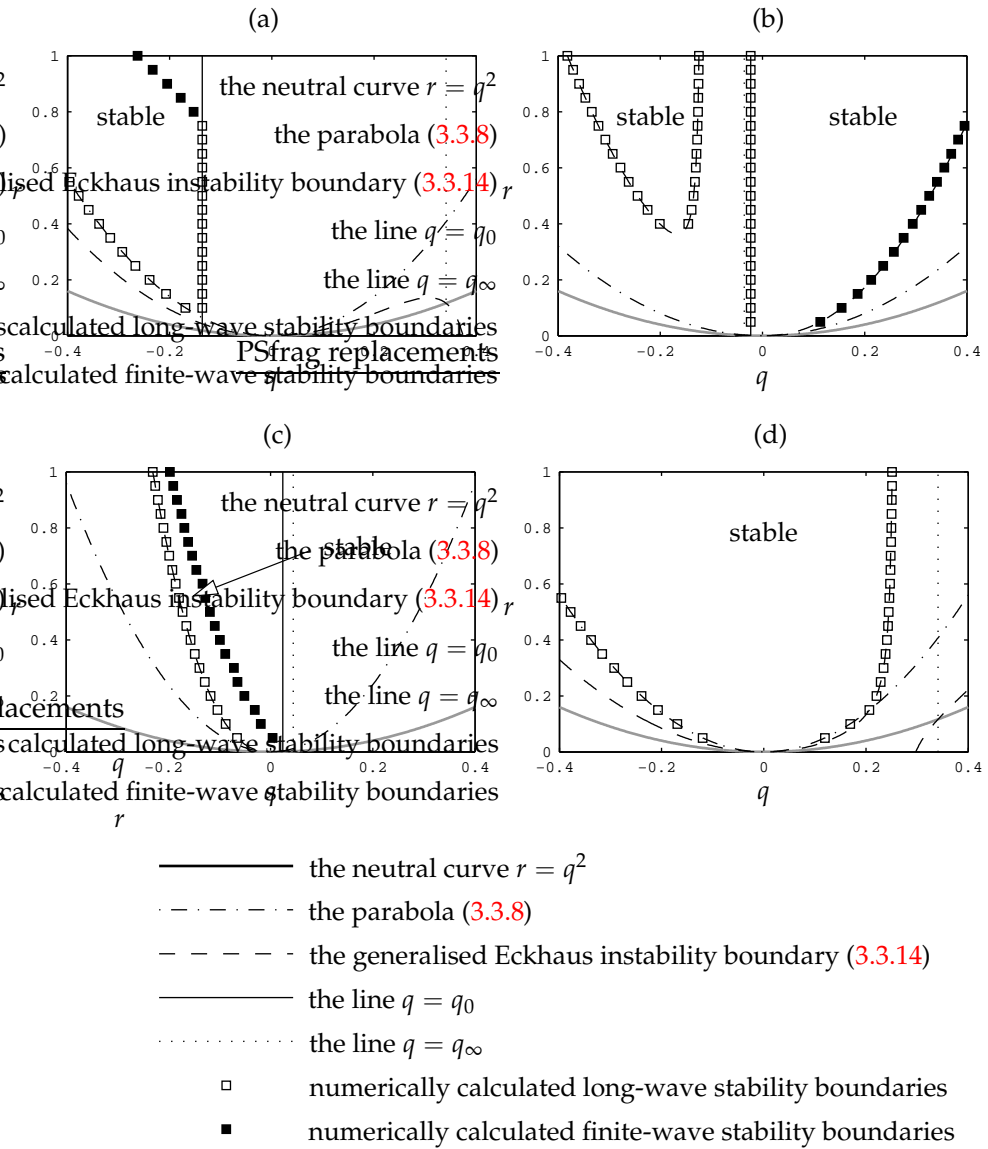


Figure 3.6: Full stability regions for TWs for the parameter sets of figure 3.3. Within the indicated regions, TW are stable to all disturbances (whether long-wave or not). The plots distinguish between long-wave (hollow squares) and finite-wavelength instability (solid squares).

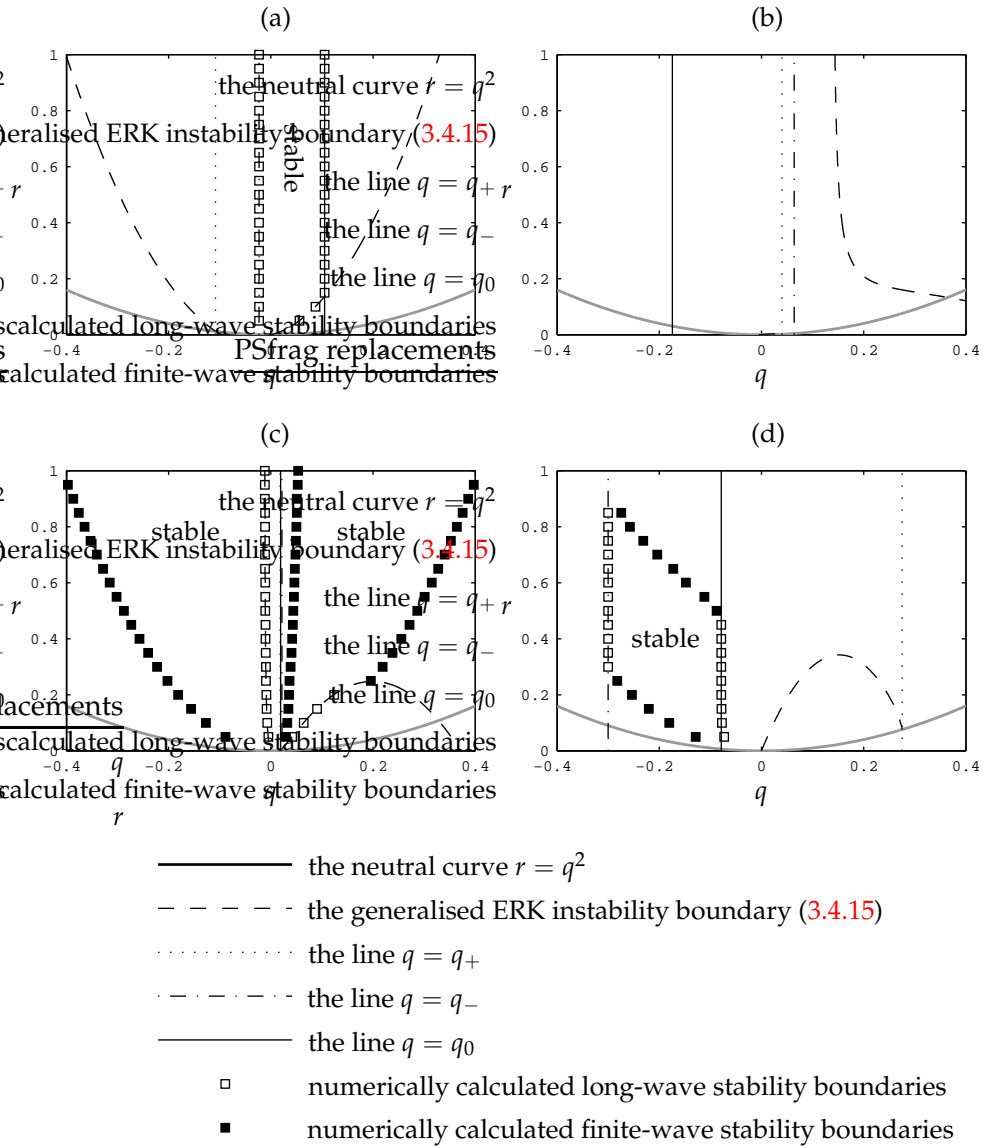


Figure 3.7: Full stability regions for SWs for the parameter sets of figure 3.5. Within the indicated regions, SW are stable to all disturbances (whether long-wave or not). The plots distinguish between long-wave (hollow squares) and finite-wavelength instability (solid squares). Note that in (b) all SWs are unstable.

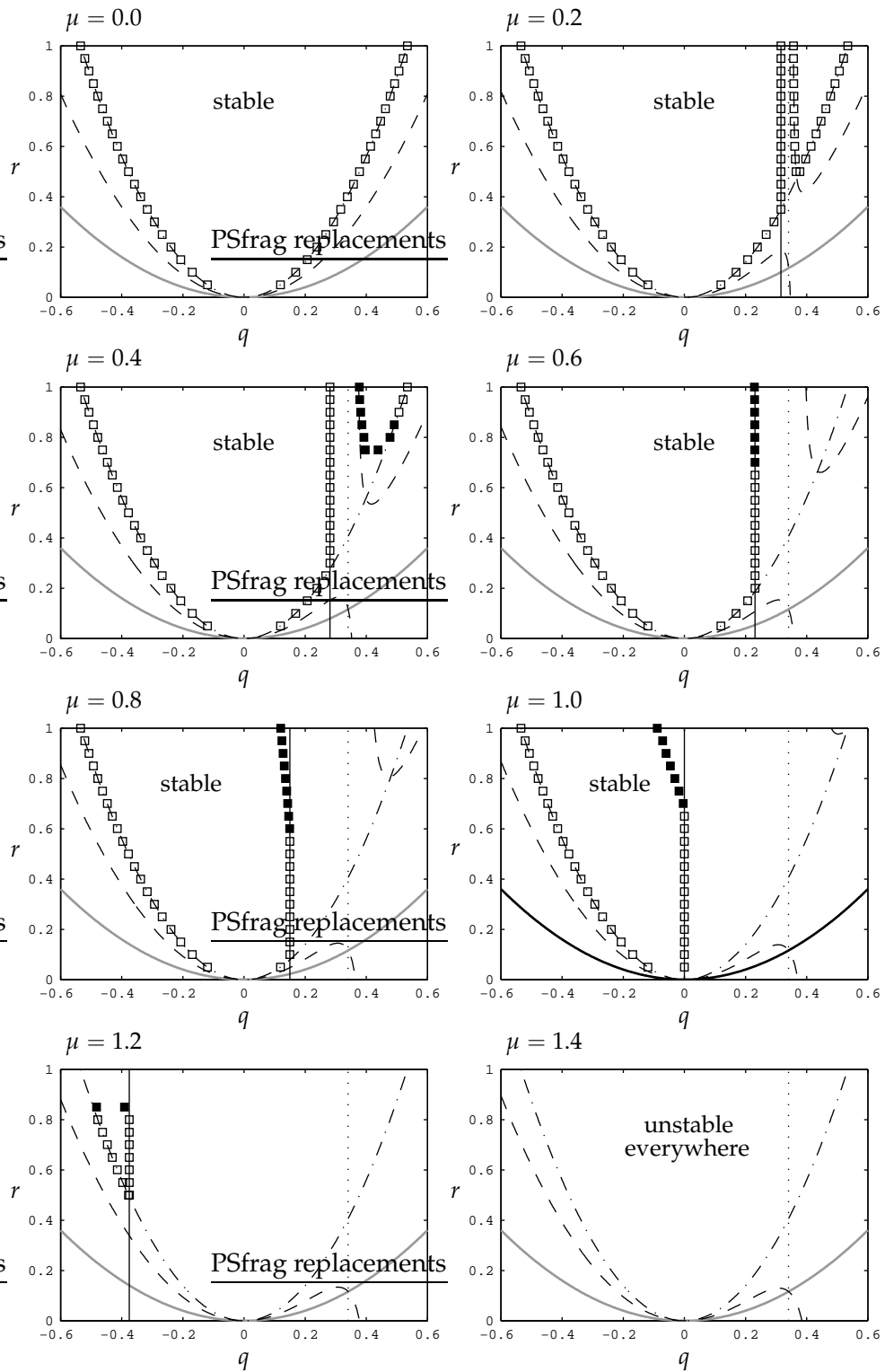


Figure 3.8: Full stability regions for TWs with the parameter set from figure 3.3(a) and increasing values of μ . (See figure 3.6 for the appropriate legend.)

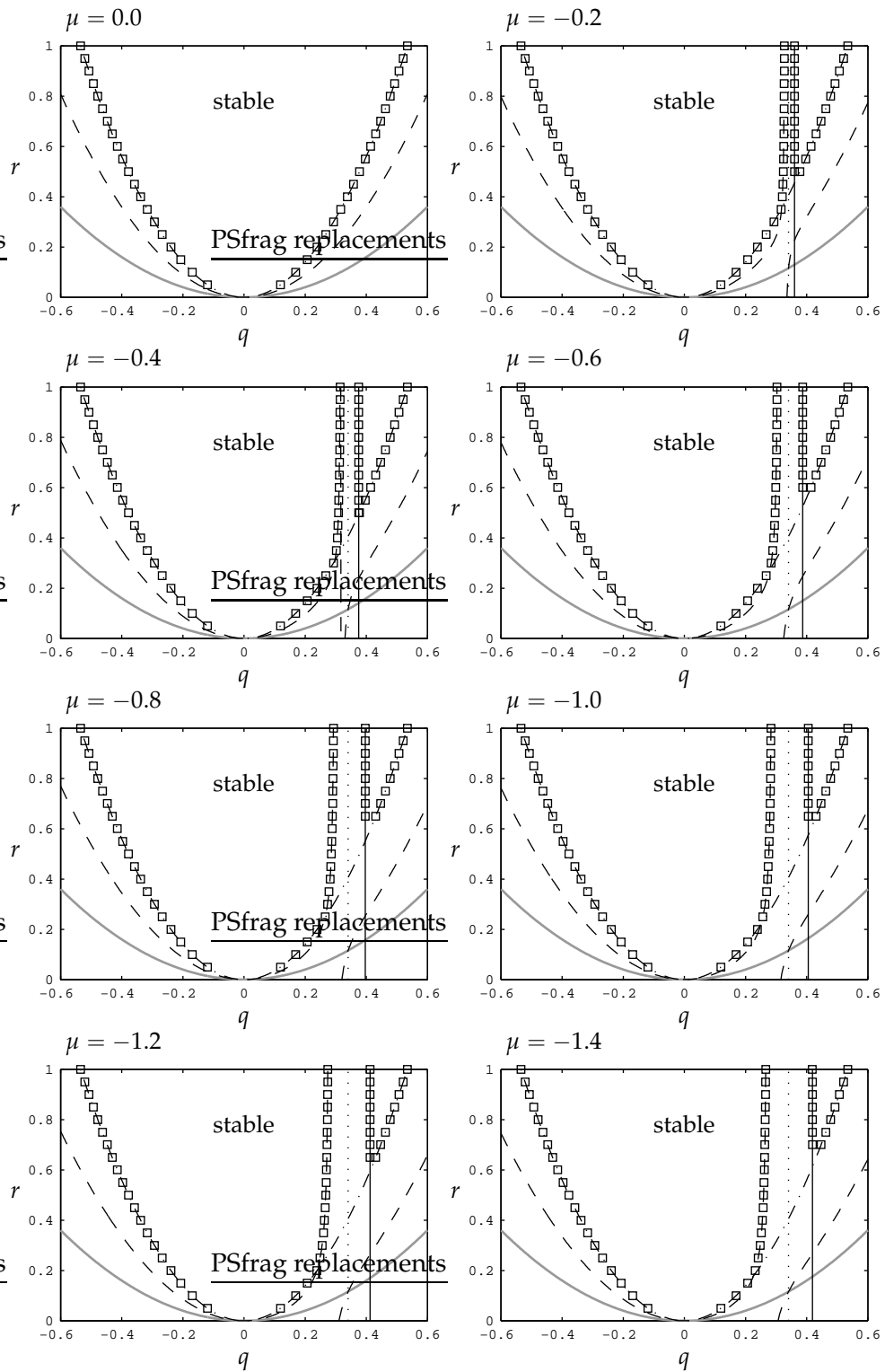


Figure 3.9: Full stability regions for TWs with the parameter set from figure 3.3(d) and decreasing values of μ . (See figure 3.6 for the appropriate legend.)

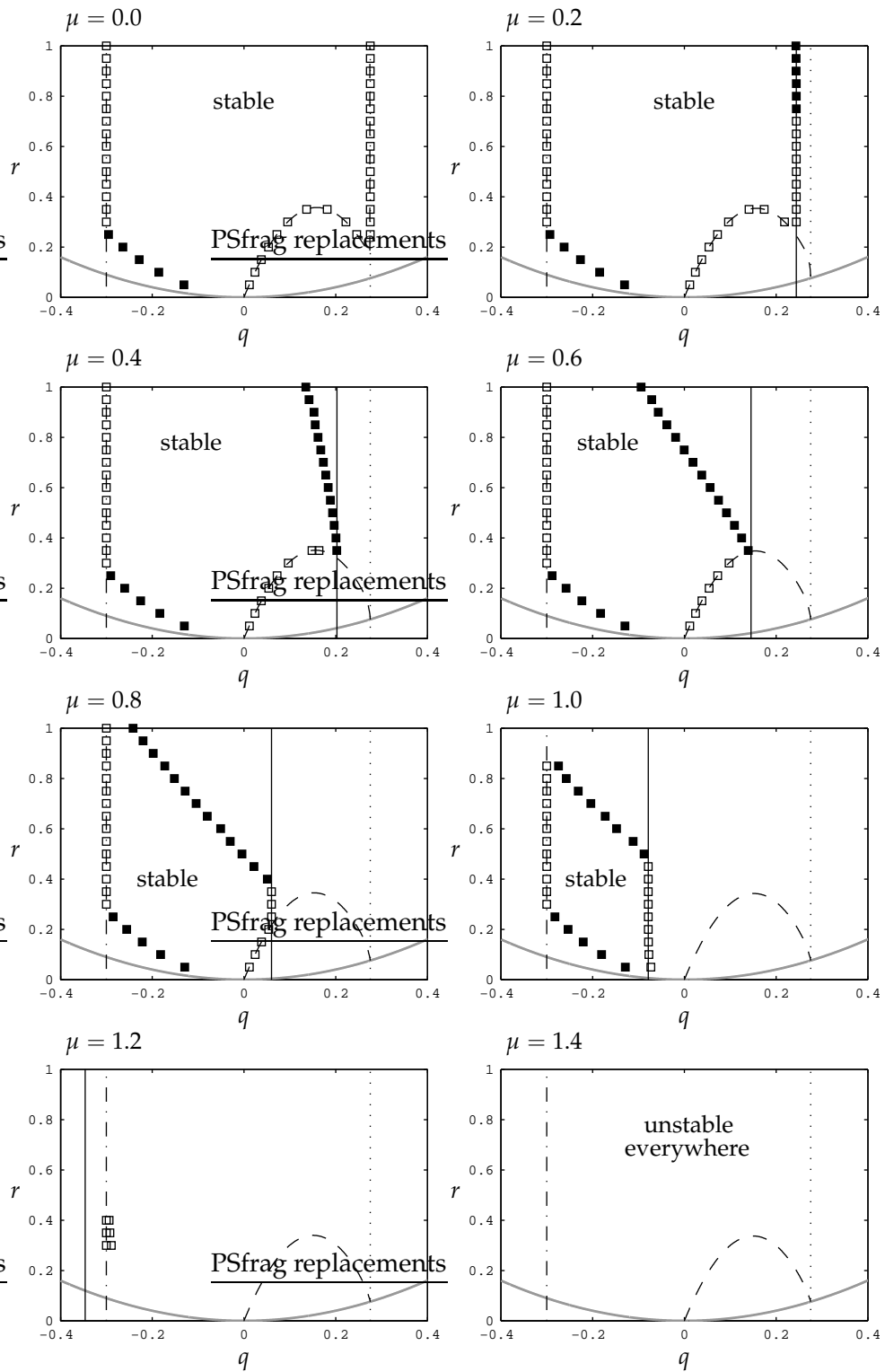


Figure 3.10: Full stability regions for SWs with the parameter set from figure 3.5(d) and increasing values of μ . (See figure 3.5 for the appropriate legend.)

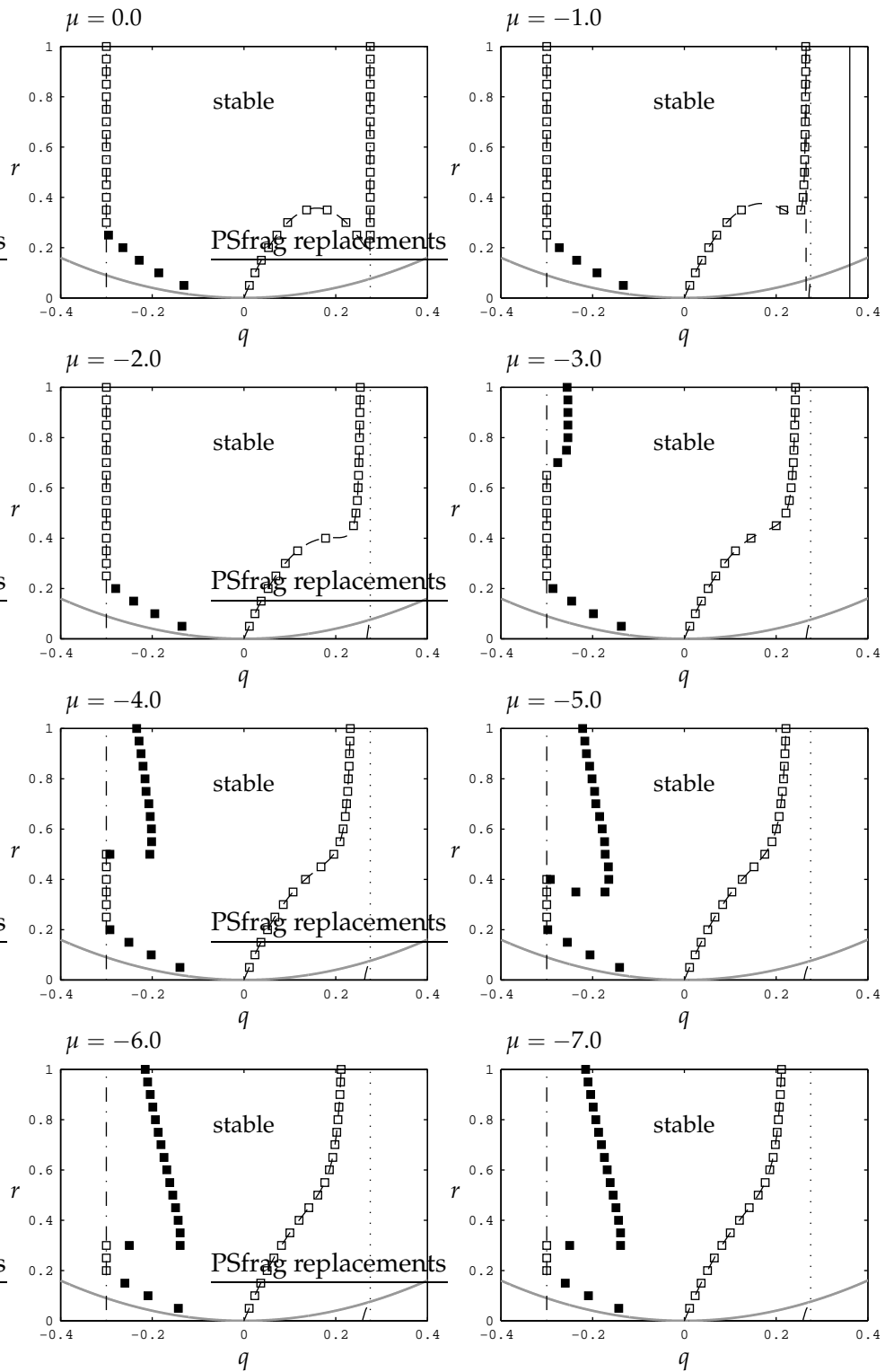


Figure 3.11: Full stability regions for SWs with the parameter set from figure 3.5(d) and decreasing values of μ . (See figure 3.5 for the appropriate legend.)

the partial picture obtained from the long-wave analysis, they are often not the dominant instability mechanism. Thus in these examples (and in many others which are not presented here) the analytical results of §3.3.1 and §3.4.1 are widely applicable, and the dominance of long-wave stability boundaries extends to much of parameter space.

Another point of interest is the influence of the strength of coupling between the pattern and mean modes μ on the full stability region. We can see in figures 3.8 and 3.10 that, as μ is increased, the stability regions of both TWs and SWs shrink, often due to the rise of finite-wave instability, until the region eventually disappears. This behaviour has been found to be characteristic of much of parameter space. For decreasing μ , as illustrated in figures 3.9 and 3.11, the stability regions of TWs and SWs approach a fixed shape, delimited in part by finite-wave instability boundaries and the $\mu \rightarrow -\infty$ limits of the previously detailed long-wave boundaries.

3.6 Simulation results

In this section, numerical simulations of the amplitude equations (3.2.14) are presented. The new instabilities of TWs and SWs are examined through using initial conditions comprising an unstable TW or SW, perturbed with small-amplitude noise, and simulating the subsequent nonlinear development. The numerical simulations are carried out using pseudo-spectral methods for spatial discretisation together with the **ETD2** time-stepping of Cox and Matthews [138] (outlined in §2.4.1). The general structure of the program is similar that used to generate the numerical results of chapter 2 (see appendix B for further details).

We choose a periodic spatial domain $-L/2 \leq X \leq L/2$, where the domain size is either $L = 50$ or $L = 100$. Although this domain is relatively small compared with many other simulations of Ginzburg–Landau-type equations (see, e.g., [48, 50]), it is large enough that the characteristic behaviours of the system are found. Since the instabilities of interest here manifest themselves through the slow growth of disturbances of large wavelength, large containers give rise to extremely slow growth of disturbances which can only be investigated through computationally expensive simulations. We find smaller container sizes are both computationally efficient and accurately reflect the nature of the instability. We use a time-step of 0.05 which is sufficiently small to capture accurately all predicted instabilities, while 512 grid points provide sufficient spatial resolution. In all the exhibited results, the initial condition is a TW or SW perturbed by small-amplitude Gaussian noise; simulations are then run for long times ($T = O(10^5)$) in order for all transients to decay and any modulational instability to

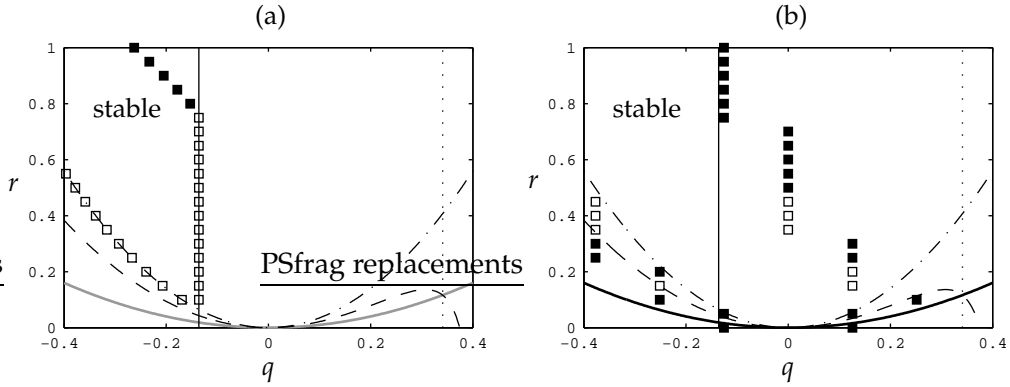


Figure 3.12: Stability regions for TWs with the parameter set of figure 3.3(a) for (a) a container of infinite horizontal extent and (b) $L = 50$. In (b), TWs are stable up to the hollow or filled squares, the long-wave boundaries no longer give an accurate guide to the stability region. We reuse the plotting conventions of figure 3.6.

take place.

It is well known that the CCGL equations are capable of exhibiting a rich variety of dynamical behaviour [55, 57, 173, 178]. Naturally, the same is true of (3.2.14), since this system contains the CCGL equations as a special case when the coupling to the conserved mode is removed ($\mu = 0$). Many of the coherent structures found in the CCGL, such as fronts, sources, sinks and pulses and can also be found in (3.2.14), and it is to be expected that the conserved quantity influences the existence and stability of these solutions. However, we choose not to pursue this interesting matter here; rather, we concentrate on the long-time behaviour of the system slightly beyond the boundaries for the new instabilities for TWs and SWs.

3.6.1 Travelling wave instabilities

Our analysis of TWs uses the parameter set of figure 3.3(a), whose stability diagram is recalled in figure 3.12(a). In choosing an initial condition, one must take into account the quantisation induced through using a finite container. In a periodic domain of size L , only wavenumbers that fit into the domain are permitted. Hence, when choosing an unstable TW—which is defined by the pair (q, r) —as an initial condition, q must be an integer multiple of $2\pi/L$. Also, for finite L , the stability region will change as the perturbation wavenumbers that first become unstable in the infinite case may no longer be available; this leads to a widening of the stability region. The appropriate stability diagram for TWs in a container of size $L = 50$ is illustrated in figure 3.12(b), where one can see the stability region for finite L is considerably wider. Figures 3.13–

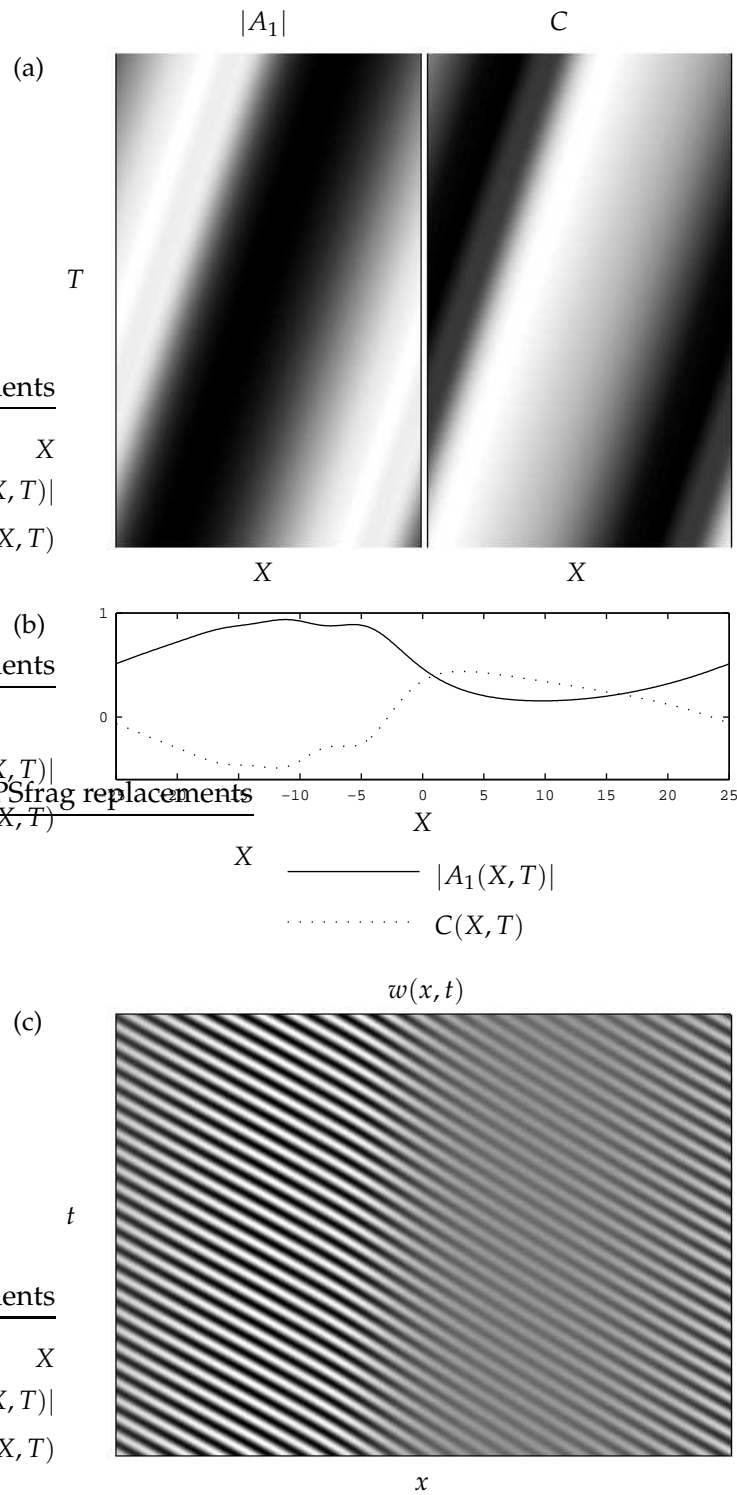


Figure 3.13: TW behaviour I: (a) space-time plots of $|A_1|$ and C ; (b) an example configuration of $|A_1|$ and C ; (c) a reconstruction of a physical field $w(x, t)$ using (3.2.1) and suitable values of ω_c and k_c . The initial condition for this simulation was a perturbed TW with $(q, r) = (0, 0.4)$.

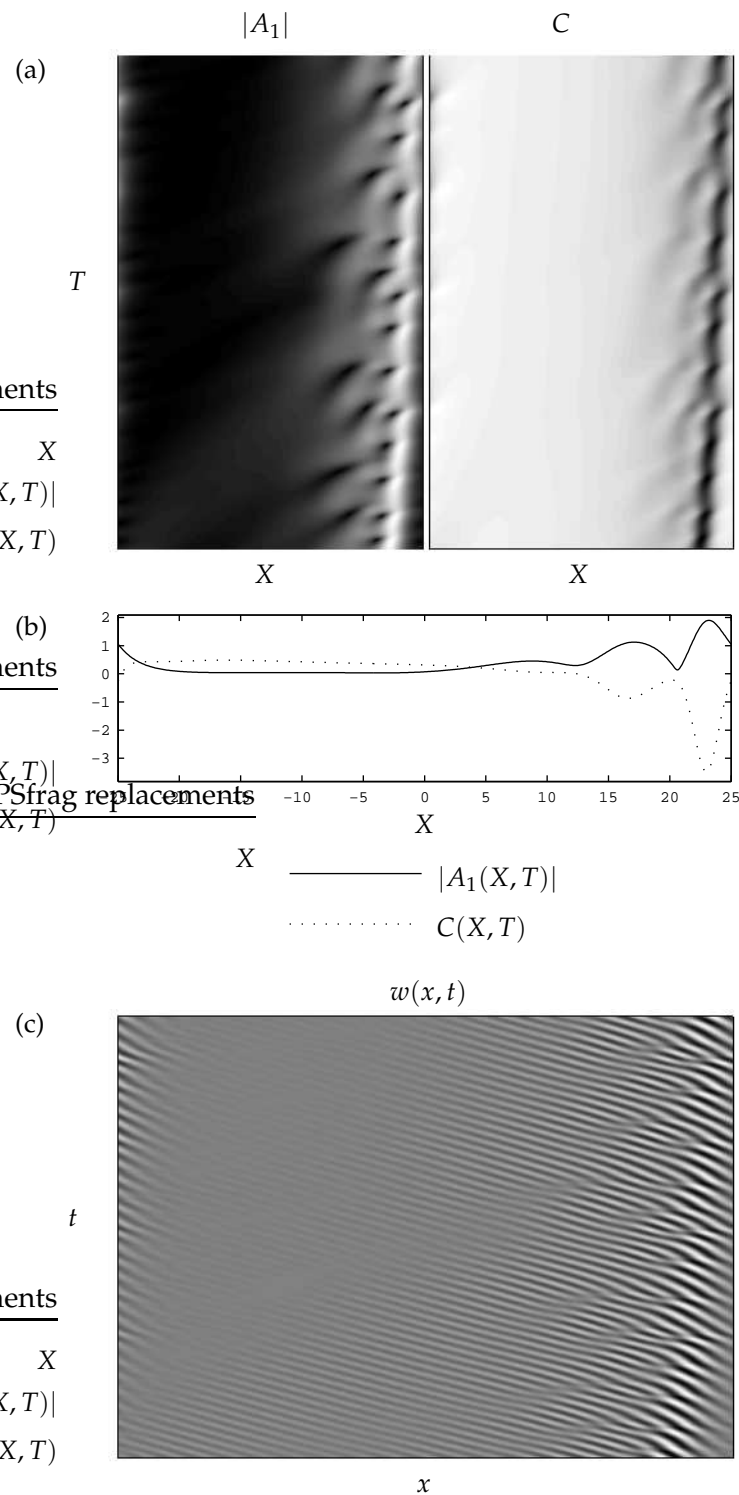


Figure 3.14: TW behaviour II: (a) space-time plots of $|A_1|$ and C ; (b) an example configuration of $|A_1|$ and C ; (c) a reconstruction of a physical field $w(x, t)$ using (3.2.1) and suitable values of ω_c and k_c . The initial condition for this simulation was a perturbed TW with $(q, r) = (0, 0.5)$.

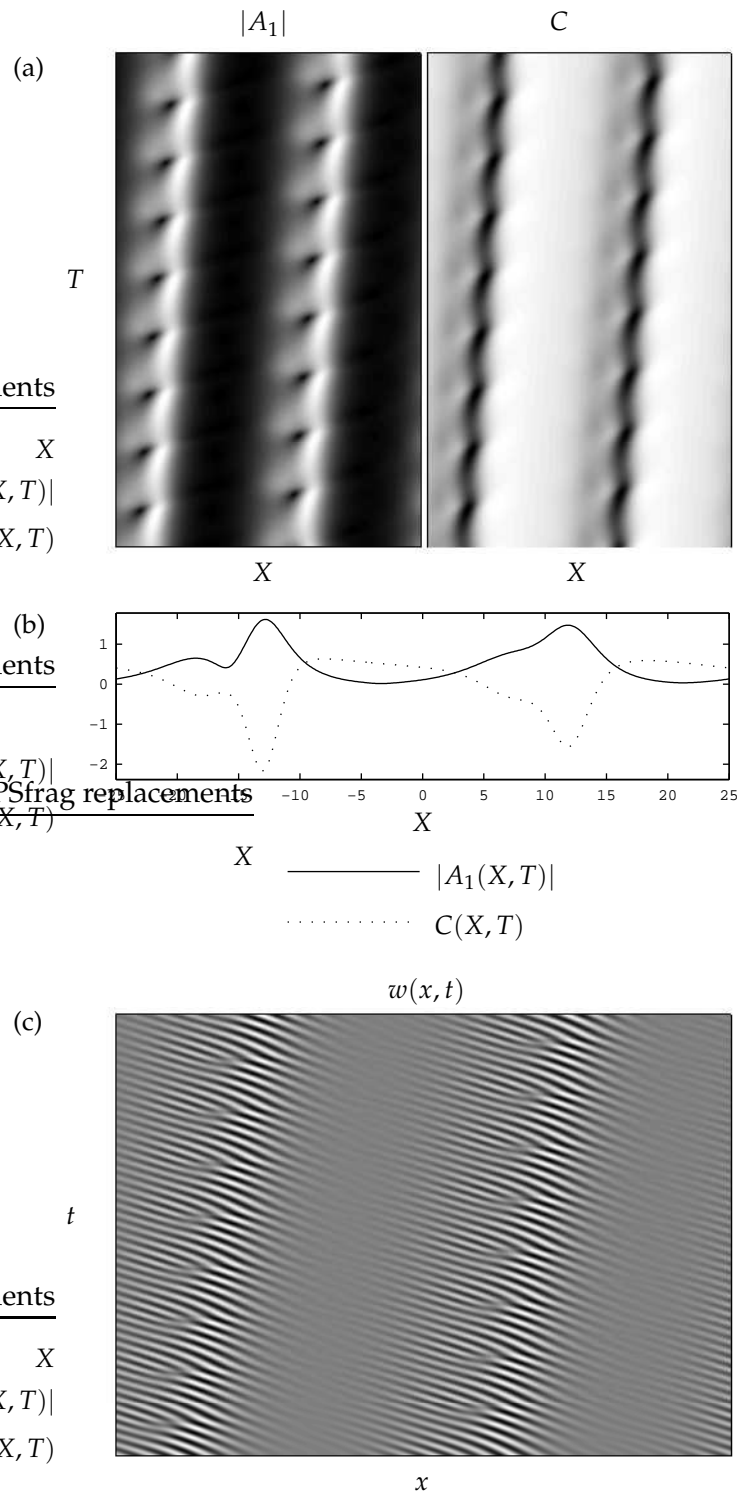


Figure 3.15: TW behaviour III: (a) space-time plots of $|A_1|$ and C ; (b) an example configuration of $|A_1|$ and C ; (c) a reconstruction of a physical field $w(x, t)$ using (3.2.1) and suitable values of ω_c and k_c . The initial condition for this simulation was a perturbed TW with $(q, r) = (0, 0.6)$.

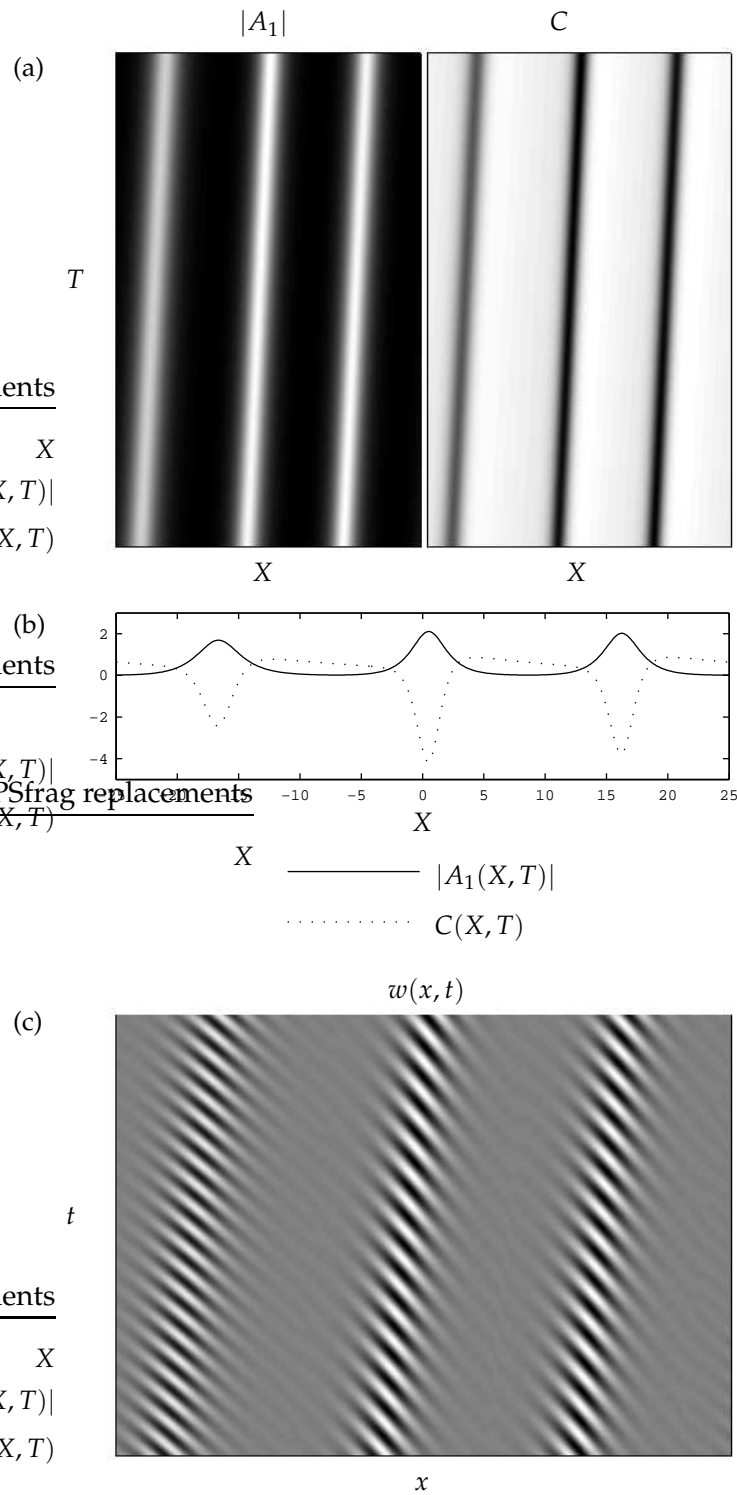


Figure 3.16: TW behaviour IV: (a) space-time plots of $|A_1|$ and C ; (b) an example configuration of $|A_1|$ and C ; (c) a reconstruction of a physical field $w(x, t)$ using (3.2.1) and suitable values of ω_c and k_c . The initial condition for this simulation was a perturbed TW with $(q, r) = (0, 0.7)$.

3.15 illustrate three typical behaviours realised in this region, each generated with an initial condition of a TW with $q = 0$ plus noise.

In figure 3.13 (and figure 3.15), we see strongly amplitude-modulated coherent structures, that is, uniformly propagating amplitude profiles. The modulation has a single spatial period, and is found to develop smoothly from the TW profile. Similar solutions are observed for a range of initial conditions and under different parameter sets. The slight kink in the profile for $|A_1|$ is characteristic of the stable attractors of this form, although it seems to disappear in simulations in large containers.

In figure 3.14, we see a snapshot over a small time interval of a highly complicated behaviour. This is characterised by a localised region of amplitude behaving chaotically, and drifting slowly. From the reconstructions of the physical field, this unpredictable behaviour can be seen to include space-time defects (detailed in §1.3), where the amplitude is locally zero and a wave is created or destroyed. With behaviour of this type, one often finds the system to undergo a persistent and unpredictable switching in the dominant mode between A_1 and A_2 (not illustrated in the figure). In these cases, the chaotic behaviour takes the form of localised pulse-like structures with intricate evolution. In other simulations we have found that such localised pulses can also periodically pass through a state similar to that in figure 3.13 before a counter-propagating mode becomes dominant again.

Figure 3.15 shows a similar behaviour to that of figure 3.14, except where the fluctuations to the amplitude pulse take a time-periodic form. It can be seen that the pulse's shape evolves in time, but propagates with constant speed. Again, we can observe the presence of space-time defects, which cause the TWs to periodically split in two or coalesce in the region of strongly suppressed amplitude.

The $|A_1|$ profile in figure 3.16 comprises three localised pulse-like structures that correspond to localised dips in C . Under certain conditions, the pulses have been observed to split in two or to coalesce to form a single pulse; these behaviours usually occur in the early stages of a simulation. Furthermore, for such pulse-like states, the counter-propagating mode (in this case, A_2) does not always remain zero; long-time simulations reveal intermittent and localised occurrences of positive amplitude. It should also be noted that, as can be seen in the figure, the pulses can vary in size, each pulse giving rise to a different wave frequency. Simulations run over very long times ($T > 50000$) show that the pulses do not generally converge to a stationary amplitude profile; the individual amplitudes of the pulses can be observed to undergo persistent, small-scale, periodic fluctuations.

3.6.2 Standing wave instabilities

We now turn to the long-time behaviour of SWs, and focus on the ramifications of the new instability, which is bounded by the vertical line (3.4.20) in parameter space. We follow the same procedure as the previous section but with an initial condition comprising an unstable SW plus noise. In this case, we use the parameter set of figure 3.5(d) and carry out simulations in a container of size $L = 100$. Four typical behaviours are illustrated in figures 3.17–3.20, where plots of the space-time evolution, the configuration of modes and a reconstruction of a corresponding physical field, are exhibited.

In figure 3.17, the illustrated pattern is a coherent structure in the form of a slight amplitude modulation of both A_1 and A_2 . These modulations can be seen to have a regular period; furthermore, we note that the peak amplitude of the left-travelling component occurs at a different location to that of the right-travelling component. Generally, such solutions develop smoothly from standard SWs, giving the impression of a supercritical bifurcation. Figure 3.18 shows a similar form of amplitude modulation, but now the modulation is time-periodic and has a more complicated spatial character. Figure 3.19 exhibits an apparently chaotic modulation, similar to that in figure 3.18, but with less predictable amplitude fluctuations.

Figure 3.20 illustrates the most interesting of the behaviours shown here, with strong spatial localisation of the pattern, which comprises several pulse-like structures, similar to those found for TWs (cf. figure 3.16). The SW phases within these structures appear to be mutually independent, as can be seen from the reconstruction of $w(x, t)$; furthermore, we observe that the periods of the SWs are different within different pulses. It can also be seen that the pulse structure is not steady, and there is a time-periodic fluctuation in amplitude near the largest pulse. However, in other parameter regimes, a genuinely steady set of amplitude profiles has been found. In yet other parameter regimes, complicated spatiotemporal behaviour of these pulses is possible, with no steady profile being realised. Analogous solutions to these are observed in a 1D *monotonic* bifurcation with a conserved quantity (cf. figure 11 of [74]), although in this case the amplitude profile is stationary.

In all the solutions presented above and from the previous section for TWs, significant amplitude modulation is present. This suggests that, as in the stationary case [74], the presence of a conserved quantity facilitates the stabilisation of localised structures. It is also apparent that the amplitude equations (3.2.14) are capable of a wide range of dynamical behaviour, since all the examples of figures 3.13–3.20 are generated under just two parameter sets.

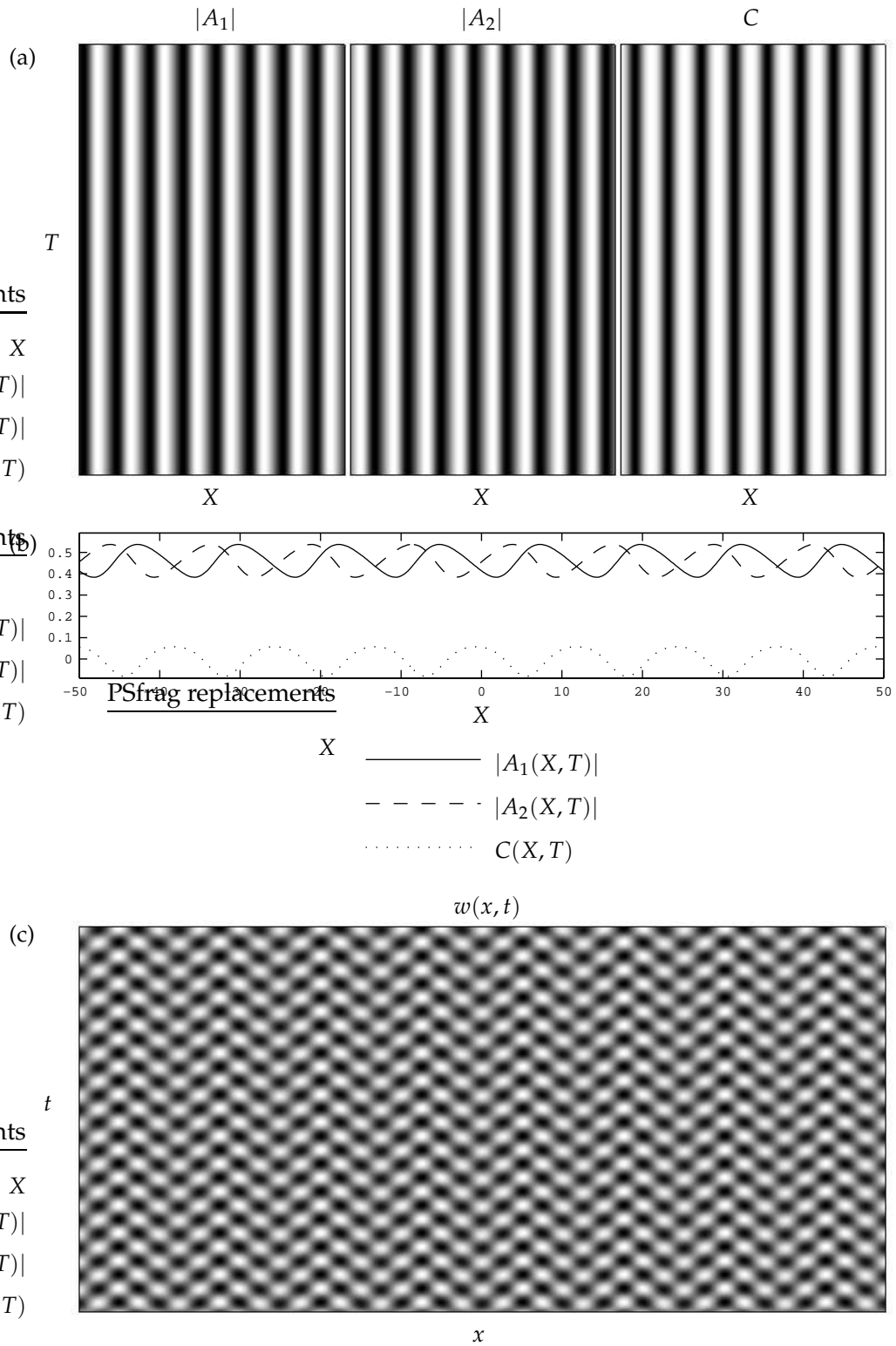


Figure 3.17: SW behaviour I: (a),(b) space-time plots and the final configuration of $|A_1|$, $|A_2|$ and C ; (c) a reconstruction of a physical field $w(x, t)$ using (3.2.1) and suitable values of ω_c and k_c . The initial condition for this simulation was a perturbed SW with $(q, r) = (0, 0.4)$.

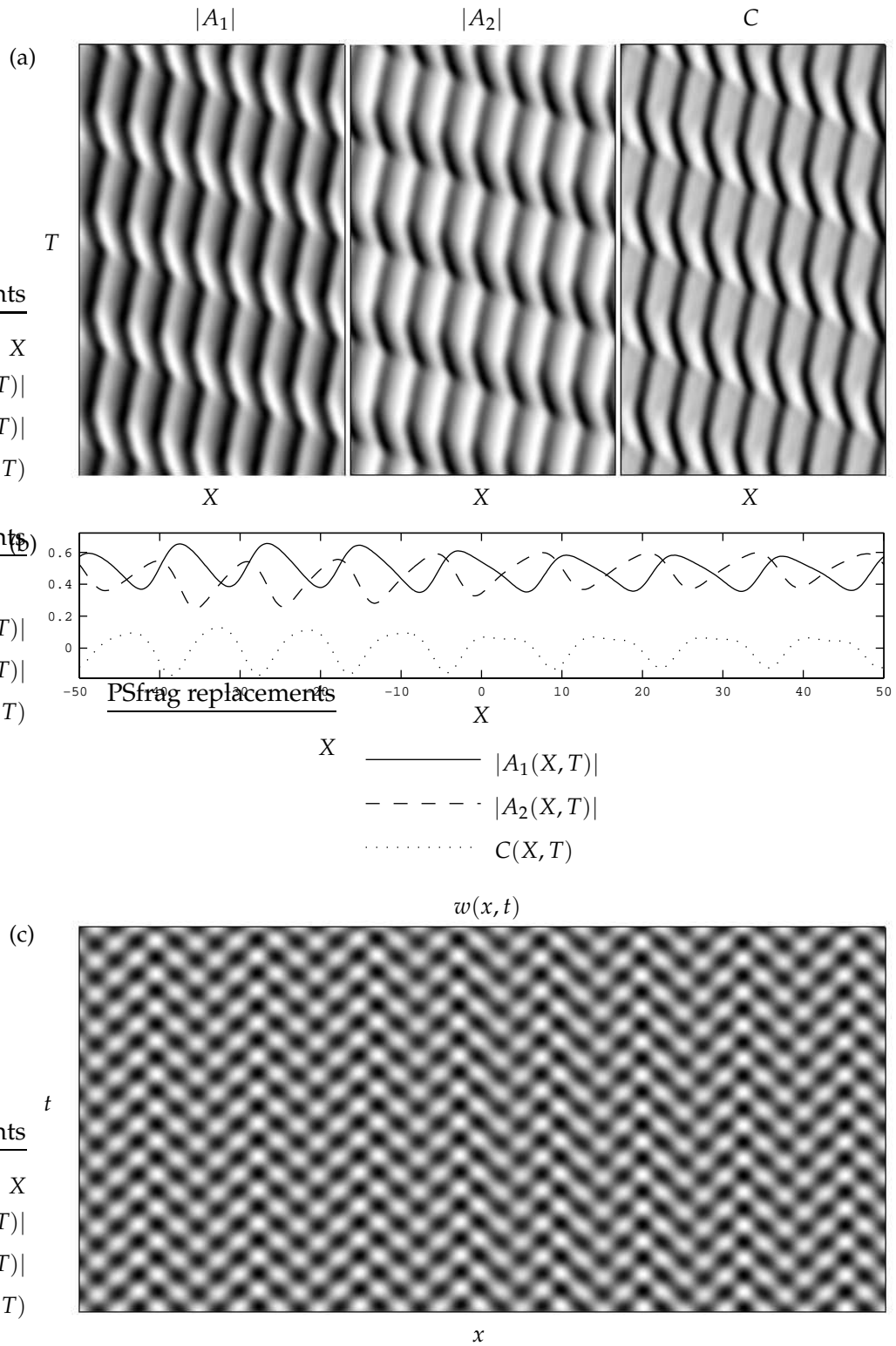


Figure 3.18: SW behaviour II: (a),(b) space-time plots and the final configuration of $|A_1|$, $|A_2|$ and C ; (c) a reconstruction of a physical field $w(x,t)$ using (3.2.1) and suitable values of ω_c and k_c . The initial condition for this simulation was a perturbed SW with $(q,r) = (0,0.45)$.

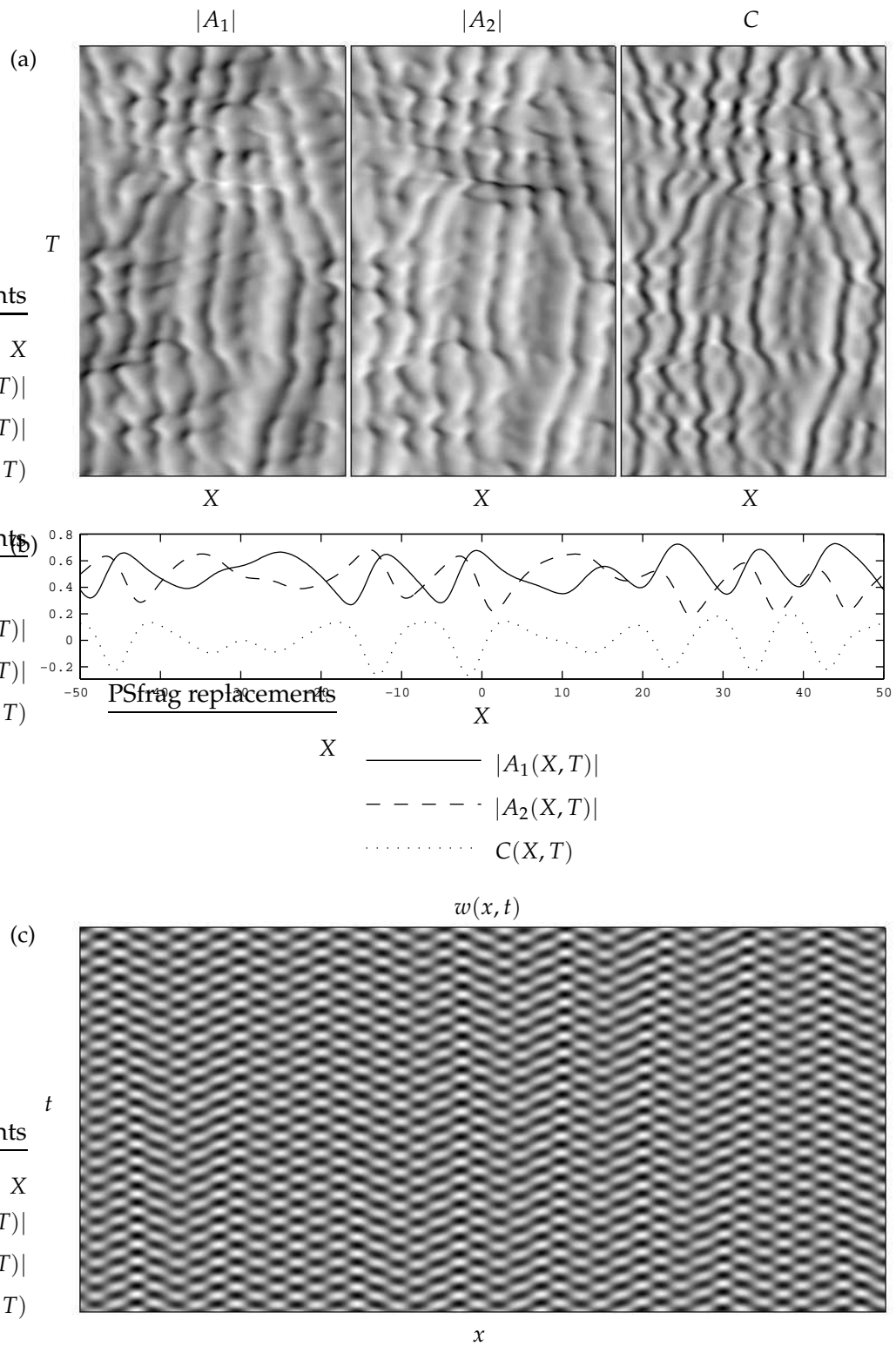


Figure 3.19: SW behaviour III: (a),(b) space-time plots and the final configuration of $|A_1|$, $|A_2|$ and C ; (c) a reconstruction of a physical field $w(x,t)$ using (3.2.1) and suitable values of ω_c and k_c . The initial condition for this simulation was a perturbed SW with $(q,r) = (0,0.5)$.

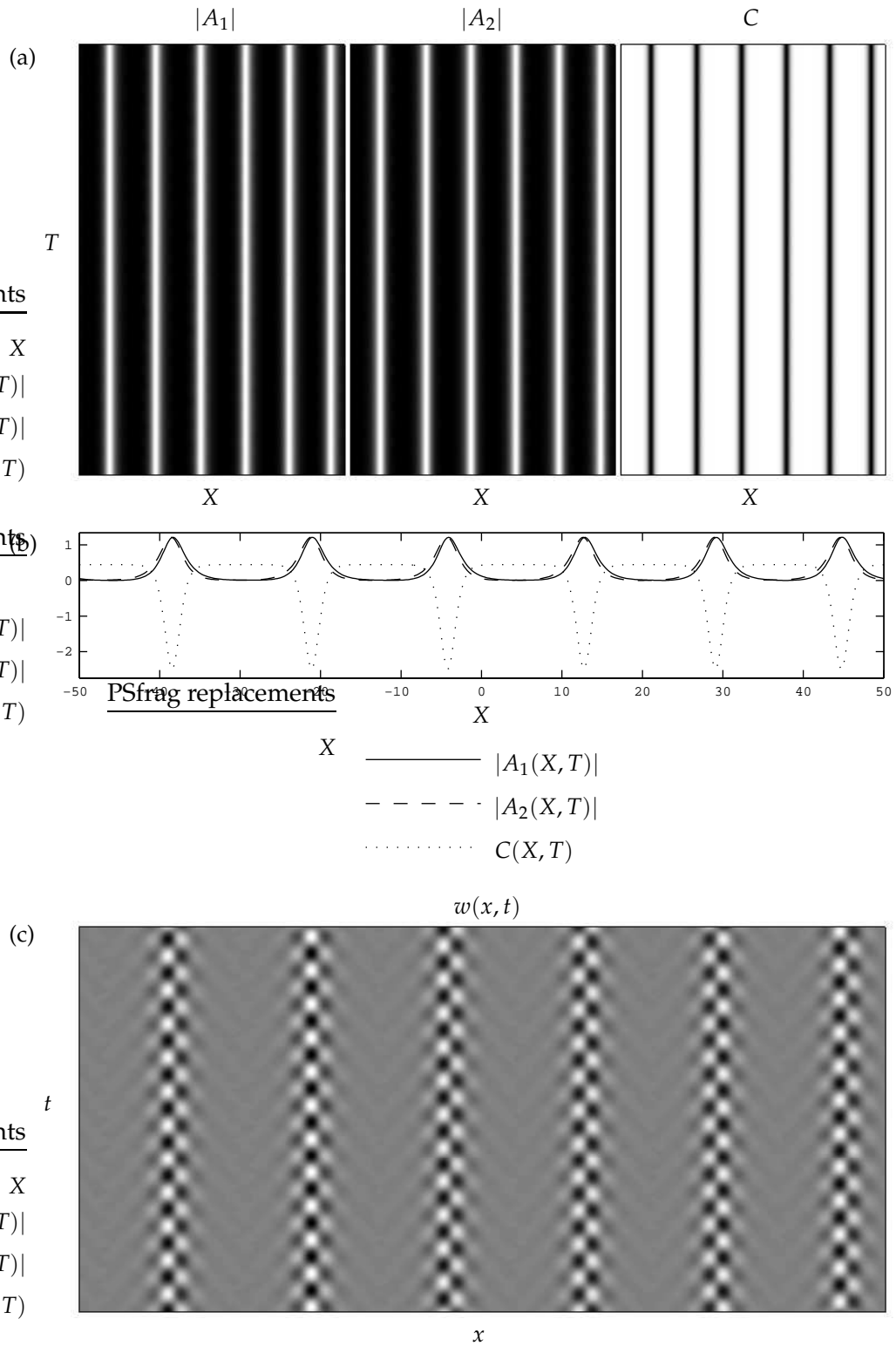


Figure 3.20: SW behaviour IV: (a),(b) space-time plots and the final configuration of $|A_1|$, $|A_2|$ and C ; (c) a reconstruction of a physical field $w(x, t)$ using (3.2.1) and suitable values of ω_c and k_c . The initial condition for this simulation was a perturbed SW with $(q, r) = (0, 0.55)$.

3.7 Behaviour for $O(1)$ group velocity

In the absence of a conserved quantity, it has been shown that the CCGL equations are only asymptotically valid for small group velocity, $c_g = O(\epsilon)$ [69, 72]. In the more widely applicable scenario where $c_g = O(1)$, the appropriate amplitude equations are the MFGL equations [69, 176, 177] (see §1.4.2), coupled nonlocally, interacting only through their spatial average. Since the amplitude system (3.2.14) is an extension of the CCGL equations, the question naturally arises of how one might correspondingly accommodate $O(1)$ group velocity in the presence of a conserved quantity. It has been shown by both Knobloch [71] and Riecke and Kramer [54] that a connection between the SW stability results of the CCGL and MFGL equations can be found through considering the non-commuting limits of small amplitudes ($r \rightarrow 0$) and small wavenumbers ($l \rightarrow 0$). Here, we consider the equivalent limits of ‘large’ group velocity ($s \rightarrow \infty$) and small wavenumbers. Again, these limits are found not to commute; however, the correct order is to consider $s \rightarrow \infty$ before the long-wave limit. This fact is clearly demonstrated if one considers taking these limits in the *wrong* order: for instance, the $O(l)$ behaviour of the growthrates $\lambda^{(4)}$ for TWs (3.3.12) and $\lambda^{(3,4)}$ for SWs (3.4.10), in the limit $s \rightarrow \infty$, have frequency tending to infinity, which is indicative of the wrong order for taking the two limits.

Considering TWs first, we let l remain $O(1)$ and expand the solutions to (3.3.9) in s^{-1} , which we take to be small:

$$\lambda^{(A,B)} = ils + r - l^2 - b_3 Q^2 \pm i(c_1 l^2 - c_3 Q^2) + O(s^{-1}), \quad (3.7.1a)$$

$$\begin{aligned} \lambda^{(C,D)} = & -ils - Q^2 - l^2 - 2iqlc_1 \\ & \pm \sqrt{Q^4 - 4iqc_2 l Q^2 + (2c_1 c_2 q^2 Q^2 + 4q^2) l^2 + 4iqc_1 l^3 - c_1^2 l^4} + O(s^{-1}), \end{aligned} \quad (3.7.1b)$$

$$\lambda^{(E)} = -\sigma l^2 + 2il\mu Q^2 s^{-1} + O(s^{-2}). \quad (3.7.1c)$$

Immediately we see that $\lambda^{(E)}$, which corresponds to the new TW instability from the growthrate (3.3.17), cannot lead to instability. Also, (3.7.1a) matches the growthrates of (3.3.5), while writing $\lambda^{(C,D)} = -ils + \lambda_0^{(C,D)} + O(s^{-1})$ and expanding in the long-wave limit gives:

$$\lambda_0^{(C)} = -2Q^2 - 2iql(c_1 - c_2) + O(l^2), \quad (3.7.2a)$$

$$\lambda_0^{(D)} = -2iql(c_1 + c_2) + \left(c_1 c_2 - 1 + \frac{2q^2(1 + c_2^2)}{Q^2} \right) l^2 + O(l^3). \quad (3.7.2b)$$

This manoeuvre recovers the BFE behaviour of TWs in the CGL/CCGL equation; thus, the new and interesting behaviour induced by the presence of a conserved quantity is lost.

For SWs, we expand the solutions to (3.4.7) as series in s^{-1} , and find four eigenvalues with leading-order component $\pm ils$, but algebraically cumbersome expressions for higher order terms. We write

$$\lambda^{(A,B)} = ils + \lambda_0^{(A,B)} + O(s^{-1}), \quad (3.7.3a)$$

$$\lambda^{(C,D)} = -ils + \lambda_0^{(C,D)} + O(s^{-1}), \quad (3.7.3b)$$

and consider the long-wave limit to find

$$\lambda_0^{(A,B)} = -2Q^2 + O(l) \quad (3.7.4a)$$

$$\lambda_0^{(C,D)} = 2iq(c_1 + c_2)l + \left(c_1c_2 - 1 + \frac{2q^2(1 + c_2^2)}{Q^2} \right) l^2 + O(l^3). \quad (3.7.4b)$$

We see that the stability criterion for SWs is

$$c_1c_2 - 1 + \frac{2q^2(1 + c_2^2)}{Q^2} < 0, \quad (3.7.5)$$

matching the equivalent condition for TWs (cf. (3.7.2b)), although the value of Q^2 is different for SWs. Thus, we see that the stability boundaries for SWs are the neutral curve and also

$$r = q^2 \left(1 + \frac{2(1 + b_3)(1 + c_2^2)}{1 - c_1c_2} \right). \quad (3.7.6)$$

This curve matches the stability parabola for SWs that can be derived from the MFGL equations. The final growthrate is found to be

$$\lambda^{(E)} = -\sigma l^2 + \frac{4\mu Q^2}{s^2} [2(1 - b_3)Q^2 + l^2(c_1c_4 + 1 - \sigma)] + O(s^{-3}); \quad (3.7.7)$$

which is strictly negative at leading-order in s , and unable to give rise to instability.

Overall, for both TWs and SWs, we see the limit of $O(1)$ group velocity removes the new instability behaviour associated with the influence of a conserved quantity. Since we recover the stability properties of the CGL and MFGL equations for TWs and SWs, respectively, the latter equations would appear to be the appropriate amplitude descriptions when $c_g = O(1)$.

3.8 Summary

In this chapter, we have derived amplitude equations for the near-threshold evolution of a one-dimensional pattern-forming system undergoing an oscillatory bifurcation from a uniform state. The system is taken to have translational and reflectional symmetries in space, and, crucially for the results presented here, to possess a conserved quantity. We have examined the generic amplitude description for systems with

a pseudoscalar conserved quantity, such as magnetoconvection and rotating convection. It is also expected that our results will apply to systems with a scalar conserved quantity although our choice of coupling is not generic in this case. The system is capable of supporting both travelling and standing waves, and we have provided here detailed stability analyses of these two wave types. In each case we have found a modification to the existing stability boundaries from the CCGL equations and a qualitatively new instability, with no analogue in the absence of a conserved quantity.

For travelling waves, the coupling to a conserved quantity significantly alters the classical Benjamin–Feir–Eckhaus stability boundary and introduces a new instability, whose boundary, at least in the context of the weakly nonlinear framework developed here, takes the form of two vertical lines in (q, r) -space. The full demarcation of (q, r) -space into regions of stable and unstable TWs can be very complicated. As with the corresponding case in which the pattern arises through a stationary bifurcation [74], it is also possible for all TWs to be destabilised. However, whereas the destabilisation of all regular patterns is due to a single type of instability in the case of a stationary primary bifurcation, here two instability mechanisms compete to generate complete destabilisation. The influence of the conserved quantity is similar for standing waves: we find that the analogue of the Eckhaus stability boundary (see Riecke and Kramer [54]) is significantly altered, and that a qualitatively new instability is engendered by the presence of the conserved quantity. Again a wide range of qualitatively different stability regions is possible for standing waves in (q, r) -space. For both travelling and standing waves, we have shown that the boundary to the region of stability generally involves both long- and short-wave instabilities; long-wave instabilities are often responsible for large parts of the stability boundary.

Numerical simulation of the amplitude system (3.2.14) has revealed that unstable travelling or standing waves can evolve into stable, highly localised structures, either coherent, time-periodic or chaotic. These structures occur in regions of parameter space with strong coupling between the conserved mode and the pattern. Similar patterns, known as ‘worms’, have been numerically observed in a two-dimensional Ginzburg–Landau system coupled to a slowly varying scalar mode [62]. In this case, the slow mode evolves in an analogous manner to the conserved mode of this chapter (see (3.2.14)) but is linearly damped and feeds back *positively* into the growthrates of the travelling modes. The results of Riecke and Granzow [62] and this chapter strongly suggest that coupling with a slow scalar mode, either conserved or damped, provides a general localisation mechanism for supercritical systems¹.

¹We note that there are numerous slightly differing definitions of what constitutes a “localised” pattern.

In some contexts, not only should the localised pattern be surrounded by a quiescent region, as here, but the same number of pulses should arise, regardless of the size of the domain [179]. This rather more restrictive definition is not intended here.

Faraday waves

4.1 Introduction

SINCE THE OBSERVATIONS of Michael Faraday [111] in 1831, it has been well known that ordered, standing wave patterns are generated when a layer of incompressible fluid is subject to sufficiently large vertical oscillation; generally, these waves are sub-harmonic, i.e., they oscillate at half the driving frequency. Through variation of the amplitude and frequency of the forcing, or the use of fluids with differing viscosities, patterns of a wide range of symmetries and orientations have been observed just above the threshold of this parametric instability. These patterns, known as *Faraday waves*, are an archetypal example of a pattern-forming system and, in recent years, have been the subject of intensive experimental and theoretical investigation; a detailed review of the subject is provided by Miles and Henderson [180].

Theoretical studies of the Faraday instability often assume that the fluid depth is infinite or, at least, much larger than the pattern wavelength. This simplifies the analysis but does not allow long-wave modes, which must be present due to the conservation of fluid material, to influence the evolution of the surface waves. In this chapter, we account for the influence of long-wave modes on the surface patterns through a modification of an existing model of Faraday waves. This simple alteration tailors the model for finite-depth fluids and gives rise to new behaviour of large-scale modes, quite different to the corresponding large-scale behaviour of chapters 2 and 3.

4.1.1 Experimental background

A schematic illustration of the experimental setup can be seen in figure 4.1. The basic behaviour is very similar to that of vibrated granular layers (discussed in §2.1): for low accelerations, the fluid is merely translated up and down, but when the acceleration

of the vertical forcing exceeds a certain threshold, the initially flat surface undergoes a parametric instability and a pattern of standing waves is formed. Through variation of the forcing frequency and amplitude, an exotic cornucopia of surface wave patterns can be observed. Concentrating on experiments performed in large containers, where the pattern is independent of boundary effects [107], the experimental results can be summarised as follows:

1. For low viscosity fluids—such as water or ethanol—we differentiate between two regimes:
 - (a) For high frequency oscillations, the effects of gravity are negligible and the dispersion relation is dominated by surface-tension effects. In this so-called ‘capillary wave’ regime, quasicrystalline patterns can be observed just above threshold, but generally give way to hexagonal and, most commonly, square patterns, as the forcing amplitude is increased [181]. Further increases in amplitude can lead to three-wave patterns [181].
 - (b) At lower frequencies, where both gravity and capillary forces are present (the mixed ‘capillary–gravity’ regime), a cascade of patterns with increasing rotational symmetry are observed; these include hexagons as well as 8- and 10-fold quasipatterns (see [107, 108, 109, 182, 183] and references therein).
2. For high viscosity fluids—such as mixtures of glycerol and water—striped patterns dominate at onset [107, 184]. In addition, rotating spirals [140] as well as localised or ‘confined’ states have also been observed [185, 186].

Increasing the amplitude of the driving force further can lead to secondary instabilities [187, 188] of the primary patterns and, at larger amplitude still, spatio-temporally chaotic states are found [109, 182]. A detailed review of experimental results in large containers has been presented by Kudrolli and Gollub [109]; four examples of the patterns observed in experiments are presented in figure 4.2.

As first shown by Edwards and Fauve [107], the addition of a second commensurate-frequency forcing component can lead to an even broader range of responses than the single frequency case, due to the introduction of a second length scale. Two-frequency forcing can give rise to superlattice patterns [191, 192], quasipatterns [107] as well as localised structures [193]. It was in these seminal experiments (see [107, figure 19]) that it was also appreciated that for large aspect ratio (the ratio of lateral size to the characteristic wavelength of the system) containers, the realised pattern is independent of the lateral boundaries. This branch of the study of Faraday waves has itself been

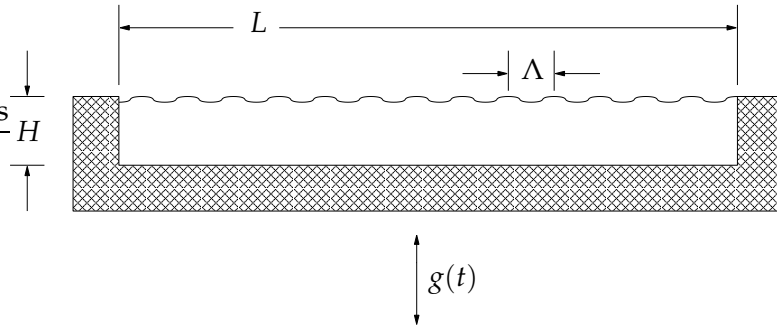


Figure 4.1: The experimental setup. An open-topped rigid container with horizontal dimension L is filled with the subject fluid to a depth H . The container is then subjected to periodic vertical acceleration $g(t)$. Subsequently, as some critical acceleration threshold is breached, standing waves of wavelength Λ appear on the surface.

the subject of considerable research; however, in this chapter, we consider only single frequency forcing; the reader is directed towards Arbell and Fineberg [192, 193, 194] for further reading regarding multi-frequency forcing.

The fact that Faraday waves have attracted so much of interest over the latter half of the twentieth century can be attributed to several causes. Foremost is the ease of experimentation, due to short characteristic timescales (of order 10^{-2} s) coupled with the ability to reach very large aspect ratios (of order 10^2) [195]. Also, adjusting the spatial and temporal timescales places only a moderate demand on the experimental setup. Along with Rayleigh–Bénard convection, Faraday waves are one of the few weakly nonlinear systems for which amplitude equations can be derived from first principles (i.e., from the Navier–Stokes equations). Thus, they provide a tractable problem for the testing of amplitude description methods as well as the techniques of bifurcation and chaos.

4.1.2 Theoretical approaches

Beginning with the work of Faraday [111] and later, Lord Rayleigh [196], a great volume of literature has been devoted to the analysis of Faraday waves (see [1, 180]). The system presents a number of theoretical challenges due to the explicit time-dependence of the forcing as well as the free-boundary nature of the problem. As a consequence, models often incorporate simplifying assumptions or approximations such as solving the linear problem by a perturbative [96] or numerical [197] scheme, or by ignoring the role of dissipation [198].

The first linear stability analysis of a vertically vibrated *inviscid* fluid layer was per-

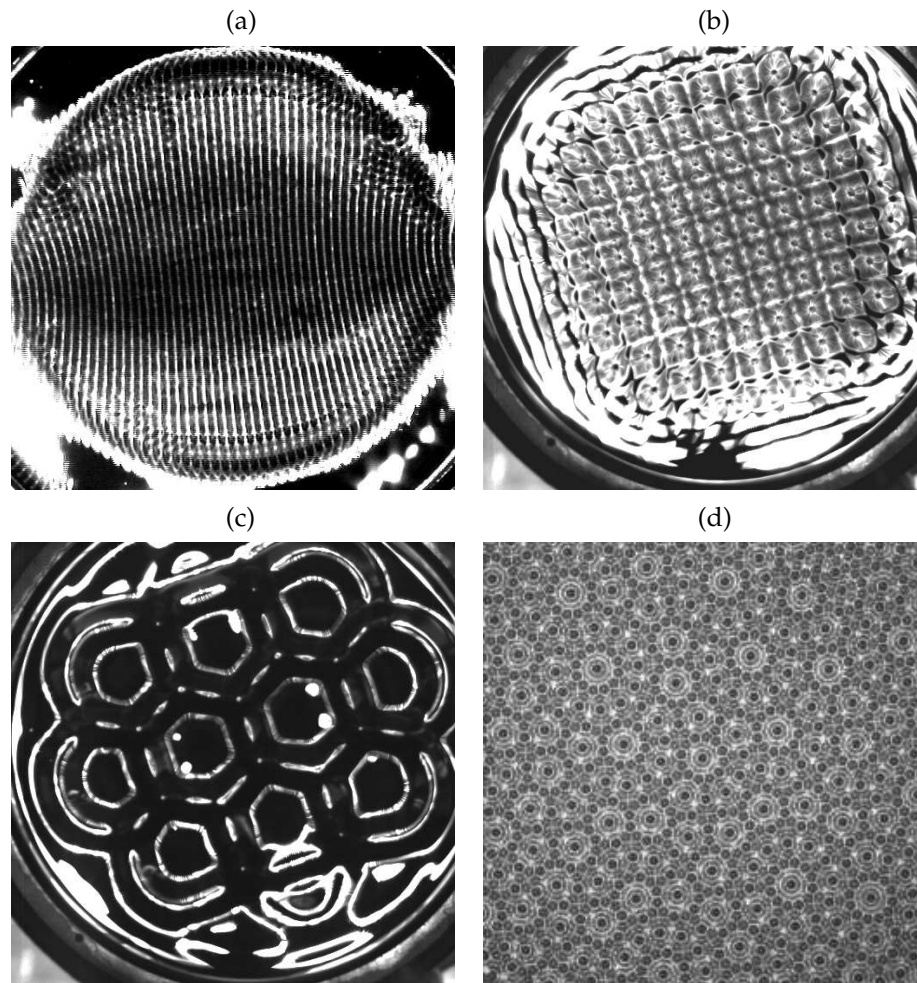


Figure 4.2: Patterns observed in the Faraday experiment: (a) stripes, (b) squares, (c) hexagons and (d) quasipatterns. (Subfigures (a),(b) and (c) are from [189] while (d) is taken from [190].)

formed by Benjamin and Ursell [198], where it was shown that the amplitude of an eigenmode obeys the Mathieu equation (as proposed by Rayleigh [196]), which supports both harmonic and subharmonic solutions. Later, Ockendon and Ockendon [199] extended this analysis to include small but finite perturbations and nonlinear terms. In the experimentally relevant situation where viscosity is included, the damping induced by viscosity is greater for the harmonic mode, and so in general, the subharmonic mode is excited first. Kumar and Tuckerman [197] were the first to derive and solve the linear stability problem for the interface of two viscous fluids subject to vertical oscillation. Through a numerical stability analysis of the Navier–Stokes and continuity equations, results were obtained which compared favourably with both ensuing laboratory [200, 201] and numerical experiments [202]. Further verification was reported by Mancebo and Vega [203] who used a Floquet analysis.

A great deal of effort has been devoted into applying weakly nonlinear theories to pattern selection in low viscosity fluids [96, 204, 205, 206, 207] and the use of amplitude equations has proved highly successful. In the standard description of parametrically forced counter-propagating waves arising at a subharmonic response, the physical variables take the form

$$\mathbf{u} = \left[A^+(X, T)e^{i\omega t + ikx} + A^-(X, T)e^{i\omega t - ikx} + \text{c.c.} \right] \mathbf{u}_0 + \dots, \quad (4.1.1)$$

where ω is half the forcing frequency and k the corresponding wavenumber, determined from the dispersion relation; \mathbf{u}_0 is the appropriate eigenfunction of a weakly unstable Faraday wave. The complex amplitudes A^\pm depend on the slow scales T and (less frequently in the analysis performed up till now) X . Sufficiently close to threshold (that is, with small $|A^\pm|$), it is found that $|A^+| \approx |A^-|$ and so one can write $(A^+, A^-) = (A, A^*)e^{i\nu}$ for some complex amplitude A and real phase ν . Hence, (4.1.1) becomes

$$\mathbf{u} = 2 \cos(\omega t + \nu) \left[A(X, T)e^{ikx} + \text{c.c.} \right] \mathbf{u}_0 + \dots. \quad (4.1.2)$$

To rephrase, at sufficiently small amplitude, the parametric forcing favours an equal superposition of counter-propagating waves that builds standing waves (SWs) as the primary pattern.

Early attempts in deriving the appropriate amplitude equations in the small viscosity limit by Miles [208, 209] and Milner [204] assumed the fluid to be inviscid and nonlinear damping terms were introduced through the heuristic addition of a dissipation function to the underlying Hamiltonian formulation. In one spatial dimension, Milner [204] supposed the appropriate equation to be (after some suitable scalings)

$$A_T = (r - r_c)A + \beta_1 \gamma^{-1} A_{XX} - \gamma \beta_2 |A|^2 A - \beta_3 \gamma^{-1} |A|^4 A, \quad (4.1.3)$$

where $\gamma \ll 1$ is the dimensionless viscosity and $r_c \sim \gamma$ is the critical value of the forcing amplitude r . This equation is valid in a close neighbourhood of the instability threshold, where $|k - k_c| \sim \gamma^2$ and $|r - r_c| \sim \gamma^3$, but closer still ($|k - k_c| \ll \gamma^2$, $|r - r_c| \ll \gamma^3$), (4.1.3) reduces down to the Ginzburg–Landau equation [210]

$$A_T = (r - r_c)A + \beta_1 \gamma^{-1} A_{XX} - \gamma \beta_2 |A|^2 A. \quad (4.1.4)$$

Up to rescaling, this is the most common equation used for theoretical analysis of the weakly nonlinear dynamics of Faraday waves. Mancebo and Vega [210] noted however, that all the above descriptions were deficient in that they neglected the full effects of a small change in wavenumber. The correct equation requires the inclusion of three

additional terms and takes the form:

$$A_T = (r - r_c)A + \beta_1 \gamma^{-1} A_{XX} - \gamma \beta_2 |A|^2 A - i\beta_3 \gamma^{-1} (|A|^2)_X A - i\beta_4 \gamma^{-1} |A|^2 A_X - \gamma \beta_5 |A|^4 A. \quad (4.1.5)$$

All terms in this equation are of the same order in the distinguished limit

$$|A|^2 \sim |\partial_x| \sim \gamma^2, \quad |r - r_c| \sim |\partial_t| \sim \gamma^3. \quad (4.1.6)$$

This equation is relevant to the analysis of §4.6 and further discussion is reserved till then. For $|r - r_c| \sim \gamma$, a description of the system behaviour in terms of SWs is no longer relevant and the two counter-propagating waves that constitute SWs must be considered separately [210].

In two spatial dimensions, the amplitude equations for N interacting SWs (ignoring modulational effects) generally take the form

$$\frac{dA_n}{dT} = (r - r_c)A_n - \sum_{m=1}^N \mathcal{P}(\cos(\theta_{nm})) |A_m|^2 A_n, \quad (4.1.7)$$

where θ_{nm} is the angle between the SWs with amplitudes A_n and A_m , and the coupling function $\mathcal{P}(\cos(\theta_{nm}))$ determines the nonlinear saturation of growth. Quadratic terms are not permitted in (4.1.7) due to the invariance of the dynamics under a shift of one period of excitation, and there is a corresponding simplification in the dynamics (no such invariance exists for multi-frequency forcing and so this case permits a wider range of pattern dynamics.) The challenge facing theorists over recent decades has been the derivation of the coupling function $\mathcal{P}(\cos(\theta))$ from first principles.

Significant progress was reported by Zhang and Viñals [96, 195, 211], where a set of amplitude equations incorporating weak viscosity were derived from the Navier–Stokes equations. This analysis was built upon a *quasi-potential* approximation, where viscosity is restricted to a thin boundary layer near the free surface and viscous effects are then incorporated through modified boundary conditions at the free surface. This model forms the basis for the work of this chapter, and a more detailed discussion is reserved for §4.2.

The weakly nonlinear theory for pattern formation not restricted to small viscosity was presented by Chen and Viñals [205]. They showed that a rotational component of the flow, which can be ignored for a linear analysis, contributes to $\mathcal{P}(\cos(\theta))$ and allows a gradient-form amplitude description to be derived. This theory has been found to show remarkable agreement with experimental results [108].

Mean flows

Aside from providing saturation, dissipation plays another important role in the behaviour of Faraday waves. Oscillatory viscous boundary layers along the rigid walls and free surface are capable of driving a large-scale mean flow (often called a ‘streaming flow’), due to nonzero (time-averaged) Reynolds stresses in the boundary layers [212]. This mean flow is then found to interact at leading-order with the SWs that drive it and should not be ignored, although it has not been treated consistently in the literature until recently. The presence of these mean modes was first brought to attention through the work of Douady et al. [213], where slowly drifting modes were observed in annular containers. Such a phenomenon could not be accounted for through the traditional framework and required the presence of mean modes in the amplitude description.

The derivation of consistent equations for Faraday waves incorporating these mean flows requires highly involved analyses. The aspect ratio L of the container plays a crucial role and the inverse ratio L^{-1} is often treated as an independent small parameter along with the dimensionless viscosity γ [212]. The case of small viscosity in moderate containers has been analysed previously by Martín et al. [214, 215] and Higuera et al. [216]. When the aspect ratio of the container is large, the behaviour is complicated further due to the existence of an additional *inviscid* mean flow; this case has been analysed by Vega et al. [212] and Lapuerta et al. [217]. The case of large aspect ratio but with arbitrary viscosity was considered by Mancebo and Vega [94], who derived three types of Ginzburg–Landau-type equations, whose applicability is dependent on the ratio between wavelength, depth and a characteristic viscous lengthscale. In regimes with low frequency forcing or shallow depth, the appropriate amplitude equations take the form (1.5.6), matching the amplitude equations derived by Matthews and Cox [74] for a stationary bifurcation in the presence of a conservation law.

4.1.3 Structure of chapter

The aim of this chapter is to examine the influence of long-wave modes in the model of Zhang and Viñals [195, 211, 218] when it is modified to account for finite depth. We begin in §4.2 with a discussion of their model equations and a brief presentation of some of the associated results. This section also details the modification we make to their model, taking into account finite depth. In §4.3, we analyse the linear problem, deriving the correct stability results and plotting the neutral curve. Subsequently, in §4.4, §4.5 and §4.6, we present three weakly nonlinear analyses: §4.4 is concerned with the

simple case of no spatial modulation, whereas §4.5 treats the full, spatially modulated problem; in §4.6, we examine a particular distinguished limit of scalings. The results of an extensive numerical investigation into the model equations are then presented in §4.7; conclusions are reserved for §4.8.

4.2 The model

We now examine the quasi-potential equations (QPEs) of Zhang and Viñals, valid for weakly damped surface waves. The underlying idea behind the quasi-potential approximation was developed by Lundgren and Mansour [219] and Ruvinsky et al. [220] for unforced surface waves. It involves assuming potential flow in the bulk and making a perturbation expansion in the small thickness of a viscous boundary layer at the fluid surface. The hydrodynamic equations can then be recast in two-dimensional, nonlocal form and expanded up to cubic order in wave steepness to yield a set of coupled equations involving only the surface displacement $h(x, t)$ and the surface velocity potential $\phi(x, t)$. The resulting equations take the form:

$$h_t = 2\nu\nabla^2 h + \hat{\mathcal{D}}\phi - \nabla \cdot (h\nabla\phi) + \frac{1}{2}\nabla^2(h^2\hat{\mathcal{D}}\phi) - \hat{\mathcal{D}}(h\hat{\mathcal{D}}\phi) + \hat{\mathcal{D}}[h\hat{\mathcal{D}}(h\hat{\mathcal{D}}\phi) + \frac{1}{2}\nabla^2 h^2\phi], \quad (4.2.1a)$$

$$\phi_t = 2\nu\nabla^2\phi + g(t)h + \frac{\Gamma}{\rho}\nabla^2 h + \frac{1}{2}(\hat{\mathcal{D}}\phi)^2 - \frac{1}{2}(\nabla\phi)^2 - (\hat{\mathcal{D}}\phi)[h\nabla^2\phi + \hat{\mathcal{D}}(h\hat{\mathcal{D}}\phi)] - \frac{\Gamma}{2\rho}\nabla \cdot (\nabla h(\nabla h)^2), \quad (4.2.1b)$$

where ν, ρ and Γ are the kinematic viscosity, density and surface tension respectively, and $\hat{\mathcal{D}}$ is a Fourier-integral operator, defined for an arbitrary function $u(\mathbf{x})$ as

$$\hat{\mathcal{D}}u(\mathbf{x}) = \int_{\mathbb{R}^2} |\mathbf{k}| \hat{u}(\mathbf{k}) \exp(i\mathbf{k} \cdot \mathbf{x}) d\mathbf{k}, \quad (4.2.2)$$

where $\hat{u}(\mathbf{k})$ is the Fourier transform of $u(\mathbf{x})$. This operator, which is often written as $\hat{\mathcal{D}} \equiv (-\nabla^2)^{1/2}$, is linear but depends nonlocally on u . The effective acceleration $g(t)$ is written as $g_0 - g_z \sin \Omega t$, where g_0 is the acceleration due to gravity, and Ω and g_z are the frequency and amplitude of the driving force, respectively. Equation (4.2.1a) is also a conservation law for h as incompressibility implies that the average level of the surface displacement is constant, that is,

$$\int_S h(\mathbf{x}, t) d\mathbf{x} = \text{constant}, \quad (4.2.3)$$

where S is the undisturbed upper surface. Note that, ignoring dissipation and forcing, solutions proportional to $e^{i\omega_0 t \pm ik_0 x}$ satisfy the dispersion relation

$$\omega_0^2 = |k_0| \left[g_0 + \frac{\Gamma}{\rho} k_0^2 \right]; \quad (4.2.4)$$

when the term g_0 dominates the sum, the mode is termed a ‘gravity wave’, while if Γ/ρ dominates, it is a ‘capillary wave’. Including dissipation, this relationship becomes

$$\omega_0^2 = |k_0| \left[g_0 + \frac{\Gamma}{\rho} k_0^2 \right] + 4i\omega_0\nu k_0^2 + 4\nu^2 k_0^4. \quad (4.2.5)$$

4.2.1 Previous results

Zhang and Viñals [96, §3.1] reported a linear stability analysis of a nondimensional version of (4.2.1), solving the linearised equations perturbatively, using the dimensionless dissipation γ as a small parameter. With $0 < \gamma \ll 1$, the stability threshold of the undisturbed state to SWs is shown to be $f = \gamma$, where f is the dimensionless forcing amplitude (see (4.2.20) for the explicit scaling relationships). In addition, the neutrally stable solutions at onset are given approximately by:

$$h(\mathbf{x}, t) = \left(\cos t + \frac{1}{4}\gamma \sin 3t + \dots \right) \sum_{j=1}^N \left[A_j(T) \exp \left(i\hat{\mathbf{k}}_j \cdot \mathbf{x} \right) + \text{c.c.} \right], \quad (4.2.6a)$$

$$\phi(\mathbf{x}, t) = \left(\sin t + \gamma \cos t + \frac{3}{4}\gamma \cos 3t + \dots \right) \sum_{j=1}^N \left[A_j(T) \exp \left(i\hat{\mathbf{k}}_j \cdot \mathbf{x} \right) + \text{c.c.} \right], \quad (4.2.6b)$$

where the $A_j = A_j(T), j = 1, \dots, N$ are slowly varying complex amplitudes and the SWs are assumed to be composed of an arbitrary set of wavevectors in two-dimensional space, each with $|\mathbf{k}_j| = 1$. A second solution to the linear problem,

$$h(\mathbf{x}, t) = \left(\sin t - \frac{1}{4}\gamma \cos 3t + \dots \right) \sum_{j=1}^N \left[B_j(T) \exp \left(i\hat{\mathbf{k}}_j \cdot \mathbf{x} \right) + \text{c.c.} \right], \quad (4.2.7a)$$

$$\phi(\mathbf{x}, t) = \left(\cos t + \gamma \sin t - \frac{3}{4}\gamma \sin 3t + \dots \right) \sum_{j=1}^N \left[B_j(T) \exp \left(i\hat{\mathbf{k}}_j \cdot \mathbf{x} \right) + \text{c.c.} \right], \quad (4.2.7b)$$

is also noted, but is found to decay with an $O(\gamma)$ growthrate and is subsequently ignored. Introducing the small parameter $\delta = (f - \gamma)\gamma^{-1}$, a complicated weakly nonlinear analysis based on the neutral solutions (4.2.6) is conducted, leading to amplitude equations of the form

$$\frac{dA_j}{dT} = \gamma A_j - \left[\gamma p(1)|A_j|^2 + \gamma \sum_{\substack{l=1 \\ l \neq j}}^N p(c_{lj})|A_l|^2 \right] A_j, \quad (4.2.8)$$

where $j = 1, \dots, N$ and $c_{jl} \equiv \cos \theta_{jl} = \mathbf{k}_j \cdot \mathbf{k}_l$. The nonlinearity function $p(c_{ij})$ is defined by a complicated expression which we do not exhibit here.

The amplitude equations (4.2.8) are of gradient form, allowing the selection of two-dimensional, spatially periodic patterns to be studied through minimisation of Lyapunov functionals. Patterns exhibiting square symmetry are predicted to be stable in

the capillary wave regime, while stable patterns of hexagonal and quasi-crystalline symmetry are forecast for mixed capillary-gravity waves. These results have been compared favourably with both numerical simulation [221] and experiment [108, 109, 183]. Furthermore, by expanding the growthrate about the critical wavenumber, the coherence length can be calculated, allowing (4.2.8) to be formally extended to an envelope equation:

$$\frac{\partial A_j}{\partial T} = \gamma A_j + \frac{1}{8}\gamma^{-1} (G_0 + 3\Gamma_0)^2 (\hat{\mathbf{k}}_j \cdot \nabla)^2 A_j - \gamma \left[p(1)|A_j|^2 + \sum_{\substack{l=1 \\ l \neq j}}^N p(c_{ij})|A_l|^2 \right] A_j, \quad (4.2.9)$$

with the usual issue of different slow scales being appropriate in different directions; the parameters G_0 and Γ_0 are nondimensional versions of the terms g_0 and Γ/ρ respectively. One difficulty associated with this model is that the linear problem cannot be fully solved analytically. Rather, in order to determine stability condition, weak dissipation and forcing must be assumed small to facilitate a weakly nonlinear investigation. This difficulty is a consequence of the sinusoidal forcing present in the model and can be eliminated through consideration of impulsive forcing. Such a venture is reported by Catllà et al. [222] who, adopting the framework introduced by Bechhoefer and Johnson [223], consider excitation in the form of N delta-function impulses. This allows the neutral curve and analytic expressions for the amplitude of surface waves to be derived exactly. The model (4.2.1) has also proved useful for testing ideas of pattern formation from a symmetry point of view [224, 225].

4.2.2 Finite depth

One of the founding principles of the theoretical description of the Faraday experiment is the conservation of fluid material. However, as observed by Edwards and Fauve [107], the common assumption of infinite depth in theoretical work prevents this conservation law from affecting the stability of long-wave modes, and an important dynamical effect is often overlooked. In this section, we adapt the model equations of Zhang and Viñals to account for Faraday waves in a finite-depth container. This modification then leads to new behaviour of the large-scale modes and, unlike the finite-depth case, they must be included in the amplitude description. Importantly, the ‘mean’ modes considered elsewhere [94, 210, 214, 215, 216, 217, 226], differ from those in the spotlight here since they are induced by oscillatory boundary layers along the rigid walls rather than a conservation law and are not large-scale in nature. Of course,

one would like to incorporate both forms of mean mode into a model; however, for simplicity and in keeping with the spirit of this thesis, we ignore mean flows driven by the viscous boundary layers and concentrate purely on the implications of a conservation law.

We modify the derivation of Zhang and Viñals [96] concomitant with the work of Craig and Sulem [227] and Guyenne and Nicholls [228] on surface water waves in channels with finite depth. We adopt the derivation of Zhang and Viñals [96, pages 303–305] up to the casting of the quasi-potential equations into nonlocal form, governing the evolution of the surface height $h(x, t)$ and the surface velocity potential $\phi(x, t)$. At this stage, we restrict our attention to one-dimensional dynamics, which allows the model to be written as:

$$\partial_t h = 2\nu h_{xx} + (1 + (h_x)^2)^{1/2} \partial_n \phi, \quad (4.2.10a)$$

$$\begin{aligned} \partial_t \phi = 2\nu \phi_{xx} - \frac{1}{2} (\phi_x)^2 + \frac{[(1 + (h_x)^2)^{1/2} \partial_n \phi + \phi_x h_x]^2}{2[1 + (h_x)^2]} \\ + g(t)h + \frac{\Gamma}{\rho} \partial_x \left(\frac{h_x}{(1 + (h_x)^2)^{1/2}} \right), \end{aligned} \quad (4.2.10b)$$

where $\partial_n \phi$ is the normal derivative of ϕ . The normal derivative of ϕ at the boundary is related to the value of ϕ at the boundary by the Dirichlet–Neumann operator $\hat{\mathcal{G}}(h)$

$$\hat{\mathcal{G}}(h)\phi(x, t) = (1 + h_x^2)^{1/2} \partial_n \phi. \quad (4.2.11)$$

The analyticity of this operator has been studied previously (see [228] and references therein) with the important result that $\hat{\mathcal{G}}$ can be written as a convergent Taylor expansion

$$\hat{\mathcal{G}}(\epsilon h) = \sum_{n=0}^{\infty} \epsilon^n \hat{\mathcal{G}}^{(n)}(h), \quad (4.2.12)$$

for sufficiently small ϵ and where the first three operators are:

$$\hat{\mathcal{G}}^{(0)} \equiv D \tanh(HD), \quad (4.2.13a)$$

$$\hat{\mathcal{G}}^{(1)} \equiv DhD - \hat{\mathcal{G}}^{(0)} h \hat{\mathcal{G}}^{(0)}, \quad (4.2.13b)$$

$$\hat{\mathcal{G}}^{(2)} \equiv \frac{1}{2} \left(\hat{\mathcal{G}}^{(0)} Dh^2 D - D^2 h^2 \hat{\mathcal{G}}^{(0)} - 2\hat{\mathcal{G}}^{(0)} h \hat{\mathcal{G}}^{(1)} \right), \quad (4.2.13c)$$

and D is an operator defined by $D \equiv -i\partial_x$. We can thus write $\hat{\mathcal{G}}$ as the truncated series (cf. [96, equation 2.21])

$$\begin{aligned} \hat{\mathcal{G}}\phi(x, t) = \hat{\mathcal{E}}\phi - \nabla \cdot (h\nabla\phi) - \hat{\mathcal{E}}(h\hat{\mathcal{E}}\phi) + \hat{\mathcal{E}}[h\hat{\mathcal{E}}(h\hat{\mathcal{E}}\phi) + \frac{1}{2}h^2\nabla^2\phi] \\ + \frac{1}{2}\nabla^2(h^2\hat{\mathcal{E}}\phi) - \nabla^2\left[\frac{1}{2}h^2\hat{\mathcal{E}}(h\hat{\mathcal{E}}\phi) + \frac{1}{3}h^3\nabla^2\phi\right], \end{aligned} \quad (4.2.14)$$

where $\hat{\mathcal{E}}$ is a linear Fourier-integral operator, defined for an arbitrary function $u(x)$ as

$$\hat{\mathcal{E}}u(x) = \int_{-\infty}^{\infty} k \tanh(kH) \hat{u}(k) e^{ikx} dk. \quad (4.2.15)$$

Note that the operation of $\hat{\mathcal{D}}$ —given in (4.2.2)—is recovered in the limit of $H \rightarrow \infty$. Thus, our model equations (in dimensional form) are:

$$\begin{aligned} h_t &= 2v h_{xx} + \hat{\mathcal{E}}\phi - (h\phi_x)_x + \frac{1}{2}(h^2 \hat{\mathcal{E}}\phi)_{xx} - \hat{\mathcal{E}}(h\hat{\mathcal{E}}\phi) \\ &\quad + \hat{\mathcal{E}} \left[h\hat{\mathcal{E}}(h\hat{\mathcal{E}}\phi) + \frac{1}{2}(h^2\phi)_{xx} \right], \end{aligned} \quad (4.2.16a)$$

$$\begin{aligned} \phi_t &= 2v\phi_{xx} + g(t)h + \frac{\Gamma}{\rho} h_{xx} + \frac{1}{2}(\hat{\mathcal{E}}\phi)^2 - \frac{1}{2}\phi_x^2 \\ &\quad - (\hat{\mathcal{E}}\phi) \left[h\phi_{xx} + \hat{\mathcal{E}}(h\hat{\mathcal{E}}\phi) \right] - \frac{\Gamma}{2\rho} (h_x^3)_x. \end{aligned} \quad (4.2.16b)$$

Nondimensionalisation

We now introduce scalings to nondimensionalise the system (4.2.16). Before we proceed, let us first examine the effect rescaling has on the new Fourier operator $\hat{\mathcal{E}}$. Rescaling length as $x = X_0 x^*$, where X_0 is some scaling factor to be determined later, the Fourier transform of a variable $u(x)$ becomes

$$\begin{aligned} \hat{u}(k) &\equiv \int_{-\infty}^{\infty} u(x) e^{-ikx} dx, \\ &\equiv \int_{-\infty}^{\infty} u(x^*) e^{-ikX_0 x^*} X_0 dx^*, \\ &\equiv X_0 \int_{-\infty}^{\infty} u(x^*) e^{-ik^* x^*} dx^*, \quad \text{where } k^* = X_0 k, \\ &\equiv X_0 \hat{u}(k^*). \end{aligned} \quad (4.2.17)$$

Subsequently, we can expand the action of $\hat{\mathcal{E}}$:

$$\begin{aligned} \hat{\mathcal{E}}u(x) &\equiv \int_{-\infty}^{\infty} k \tanh(Hk) \hat{u}(k) e^{ikx} dk, \\ &\equiv \int_{-\infty}^{\infty} \left(\frac{k^*}{X_0} \right) \tanh\left(\frac{Hk^*}{X_0} \right) X_0 \hat{u}(k^*) e^{ik^* x^*} \left(\frac{1}{X_0} \right) dk^*, \quad \text{using (4.2.17),} \\ &\equiv \frac{1}{X_0} \int_{-\infty}^{\infty} k^* \tanh(H^* k^*) e^{ik^* x^*} dk^*, \quad \text{where } H^* = H/X_0, \\ &\equiv \frac{1}{X_0} \hat{\mathcal{E}}u(x^*). \end{aligned} \quad (4.2.18)$$

We now carry out a nondimensionalisation. Adopting the conventions of Zhang and Viñals [96], we choose $2/\Omega \equiv 1/\omega_0$ as the unit of time, ω_0/k_0^2 as the unit measure for ϕ and $X_0 = 1/k_0$ as the unit of length, where k_0 is related to ω_0 by the dispersion relation

$$\omega_0^2 = k_0 \tanh(Hk_0) \left[g_0 + \frac{\Gamma}{\rho} k_0^2 \right]. \quad (4.2.19)$$

Next, we define the following dimensionless parameters:

$$\gamma \equiv \frac{2\nu k_0^2}{\omega_0}, \quad G_0 \equiv \frac{g_0 k_0}{\omega_0^2}, \quad \Gamma_0 \equiv \frac{\Gamma k_0^3}{\rho \omega_0^2}, \quad f \equiv \frac{g_z k_0}{4\omega_0^2}, \quad (4.2.20)$$

which facilitate the simplification of the quasi-potential equations (4.2.16) to

$$h_t = \gamma h_{xx} + \hat{\mathcal{E}}\phi - (h\phi_x)_x + \frac{1}{2}(h^2 \hat{\mathcal{E}}\phi)_{xx} - \hat{\mathcal{E}}(h\hat{\mathcal{E}}\phi) + \hat{\mathcal{E}}[h\hat{\mathcal{E}}(h\hat{\mathcal{E}}\phi) - \frac{1}{2}h^2\phi_{xx}], \quad (4.2.21a)$$

$$\phi_t = \gamma\phi_{xx} - (G_0 - \Gamma_0\partial_x^2)h - 4fh \sin 2t + \frac{1}{2}(\hat{\mathcal{E}}\phi)^2 - \frac{1}{2}\phi_x^2 - (\hat{\mathcal{E}}\phi)[h\phi_{xx} + \hat{\mathcal{E}}(h\hat{\mathcal{E}}\phi)] - \frac{1}{2}\Gamma_0(h_x^3)_x. \quad (4.2.21b)$$

These are the model equations upon which the rest of the work in this chapter is based. Note that, by construction,

$$G_0 + \Gamma_0 = \coth H \quad (4.2.22)$$

(cf. the corresponding result for the model (4.2.1), $G_0 + \Gamma_0 = 1$).

4.2.3 Large-scale modes

In the system (4.2.21), the inviscid dispersion relation for modes of form $e^{i\omega t + ikx}$ is

$$\omega^2 = k \tanh(Hk) [G_0 + \Gamma_0 k^2]. \quad (4.2.23)$$

In figure 4.3, we compare the behaviour of this relationship with the infinite-depth case for a range of values of G_0 . Note that for both cases, by construction, the wavenumber of subharmonic modes ($\omega = 1$) is always $k = 1$, while harmonic modes ($\omega = 2$) are spread over a range of k values depending on the value of G_0 . The key difference between the infinite- and finite-depth cases can be seen in the behaviour of large-scale ($k \approx 0$) modes. One can observe that for $G_0 \neq 0$ in the finite-depth case (figure 4.3d), the dispersion of large-scale modes is linear whilst for infinite depth, ω scales with $k^{1/2}$. This behaviour plays a key role in the construction of amplitude equations.

Continuing in this theme, consider the growth rate λ of perturbations of the form $e^{\lambda t + ikx}$, which is defined by

$$\lambda^2 = -k \tanh Hk [G_0(1 - k^2) + k^2 \coth H]. \quad (4.2.24)$$

In the long-wave ($k \rightarrow 0$) limit, we find

$$\lambda^2 \approx -G_0 H k^2 + [G_0 (H + \frac{1}{3}H^3) - H \coth H] k^4 + O(k^6), \quad (4.2.25)$$

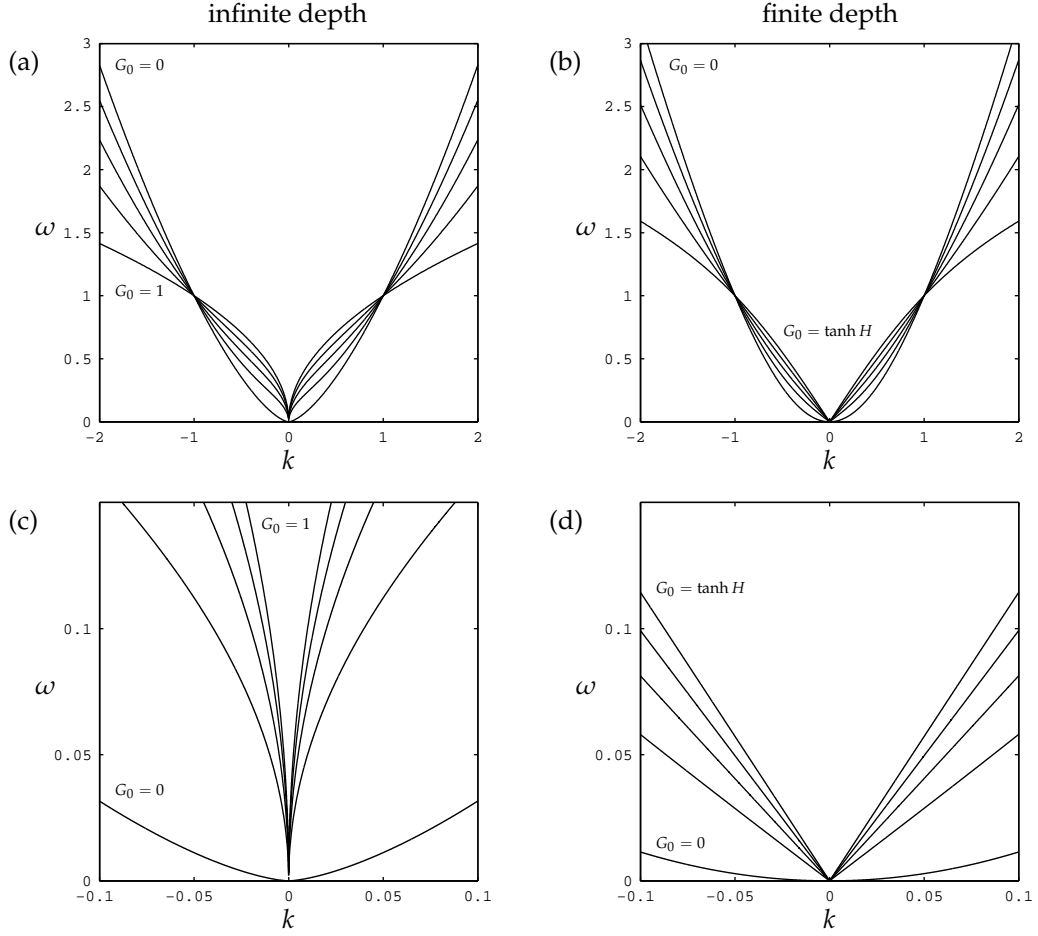


Figure 4.3: The dispersion relations for Faraday waves in containers with (a),(c) infinite depth and (b),(d) finite depth; the subfigures (c) and (d) are magnifications of (a) and (b) respectively. Each plot shows the frequency ω against wavenumber k for a range of G_0 values ($H = 1$ is used in (b) and (d)).

and so large-scale modes always have oscillatory growth at leading order. Moreover, when we expand (4.2.25) to give expressions for λ , we need to distinguish between two cases: gravity-capillary waves ($G_0 \neq 0$) and pure capillary waves ($G_0 = 0$):

$$\lambda|_{G_0 \neq 0} = \pm i(G_0 H)^{1/2} k + O(k^3), \quad (4.2.26a)$$

$$\lambda|_{G_0 = 0} = \pm i(H \coth H)^{1/2} k^2 + O(k^4). \quad (4.2.26b)$$

These forms of large-scale growth are unlike any of the other large-scale modes considered so far in this thesis. For gravity-capillary waves, large-scale modes behave in a wave-like manner, with λ linearly dependent on k . On the other hand, large-scale modes in the capillary regime evolve by a symmetric oscillatory growth rate. Including dissipation, λ is defined by

$$\lambda^2 + 2k^2 \gamma \lambda + k^4 \gamma^2 + k \tanh(Hk) [G_0(1 - k^2) + k^2 \coth H] = 0 \quad (4.2.27)$$

which gives rise to the solutions

$$\lambda|_{G_0 \neq 0} = \pm i(G_0 H)^{1/2} k - \gamma k^2 + O(k^3), \quad (4.2.28a)$$

$$\lambda|_{G_0=0} = \left(-\gamma \pm i(H \coth H)^{1/2} \right) k^2 + O(k^4), \quad (4.2.28b)$$

where we now see a viscous contribution to the leading-order behaviour of capillary waves; the leading-order behaviour of mixed capillary–gravity waves remains the same. For comparative purposes, we note that the corresponding large-scale growth rates in the infinite-depth case are:

$$\lambda|_{G_0 \neq 0} = \pm i \sqrt{G_0} k^{1/2} \mp \frac{if^2}{\sqrt{G_0}} k^{3/2} - \gamma k^2 + O(k^{5/2}), \quad (4.2.29)$$

$$\lambda|_{G_0=0} = \pm i \sqrt{2} \gamma k + \left(-\gamma + i \gamma^2 + \frac{i \Gamma_0}{2\sqrt{2} \gamma} \right) k^2 + O(k^3). \quad (4.2.30)$$

4.3 Solutions of the linear problem

In this section, we consider the linearised problem arising from the system (4.2.21). It is well known that the linear equation governing a parametric instability of surface waves takes the form of a damped Mathieu equation [198], for which Faraday waves correspond to a subharmonic resonance. Although this Mathieu equation is linear, it has time-dependent coefficients and cannot be solved exactly. Thus, the usual procedure of a weakly nonlinear analysis (see §1.2.3), where the linear problem admits an exact solution, cannot be employed. Rather, we must solve the linear problem perturbatively, using the dissipation and driving amplitude as small parameters. Our analytic method here follows closely that of Zhang and Viñals [96, §3.2].

By linearising the quasi-potential system (4.2.21) with respect to the surface displacement h and surface velocity potential ϕ , then transforming to Fourier space (where k is the wavenumber), we obtain

$$\hat{h}_t = -\gamma k^2 \hat{h} + k \tanh(kH) \hat{\phi}, \quad (4.3.1a)$$

$$\hat{\phi}_t = -\gamma k^2 \hat{\phi} - [G_0 + 4f \sin(2t)] \hat{h} - k^2 \Gamma_0 \hat{h}. \quad (4.3.1b)$$

Subsequently, a little manipulation yields the damped Mathieu equation,

$$\hat{h}_{tt} + 2\gamma k^2 \hat{h}_t + \hat{h} \left[k^4 \gamma^2 + k \tanh(kH) (G_0 + 4f \sin(2t) + k^2 \Gamma_0) \right] = 0. \quad (4.3.2)$$

For nonzero γ , it is well known that the first solution to become unstable in this equation is the subharmonic response (composed of the mode with half the driving frequency). Later in this section, we derive such a solution; however, it is instructive at this stage to digress briefly, and examine the implications of subharmonic solutions to (4.3.2).

Subharmonic modes: We can examine the properties of the subharmonic resonance in (4.3.2) when it is neutrally stable by setting $\hat{h} = \sin t$, and integrating over a single period. This yields the relationship

$$k^4 \gamma^2 + k \tanh(kH) (G_0 + k^2 \Gamma_0) = 1. \quad (4.3.3)$$

For weakly dissipative fluids ($0 < \gamma \ll 1$), and to be consistent with the quasi-potential approximation, we neglect terms proportional to γ^2 . Thus, subharmonic waves have wavenumber k satisfying

$$k \tanh(kH) (G_0 + k^2 \Gamma_0) = 1, \quad (4.3.4)$$

which, via (4.2.22), has solution $k = 1$. We draw attention however, to the fact that setting $k = 1$ is only an approximation to the wavenumber of a marginal mode; including small dissipation, k can be expanded as

$$k = 1 - \gamma^2 (1 + 2\Gamma_0 \tanh H + 2 \operatorname{csch}(2H))^{-1} + O(\gamma^4). \quad (4.3.5)$$

The nonlinear analysis described below is based on the solution (4.3.25) which has wavenumber $k = 1$. However, this mode is only neutrally stable in the inviscid limit ($\gamma = 0$); with weak dissipation, the growthrate λ of unforced modes of form $e^{\lambda t + i x}$ is $\lambda = -\gamma + i$. Importantly, this expansion contains $O(\gamma)$ corrections, which play a key role in the nonlinear behaviour detailed in §4.5.

For near-subharmonic resonance, we seek analytic solutions of (4.3.2) perturbatively in the limit of weak dissipation. If we retain only leading-order terms in γ and set $k = 1$ in (4.3.2), then we find an undamped Mathieu equation of the form

$$\hat{h}_{tt} + \hat{h} [1 + 4f \tanh H \sin 2t] = 0, \quad (4.3.6)$$

and by introducing $\tau = 2t + \frac{\pi}{2}$, we can write (4.3.6) as

$$\hat{h}_{\tau\tau} + \hat{h} \left[\frac{1}{4} + f \tanh H \cos \tau \right] = 0. \quad (4.3.7)$$

From the well-known theory for a Mathieu equation in canonical form,

$$\ddot{x} + [c_1 + c_2 \cos t]x = 0, \quad (4.3.8)$$

we know that the transition lines for solutions to (4.3.8) with period 4π in τ (which correspond to solutions to (4.3.6) with period 2π in t) pass through the point $(c_1, c_2) = (\frac{1}{4}, 0)$ [9, §9.4]. Hence, in the limit of vanishing dissipation, the condition for subharmonic solutions to (4.3.6) to be neutrally stable is $f = 0$. Thus, in our weakly dissipative framework where γ is small, we must also treat the driving amplitude, f , as a small parameter.

We now consider solutions to the linear equations (4.3.1) through a perturbation analysis using the weak dissipation to provide a small parameter. Thus, let us introduce a book-keeping parameter $0 < \chi \ll 1$ and set $\gamma = \chi\gamma_1$. In addition, motivated by the above considerations, we also set $f = \chi f_1$. We expand \hat{h} and k as series in χ :

$$\hat{h} = \hat{h}_0 + \chi \hat{h}_1 + \chi^2 \hat{h}_2 + \dots, \quad (4.3.9a)$$

$$k = 1 + \chi k_1 + \chi^2 k_2 + \dots, \quad (4.3.9b)$$

where $\hat{h}_0, \hat{h}_1, \dots$ are functions of both t and a slow time-scale $T_1 = \chi t$. In addition, we use the Taylor expansion of $\tanh(kH)$:

$$\tanh(kH) = \tanh H + \chi k_1 H \operatorname{sech}^2(H) + \dots. \quad (4.3.10)$$

At leading order, we find the analytically tractable problem,

$$(\partial_t^2 + 1)\hat{h}_0 = 0, \quad (4.3.11)$$

which has general solution

$$\hat{h}_0 = A \cos t + B \sin t, \quad (4.3.12)$$

where A and B are complex amplitudes, dependent on T_1 . Subsequently at $O(\chi)$, solvability conditions (see §1.2.10) must be applied to avoid unbounded growth of certain ('secular') terms in the perturbation expansion. Since the operator $(\partial_t^2 + 1)$ is self-adjoint, the adjoint solutions to (4.3.11) are of the same form as (4.3.12) and so solvability conditions are imposed by simply setting the coefficients of $\sin t$ and $\cos t$ to zero. This yields a pair of evolution equations for the amplitudes A and B :

$$A_{T_1} = A [f_0 \tanh H - \gamma_0] + \frac{1}{2} k_1 B \left[\tanh H (G_0 + 3\Gamma_0) + H \operatorname{sech}^2 H (G_0 + \Gamma_0) \right], \quad (4.3.13a)$$

$$B_{T_1} = -B [f_0 \tanh H + \gamma_0] - \frac{1}{2} k_1 A \left[\tanh H (G_0 + 3\Gamma_0) + H \operatorname{sech}^2 H (G_0 + \Gamma_0) \right]. \quad (4.3.13b)$$

Solutions to (4.3.13) proportional to $e^{\lambda t}$ are defined by the growth rates

$$\lambda_{\pm} = -\gamma_1 \pm (a_1 - a_2)^{1/2}, \quad (4.3.14)$$

where

$$a_1 = f_1^2 \tanh^2 H, \quad (4.3.15a)$$

$$a_2 = \frac{1}{4} k_1^2 \left[\tanh^2 H (G_0 + 3\Gamma_0)^2 + H^2 \operatorname{sech}^2 H (G_0 + \Gamma_0)^2 + 2H \operatorname{sech}^2 H \tanh H (G_0 + 3\Gamma_0)(G_0 + \Gamma_0) \right], \quad (4.3.15b)$$

and thus there is a growing mode (with growthrate λ_+) and a decaying mode. Setting $k_1 = 0$, these growthrates simplify to

$$\lambda_{\pm} = -\gamma_1 \pm f_1 \tanh H, \quad (4.3.16)$$

from which we easily read off the instability condition for subharmonic modes:

$$f_1 > \gamma_1 \coth H. \quad (4.3.17)$$

Hence, as the layer depth is decreased, the required forcing amplitude to drive instability is increased. Expressed differently, the deeper a layer, the less stable it is to parametric forcing.

Considering the balance of terms at this order, we find the particular solution for \hat{h}_1 to be

$$\hat{h}_1 = \frac{1}{4}f_1 \tanh(H) [A \sin 3t - B \cos 3t] + C \cos t + D \sin t, \quad (4.3.18)$$

where $C = C(T)$ and $D = D(T)$ are undetermined complex amplitudes, required to balance higher-order terms. At $O(\chi^2)$, applying solvability conditions yields the following evolution equations for C and D :

$$C_{T_1} = C(f_1 \tanh H - \gamma_1) + \frac{1}{2}k_1 \left(\tanh H(G_0 + 3\Gamma_0) + H \operatorname{sech}^2 H(G_0 + \Gamma_0) \right) D - k_1 \left(2\gamma_1 - f_1(\tanh H + H \operatorname{sech}^2 H) \right) A + \mathcal{G}(\gamma_1^2, f_1^2, k_1^2, G_0, \Gamma_0, B), \quad (4.3.19a)$$

$$D_{T_1} = -D(f_1 \tanh H + \gamma_1) - \frac{1}{2}k_1 \left(\tanh H(G_0 + 3\Gamma_0) + H \operatorname{sech}^2 H(G_0 + \Gamma_0) \right) C - k_1 \left(2\gamma_1 - f_1(\tanh H + H \operatorname{sech}^2 H) \right) B - \mathcal{G}(\gamma_1^2, f_1^2, k_1^2, G_0, \Gamma_0, A), \quad (4.3.19b)$$

where \mathcal{G} is a complicated function, omitted here for simplicity. We note that, for waves with wavenumber $k = 1$ (hence $k_1 = 0$) at threshold ($f_1 = \gamma_1 \coth H$), (4.3.19) reduces to

$$C_{T_1} = \frac{3}{4}\gamma_1^2 B, \quad (4.3.20a)$$

$$D_{T_1} = -2\gamma_1 D_1 - \frac{3}{4}\gamma_1^2 A. \quad (4.3.20b)$$

As described below, these equations are essential to deriving the correct linear solution.

We now construct the corresponding solution for ϕ by substituting the expansions (4.3.9), (4.3.10) and $\hat{\phi} = \hat{\phi}_0 + \chi\hat{\phi}_1 + \dots$ into (4.3.1a) and solving at successive orders of χ . This leads to the solutions

$$\hat{\phi}_0 = -A \coth H \sin t + B \coth H \cos t \quad (4.3.21)$$

and

$$\begin{aligned}\hat{\phi}_1 = & \frac{3}{4}f_1 \cos(3t)A + \frac{3}{4}f_1 \sin(3t)B \\ & + \coth H \sin t [(1 + H \coth H - H \tanh H)A + \gamma_1 B - C + B_{T_1}] \\ & + \coth H \cos t [-(1 + H \coth H - H \tanh H)B + \gamma_1 A + D + A_{T_1}].\end{aligned}\quad (4.3.22)$$

Combining our expressions for $\hat{h}_0, \hat{h}_1, \hat{\phi}_0, \hat{\phi}_1$, we can form an approximate linear solution for the behaviour near the subharmonic resonance. If we restrict attention to the mode with $k_1 = 0$ at onset ($f_1 = \gamma_1 \coth H$), then this linear solution takes the form

$$\hat{h} = (\cos t + \frac{1}{4}\gamma_1 \sin 3t) A + (\sin t - \frac{1}{4}\gamma_1 \cos 3t) B + C \cos t + D \sin t, \quad (4.3.23a)$$

$$\begin{aligned}\hat{\phi} = & \coth H (-\sin t + \gamma_1 \cos t + \frac{3}{4}\gamma_1 \cos 3t) A + (\cos t - \gamma_1 \sin t + \frac{3}{4}\gamma_1 \sin 3t) B \\ & - C \coth H \sin t + D \coth H \cos t.\end{aligned}\quad (4.3.23b)$$

Now, imposing the same conditions, $k_1 = 0$ and $f_1 = \gamma_1 \coth H$, on the evolution equations (4.3.13), we find

$$A_{T_1} = 0, \quad (4.3.24a)$$

$$B_{T_1} = -2\gamma_1. \quad (4.3.24b)$$

From (4.3.24a), we see that the mode proportional to A is neutrally stable, while (4.3.24b) indicates that the B -mode decays weakly. For the analysis of this chapter, we restrict our attention to the neutrally stable mode, and thus set $B = 0$. From (4.3.20a), we can set $C = 0$ as it is no longer driven by the primary modes and simply renormalises A ; choosing $D = -\frac{3}{8}\gamma_1 A$ satisfies (4.3.20b). Thus the linear solution, in physical space, takes the form (cf. (4.2.6b)),

$$h_{\text{lin}} = (\cos t + \frac{1}{4}\gamma \sin 3t - \frac{3}{8}\gamma \sin t) (Ae^{ix} + A^*e^{-ix}), \quad (4.3.25a)$$

$$\phi_{\text{lin}} = \coth H (-\sin t + \frac{5}{8}\gamma \cos t + \frac{3}{4}\gamma \cos 3t) (Ae^{ix} + A^*e^{-ix}). \quad (4.3.25b)$$

In the analysis of Zhang and Viñals [96], the (corresponding) term proportional to D in (4.3.23) was omitted; however, it is important that this term is included as it contributes to the coefficients in the amplitude equations; higher-order terms in γ can be neglected as they do not.

4.3.1 Numerically solving the linear problem

We now complement our perturbation analysis by numerically solving the linear stability problem. We determine the neutral curve by rewriting the Mathieu equation (4.3.2)

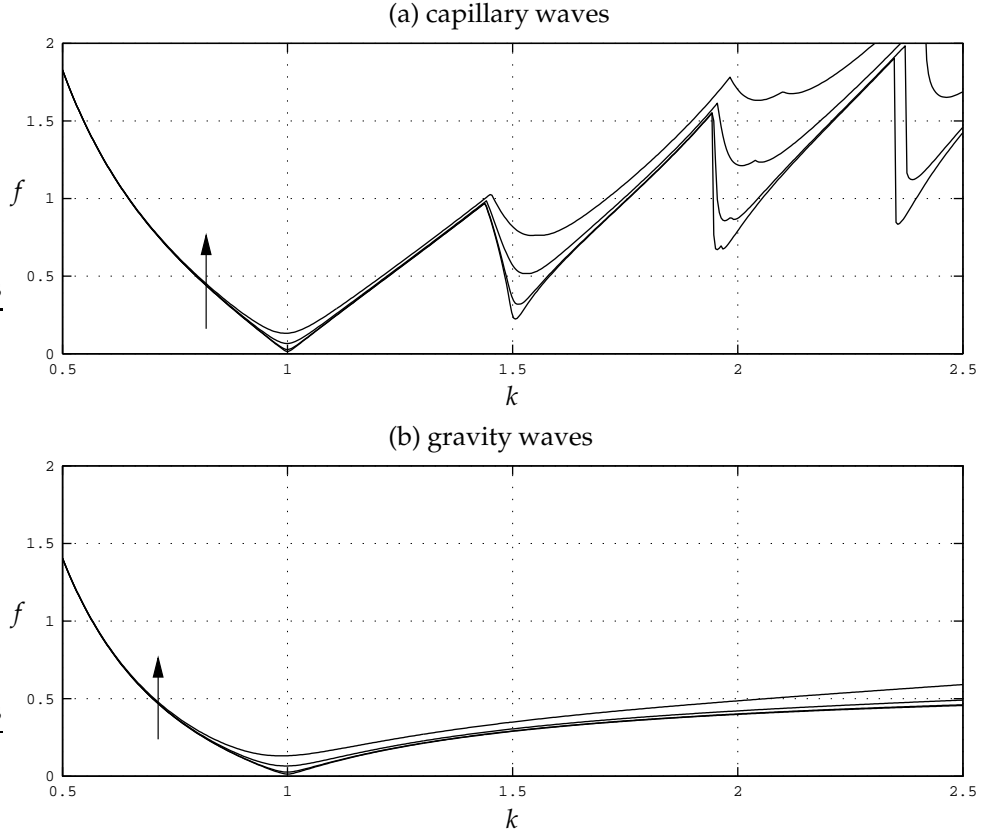


Figure 4.4: The neutral curves for (a) capillary waves ($G_0 = 0$) and (b) gravity waves ($G_0 = \coth H$) for various values of γ and $H = 1$. The dissipation parameter γ takes the values 0.01, 0.02, 0.05 and 0.1 (from bottom to top respectively).

as follows. First we rewrite (4.3.2) as a system of two first order equations:

$$h_t = g, \quad (4.3.26a)$$

$$g_t = -z_1 g - z_2 h - z_3 \sin(2t)h, \quad (4.3.26b)$$

where hats have been dropped and

$$z_1 = 2\gamma k^2, \quad (4.3.27a)$$

$$z_2 = k^4 \gamma^2 + k \tanh(kH) k^2 \Gamma_0 + G_0, \quad (4.3.27b)$$

$$z_3 = 4k \tanh(kH) f. \quad (4.3.27c)$$

We now specify that $h = \tilde{h}(t)e^{\lambda t}$ and $g = \tilde{g}(t)e^{\lambda t}$ where $\tilde{h}(t+1) = \tilde{h}(t)$ and $\tilde{g}(t+1) = \tilde{g}(t)$ for all t , and hence we may introduce the Fourier series

$$\tilde{h} = \frac{1}{2}a_0 + \sum_{n=1}^{\infty} [a_n \cos nt + b_n \sin nt], \quad (4.3.28a)$$

$$\tilde{g} = \frac{1}{2}c_0 + \sum_{n=1}^{\infty} [c_n \cos nt + d_n \sin nt], \quad (4.3.28b)$$

and note that

$$e^{-\lambda t} h_t = \frac{1}{2} \lambda a_0 + \sum_{n=1}^{\infty} [(\lambda a_n + n b_n) \cos nt + (\lambda b_n - n a_n) \sin nt],$$

$$e^{-\lambda t} g_t = \frac{1}{2} \lambda c_0 + \sum_{n=1}^{\infty} [(\lambda c_n + n d_n) \cos nt + (\lambda d_n - n c_n) \sin nt],$$

$$e^{-\lambda t} \sin(2t) h = \frac{1}{2} b_0 + \frac{1}{2} (b_1 + b_3) \cos t + \frac{1}{2} b_4 \cos 2t + \frac{1}{2} (a_1 - a_3) \sin t + \frac{1}{2} (a_0 - a_4) \sin 2t \\ + \frac{1}{2} \sum_{n=3}^{\infty} (b_{n+2} - b_{n-2}) \cos nt + \frac{1}{2} \sum_{n=3}^{\infty} (a_{n-2} - a_{n+2}) \sin nt.$$

Thus, equating coefficients of the various Fourier components, we see that

$$c_0 = \lambda a_0, \quad (4.3.29a)$$

$$c_n = \lambda a_n + n b_n \quad \text{for } n > 0, \quad (4.3.29b)$$

$$d_n = \lambda b_n - n a_n \quad \text{for } n > 0, \quad (4.3.29c)$$

$$\lambda c_0 = -z_1 c_0 - z_2 a_0 - z_3 b_2, \quad (4.3.29d)$$

$$\lambda c_1 + d_1 = -z_1 c_1 - z_2 a_1 - \frac{1}{2} z_3 (b_1 + b_3), \quad (4.3.29e)$$

$$\lambda c_2 + 2d_2 = -z_1 c_2 - z_2 a_2 - \frac{1}{2} z_3 b_4, \quad (4.3.29f)$$

$$\lambda c_n + n d_n = -z_1 c_n - z_2 a_n - \frac{1}{2} z_3 (b_{n+2} - b_{n-2}) \quad \text{for } n > 2, \quad (4.3.29g)$$

$$\lambda d_1 - c_1 = -z_1 d_1 - z_2 b_1 - \frac{1}{2} z_3 (a_1 - a_3), \quad (4.3.29h)$$

$$\lambda d_n - n c_n = -z_1 d_n - z_2 b_n - \frac{1}{2} z_3 (a_{n-2} - a_{n+2}) \quad \text{for } n > 1. \quad (4.3.29i)$$

After truncating the Fourier series at n terms in the sum, we can rewrite (4.3.29) as the eigenvalue problem

$$\mathbf{A} \mathbf{x} = \lambda \mathbf{x}, \quad (4.3.30)$$

where \mathbf{x} is the $(4n + 2) \times 1$ vector of form

$$\mathbf{x} = (a_0, \dots, a_n, b_1, \dots, b_n, c_0, \dots, c_n, d_1, \dots, d_n)^\top, \quad (4.3.31)$$

and \mathbf{A} is the $(4n + 2) \times (4n + 2)$ matrix describing the linear equations (4.3.29). Numerically solving (4.3.30) now allows us to find neutral curves for the system (4.3.2). We do this by fixing k and using a bisection method to determine the critical value of f , where the eigenvalue λ passes through zero. Figure 4.4 illustrates the neutral curves for the pure gravity and capillary regimes for various γ values; intermediate values of G_0 interpolate between these two limits. We see that in both regimes, subharmonic modes (which have $k \approx 1$) are the first to lose stability; the subsequent minima in figure 4.4 (a) correspond to harmonic and then higher order responses.

4.4 Nonlinear analysis I: Spatially uniform amplitudes

In this section, we derive an amplitude equation for weakly nonlinear SW solutions to the model equations (4.2.21) in which spatial modulation is neglected. Such an approach is in correspondence with the derivation exhibited by Zhang and Viñals [96, §3.2], although, as we are only considering one spatial dimension, the details are more straightforward here. Neglecting spatial modulation also obviates consideration of large-scale modes here, and the consequences of the conservation law (4.2.3) for the dynamics of these modes will not be apparent. Nevertheless, this analysis remains important for two reasons. Firstly, this section contains an important derivation of solvability conditions, applicable to the modulational problem. These conditions correct those of Zhang and Viñals [96, equation (3.32)], who use a simpler but ultimately inconsistent condition. Secondly, this section also sets several notational precedents that are adopted throughout the rest of this chapter.

For the analysis of this section and its successor §4.5, we follow an analogous procedure to Zhang and Viñals [96], adopting the convention of using two independent small parameters. We introduce $0 < \epsilon \ll 1$ to parameterise the difference between the forcing amplitude and its critical value (c.f. (4.4.1)), as well as facilitating expansions in the surface height and flow potential. In addition, following the paradigmatic linear analysis of §4.3, we treat the dimensionless viscosity γ as a small quantity to allow the various $O(\epsilon^n)$ problems to be solved perturbatively. This somewhat ad hoc technique assumes that whilst γ is significantly greater than ϵ , it is also small enough to neglect $O(\gamma^2)$ terms at each order of ϵ . An alternative (and less ad hoc) procedure is adopted in §4.6, where ϵ is explicitly defined in terms of γ .

We begin by setting the forcing amplitude f to a slightly supercritical value:

$$f = \gamma \coth H + \epsilon^2 f_2, \quad (4.4.1)$$

ensuring subharmonic SWs are neutrally stable. Additionally, we introduce a slow timescale $T = \epsilon^2 t$ and expand the field variables as

$$h(x, t, T) = \sum_{n=1} \epsilon^n h_n(x, t, T), \quad (4.4.2a)$$

$$\phi(x, t, T) = \Phi_0(T) + \sum_{n=1} \epsilon^n \phi_n(x, t, T), \quad (4.4.2b)$$

where our inclusion of the $O(1)$ mode $\Phi_0(T)$ has been motivated with hindsight gained during the calculation below; this mode is required to balance the resonances at $O(\epsilon^2)$. We note that since ϕ is a velocity potential, only its gradients affect the bulk flow and so the local value of $\Phi_0(T)$ has no effect on the flow field.

4.4.1 $O(\epsilon)$ analysis

After substitution of the expansions (4.4.2) into the model equations (4.2.21), we can collect linear terms to give:

$$\mathbf{L} \begin{pmatrix} h_1 \\ \phi_1 \end{pmatrix} = \begin{pmatrix} 0 \\ 0 \end{pmatrix}, \quad \text{where} \quad \mathbf{L} \equiv \begin{pmatrix} \partial_t - \gamma \partial_x^2 & -\hat{\mathcal{E}}_0 \\ G_0 - \Gamma_0 \partial_x^2 + 4\gamma \coth H \sin 2t & \partial_t - \gamma \partial_x^2 \end{pmatrix}. \quad (4.4.3)$$

For reasons that will become clear (on page 143), throughout this section, we now refer to the Fourier operator $\hat{\mathcal{E}}$ as $\hat{\mathcal{E}}_0$ —its operation is still defined by (4.2.15). The system (4.4.3) is equivalent to the Mathieu equation (4.3.2) of §4.3, except that f has been replaced by its critical value $f = f_c \equiv \gamma \coth H$. Recall that the appropriate solutions to these equations are (cf. (4.3.25)):

$$h_1 = [\cos t + \frac{1}{4}\gamma \sin 3t - \frac{3}{8}\gamma \sin t] (Ae^{ix} + A^*e^{-ix}), \quad (4.4.4a)$$

$$\phi_1 = \coth H [-\sin t + \frac{5}{8}\gamma \cos t + \frac{3}{4}\gamma \cos 3t] (Ae^{ix} + A^*e^{-ix}), \quad (4.4.4b)$$

where $A = A(T)$ is a complex amplitude and terms of order $O(\gamma^2)$ have been neglected as they do not contribute to the amplitude description.

4.4.2 $O(\epsilon^2)$ analysis

Collecting second-order terms, we find

$$\mathbf{L} \begin{pmatrix} h_2 \\ \phi_2 \end{pmatrix} = \begin{pmatrix} -(h_1 \phi_{1x})_x - \hat{\mathcal{E}}_0(h_1 \hat{\mathcal{E}}_0 \phi_1) \\ \frac{1}{2}(\hat{\mathcal{E}}_0 \phi_1)^2 - \frac{1}{2}(\phi_{1x})^2 - \Phi_{0T} \end{pmatrix}, \quad (4.4.5)$$

and eliminating ϕ_2 yields

$$h_{2tt} - 2\gamma h_{2xxt} + (G_0 - \Gamma_0 \partial_x^2 + 4\gamma \coth H \sin 2t) \hat{\mathcal{E}}_0 h_2 = (\partial_t - \gamma \partial_x^2) [-(h_1 \phi_{1x})_x - \hat{\mathcal{E}}_0(h_1 \hat{\mathcal{E}}_0 \phi_1)] + \hat{\mathcal{E}}_0 [\frac{1}{2}(\hat{\mathcal{E}}_0 \phi_1)^2 - \frac{1}{2}(\phi_{1x})^2]. \quad (4.4.6)$$

At this order, there are no terms proportional to $\sin t$, $\cos t$ or any other component of the linear solution (4.4.4a) generated requiring the imposition of a solvability condition.

Thus, we introduce the planform

$$h_2 = (h_{21} + h_{22} \cos 2t + \gamma h_{23} \sin 2t + \gamma h_{24} \sin 4t) [A^2 e^{2ix} + A^{*2} e^{-2ix}] \quad (4.4.7)$$

and neglect terms proportional to γ^2 in the right-hand side of (4.4.6). The form of (4.4.7) has been chosen to ensure that the coefficients, h_{21}, \dots, h_{24} , are independent of γ ; this

convention is adopted throughout the rest of the chapter. After some highly tedious calculations, these coefficients are found to be (cf. [96, equations (3.19)–(3.24)]):

$$h_{21} = \frac{1}{4}M \coth H - \gamma^2 M T h_{23}, \quad (4.4.8a)$$

$$h_{22} = \frac{(R_1 - 4\gamma^2 T R_3 D_2^{-1})(D_1 - 8\gamma^2 M T^2) - 16\gamma^2 R_2 + 32\gamma^2 M T \coth H}{(D_1 - 16\gamma^2 T^2 D_2^{-1})(D_1 - 8\gamma^2 M T^2) + 256\gamma^2}, \quad (4.4.8b)$$

$$h_{23} = \frac{(R_2 - 2M T \coth H)(D_1 - 16\gamma^2 T D_2^{-1}) + 16R_1 - 64\gamma^2 T R_3 D_2^{-1}}{(D_1 - 16\gamma^2 T^2 D_2^{-1})(D_1 - 8\gamma^2 M T^2) + 256\gamma^2}, \quad (4.4.8c)$$

$$h_{24} = (R_3 - 4T h_{22})D_2^{-1}, \quad (4.4.8d)$$

where

$$D_1 = 2(G_0 + 4\Gamma_0) \tanh(2H) - 4 + 16\gamma^2,$$

$$D_2 = 2(G_0 + 4\Gamma_0) \tanh(2H) - 16 + 16\gamma^2,$$

$$M = 2 \coth(2H)(G_0 + 4\Gamma_0)^{-1},$$

$$T = 1 + \operatorname{sech}(2H),$$

and

$$R_1 = -\coth(H) \operatorname{sech}(2H)(\cosh(2H) + 2),$$

$$R_2 = \frac{1}{4} \coth(H) \operatorname{sech}(2H)(\cosh(2H) - 22),$$

$$R_3 = -\frac{1}{2} \coth H \operatorname{sech}(2H)(3 \cosh(3H) + 8).$$

Note that quadratic powers of γ have been retained in (4.4.8) as these become important near the 2 : 1 resonance point, $\Gamma_0 = \frac{1}{3} \tanh H$. Neglecting these terms gives rise to coefficients which are singular at this point. For $\Gamma_0 = \frac{1}{3} \tanh H$, a resonant three-wave interaction occurs, where the mode driven by quadratic interaction of the primary modes has a ‘natural’ frequency matching the driving frequency [96]. Although this mode is linearly damped, it will grow to large amplitude due to the resonance and weak damping; subsequently, it will strongly influence the cubic coefficient of the amplitude equation. Three-wave resonant interactions have greater relevance to the two-dimensional problem as they influence the preferred angle between wavevectors. However, this is not an issue in the one-dimensional problem in question here and we do not study this resonance point further; see Zhang and Viñals [96, page 312] for more details. Although we keep these terms away from the resonance point, they are small for weak damping and should not affect the validity of the perturbation expansion. Figure 4.5 illustrates the variation of h_{21}, \dots, h_{24} with Γ_0 for $H = 1$ and several values of γ . We see that, without viscosity, the coefficients are unbounded in a neighbourhood of $\Gamma_0 = \frac{1}{3} \tanh H$, but the inclusion of γ prevents this behaviour.

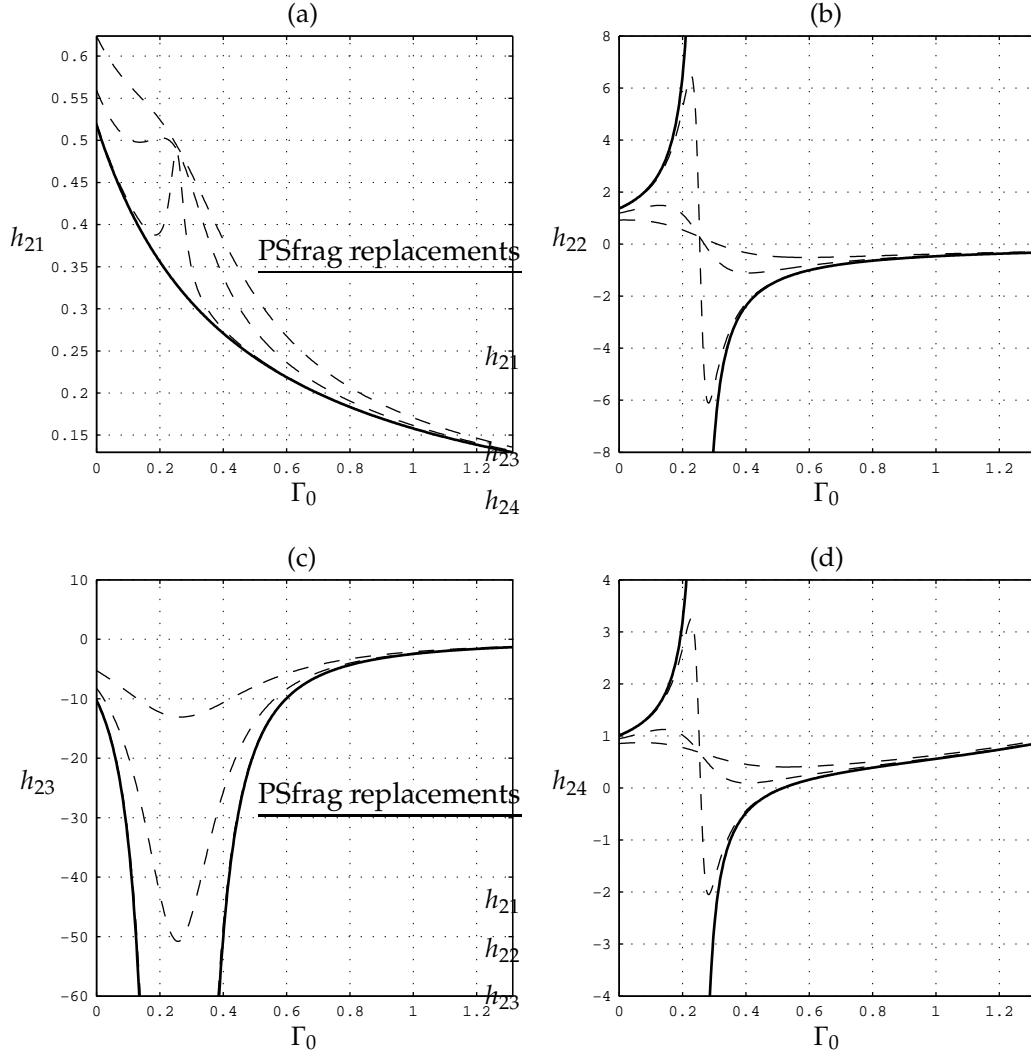


Figure 4.5: Plots of (a) h_{21} , (b) h_{22} , (c) h_{23} and (d) h_{24} against Γ_0 for $H = 1$ and $\gamma = 0, 0.01, 0.05, 0.1$. The inviscid case ($\gamma = 0$) is plotted in a thick solid line. Note the $\gamma = 0$ and $\gamma = 0.01$ curves for h_{23} are indistinguishable.

Now, from (4.4.5) we have

$$\hat{\mathcal{E}}_0 \phi_2 = h_{2t} - \gamma h_{2xx} + (h_1 \phi_{1x})_x + \hat{\mathcal{E}}_0 (h_1 \hat{\mathcal{E}}_0 \phi_1), \quad (4.4.9)$$

and after substituting for h_1 and ϕ_1 it is apparent that a planform of the form

$$\phi_2 = (\gamma \phi_{21} + \phi_{22} \sin 2t + \gamma \phi_{23} \cos 2t + \gamma \phi_{24} \cos 4t) \left[A^2 e^{2ix} + A^{*2} e^{-2ix} \right] + \Phi_2(t, T) \quad (4.4.10)$$

is warranted. The additional function $\Phi_2(t, T)$ has been introduced since (4.4.6) only allows ϕ_2 to be determined up to the addition of x -independent modes (see the intermission on page 143 for more details of this procedure). The coefficients $\phi_{21}, \dots, \phi_{24}$ are

found to be:

$$\phi_{21} = (\tanh H + \coth H)h_{21} - \frac{1}{4} \operatorname{csch}^2 H, \quad (4.4.11a)$$

$$\phi_{22} = -\frac{1}{2}(\tanh H + \coth H)h_{22} + \frac{1}{4} \operatorname{csch}^2 H, \quad (4.4.11b)$$

$$\phi_{23} = (\tanh H + \coth H)(h_{22} + \frac{1}{2}h_{22}) - \frac{3}{16} \operatorname{csch}^2 H, \quad (4.4.11c)$$

$$\phi_{24} = 2 \coth(2H)h_{24} - \frac{1}{4} \operatorname{csch}^2 H. \quad (4.4.11d)$$

We now determine $\Phi_2(t, T)$ by considering the spatial average of the ϕ component of (4.4.5), where we find purely temporal modes proportional to $\sin 2t$, $\cos 2t$, $\sin 4t$ as well as a zero mode. Hence, we set

$$\Phi_2 = \phi_{25}|A|^2 \sin 2t + \gamma\phi_{26}|A|^2 \cos 2t + \gamma\phi_{27}|A|^2 \cos 4t, \quad (4.4.12)$$

where the coefficients $\phi_{25}, \phi_{26}, \phi_{27}$ are given by

$$\phi_{25} = \frac{1}{4} \operatorname{csch}^2 H, \quad \phi_{26} = \frac{1}{16} \operatorname{csch}^2 H, \quad \phi_{27} = -\frac{3}{16} \operatorname{csch}^2 H. \quad (4.4.13)$$

Finally at this order, integrating the ϕ component of (4.4.5) over a single period of both x and t , we find the evolution of Φ_0 to be governed by

$$\Phi_{0T} = -\frac{1}{2} \operatorname{csch}^2 H |A|^2, \quad (4.4.14)$$

which suggests that Φ_0 has unbounded growth. We reiterate that this behaviour is not problematic as Φ_0 has no direct physical relevance.

4.4.3 $O(\epsilon^3)$ analysis

At this order, we have

$$\begin{aligned} \mathbf{L} \begin{pmatrix} h_3 \\ \phi_3 \end{pmatrix} = & \begin{pmatrix} -h_{1T} - (h_1\phi_{2x} + h_2\phi_{1x})_x - \hat{\mathcal{E}}_0 (h_1\hat{\mathcal{E}}_0\phi_2 + h_2\hat{\mathcal{E}}_0\phi_1) \\ -\phi_{1T} + \hat{\mathcal{E}}_0\phi_1\hat{\mathcal{E}}_0\phi_2 - \phi_{1x}\phi_{2x} \end{pmatrix} \\ & + \begin{pmatrix} \hat{\mathcal{E}}_0 [h_1\hat{\mathcal{E}}_0(h_1\hat{\mathcal{E}}_0\phi_1) + \frac{1}{2}h_1^2\phi_{1xx}] + \frac{1}{2}(h_1^2\hat{\mathcal{E}}_0\phi_1)_{xx} \\ -\hat{\mathcal{E}}_0\phi_1 [h_1\phi_{1xx} + \hat{\mathcal{E}}_0(h_1\hat{\mathcal{E}}_0\phi_1)] - \frac{1}{2}\Gamma_0(h_{1x}^3)_x \end{pmatrix}, \end{aligned} \quad (4.4.15)$$

and we are now in a position to apply solvability conditions. However, due to the perturbative nature of the linear solution, the precise form of these conditions requires careful attention. Thus, we digress for a moment to consider this point in some detail.

Solvability conditions: The adjoint of the linear problem (4.4.3) is

$$\mathbf{L}^\dagger \begin{pmatrix} h_1^\dagger \\ \phi_1^\dagger \end{pmatrix} = \begin{pmatrix} 0 \\ 0 \end{pmatrix}, \quad (4.4.16)$$

where the adjoint operator \mathbf{L}^\dagger is implicitly defined by

$$\int_0^{2\pi} \int_0^{2\pi} \begin{pmatrix} h_1^\dagger \\ \phi_1^\dagger \end{pmatrix} \cdot \mathbf{L} \begin{pmatrix} h_1 \\ \phi_1 \end{pmatrix} dxdt = \int_0^{2\pi} \int_0^{2\pi} \begin{pmatrix} h_1 \\ \phi_1 \end{pmatrix} \cdot \mathbf{L}^\dagger \begin{pmatrix} h_1^\dagger \\ \phi_1^\dagger \end{pmatrix} dxdt. \quad (4.4.17)$$

After some integration by parts, we find

$$\mathbf{L}^\dagger \equiv \begin{pmatrix} -\partial_t - \gamma \partial_x^2 & G_0 - \Gamma_0 \partial_x^2 + 4\gamma \coth H \sin(2t) \\ -\hat{\mathcal{E}}_0 & -\partial_t - \gamma \partial_x^2 \end{pmatrix}. \quad (4.4.18)$$

Now, eliminating h_1^\dagger from (4.4.16) yields

$$\phi_{tt}^\dagger + 2\gamma \phi_{xxt}^\dagger + \gamma^2 \phi_{xxxx}^\dagger + \hat{\mathcal{E}}_0 [G_0 \phi^\dagger - \Gamma_0 \phi_{xx}^\dagger + 4\gamma \coth H \phi^\dagger \sin 2t] = 0. \quad (4.4.19)$$

In line with the derivation of the linear solutions (4.3.25), we solve this equation at successive orders of γ by making the substitution

$$\phi^\dagger(x, t) = \left(\phi_0^\dagger(t) + \gamma \phi_1^\dagger(t) + \gamma^2 \phi_2^\dagger(t) + \dots \right) e^{\pm ix}. \quad (4.4.20)$$

At leading order, we have

$$\phi_{0tt}^\dagger + \hat{\mathcal{E}}_0 [G_0 - \Gamma_0 \partial_x^2] \phi_0^\dagger = 0, \quad (4.4.21)$$

with solution

$$\phi_0^\dagger = \phi_{01}^\dagger \sin t + \phi_{02}^\dagger \cos t, \quad (4.4.22)$$

where ϕ_{01}^\dagger and ϕ_{02}^\dagger are constants. At $O(\gamma)$, we find that $\phi_{02}^\dagger = 0$ and

$$\phi_1^\dagger = \phi_{10}^\dagger \cos t - \frac{1}{4} \phi_{01}^\dagger \cos 3t, \quad (4.4.23)$$

where ϕ_{10}^\dagger is undetermined at this stage. Subsequently, from the terms at $O(\gamma^2)$, we find $\phi_{10}^\dagger = -\frac{3}{8}$. Thus, we write approximate solutions for ϕ^\dagger as

$$\phi^\dagger = \left(\sin t - \frac{1}{4} \gamma \cos 3t - \frac{3}{8} \gamma \cos t + \dots \right) e^{\pm ix}. \quad (4.4.24)$$

By performing a similar procedure on the ϕ^\dagger component of (4.4.16), we can construct the corresponding solutions for h^\dagger :

$$h^\dagger = \coth H \left(-\cos t + \frac{5}{8} \gamma \sin t - \frac{3}{4} \gamma \sin 3t + \dots \right) e^{\pm ix}. \quad (4.4.25)$$

Thus, by the Fredholm alternative theorem (see §1.2.10), the solvability conditions for problems of the form

$$\mathbf{L} \begin{pmatrix} h \\ \phi \end{pmatrix} = \begin{pmatrix} \text{RHS}_1 \\ \text{RHS}_2 \end{pmatrix} \quad (4.4.26)$$

are

$$\int_0^{2\pi} \int_0^{2\pi} \begin{pmatrix} h^\dagger \\ \phi^\dagger \end{pmatrix} \cdot \begin{pmatrix} \text{RHS}_1 \\ \text{RHS}_2 \end{pmatrix} dx dt = 0. \quad (4.4.27)$$

where the solutions ϕ^\dagger and h^\dagger are given by (4.4.24) and (4.4.25) respectively.

A more convenient form of this solvability condition can be derived if we first eliminate ϕ_2 from the linear problem (4.4.5) before considering the adjoint problem. In this case, the adjoint equation takes the form

$$q_{tt}^\dagger + 2\gamma q_{xxt}^\dagger + \gamma^2 q_{xxxx}^\dagger + \hat{\epsilon}_0 \left[G_0 q^\dagger - \Gamma_0 q_{xx}^\dagger + 4\gamma q^\dagger \coth H \sin 2t \right] = 0. \quad (4.4.28)$$

This equation is identical to (4.4.19) and so the appropriate solutions are

$$q^\dagger = \left(\sin t - \frac{1}{4}\gamma \cos 3t - \frac{3}{8}\gamma \cos t + \dots \right) e^{\pm ix}, \quad (4.4.29)$$

and the solvability condition for (4.5.17) can be written

$$\int_0^{2\pi} \int_0^{2\pi} [(\partial_t - \gamma \partial_x^2) \text{RHS}_{1n} + \hat{\epsilon}_0 \text{RHS}_{2n}] e^{\pm ix} q^\dagger(x, t) dx dt = 0, \quad (4.4.30)$$

where $q^\dagger(x, t)$ is given by (4.4.29). This condition is equivalent to (4.4.27).

The amplitude equations derived by Zhang and Viñals [96] use a simpler but inconsistent solvability condition:

$$\int_0^{2\pi} \int_0^{2\pi} [(\partial_t - \gamma \partial_x^2) \text{RHS}_{1n} + \hat{\epsilon}_0 \text{RHS}_{2n}] e^{\pm ix} \sin t dx dt = 0, \quad (4.4.31)$$

where only the leading-order component of the adjoint solution is used in the integral. However, the neglect of $O(\gamma)$ terms in the adjoint solution causes the coefficients in the final amplitude equation to differ at leading order. We maintain that the condition (4.4.27) (or equivalently, (4.4.30)) is the correct condition.

Returning to the problem at hand, applying the condition (4.4.27) to the third-order terms, (4.4.15), we derive the amplitude equation

$$A_T = f_2 \tanh HA - \gamma \alpha_{\text{cub}} |A|^2 A, \quad (4.4.32)$$

where the nonlinear coefficient is given by

$$\begin{aligned} \alpha_{\text{cub}} = \frac{3}{64} \left[4 \text{csch}^2 H + 4 - 7\Gamma_0 \tanh H \right] + \frac{5}{4} \coth(2H) h_{21} \\ - 2 \text{csch}(2H) h_{22} - \frac{1}{2} \text{csch}(2H) (2 + \cosh(2H)) h_{23}. \end{aligned} \quad (4.4.33)$$

We see from figure 4.6 that, with $H = 1$, α_{cub} is positive for all Γ_0 but becomes singular at the 2 : 1 resonance point in the limit $\gamma \rightarrow 0$; Similar behaviour is realised for all

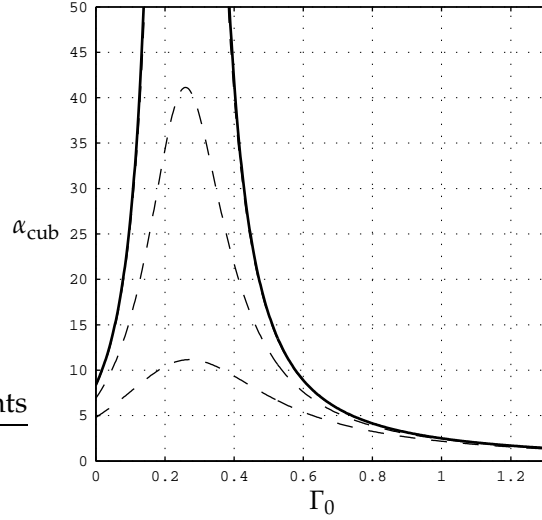


Figure 4.6: The cubic coefficient α_{cub} of the spatially homogeneous amplitude equation (4.4.32) plotted against the capillary number Γ_0 for $H = 1$ and $\gamma = 0, 0.01, 0.05, 0.1$. The thick, solid line corresponds to $\gamma = 0$.

positive H values. It is clear from this figure that the amplitude of the realised SWs will be small in the vicinity of the 2 : 1 resonance point at $\Gamma_0 = \frac{1}{3} \tanh H$. Note that in the limit of $H \rightarrow \infty$, this cubic coefficient reduces to

$$\alpha_{\text{cub}}|_{H \rightarrow \infty} = \frac{12 - 21\Gamma_0}{64} + \frac{5}{4}h_{21} - \frac{1}{2}h_{23}, \quad (4.4.34)$$

which differs from the cubic coefficient calculated by Zhang and Viñals (see [96, equation (3.35)]) for two reasons. Firstly, as detailed in §4.3, we have calculated a more accurate linear solution, with an extra $O(\gamma)$ term which turns out to be necessary to determine α_{cub} accurately. Also, we have applied the correct solvability conditions which also require the presence of previously neglected $O(\gamma)$ terms in the adjoint solutions.

4.4.4 Summary

We have seen in this section that the incorporation of finite depth in the model proposed by Zhang and Viñals [96] has relatively little effect on the SW amplitude equation without considering spatial modulation. Neglecting the influence of spatial modulation obviates consideration of the large-scale modes that are neutrally stable, and so the additional dynamical behaviour that a conservation law can induce on these modes is absent. Through our examination of this problem, not only have we achieved an extension to finite depth H , but in a consideration of the limit $H \rightarrow \infty$, we have also identified two flaws in the analysis of Zhang and Viñals [96]: the omission of $O(\gamma)$ terms in both the linear solution and the adjoint solution used to derive solvability conditions.

Curiously, it has been commented [221] that there is a slight mismatch between the predictions of the Zhang and Viñals [96] model and experimental results. This poses an interesting question: whether a correctly derived amplitude equation from the model equations (4.2.1) with infinite depth would account for this disharmony. However, the focus of this chapter is the behaviour of large-scale modes in the model equations and the influence of the conservation law (4.2.3) and so we do not pursue this interesting matter further.

4.5 Nonlinear analysis II: Spatial modulation

In this section we extend the weakly nonlinear analysis of the previous section to incorporate spatial modulation. Zhang and Viñals [96, §3.4] carried out a similar procedure, extending their amplitude equation (4.2.8) to include slow spatial derivatives through symmetry considerations. In effect, they added a diffusion term to (4.2.8) with an appropriate coefficient determined by considering the growthrate of the linearly unstable mode. Whilst such an envelope equation could be derived from first principles, in practice, such a derivation is highly nontrivial and involves several subtleties not found in the unmodulated problem. We do not include such a derivation here; however, we instead perform the analogous derivation for the finite-depth problem where the same analytic complications arise and are appropriately dealt with.

The key development in this section is the introduction of a slow space scale $X = \epsilon x$, so that

$$\frac{\partial}{\partial x} \mapsto \frac{\partial}{\partial x} + \epsilon \frac{\partial}{\partial X}. \quad (4.5.1)$$

With this in mind, we must pay careful attention to the operation of the Fourier–integral operation $\hat{\mathcal{E}}$ (defined in (4.2.15)), which is perturbed by slow spatial variations. It is instructive to examine the action of $\hat{\mathcal{E}}$ on a single mode $e^{ipx}e^{iqx}$:

$$\begin{aligned} \hat{\mathcal{E}} \left(e^{ipx} e^{iqx} \right) &= e^{ipx} e^{iqx} (p + iq) \tanh [(p + iq)H], & \text{by (4.2.15),} \\ &\approx e^{ipx} e^{iqx} \left[p \tanh pH + iq \left(\tanh pH + pH \operatorname{sech}^2 pH \right) \right. \\ &\quad \left. + \epsilon^2 q^2 H \operatorname{sech}^2 pH (1 - pH \tanh pH) + \dots \right]. \end{aligned} \quad (4.5.2)$$

Transforming back to physical space, we interpret each occurrence of q as $-i\partial_X$ and write

$$\begin{aligned} \hat{\mathcal{E}} \left(A(X, T) e^{ipx} \right) &= p \tanh (pH) A - i\epsilon \left[\tanh pH + pH \operatorname{sech}^2 pH \right] A_X \\ &\quad - \epsilon^2 H \operatorname{sech}^2 pH [1 - pH \tanh pH] A_{XX} + \dots, \end{aligned} \quad (4.5.3)$$

prompting the corresponding partition of $\hat{\mathcal{E}}$ into distinct operators, acting at successive orders of ϵ :

$$\hat{\mathcal{E}} = \hat{\mathcal{E}}_0 + \epsilon \hat{\mathcal{E}}_1 + \epsilon^2 \hat{\mathcal{E}}_2 + \dots \quad (4.5.4)$$

To derive envelope equations for A , we require only the operators up to $\hat{\mathcal{E}}_2$:

$$\hat{\mathcal{E}}_0 u(x, X) = \int_{-\infty}^{\infty} k \tanh(Hk) \hat{u}(k) e^{ikx} dx, \quad (4.5.5a)$$

$$\hat{\mathcal{E}}_1 u(x, X) = -i \frac{\partial}{\partial X} \int_{-\infty}^{\infty} \left[\tanh(Hk) + Hk \operatorname{sech}^2(Hk) \right] \hat{u}(k) e^{ikx} dx, \quad (4.5.5b)$$

$$\hat{\mathcal{E}}_2 u(x, X) = -H \frac{\partial^2}{\partial X^2} \int_{-\infty}^{\infty} \operatorname{sech}^2(Hk) [1 - Hk \tanh(Hk)] \hat{u}(k) e^{ikx} dx. \quad (4.5.5c)$$

Finally, we expand h and ϕ consistently in ϵ :

$$h(x, X, t, \tau, T) = \sum_{n=1}^{\infty} \epsilon^n h_n(x, X, t, \tau, T), \quad (4.5.6a)$$

$$\phi(x, X, t, \tau, T) = \sum_{n=1}^{\infty} \epsilon^n \phi_n(x, X, t, \tau, T), \quad (4.5.6b)$$

where a new timescale, $\tau = \epsilon t$, has been introduced. This time-scale is not required in the spatially uniform case considered in the previous section, but is required when spatial modulation over a long scale is included, to account for the behaviour of large-scale modes. Time differentiation now acts like

$$\frac{\partial}{\partial t} \mapsto \frac{\partial}{\partial t} + \epsilon \frac{\partial}{\partial \tau} + \epsilon^2 \frac{\partial}{\partial T}. \quad (4.5.7)$$

Note also that the $O(1)$ mode for ϕ of the previous section is no longer required.

4.5.1 $O(\epsilon)$ analysis

At linear order we recover the problem (4.4.3) from the previous section; however, before we proceed by adopting the linear solutions (4.3.25), let us briefly examine the process by which mean modes (with no x or t dependence) or purely temporal modes are introduced into h_n and ϕ_n .

Solving for h_n and ϕ_n : Digressing briefly, recall that for each $n \in \mathbb{Z}^+$, a light manipulation of the terms proportional to ϵ^n yields a problem (cf. (4.4.26))

$$\mathbf{L} \begin{pmatrix} h_n \\ \phi_n \end{pmatrix} = \begin{pmatrix} \text{RHS}_{1n} \\ \text{RHS}_{2n} \end{pmatrix}, \quad (4.5.8)$$

where \mathbf{L} is defined in (4.4.3), from which the elimination of ϕ_n produces an equation of the form (cf. (4.4.6))

$$\begin{aligned} \partial_t^2 h_n - 2\gamma \partial_x^2 \partial_t h_n + (G_0 - \Gamma_0 \partial_x^2 + 4\gamma \coth H \sin 2t) \hat{\mathcal{E}}_0 h_n \\ = (\partial_t - \gamma \partial_x^2) \text{RHS}_{1n} + \hat{\mathcal{E}}_0 [\text{RHS}_{2n}]. \end{aligned} \quad (4.5.9)$$

Now, (4.5.9) allows h_n to be determined up to the addition of a mean term (independent of x and t):

$$h_n = \cdots + H_n(X, \tau, T). \quad (4.5.10)$$

Subsequently, rearranging the h component of (4.5.8) to give

$$\hat{\mathcal{E}}_0 \phi_2 = -(\partial_t - \gamma \partial_x^2) h_n - \text{RHS}_{1n}, \quad (4.5.11)$$

allows ϕ_n to be found up to the addition of x -independent terms,

$$\phi_n = \cdots + \Phi_n(X, t, \tau, T). \quad (4.5.12)$$

Consequently, terms of the type (H_n, Φ_n) should be added to (h_n, ϕ_n) at each order to ensure that the conditions

$$\int_0^{2\pi} \int_0^{2\pi} [(\partial_t - \gamma \partial_x^2) h_p - \hat{\mathcal{E}}_0 \phi_p - \text{RHS}_{1p}] dx dt = 0 \quad (4.5.13)$$

and

$$\int_0^{2\pi} [(G_0 - \Gamma_0 \partial_x^2 + 4\gamma \coth H \sin 2t) h_p + (\partial_t - \gamma \partial_x^2) \phi_p - \text{RHS}_{2p}] dx = 0, \quad (4.5.14)$$

can be satisfied for $p \geq n$, that is, to ensure that at each order, the mean terms of the h component of (4.5.8) as well as the x -independent terms of the ϕ component are balanced. In general, the inclusion and form of (H_n, Φ_n) are motivated by $O(\epsilon^{n+1})$ balances.

For the present problem, the linear solutions are given by (4.3.1). However, we find $H_1 = 0$ and that Φ_1 is not required to vary with t . Thus, our linear solutions are:

$$h_1 = \left(\cos t + \frac{1}{4}\gamma \sin 3t - \frac{3}{8}\gamma \sin t \right) \left[A e^{ix} + A^* e^{-ix} \right], \quad (4.5.15a)$$

$$\phi_1 = \coth H \left(-\sin t + \frac{5}{8}\gamma \cos t + \frac{3}{4}\gamma \cos 3t \right) \left[A e^{ix} + A^* e^{-ix} \right] + \Phi_1. \quad (4.5.15b)$$

where $A = A(X, \tau, T)$ and $\Phi_1 = \Phi_1(X, \tau, T)$.

4.5.2 $O(\epsilon^2)$ analysis

Collecting second-order terms yields

$$\mathbf{L} \begin{pmatrix} h_2 \\ \phi_2 \end{pmatrix} = \begin{pmatrix} -(h_1 \phi_{1x})_x - \hat{\mathcal{E}}_0(h_1 \hat{\mathcal{E}}_0 \phi_1) + \hat{\mathcal{E}}_1 \phi_1 + 2\gamma h_{1xX} - h_{1\tau} \\ \frac{1}{2}(\hat{\mathcal{E}}_0 \phi_1)^2 - \frac{1}{2}(\phi_{1x})^2 + 2\Gamma_0 h_{1xX} + 2\gamma \phi_{1xX} - \phi_{1\tau} \end{pmatrix}, \quad (4.5.16)$$

which, after eliminating ϕ_2 , can be written

$$\begin{aligned} h_{2tt} - 2\gamma h_{2xxt} + (G_0 - \Gamma_0 \partial_x^2 + 4\gamma \coth H \sin 2t) \hat{\mathcal{E}}_0 h_2 \\ = (\partial_t - \gamma \partial_x^2) [-(h_1 \phi_{1x})_x - \hat{\mathcal{E}}_0(h_1 \hat{\mathcal{E}}_0 \phi_1) + \hat{\mathcal{E}}_1 \phi_1 + 2\gamma h_{1xX} - h_{1\tau}] \\ + \hat{\mathcal{E}}_0 \left[\frac{1}{2}(\hat{\mathcal{E}}_0 \phi_1)^2 - \frac{1}{2}(\phi_{1x})^2 + 2\Gamma_0 h_{1xX} + 2\gamma \phi_{1xX} - \phi_{1\tau} \right]. \end{aligned} \quad (4.5.17)$$

In contrast to the case of unmodulated amplitudes where no secular contributions are found at $O(\epsilon^2)$, the right-hand side (4.5.17) now contains terms of the same form as the linear solution and solvability conditions need to be applied. Applying the condition (4.4.27), we find

$$A_\tau = \frac{1}{8}i\gamma [11 + 6\Gamma_0 \tanh H - 10H \operatorname{csch}(2H)] A_X, \quad (4.5.18)$$

which indicates that the linear solution (4.3.25) does not quite lie at the minimum of the marginal curve. This is due to the linear solutions (4.5.15) having wavenumber $k = 1$ while the wavenumber of solution at the bottom of the neutral curve is only approximately $k = 1$. This fact was noted earlier in §4.3 (page 128) where the fact that the critical wavenumber has form $k = 1 + O(\gamma^2)$ was discussed. We interpret (4.5.18) as an indication that the wavenumber should be slightly different from 1 and, in an admittedly ad hoc step, ignore the right-hand side of (4.5.18) on the basis that, were we indeed to take a basic wavenumber *exactly* at the minimum of the marginal curve, there would be no equation to satisfy at $O(\epsilon^2)$, and the coefficients in the remainder of the calculation would be slightly altered. Such a change to k would significantly complicate the algebra with little reward. This assumption allows us to specify $A_\tau = 0$ for the remainder of this section.

We now balance the terms on the right-hand side of (4.5.17). Substituting the expressions for h_1 and ϕ_1 into (4.5.17) and neglecting terms proportional to γ^2 motivates a particular solution for h_2 of the form

$$\begin{aligned} h_2 = (h_{21} + h_{22} \cos 2t + \gamma h_{23} \sin 2t + \gamma h_{24} \sin 4t) \left(A^2 e^{2ix} + A^{*2} e^{-2ix} \right) \\ + (\gamma^{-1} J_{21} \sin t + \gamma J_{22} \sin 3t + J_{23} \cos 3t) e^{ix} + \text{c.c.} + H_2(X, \tau, T) \\ + [\cos t + \frac{1}{4}\gamma \sin 3t - \frac{3}{8}\gamma \sin t] \left(E e^{ix} + E^* e^{-ix} \right), \end{aligned} \quad (4.5.19)$$

where J_{21}, J_{22}, J_{23} are complex functions of X, τ, T and the coefficients h_{21}, \dots, h_{24} are defined in (4.4.8). As well as terms included to balance the $O(\epsilon^2)$ harmonics, we have also made two further additions. Firstly, we have included a mean mode $H_2(X, \tau, T)$ which will be required at $O(\epsilon^3)$ and secondly, (4.5.19) contains terms of the same form as the linear solution but with a new complex amplitude $E = E(X, \tau, T)$. These are included to allow the correct amplitude equation to be derived at $O(\epsilon^3)$.

After substitution, we collect terms proportional to e^{ix} to find

$$J_{21} = \frac{1}{4}i [1 + 2\Gamma_0 \tanh H + 2H \operatorname{csch}(2H)] A_X, \quad (4.5.20a)$$

$$J_{22} = -\frac{1}{64}i [15 - 2\Gamma_0 \tanh H + 30H \operatorname{csch}(2H)] A_X, \quad (4.5.20b)$$

$$J_{23} = -\frac{1}{16}i [1 + 2\Gamma_0 \tanh H + 2H \operatorname{csch}(2H)] A_X. \quad (4.5.20c)$$

Note that collecting terms proportional to $\sin t e^{ix}$ in (4.5.17) and making the substitutions (4.5.20) allows the solvability condition (4.5.18) to be recovered. This is indicative of our correct choice of linear solution (4.5.15). Had we ignored the new $O(\gamma)$ term proportional to $\sin t$ in h_1 (which implies a corresponding change in ϕ_1), then an inconsistent condition would have been derived here.

We now construct ϕ_2 . From (4.5.16), we have

$$\hat{\mathcal{E}}_0 \phi_2 = h_{2t} - \gamma h_{2xx} + (h_1 \phi_{1x})_x + \hat{\mathcal{E}}_0 (h_1 \hat{\mathcal{E}}_0 \phi_1) - \hat{\mathcal{E}}_1 \phi_1 - 2\gamma h_{1xX} + h_{1\tau}. \quad (4.5.21)$$

After substitution of the expressions for h_1, h_2 and ϕ_1 into the above equation, it is apparent that the following particular solution for ϕ_2 is required:

$$\begin{aligned} \phi_2 = & [\gamma \phi_{21} + \phi_{22} \sin 2t + \gamma \phi_{23} \cos 2t + \gamma \phi_{24} \cos 4t] (A^2 e^{2ix} + A^{*2} e^{-2ix}) \\ & + [K_{21} \sin t + K_{22} \gamma^{-1} \cos t + \gamma K_{23} \cos 3t + K_{24} \sin 3t] e^{ix} + \text{c.c.} \\ & + \gamma K_{2a} \cos 2t + K_{2b} \sin 3t + \gamma K_{2c} \cos 4t \\ & + \operatorname{coth} H [-\sin t + \frac{5}{8} \gamma \cos t + \frac{3}{4} \gamma \cos 3t] (E e^{ix} + E^* e^{-ix}). \end{aligned} \quad (4.5.22)$$

where $\phi_{21}, \dots, \phi_{24}$ are defined in (4.4.11) and

$$K_{21} = \operatorname{coth} H J_{21} - i (\operatorname{coth} H + H \operatorname{csch}^2 H) A_X, \quad (4.5.23a)$$

$$K_{22} = \operatorname{coth} H J_{21}, \quad (4.5.23b)$$

$$K_{23} = \operatorname{coth} H (3J_{22} + J_{23}) + \frac{3}{4}i (\operatorname{coth} H + H \operatorname{csch}^2 H) A_X, \quad (4.5.23c)$$

$$K_{24} = -3 \operatorname{coth} H J_{23} \quad (4.5.23d)$$

$$K_{2a} = -\frac{1}{8} \operatorname{csch}^2 H (|A|^2 - 8 \sinh(2H) H_2), \quad (4.5.23e)$$

$$K_{2b} = \frac{1}{4} \operatorname{csch}^2 H |A|^2, \quad (4.5.23f)$$

$$K_{2c} = -\frac{3}{16} \operatorname{csch}^2 H |A|^2, \quad (4.5.23g)$$

and again, the appropriate linear solution terms, with amplitude E , have been added. We complete the $O(\epsilon^2)$ analysis by considering the mean of the ϕ component of (4.5.16). Here we recover an evolution equation for Φ_1 :

$$\Phi_{1\tau} = -\frac{1}{2} \operatorname{csch}^2 H |A|^2 - G_0 H_2. \quad (4.5.24)$$

4.5.3 $O(\epsilon^3)$ analysis

Continuing our expansion to third order in ϵ , we find

$$\begin{aligned} \mathbf{L} \begin{pmatrix} h_3 \\ \phi_3 \end{pmatrix} = & \begin{pmatrix} -h_{1T} - (h_1 \phi_{2x} + h_2 \phi_{1x})_x - \hat{\mathcal{E}}_0 (h_1 \hat{\mathcal{E}}_0 \phi_2 + h_2 \hat{\mathcal{E}}_0 \phi_1) \\ -\phi_{1T} + \hat{\mathcal{E}}_0 \phi_1 \hat{\mathcal{E}}_0 \phi_2 - \phi_{1x} \phi_{2x} \end{pmatrix} \\ & + \begin{pmatrix} \hat{\mathcal{E}}_0 [h_1 \hat{\mathcal{E}}_0 (h_1 \hat{\mathcal{E}}_0 \phi_1) + \frac{1}{2} h_1^2 \phi_{1xx}] + \frac{1}{2} (h_1^2 \hat{\mathcal{E}}_0 \phi_1)_{xx} \\ -\hat{\mathcal{E}}_0 \phi_1 [h_1 \phi_{1xx} + \hat{\mathcal{E}}_0 (h_1 \hat{\mathcal{E}}_0 \phi_1)] - \frac{1}{2} \Gamma_0 (h_{1x}^3)_x \end{pmatrix} \\ & + \begin{pmatrix} \gamma h_{1XX} + 2\gamma h_{2xX} - h_{1x} \phi_{1X} - h_{1X} \phi_{1x} - 2h_1 \phi_{1xX} \\ \gamma \phi_{1XX} + 2\gamma \phi_{1xX} + \Gamma_0 h_{1XX} + 2\Gamma_0 h_{2xX} - \phi_{1x} \phi_{1X} \end{pmatrix} \\ & + \begin{pmatrix} \hat{\mathcal{E}}_1 \phi_2 + \hat{\mathcal{E}}_2 \phi_1 - \hat{\mathcal{E}}_0 [h_1 \hat{\mathcal{E}}_1 \phi_1] - \hat{\mathcal{E}}_1 [h_1 \hat{\mathcal{E}}_0 \phi_1] - h_{2\tau} \\ \hat{\mathcal{E}}_0 \phi_1 \hat{\mathcal{E}}_1 \phi_1 - 4f_2 h_1 \sin 2t \phi_{2\tau} \end{pmatrix}. \end{aligned} \quad (4.5.25)$$

Before we apply the solvability conditions, we must consider the mean of the h_3 component of this system (which is independent of our actual choice of h_3 and ϕ_3). We find an evolution equation for H_2 :

$$H_{2\tau} + H \Phi_{1XX} = 0, \quad (4.5.26)$$

which, once H_2 is eliminated via (4.5.24), becomes a forced wave equation

$$\Phi_{1\tau\tau} = G_0 H \Phi_{1XX} + \frac{1}{2} \operatorname{csch}^2 H (|A|^2)_\tau, \quad (4.5.27)$$

Now, applying our wavenumber shift assumption ($A_\tau = 0$), this becomes a simple wave equation

$$\Phi_{1\tau\tau} = G_0 H \Phi_{1XX}, \quad (4.5.28)$$

with solution $\Phi_1 = G_1(\eta, T) + G_2(\xi, T)$, where G_1 and G_2 are arbitrary functions and η, ξ are co-moving variables, defined by:

$$\eta = (G_0 H)^{1/2} \tau - X, \quad \xi = (G_0 H)^{1/2} \tau + X. \quad (4.5.29)$$

Noting that $\partial_\tau \equiv (G_0 H)^{1/2} (\partial_\eta + \partial_\xi)$ and $\partial_X \equiv (\partial_\xi - \partial_\eta)$, we now construct the solution for H_2 from (4.5.24). We find

$$H_2 = -\frac{1}{2G_0} \operatorname{csch}^2 H |A|^2 - \left(\frac{H}{G_0} \right)^{1/2} [G_{1\eta} + G_{2\xi}]. \quad (4.5.30)$$

Since this expression is singular at $G_0 = 0$, we see that the analysis of this section is only valid for mixed gravity–capillary waves ($G_0 \neq 0$). Eliminating Φ_1 from (4.5.26) gives rise to the equation

$$H_{2\tau\tau} = G_0 H H_{2XX} + \frac{1}{2} \operatorname{csch}^2 H (|A|^2)_{XX}. \quad (4.5.31)$$

Such behaviour of the large-scale mode H_2 is qualitatively different from the corresponding large-scale modes of chapter 2 (cf. (2.3.48)) and chapter 3 (cf. (3.2.14c)). This wave-like behaviour of the large-scale mode is responsible for the increased difficulty in deriving amplitude equations. It is notable that for the finite-depth problem but with larger viscosity, the appropriate equations are (1.5.6) [226], where the leading-order behaviour of the large-scale mode is diffusive.

We now apply the solvability condition (4.4.27) at this order to yield

$$\begin{aligned} E_\tau - \frac{1}{8} i \gamma (11 + 6\Gamma_0 \tanh H - 10H \operatorname{csch}(2H)) E_X = \\ - A_T + f_2 \tanh H A + \gamma^{-1} \alpha_{\text{diff}} A_{XX} - \gamma \alpha_{\text{cub}} |A|^2 A - A [i\Phi_{1X} - \frac{5}{4} \gamma \operatorname{csch}(2H) H_2], \end{aligned} \quad (4.5.32)$$

where

$$\alpha_{\text{diff}} = \frac{1}{8} (1 + H \coth H - (H - 2\Gamma_0) \tanh H)^2, \quad (4.5.33)$$

and the cubic coefficient α_{cub} retains its definition (4.4.33) from the previous section. The terms proportional to E on the left-hand side of this equation are an analogous condition to (4.5.18) and hence, we apply our assumption that the wavenumber shift terms can be neglected to yield

$$\begin{aligned} E_\tau = -A_T + f_2 \tanh H A + \gamma^{-1} \alpha_{\text{diff}} A_{XX} \\ - \gamma \alpha_{\text{cub}} |A|^2 A - A [i\Phi_{1X} - \frac{5}{4} \gamma \operatorname{csch}(2H) H_2]. \end{aligned} \quad (4.5.34)$$

Now, in order for the expansions for h and ϕ to remain asymptotic, the right-hand side of (4.5.34) must vanish when averaged over τ [69, 72]. However, due to the change of variables employed previously, for the terms of (4.5.34) proportional to Φ_{1X} and H_2 , this integration is nontrivial and it is helpful to consider each term individually.

Let us first consider the general integral

$$\int_0^P F(\eta, \zeta) d\tau, \quad (4.5.35)$$

where F is an arbitrary function of η and ζ and P is a suitably large period. For fixed $X = X_0$, we have $\zeta = (G_0 H)^{1/2} \tau + X_0$ and $\eta = (G_0 H)^{1/2} \tau - X_0$, which implies ζ is constrained to follow $\zeta - \eta = 2X_0$. We can also see that

$$\tau = (G_0 H)^{-1/2} (\eta + X_0) = (G_0 H)^{-1/2} (\zeta - X_0) \quad (4.5.36)$$

and so $d\tau = (G_0H)^{-1/2}d\eta = (G_0H)^{-1/2}d\xi$. Thus, there are two equivalent transformations of (4.5.35) into (η, ξ) -space:

$$\int_0^P F(\eta, \xi) d\tau = (G_0H)^{-1/2} \int_{-X_0}^{cP-X_0} F(\eta, \eta + 2X_0) d\eta, \quad (4.5.37a)$$

$$\int_0^P F(\eta, \xi) d\tau = (G_0H)^{-1/2} \int_{X_0}^{cP+X_0} F(\xi - 2X_0, \xi) d\xi. \quad (4.5.37b)$$

Hence, applying these results to the integral of Φ_{1X} , we have

$$\begin{aligned} \int_0^P \Phi_{1X} d\tau &= \int_0^P [G_{2\xi} - G_{1\eta}] d\tau, \\ &= \int_{X_0}^{cP+X_0} G_{2\xi} d\xi - \int_{-X_0}^{cP-X_0} G_{1\eta} d\eta, \\ &= [G_2]_{\xi=X_0}^{\xi=cP+X_0} - [G_1]_{\eta=-X_0}^{\eta=cP-X_0} \end{aligned}$$

By a similar procedure, we also find

$$\int_0^P H_2 d\tau = -\frac{1}{2}G_0^{-1} \operatorname{csch}^2 HP|A|^2. \quad (4.5.38)$$

Now, assuming G_1 and G_2 are bounded, then the τ -average of Φ_{1X} tends to zero as $P \rightarrow \infty$. Hence, taking the τ -average of (4.5.34) gives rise to the amplitude equation

$$A_T = f_2 \tanh HA + \gamma^{-1} \alpha_{\text{diff}} A_{XX} - \gamma \left(\alpha_{\text{cub}} + \frac{5}{16G_0} \operatorname{csch}(2H) \operatorname{csch}^2 H \right) A|A|^2, \quad (4.5.39)$$

where the only contribution of the mean modes has been to modify the cubic coefficient. As we can see from the comparison between figures 4.6 and 4.7, where the value of this coefficient is plotted, this modification has very little effect on the cubic coefficient, except near $G_0 = 0$ where this description is no longer valid. Thus, the mean modes induced by the presence of a conservation law have only a minor effect on the amplitude of the SWs; there is no new modulational instability of the primary solution, similar to those of chapters 2 and 3. This is not to say that the behaviour of the system is the same as the infinite-depth case. As detailed in §4.7, simulations of the full system (4.2.21) reveal uniformly travelling large-scale modes, matching those described in (4.5.30).

To complete the system of amplitude equations, we now derive evolution equations for Φ_1 and H_2 , over the slow timescale T . Integrating the ϕ equation found at $O(\epsilon^3)$ and also the h equation at $O(\epsilon^4)$ over a single period of x and t gives rise to

$$\Phi_{1T} = \gamma \Phi_{1XX} + i\alpha_1 (AA_X^* - A_X A^*), \quad (4.5.40a)$$

$$H_{2T} = \gamma H_{2XX} + (\alpha_2 \gamma^{-1} + \gamma \alpha_3) (|A|^2)_{XX}, \quad (4.5.40b)$$

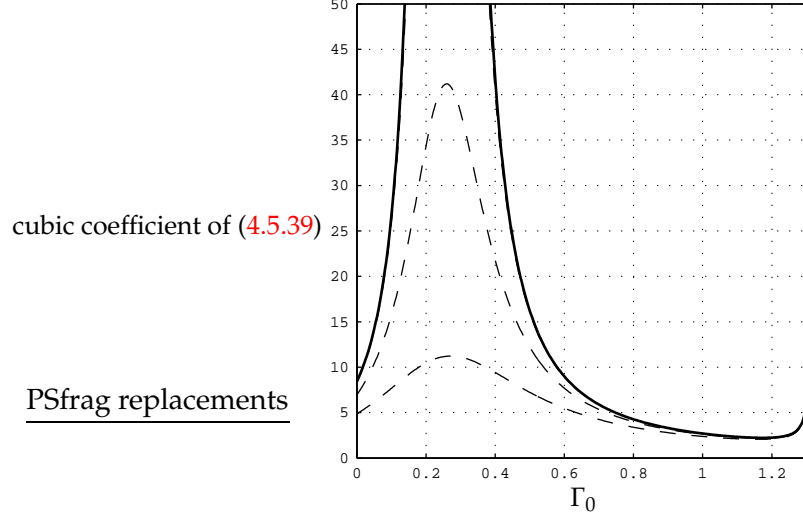


Figure 4.7: The modified cubic coefficient of (4.5.39) plotted against Γ_0 for $H = 1$ and $\gamma = 0, 0.01, 0.05, 0.1$. This figure should be contrasted with figure 4.6.

where

$$\alpha_1 = \frac{1}{64} \operatorname{csch}^3 H \operatorname{sech} H \left(-3H + 6\Gamma_0 + (32H - 6\Gamma_0) \cosh^2 H - 3 \cosh H \sinh H \right), \quad (4.5.41a)$$

$$\alpha_2 = \frac{1}{4} \left(2\Gamma_0 + \coth H + H \operatorname{csch}^2 H \right), \quad (4.5.41b)$$

$$\alpha_3 = \frac{1}{16} \left(16H - 5 \coth H + 3H \operatorname{csch}^2 H \right). \quad (4.5.41c)$$

Note that (4.5.40b) is a conserved mode equation of the same form as (1.5.6b). However, since H_2 does not appear explicitly in the amplitude equation for A , (4.5.39), the same modulational phenomena associated with this equation (see §1.5) would not appear to be possible. It is interesting to note that without the wave-like behaviour of H_2 (and Φ_1), the τ -timescale would not be needed and the amplitude equation for A would be given by the right-hand side of (4.5.34), where the coupling with H_2 takes a similar form to the generic amplitude systems (1.5.6) and (3.2). However, this is not the case; the wave-like behaviour of large-scale modes causes H_2 to be partly slaved to $|A|^2$ and prevents H_2 from coupling to A .

4.5.4 Capillary waves

The occurrence of G_0^{-1} in the cubic coefficient of (4.5.39) indicates that such an equation is not valid for describing capillary waves ($G_0 = 0$). In fact, describing the evolution of capillary waves via a weakly nonlinear analysis is particularly tricky; indeed, we have failed to find a satisfactory asymptotic balance of terms for this case. The difficulty lies

in capturing the correct leading-order large-scale mode growth, which should be (cf. (4.2.28b))

$$\lambda|_{G_0=0} = \left(-\gamma \pm i(H \coth H)^{1/2}\right) k^2 + O(k^4).$$

To match this behaviour, we must have mean modes H_m and Φ_n such that their evolution equations are coupled in the following manner:

$$H_{mT} = \gamma H_{mXX} - H\Phi_{nXX} + \text{nl.t.}, \quad (4.5.42)$$

$$\Phi_{nT} = \gamma\Phi_{nXX} + \coth HH_{mXX} + \text{nl.t} \quad (4.5.43)$$

where ‘nl.t.’ is shorthand for nonlinear terms. Our present scalings for X and T appear to be appropriate as we require $X^2 \sim T$ for (4.5.43) to be consistent. It also then follows that $H_m \sim \Phi_n$. Now, following a similar weakly nonlinear analysis as for the mixed gravity–capillary regime, the first mean resonance which must be balanced lies at $O(\epsilon^2)$ (cf. (4.5.24)). Thus, without introducing a new timescale, we must choose $\Phi_n \sim \epsilon^0$ which subsequently implies $H_m \sim \epsilon^0$. However, this cannot be correct as it breaks the assumption of the surface deformation being small. Thus, the most natural scalings that give the correct large-scale behaviour do not deliver consistent amplitude equations. Considerable research into alternative scaling arrangements has likewise failed to find a consistent amplitude description for this regime.

4.5.5 Summary

In this section, we have derived a cubic Ginzburg–Landau equation for the amplitude of SWs valid everywhere except for the capillary wave ($G_0 = 0$) regime. While the analysis has been quite involved at times, incorporating a number of co-moving frames of reference, the final amplitude equation (4.5.39) is only a slight modification from that of the infinite-depth case. The lack of coupling to a separate large-scale mode in this equation removes the possibility of the new modulational behaviour for the SW amplitude. However, we shall later (in §4.7) see that the dynamics of full numerical simulation of the model equations (4.2.21) reveal considerably richer dynamics than that suggested by a weakly nonlinear analysis that leads to a cubic Ginzburg–Landau equation with real coefficients.

4.6 Nonlinear analysis III: A distinguished limit

In this section, we perform weakly nonlinear analyses of the model equations (4.2.21) for the cases of both infinite and finite fluid depth. What differentiates the analysis

of this section from that of the previous two is that we employ only one small parameter, rather than two. This facilitates a more systematic weakly nonlinear analysis and does not require the use of ad hoc techniques to derive amplitude equations. To do this, we explicitly scale all variables with the dissipation parameter γ , adopting the distinguished limit introduced by Mancebo and Vega [210]. In the case of infinite depth, this allows the derivation of the quintic Ginzburg–Landau equation reported by Mancebo and Vega [210], which accounts for the high sensitivity of the cubic coefficient to wavenumber shifts. When the same limit is considered for the finite-depth problem, this quintic Ginzburg–Landau equation is found to be coupled to a large-scale mode.

4.6.1 Infinite depth

We consider the distinguished limit

$$|f - f_c| \sim |\partial_t| \sim \gamma^3, \quad |A|^2 \sim |\partial_x| \sim \gamma^2, \quad (4.6.1)$$

where the dissipation parameter $0 < \gamma \ll 1$ is used as the sole perturbation parameter. We implement these scalings in a nonlinear analysis by expanding h and ϕ as series in γ :

$$h(x, t, X, T) = \sum_{n=1}^{\infty} \gamma^n h_n(x, t, X, T), \quad (4.6.2a)$$

$$\phi(x, t, X, T) = \sum_{n=1}^{\infty} \gamma^n \phi_n(x, t, X, T), \quad (4.6.2b)$$

and altering the action of ∂_t and ∂_x to

$$\frac{\partial}{\partial t} \mapsto \frac{\partial}{\partial t} + \gamma^3 \frac{\partial}{\partial T}, \quad \text{and} \quad \frac{\partial}{\partial x} \mapsto \frac{\partial}{\partial x} + \gamma^2 \frac{\partial}{\partial X}. \quad (4.6.3)$$

As discussed in §4.3, the forcing amplitude is also small at onset and so we set $f = \gamma f_{1c} + \gamma^3 f_2$. Finally, we partition the operation of $\hat{\mathcal{D}}$ (defined in (4.2.2)) as $\hat{\mathcal{D}} = \hat{\mathcal{D}}_0 + \gamma^2 \hat{\mathcal{D}}_1$, where

$$\hat{\mathcal{D}}_0 u(x, X) = \int_{-\infty}^{\infty} |k| \hat{u}(k) e^{ikx} dx, \quad (4.6.4a)$$

$$\hat{\mathcal{D}}_1 u(x, X) = -i \frac{\partial u}{\partial X}; \quad (4.6.4b)$$

since $\hat{\mathcal{D}}$ is recovered in the $H \rightarrow \infty$ of $\hat{\mathcal{E}}$, the operators $\hat{\mathcal{D}}_0$ and $\hat{\mathcal{D}}_1$ can also be found by taking the limit $H \rightarrow \infty$ in their finite-depth counterparts (4.5.5). Within this framework, the linear problem is:

$$\mathbf{L}_{\text{inf}} \begin{pmatrix} h_1 \\ \phi_1 \end{pmatrix} = \begin{pmatrix} 0 \\ 0 \end{pmatrix}, \quad \text{where} \quad \mathbf{L}_{\text{inf}} \equiv \begin{pmatrix} \partial_t & -\hat{\mathcal{D}}_0 \\ G_0 - \Gamma_0 \partial_x^2 & \partial_t \end{pmatrix}. \quad (4.6.5)$$

Eliminating ϕ_1 from (4.6.5) yields a problem $\mathcal{L}_{\text{inf}}(h_1) = 0$, where

$$\mathcal{L}_{\text{inf}}(h_1) = h_{1tt} + \hat{\mathcal{D}}_0 [G_0 h_1 - \Gamma_0 h_{1xx}], \quad (4.6.6)$$

which has general solution

$$h_1 = A(X, T)e^{i\omega t + ikx} + B(X, T)e^{i\omega t - ikx} + \text{c.c.}, \quad (4.6.7)$$

where ω and k are related by the dispersion relation

$$\omega^2 = |k|(G_0 + \Gamma_0 k^2). \quad (4.6.8)$$

Subsequently, after some light manipulation of (4.6.5), we find a corresponding solution for ϕ_1 :

$$\phi_1 = \frac{i\omega}{|k|} \left[A e^{i\omega t + ikx} + B e^{i\omega t - ikx} \right] + \text{c.c.} \quad (4.6.9)$$

At this order, we are unable to determine the wavenumber and corresponding frequency of the selected solution; the values of k and ω are determined by the parametric forcing terms that occur at higher order.

The $O(\gamma^2)$ problem reads

$$\mathbf{L}_{\text{inf}} \begin{pmatrix} h_2 \\ \phi_2 \end{pmatrix} = \begin{pmatrix} h_{1xx} - (h_1 \phi_{1x})_x - \hat{\mathcal{D}}_0 (h_1 \hat{\mathcal{D}}_0 \phi_1) \\ \phi_{1xx} - 4f_{1c} \sin(2t)h_1 + \frac{1}{2}(\hat{\mathcal{D}}_0 \phi_1)^2 - \frac{1}{2}(\phi_{1x})^2 \end{pmatrix}, \quad (4.6.10)$$

and after eliminating ϕ_2 from this system, we find

$$\begin{aligned} \mathcal{L}_{\text{inf}}(h_2) = & \partial_t [h_{1xx} - (h_1 \phi_{1x})_x - \hat{\mathcal{D}}_0 (h_1 \hat{\mathcal{D}}_0 \phi_1)] \\ & + \hat{\mathcal{D}}_0 [\phi_{1xx} - 4f_{1c} \sin(2t)h_1 + \frac{1}{2}(\hat{\mathcal{D}}_0 \phi_1)^2 - \frac{1}{2}(\phi_{1x})^2], \end{aligned} \quad (4.6.11)$$

where, upon substitution of (4.6.7) and (4.6.9), the right-hand side of (4.6.11) comprises terms proportional to $e^{\pm i\omega t \pm ikx}$, $e^{\pm i\omega t \pm ikx \pm 2it}$, $e^{\pm 2i\omega t \pm 2ikx}$ and $e^{\pm 2ikx}$. We look for solutions that balance the parametric forcing terms (e.g., $e^{\pm i\omega t \pm ikx \pm 2it}$) with the natural wave-trains (i.e. $e^{\pm i\omega t \pm ikx}$) of the system. Thus, we choose to pursue subharmonic solutions with $\omega = 1$ (which, by (4.6.8), have wavenumber $k = 1$ —recall that by definition $G_0 + \Gamma_0 = 1$) as these are the first to become unstable (see figure 4.4). Now, collecting the terms proportional to the primary modes $e^{it \pm ix}$, we find the conditions:

$$f_{1c} B^* - A = 0, \quad (4.6.12a)$$

$$f_{1c} A^* - B = 0, \quad (4.6.12b)$$

and so we set the criticality condition $f_{1c} = 1$ and henceforth specify $B^* = A$. Note that, incorporating these constraints, h_1 can be rewritten as the SW

$$\begin{aligned} h_1 &= A \left(e^{it+ix} + e^{-it+ix} \right) + \text{c.c.}, \\ &\propto A e^{ix} \cos t + \text{c.c.}, \end{aligned} \quad (4.6.13)$$

matching the leading-order behaviour of the linear solution (4.3.25a) found in §4.3. In addition, this result is instructive in deriving higher-order solvability conditions, which we consider in detail now.

Solvability conditions: The adjoint problem of (4.6.5) is

$$\mathbf{L}_{\text{inf}}^{\dagger} \begin{pmatrix} h_1^{\dagger} \\ \phi_1^{\dagger} \end{pmatrix} = \begin{pmatrix} 0 \\ 0 \end{pmatrix}, \quad \text{where} \quad \mathbf{L}_{\text{inf}}^{\dagger} \equiv \begin{pmatrix} -\partial_t & G_0 - \Gamma_0 \partial_x^2 \\ -\hat{\mathcal{D}}_0 & -\partial_t \end{pmatrix}. \quad (4.6.14)$$

Solutions to this system take the form:

$$\phi_1^{\dagger} = Ae^{i\omega t + ikx} + Be^{i\omega t - ikx} + \text{c.c.}, \quad (4.6.15a)$$

$$h_1^{\dagger} = -\frac{i\omega}{|k|} \left[Ae^{i\omega t + ikx} + Be^{i\omega t - ikx} \right] + \text{c.c.}, \quad (4.6.15b)$$

where ω and k obey the dispersion relation (4.6.8). Now, using the $O(\gamma^2)$ results for the linear solution (4.6.7), we set $\omega = k = 1$ and substitute $B^* = A$ in (4.6.15b). Hence, we find h_1^{\dagger} becomes

$$h_1^{\dagger} = -iA \left[e^{it+ix} - e^{-it+ix} \right] + \text{c.c.}, \quad (4.6.16)$$

and thus our solvability condition for problems in the form

$$\mathcal{L}_{\text{inf}}(h_n) = \partial_t \text{RHS}_1 + \hat{\mathcal{D}}_0 \text{RHS}_2, \quad (4.6.17)$$

(which is the generic problem at each order of γ after ϕ_n has been eliminated) is

$$\int_0^{2\pi} \int_0^{2\pi} \left(e^{it+ix} - e^{-it+ix} \right) (\partial_t \text{RHS}_1 + \hat{\mathcal{D}}_0 \text{RHS}_2) dx dt = 0, \quad (4.6.18)$$

where we have integrated over a single period of x and t . Note that at $O(\gamma^n)$ where $n \geq 3$, terms proportional to the primary modes $e^{\pm it \pm ix}$, whose behaviour is not prescribed by the solvability conditions, can be balanced by an appropriate introduction to the h planform at $O(\gamma^{n-1})$. This introduction should comprise the usual terms required to balance the $O(\gamma^{n-1})$ harmonics, plus terms proportional to the adjoint solution (4.6.15b). More specifically, we set

$$h_{n-1} = (n-1)^{\text{th}} \text{ order harmonics} \\ + P_{n-1}(X, T) \left(e^{it+ix} - e^{-it+ix} \right) + P_{n-1}^*(X, T) \left(e^{-it-ix} - e^{it-ix} \right), \quad (4.6.19)$$

where P_{n-1} is a complex amplitude (a similar introduction to ϕ_{n-1} is also required with complex amplitude Q_{n-1}). Subsequently, the balances at $O(\gamma^n)$ will dictate that P_{n-1} is slaved to the amplitudes of the linear solution.

Returning to the $O(\gamma^2)$ problem, we introduce expressions for h_2 and ϕ_2 of the form (4.6.19). We set

$$h_2 = h_{(0,2)}A^2e^{2ix} + h_{(2,2)}A^2e^{2it+2ix} + h_{(2,-2)}A^{*2}e^{2it-2ix} + ih_{(3,1)}Ae^{3it+ix} + ih_{(3,-1)}A^*e^{3it-ix} + P_2 \left(e^{it+ix} - e^{-it+ix} \right) + \text{c.c.}, \quad (4.6.20)$$

where the coefficients $h_{(m,n)}$ are real and take the values:

$$h_{(0,2)} = 2(1 + 3\Gamma_0)^{-1}, \quad (4.6.21a)$$

$$h_{(2,2)} = h_{(2,-2)} = (1 - 3\Gamma_0)^{-1}, \quad (4.6.21b)$$

$$h_{(3,1)} = h_{(3,-1)} = -1/4. \quad (4.6.21c)$$

The corresponding solution for ϕ_2 takes the form

$$\phi_2 = \phi_{(2,2)}iA^2e^{2it+2ix} + \phi_{(2,-2)}iA^{*2}e^{2it-2ix} + \phi_{(3,1)}Ae^{3it+ix} + \phi_{(3,-1)}A^*e^{3it-ix} + Q_2 \left(e^{it+ix} - e^{-it+ix} \right) + \text{c.c.} \quad (4.6.22)$$

where

$$\phi_{(2,2)} = \phi_{(2,-2)} = (1 - 3\Gamma_0)^{-1}, \quad (4.6.23a)$$

$$\phi_{(3,1)} = \phi_{(3,-1)} = 3/4, \quad (4.6.23b)$$

while Q_2 is found to obey the relationship $Q_2 = A + iP_2$.

Ascending to $O(\gamma^3)$, the solvability condition (4.6.18) is automatically satisfied and we find the value of P_2 by collecting terms proportional to e^{it+ix} :

$$P_2 = \frac{3}{8}iA + \frac{1}{4}(2\Gamma_0 + 1)A_X + i \left(\frac{81\Gamma_0^3 + 36\Gamma_0^2 + 27\Gamma_0 - 8}{8(1 + 3\Gamma_0)(1 - 3\Gamma_0)} \right) |A|^2A. \quad (4.6.24)$$

We also balance the $O(\gamma^3)$ resonances by suitable choices of h_3 and ϕ_3 ; however, the details of this procedure are highly tedious and are not given explicitly here.

At $O(\gamma^4)$, applying the solvability condition (4.6.18) yields an amplitude equation for A :

$$A_T = f_2A + \frac{1}{8}(1 + 2\Gamma_0)^2A_{XX} + \frac{3}{16}i(2\Gamma_0 + 9)A_X - \nu_1^{\text{inf}}|A|^2A - i\nu_2^{\text{inf}}A^2A_X^* - i\nu_3^{\text{inf}}|A|^2A_X - \nu_4^{\text{inf}}|A|^4A, \quad (4.6.25)$$

where

$$\nu_1^{\text{inf}} = \frac{1}{32} \left(\frac{(9\Gamma_0 - 7)(9\Gamma_0^2 - 21\Gamma_0 - 16)}{(1 - 3\Gamma_0)(1 + 3\Gamma_0)} \right), \quad (4.6.26a)$$

$$\nu_2^{\text{inf}} = -\frac{1}{8} \left(\frac{(1 + 2\Gamma_0)(9\Gamma_0^2 - 15\Gamma_0 + 8)}{1 - 3\Gamma_0} \right), \quad (4.6.26b)$$

$$\nu_3^{\text{inf}} = -\frac{1}{2} \left(\frac{(1 + 2\Gamma_0)(27\Gamma_0^3 + 6\Gamma_0 - 1)}{(1 - 3\Gamma_0)(1 + 3\Gamma_0)} \right), \quad (4.6.26c)$$

$$\nu_4^{\text{inf}} = \frac{1}{32} \left(\frac{(81\Gamma_0^3 + 36\Gamma_0^2 + 27\Gamma_0 - 8)(81\Gamma_0^3 + 36\Gamma_0^2 + 3\Gamma_0 - 16)}{(1 - 3\Gamma_0)^2(1 + 3\Gamma_0)^2} \right). \quad (4.6.26d)$$

The term proportional to iA_X in (4.6.25) corresponds to the shift in wavenumber at threshold arising from the fact the wavenumber of the subharmonic mode is not exactly $k = 1$. This is in correspondence with the solvability condition (4.5.18) where a similar term was found, and had to be dealt with in an ad hoc fashion. In this case, we are able to eliminate this term and centre the amplitude equation by making the phase change $A = Ae^{-i\Xi X}$ where Ξ is real. Some manipulation then reveals that choosing

$$\Xi = \frac{3(9 + 2\Gamma_0)}{4(1 + 2\Gamma_0)^2} \quad (4.6.27)$$

allows the amplitude equation (4.6.25) to be rewritten as

$$A_T = \left(f_2 + \frac{9(9 + 2\Gamma_0)^2}{128(1 + 2\Gamma_0)^2} \right) A + \frac{1}{8}(1 + 2\Gamma_0)^2 A_{XX} - \mu_1^{\text{inf}} |A|^2 A - i\nu_2^{\text{inf}} A^2 A_X^* - i\nu_3^{\text{inf}} |A|^2 A_X - \nu_4^{\text{inf}} |A|^4 A, \quad (4.6.28)$$

where the cubic coefficient ν_1^{inf} has been replaced by

$$\mu_1^{\text{inf}} = -\frac{1}{16} \left(\frac{162\Gamma_0^4 + 1413\Gamma_0^3 + 654\Gamma_0^2 + 53\Gamma_0 - 218}{(1 - 3\Gamma_0)(1 + 3\Gamma_0)(1 + 2\Gamma_0)} \right). \quad (4.6.29)$$

The coefficients μ_1^{inf} , ν_2^{inf} , ν_3^{inf} and ν_4^{inf} are plotted against Γ_0 in figure 4.8. It can be seen that all the coefficients are singular at the three-wave resonance point $\Gamma_0 = 1/3$, indicating a break-down in the balance of terms near this point. As such, the amplitude equation (4.6.28) is not valid near this point and an alternative set of scalings is required in this regime to derive consistent equations. Considering spatially uniform (over the X scale) SW solutions of the form $A(X, T) = Q$, we find that solutions can always saturate for $\nu_4^{\text{inf}} > 0$, while with $\nu_4^{\text{inf}} < 0$, small-amplitude solutions can only saturate while $\mu_1^{\text{inf}} > 0$ and

$$f_2 < -\frac{\mu_1^{\text{inf}2}}{4\nu_4^{\text{inf}}} - \frac{9(9 + 2\Gamma_0)^2}{128(1 + 2\Gamma_0)^2}. \quad (4.6.30)$$

When equality holds in (4.6.30), a saddle node bifurcation takes place and no solution can saturate.

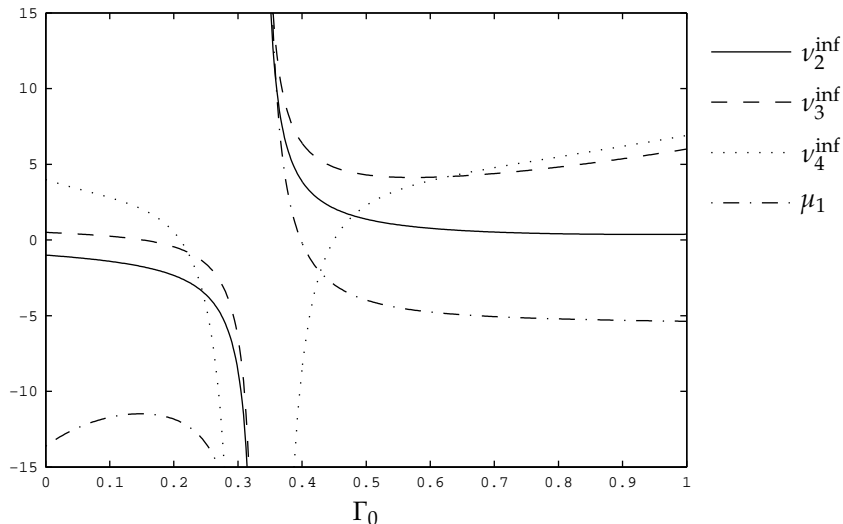


Figure 4.8: The coefficients $\mu_1^{\text{inf}}, \nu_2^{\text{inf}}, \nu_3^{\text{inf}}, \nu_4^{\text{inf}}$ of the amplitude equation (4.6.28), plotted as a function of the capillary number Γ_0 .

The amplitude equation (4.6.25) is unusual since it is derived in an asymptotically consistent manner and contains both cubic and quintic terms. This is possible since the coefficients of the cubic terms are small (cf. the Ginzburg–Landau-equation (4.5.39)) while quintic terms are generated through the nonlinear interactions of h_2 and ϕ_2 (which contain terms of quadratic and cubic order). In fact, this quintic amplitude equation is the same as that proposed and investigated by Mancebo and Vega [210] (cf. (4.1.5)). As discussed in §4.1, it is quite different from the more commonly observed form of amplitude equation (4.1.3) due to the inclusion of a quintic term plus two extra cubic terms. These additions account for the extreme sensitivity of the cubic coefficient to wavenumber changes that has generally been ignored in previous literature. It is notable that the new, derivative cubic terms in (4.6.28) prevent the existence of a Lyapunov functional, which exists for the amplitude equations of Zhang and Viñals [96]. It is thus plausible that (4.6.28) has much richer dynamics than the amplitude equations of Zhang and Viñals [96]. Since this amplitude equation is not directly related to the central theme of this thesis, we choose not to investigate the solutions and general behaviour of (4.6.28) further. The reader is referred to Mancebo and Vega [210] for more details regarding (4.6.28) and its applicability.

4.6.2 Finite depth

In this section, we investigate the finite-depth problem in the distinguished limit (4.6.1). For consistent equations to be derived in this limit, we make similar expansions to the

previous section, but introduce an additional time-scale $\tau = \gamma^2 t$ and include an $O(1)$ mean mode in the ϕ series:

$$h(x, t, X, \tau, T) = \sum_{n=1} \gamma^n h_n(x, t, X, \tau, T), \quad (4.6.31a)$$

$$\phi(x, t, X, \tau, T) = \Phi_0(X, \tau, T) + \sum_{n=1} \gamma^n \phi_n(x, t, X, \tau, T). \quad (4.6.31b)$$

Note that the action of ∂_t is now

$$\frac{\partial}{\partial t} \mapsto \frac{\partial}{\partial t} + \gamma^2 \frac{\partial}{\partial \tau} + \gamma^3 \frac{\partial}{\partial T}. \quad (4.6.32)$$

Similar to §4.5, we expand the Fourier-integral operator $\hat{\mathcal{E}}$ as $\hat{\mathcal{E}} = \hat{\mathcal{E}}_0 + \gamma^2 \hat{\mathcal{E}}_1 + \gamma^4 \hat{\mathcal{E}}_2$, where $\hat{\mathcal{E}}_0$, $\hat{\mathcal{E}}_1$ and $\hat{\mathcal{E}}_2$ retain their definitions (4.5.5).

The linear problem is

$$\mathbf{L}_{\text{fin}} \begin{pmatrix} h_1 \\ \phi_1 \end{pmatrix} = \begin{pmatrix} 0 \\ 0 \end{pmatrix}, \quad \text{where} \quad \mathbf{L}_{\text{fin}} \equiv \begin{pmatrix} \partial_t & -\hat{\mathcal{E}}_0 \\ G_0 - \Gamma_0 \partial_x^2 & \partial_t \end{pmatrix}, \quad (4.6.33)$$

and, following the procedure outlined in the previous section, we find the linear solutions to be:

$$h_1 = A e^{i\omega t + ikx} + B e^{i\omega t - ikx} + \text{c.c.}, \quad (4.6.34a)$$

$$\phi_1 = \frac{i\omega}{k \tanh(kH)} \left[A e^{i\omega t + ikx} + B e^{i\omega t - ikx} \right] + \text{c.c.}, \quad (4.6.34b)$$

where ω and k now obey the dispersion relation

$$\omega^2 = \tanh(kH) (G_0 k + \Gamma_0 k^3). \quad (4.6.35)$$

Subsequently, at $O(\gamma^2)$, we restrict attention to wavetrains with $k = 1$ and $\omega = 1$, and satisfy the ensuing solvability conditions by setting $f_{1c} = \coth H$ and $B^* = A$. Also at this order, we find an evolution equation for Φ_0 (cf. (4.5.24))

$$\Phi_{0\tau} = -2 \text{csch}^2 H |A|^2 - G_0 H_2. \quad (4.6.36)$$

(Note, the coefficients of $|A|^2$ in this equation and (4.5.24) differ due to the slightly different linear solutions.) The analysis at this order is completed by balancing the nonlinear harmonic terms through introducing appropriate expressions for h_2 and ϕ_2 . This procedure is straightforward but algebraically cumbersome and the details are omitted here. Importantly though, we introduce a large-scale mean mode H_2 to the planform for h_2 , which is required to balance higher-order terms.

At $O(\gamma^3)$, one finds the solvability condition

$$A_\tau = -iA\Phi_{0X}. \quad (4.6.37)$$

If we consider separately the evolution of the modulus and phase of A by setting $A = Q(X, \tau, T)e^{i\psi(X, \tau, T)}$, we find:

$$Q_\tau = 0, \quad (4.6.38a)$$

$$\psi_\tau = -\Phi_{0X}, \quad (4.6.38b)$$

which suggests that the gradients of the mean mode Φ_0 cause the phase of the SW amplitude to change; this is equivalent to the SWs drifting in space. Curiously, the absolute value of the amplitude does not vary over the τ timescale. Also at this order, we find $\Phi_{0T} = 0$.

At $O(\gamma^4)$, applying solvability conditions gives rise to an amplitude equation for A :

$$\begin{aligned} A_T = & f_2 \tanh(H)A + \alpha_{\text{diff}}A_{XX} + \frac{1}{16}i(27 - 5 \operatorname{csch} H \operatorname{sech} H + 6\Gamma_0 \tanh H)A_X \\ & - \nu_1^{\text{fin}}|A|^2A - i\nu_2^{\text{fin}}A^2A_X^* - i\nu_3^{\text{fin}}|A|^2A_X - \nu_4^{\text{fin}}|A|^4A + i\nu_5^{\text{fin}}H_2A_X \\ & + \nu_6^{\text{fin}}H_2A + \nu_7^{\text{fin}}|A|^2AH_2 + i\nu_8^{\text{fin}}H_{2X}A - \frac{1}{2}\operatorname{csch}^2(2H)H_2^2A, \end{aligned} \quad (4.6.39)$$

where α_{diff} retains the definition (4.5.33) but $\nu_1^{\text{fin}}, \dots, \nu_8^{\text{fin}}$ have highly cumbersome definitions which we do not give explicitly here. As in the previous section, one can eliminate the term proportional to iA_X by transforming A as $A = Ae^{-i\Xi X}$, where

$$\Xi = \frac{1}{4} \left(\frac{\sinh(2H)(27 \sinh(2H) + 6\Gamma_0 \cosh(2H) - 10H - 6\Gamma_0)}{\sinh(2H) + 2\Gamma_0 \cosh(2H) - 2\Gamma_0 + 2H} \right). \quad (4.6.40)$$

This transforms (4.6.39) to

$$\begin{aligned} A_T = & (f_2 \tanh H + \mu_2)A + \alpha_{\text{diff}}A_{XX} \\ & - \mu_1^{\text{fin}}|A|^2A - i\nu_2^{\text{fin}}A^2A_X^* - i\nu_3^{\text{fin}}|A|^2A_X - \nu_4^{\text{fin}}|A|^4A + i\nu_5^{\text{fin}}H_2A_X \\ & + \nu_6^{\text{fin}}H_2A + \nu_7^{\text{fin}}|A|^2AH_2 + i\nu_8^{\text{fin}}H_{2X}A - \frac{1}{2}\operatorname{csch}^2(2H)H_2^2A, \end{aligned} \quad (4.6.41)$$

where the cubic coefficient ν_1^{fin} of (4.6.39) has been modified to a new value μ_1^{fin} and the linear coefficient has been augmented by the addition of a complicated expression μ_2 (omitted here). The amplitude equation is composed of an equation qualitatively identical to the quintic Ginzburg–Landau equation (4.6.28) derived in the infinite-depth case, coupled to the large-scale mode H_2 via five separate terms. The coefficients $\nu_2^{\text{fin}}, \nu_3^{\text{fin}}, \nu_4^{\text{fin}}, \mu_1^{\text{fin}}$ are plotted in figure 4.9, where we see qualitatively similar behaviour to figure 4.8; unmodulated SW solutions will behave in a similar manner to the infinite-depth case.

We also find at this order

$$H_{2\tau} = -H\Phi_{0XX}, \quad (4.6.42)$$

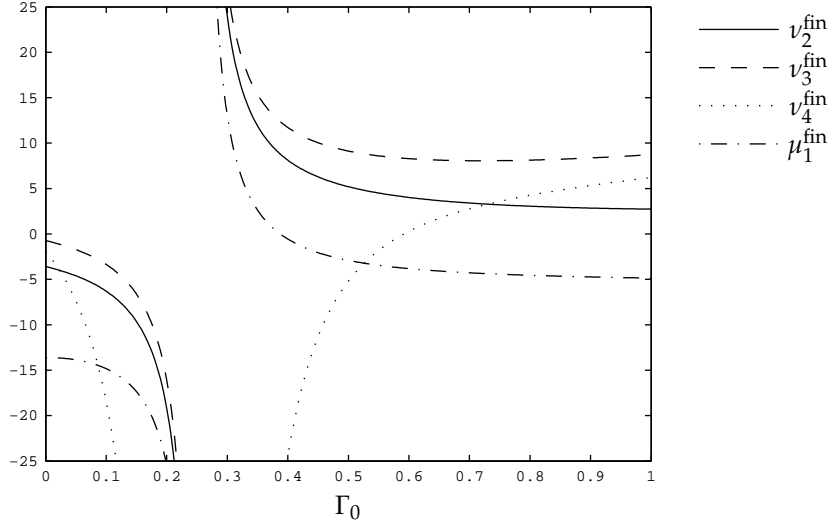


Figure 4.9: The coefficients $\mu_1^{\text{fin}}, \nu_2^{\text{fin}}, \nu_3^{\text{fin}}, \nu_4^{\text{fin}}$ of the amplitude equation (4.6.28), plotted as a function of the capillary number Γ_0 . Through comparison with figure 4.8, the behaviour of these coefficients can be seen to be qualitatively identical to the corresponding coefficients in the infinite-depth equation (4.6.28).

which, after differentiating (4.6.36) with respect to τ and substituting in (4.6.42), leads to the wave equation

$$\Phi_{0\tau\tau} = G_0 H \Phi_{0XX}. \quad (4.6.43)$$

Thus, we can write $\Phi_0 = G_1(\eta) + G_2(\xi)$, where G_1 and G_2 are arbitrary functions and η and ξ are co-moving variables, defined by (4.5.29). Further, manipulating (4.6.36), we can write (cf. (4.5.30))

$$H_2 = -2G_0^{-1} \text{csch}^2 H |A|^2 - \left(\frac{H}{G_0} \right)^{1/2} [G_{1\eta} + G_{2\xi}]. \quad (4.6.44)$$

Alternatively, Φ_0 can be eliminated to give the forced wave equation for H_2 (cf. (4.5.26)):

$$H_{2\tau\tau} = G_0 H H_{2XX} + 2H \text{csch}^2 H (|A|^2)_{XX}. \quad (4.6.45)$$

In both (4.6.45) and (4.6.43), large-scale modes obey the correct behaviour, predicted in §4.2.3.

Finally, at $O(\gamma^5)$, we find an evolution equation for H_2 :

$$H_{2T} = \left(2\Gamma_0 + \coth H + H \text{csch}^2 H \right) (|A|^2)_{XX}. \quad (4.6.46)$$

We can see that this evolution equation for H_2 takes a similar form to (4.5.40b), except H_2 does not relax diffusively (the diffusion term occurs at higher order). A corollary of this result is that since there is only one term in the right-hand side of (4.6.46), nontrivial steady states are not permitted.

4.6.3 Summary

In this section, a more systematic approach to the weakly nonlinear analysis of the model equations (4.2.21) has been utilised. Rather than employing two small parameters to derive amplitude equations (as in §4.5), we have used the distinguished limit proposed by Mancebo and Vega [210], where all quantities are scaled in terms of γ , the dissipation parameter.

Utilising this framework for the study of the infinite-depth model introduced by Zhang and Viñals [96], we have been able to re-derive the amplitude equation constructed by Mancebo and Vega [210]. This equation allows the wavenumber shift, induced by nonzero viscosity, to be systematically treated by transforming the SW amplitude; in §4.5, the terms generated by the wavenumber shift could only be dealt with by an ad hoc method. One should note though that this limit specifies $|f - f_c| \sim \gamma^3$, corresponding to a regime extremely close to threshold. As such, one expects the amplitude equation (4.6.28) to apply immediately above onset, while it is plausible that the amplitude equation derived by Zhang and Viñals [96] is relevant to larger values of the forcing parameter or to situations where the dissipation is small, but not of the same order as the distance above threshold.

In the finite-depth problem, we have derived a set of coupled amplitude equations for the amplitude of the SW and a large-scale mean mode. The amplitude equation for A takes a similar form to the corresponding equation from the infinite-depth case, but is augmented by the addition of five coupling terms, comprising A and either the large-scale mode H_2 or its gradient. This large-scale mode is partly slaved to $|A|^2$ and also features co-moving components, analogous to the results of §4.5. In addition to the new coupling terms, this amplitude system is intriguing as the SW amplitude varies over two timescales, although only the phase of A is actually dependent on both.

This amplitude system admits SWs as a solution; however, we do not examine the modulational stability problem in this present work. This is because the quintic nature of the amplitude equation for A causes SWs to have an unwieldy definition and performing a stability analysis presents sizeable algebraic hurdles. As such, we content ourselves with the derivation of a consistent set of amplitude equations for this system and leave the stability behaviour of SWs as an open question. In addition, an interesting extension to this work would also be to numerically examine the behaviour of this amplitude system.

4.7 Numerical simulation

In this section, we numerically study the modified quasi-potential equations (4.2.21) with periodic boundary conditions using Fourier spectral methods for spatial evaluation and an exponential time-differencing method. A corresponding investigation is carried out by Zhang and Viñals [221] for the two-dimensional system (4.2.1), where the fluid layer is assumed to have infinite depth. Their results compare favourably with the predictions of the corresponding multiscale analysis of §4.5 [96]. Although the weakly nonlinear analysis of the previous section suggests that, even with finite depth, there is no new modulational instability of SWs (at least in the mixed capillary–gravity regime), the simulations presented in this section do reveal amplitude-modulated solutions, although they are generally found away from threshold, where the application of the weakly nonlinear analysis is questionable.

Numerical code

To simulate the model equations (4.2.21), we employ a similar program to that used in §2.4.1 and §3.6, where nonlinear terms are computed pseudospectrally. See §2.4 and appendix B for further details of these methods. The model equations (4.2.21) are integrated from a random initial condition (Gaussian distributed noise with zero mean and variance 10^{-6}) for the surface displacement $h(x, 0)$; we also set $\phi(x, 0) = 0$. In addition, the initial spatial average of the surface displacement $\langle h(x, 0) \rangle$ is explicitly set to zero. As a consequence of the conservation law (4.2.3), the average level of the fluid surface should be a constant of the system. Monitoring the value of this mean displacement reveals that $|\langle h(x, t) \rangle| < 10^{-14}$ over large times; the conservation law is clearly preserved by the numerical scheme.

We set the system to be slightly supercritical through the condition,

$$f = \gamma(1 + \Delta) \coth H, \quad (4.7.1)$$

where Δ measures the fraction by which f exceeds the stability threshold $f = \gamma \coth H$. In addition, we use a low-pass filter which involves, at each timestep, multiplying the Fourier variables $\hat{h}(k, t)$ and $\hat{\phi}(k, t)$ by $\hat{\mathcal{F}}(k)$ where

$$\hat{\mathcal{F}}(k) = \begin{cases} 1 & \text{for } |k|/4 \leq 0.75, \\ 4(1 - \frac{1}{4}|k|) & \text{for } 0.75 < |k|/4 \leq 1, \\ 0 & \text{for } |k| > 4. \end{cases} \quad (4.7.2)$$

We note that this is equivalent to correcting alias errors. Such a real space smoothing function is introduced to remove a high wavenumber instability that can otherwise

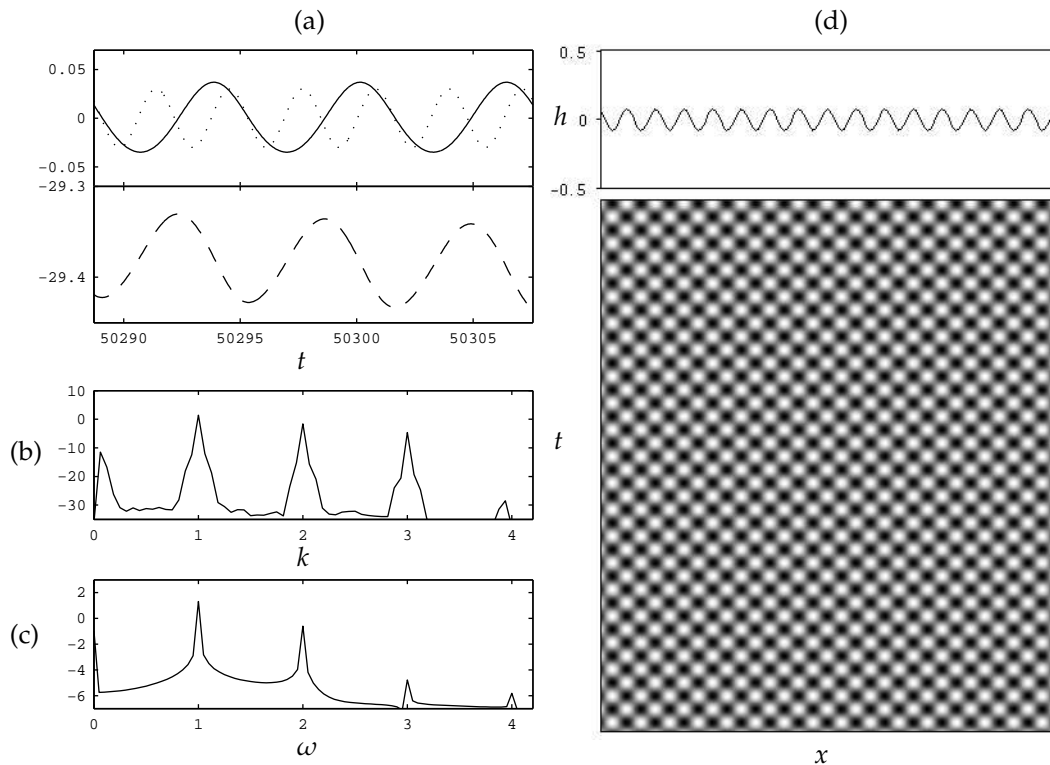


Figure 4.10: An example SW pattern from a simulation run with $G_0 = 0.3$, $\gamma = 0.01$ and $\Delta = 0.05$: (a) time series of $h(x_0, t)$ (solid line), $\phi(x_0, t)$ (dashed line) and the $\sin 2t$ forcing (dotted line); (b) power spectrum of the time series $h(x_0, t)$ (y -axis is plotted on a log scale); (c) power spectrum of the final profile $h(x, t_{\text{final}})$ (y -axis is plotted on a log scale); (d) space-time plot (over 40π units of t) and final profile of $h(x, t)$.

occur in the numerics after large times. This instability is usually found in inviscid systems; however, since the dissipation is very small here, the same instability can still occur [221]. Our computations take place in a container of size 32π , that is, 16 times the critical wavelength. A total of 512 Fourier modes are used for spatial resolution and the time step is $\Delta t = \min(1/c, 0.04)$ where c is the largest linear growthrate.

4.7.1 Mixed capillary–gravity waves

We first consider mixed capillary–gravity waves (including pure gravity waves), where $0 < G_0 \leq \coth H$. Simulations run with $\Delta = 0.01, 0.02, 0.05, 0.1$, $\gamma = 0.01, 0.05, 0.1$ and G_0 chosen to lie below a critical threshold value G_0^* (for $H = 1$, $G_0^* \approx 0.95$), have revealed only unmodulated SWs as the preferred pattern; figure 4.10 illustrates an example of the SW patterns observed. The power spectra of subfigures (b) and (c) clearly illustrate that the realised SW has wavenumber $k = 1$ and wavefrequency $\omega = 1$, con-

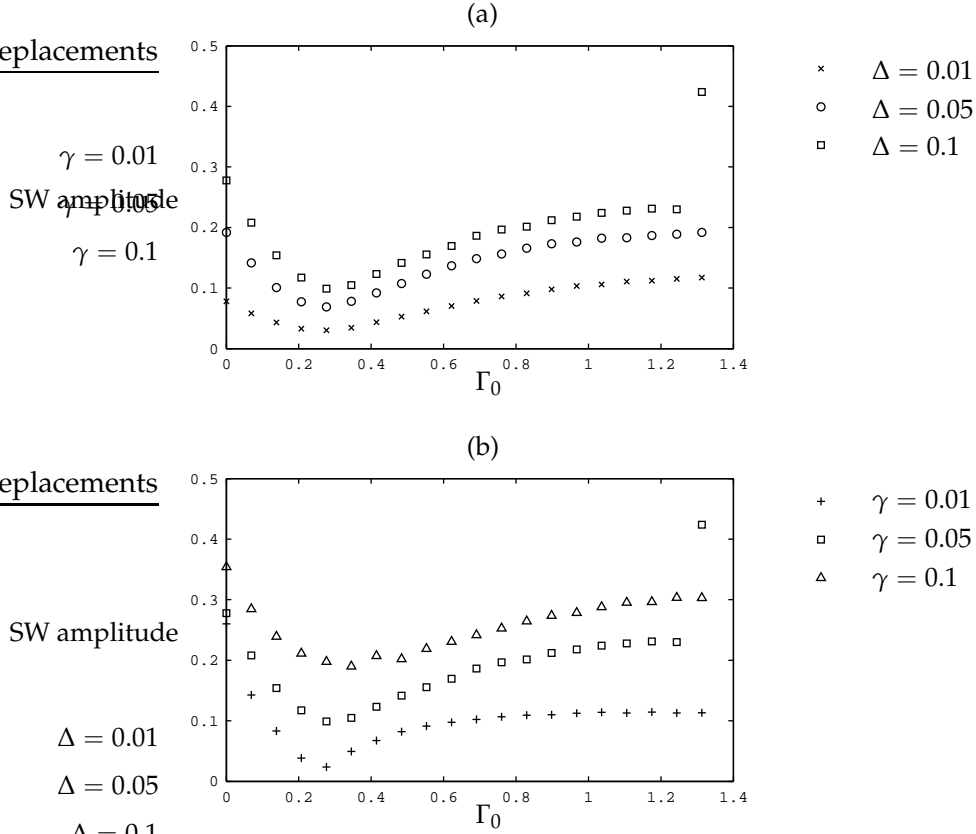


Figure 4.11: The amplitude of SWs, determined by taking the maximum of $|h(x, t)|$ over a single time period, plotted against Γ_0 . Subfigure (a) illustrates the effect of increasing Δ while (b) exhibits increasing γ values. For both subfigures $H = 1$ and we set $\gamma = 0.05$ in (a) and $\Delta = 0.1$ in (b).

firming the results of the linear analysis. We also see in (a) that the zero mode of ϕ is decreasing with time, in correspondence with the amplitude equation (4.4.14). In figure 4.11, the value of $|A|$ is plotted against Γ_0 for various values of Δ and γ . We see that, in correspondence with figure 4.7, the amplitude of SWs are smallest at the resonance point $\Gamma_0 = \frac{1}{3} \tanh H$; the outlying amplitude with $\gamma = 0.05$ and $\Delta = 0.1$ corresponds to the selection of a modulated SW pattern. SW patterns are also observed for larger values of γ ; however, their appearance, while similar to that of figure 4.10, takes a different form due to greater nonlinear contributions. In such cases, the linear approximation (4.5.15) is no longer an adequate description.

With $G_0^* < G_0 \leq \coth H$, that is, in a neighbourhood of the gravity wave limit $G_0 = \coth H$, SW solutions with uniformly propagating modulations can be found. Two such patterns are illustrated in figure 4.12, where we see that the basic SW pattern is modulated by ‘pulses’ of modulation, which travel uniformly with speed $(G_0 H)^{1/2}$, in either direction. This behaviour has a strong correspondence with the analysis of

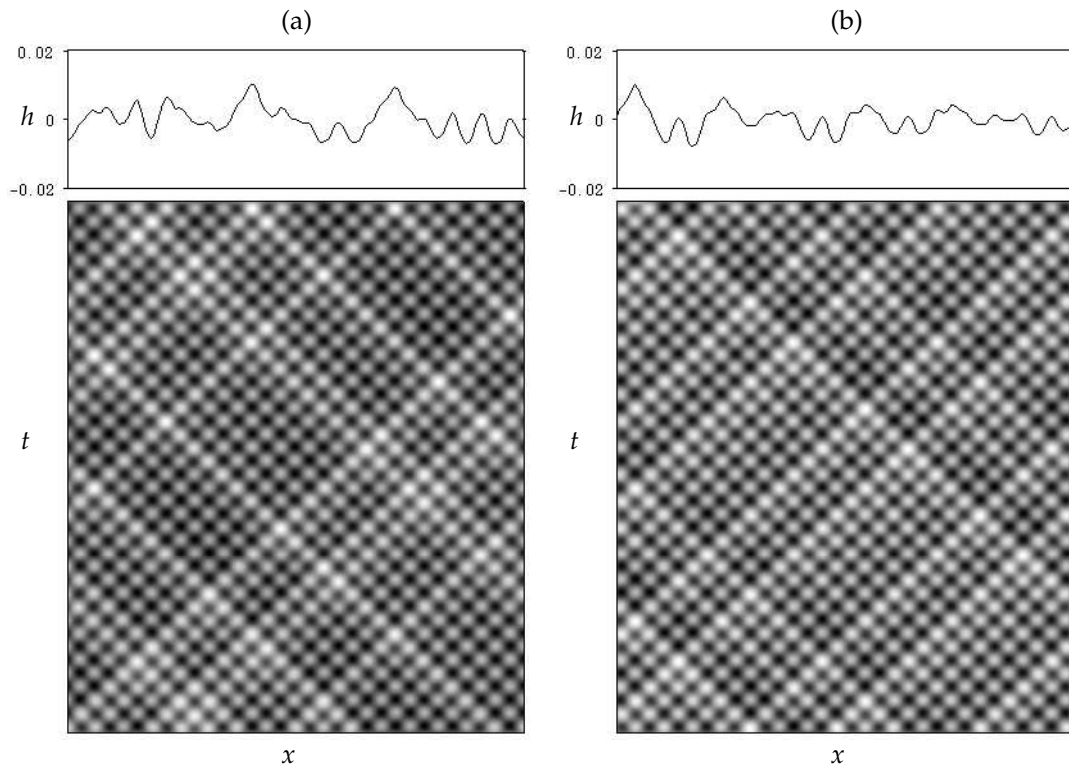


Figure 4.12: Modulated SWs in the mixed capillary-gravity regime, with (a) $\Delta = 0.1, \gamma = 0.01, G_0 = 1, H = 1$ and (b) $\Delta = 0.05, \gamma = 0.01, G_0 = 1, H = 1$. The pulses of modulation are travelling with uniform speed $(G_0 H)^{1/2}$, which in both cases here, equals one. Similar solutions have been observed with other values of H .

§4.5, where H was found to exhibit a large-scale mode which also propagated with this speed. These patterns are generally only found with small values of γ ; with $\gamma = 0.1$, only uniform SWs are found. Also, such novel patterns only occur for $\Delta > 0.05$; nearer to threshold, only unmodulated SWs are found. Thus, it would seem that the amplitude equations (4.5.24), (4.5.26) and (4.5.39) only apply quite close to threshold; however, the form of the equations indicate the possible solutions that can arise when SWs are unstable.

At larger values of either γ or Δ , new forms of modulated SW solutions are found, where, again, the modulation corresponds to the uniformly propagating modes identified in §4.5. In figure 4.13(a), we see a SW pattern where the modulation takes the form of a spatially and temporally periodic form; such patterns are only found with $\gamma > 0.2$. If we increase Δ rather than γ , then modulated patterns such as that illustrated in figure 4.13(b) are found. Here we see modulation in the form of a single uniformly propagating pulse. We note that for large γ the perturbation expansion that allows f to be calculated is no longer valid. In these circumstances, the value of Δ (as defined by

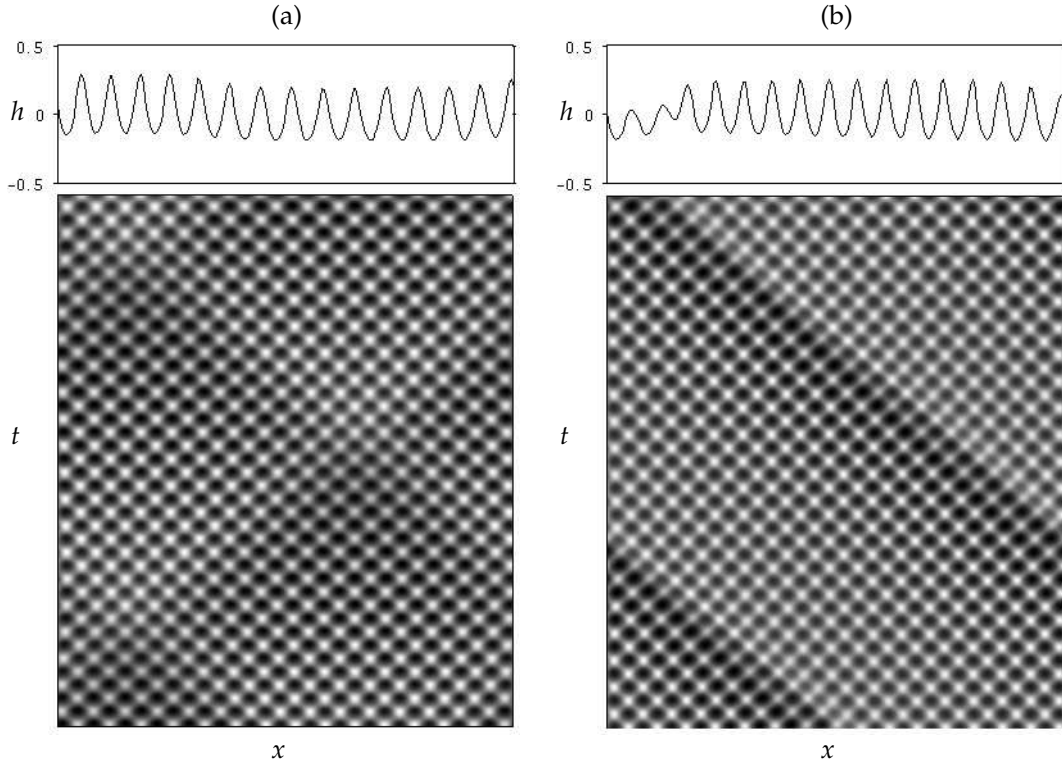


Figure 4.13: Modulated SW patterns in the pure gravity wave regime, with (a) $\Delta = 0.05, \gamma = 0.2$; (b) $\Delta = 0.2, \gamma = 0.05$. In both cases, $H = 1$ and $G_0 = \coth H$.

(4.7.1)) must be treated cautiously.

4.7.2 Capillary waves

The most interesting behaviour of the model equations is found in the capillary wave regime ($G_0 = 0$), where no corresponding weakly nonlinear theoretical results were obtainable. Intriguingly, we find modulated SW patterns where the modulation takes the form of a stationary large-scale wave; such a pattern is illustrated in figure 4.14. As can be seen from subfigure (a), this state is composed of a large-scale, steady mode of the same order as the normal SW mode; the SWs themselves are only slightly modulated in amplitude. The plots of (b) and (c) illustrate the evolution of this pattern in Fourier space; we see that the large-scale mode grows slowly until it is of a similar order to the pattern mode, and then saturates to form the selected pattern. Such behaviour of the large-scale mode is in correspondence with the large-scale growthrate (4.2.28b). Also in (c), we see the unbounded linear growth of the zero mode of ϕ , in correspondence with (4.4.14). At larger values of Δ , similar patterns to this one have been observed, but with two or more waves of modulation.

Increasing γ gives rise to SW patterns with strong suppression of the waves in certain

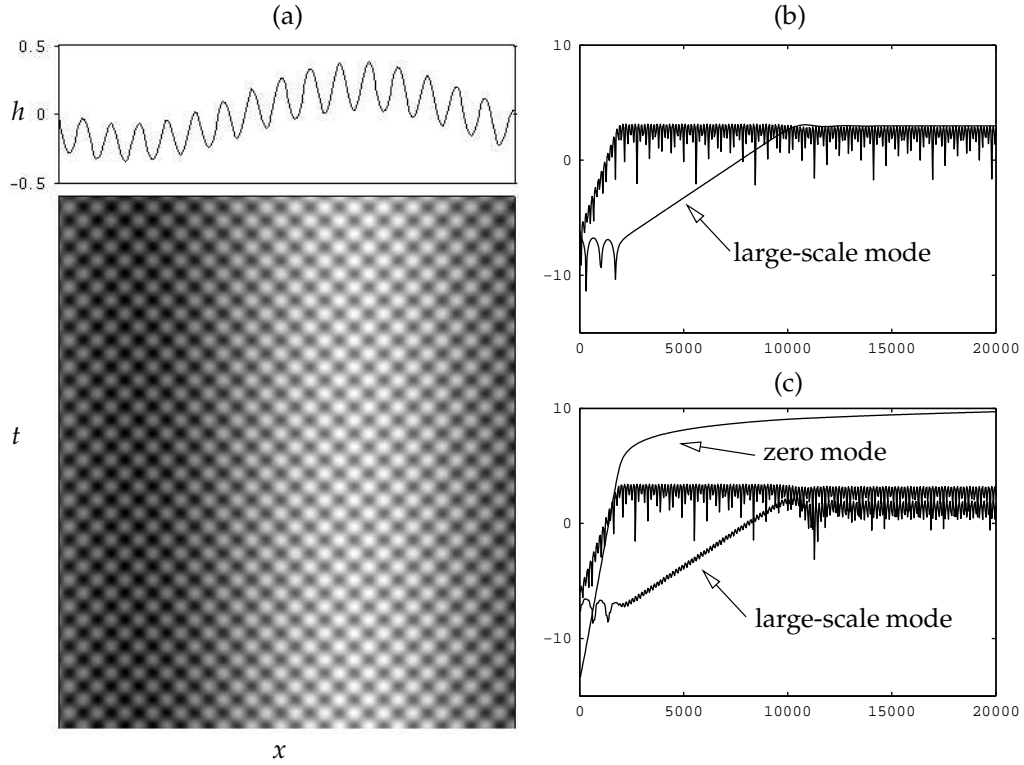


Figure 4.14: A modulated SW pattern in the pure capillary wave regime, with $\Delta = 0.1$, $\gamma = 0.05$ and $H = 1$: (a) space-time plot and final profile of the $h(x, t)$; (b) evolution of $h(x, t)$ in Fourier space; (c) evolution of $\phi(x, t)$ in Fourier space. In (b) and (c), only the largest three Fourier modes are plotted.

parts of the flow domain; the observed patterns often feature regions where the primary pattern is barely discernible. Two such patterns are illustrated in figure 4.15. In (a), the modulation is periodic in time and space, and takes the approximate form of a SW ‘superstructure’ (this isn’t entirely clear from the figure, but is apparent from plots over a large time period), in which regions of visible SWs appear and disappear periodically. In figure 4.15(b), we see a SW pattern in the form of a single localised pulse; outside the pulse, the SW amplitude is strongly suppressed.

It is remarkable that all the modulated patterns detailed in this section are only found in the finite-depth equations (4.2.21); extensive simulations of the infinite-depth version have revealed only unmodulated SWs over the same parameter regimes.

4.8 Summary

In this chapter, we have made a simple modification to the quasi-potential model of Zhang and Viñals [96, 218] to account for finite fluid depth and its associated effects.

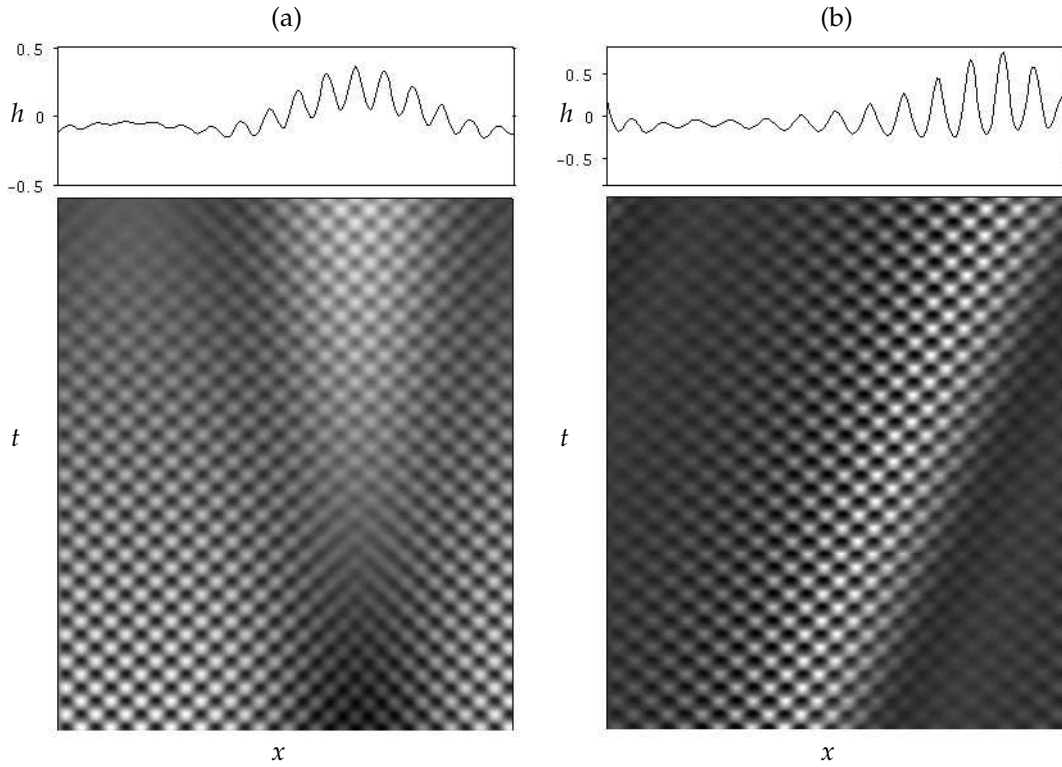


Figure 4.15: Modulated SW patterns in the capillary wave regime, with (a) $\Delta = 0.05, \gamma = 0.2$; (b) $\Delta = 0.05, \gamma = 0.5$.

Instead of infinite fluid depth, we impose a rigid, impenetrable boundary at the bottom driving plate by modifying the Fourier–integral operator $\hat{\mathcal{D}}$ [227, 228]. The main consequences of this modification are to alter the behaviour of large-scale modes, a change that has profound implications on the nonlinear analysis and subsequent amplitude description. In contrast to chapters 2 and 3 where a weakly nonlinear description of the behaviour of large-scale modes is relatively simple and has been the subject of previous study, the behaviour encountered in this chapter is new and presents unique theoretical obstacles. The difficulty in the weakly nonlinear analysis is particularly tantalising in view of the evident similarity of the localisation phenomena exhibited in (e.g.) figure 4.15 to that of figure 3.20 of chapter 3.

Ignoring spatial modulation, the analysis of Zhang and Viñals [96] can be applied in a straightforward manner to the finite-depth problem. This method involves employing two small parameters, the distance from onset and the dissipation parameter γ , to perform a multiscale analysis. A drawback of this method is that, for a weakly nonlinear analysis to be performed, the linear problem must be solved perturbatively, and one has to work with approximate solutions and neglect high-order harmonics in the nonlinear analysis. (In addition, some ad hoc approximations are necessary to com-

plete the analysis.) Physically, such an arrangement corresponds to fluids with small dissipation, but not small enough to be comparable to the distance above threshold. As outlined in §4.4, the resulting amplitude equation takes a similar form to the infinite-depth case, only with a modified cubic coefficient. Importantly though, the derivation of this equation draws attention to, and corrects, two inconsistencies in the analysis reported by Zhang and Viñals [96]. These are related to (a) the terms which are included in the linear solutions and (b) the adjoint solution used to calculate solvability conditions. In both cases, the work of Zhang and Viñals [96] omits important $O(\gamma)$ terms which contribute to the coefficients of the final amplitude equation. Thus, in light of these results, a new derivation in the infinite-depth case can be performed. Such an exercise would only lead to a minor revision to the cubic coefficient found by Zhang and Viñals [96], but it remains an interesting question as to whether this modification would account for some of the mismatch between theoretical and experimental results [109].

Including large-scale spatial modulation, the nonlinear analysis increases significantly in difficulty. Away from the special case of pure capillary waves ($G_0 \neq 0$), we have been able to derive amplitude equations in the form of a Ginzburg–Landau equation for the amplitude of SWs together with two evolution equations for large-scale modes which are both functions of co-moving coordinates. As the amplitude equation is formally uncoupled from the large-scale modes, no new instability behaviour is possible beyond that present in the Ginzburg–Landau equation with real coefficients and one expects to only get uniform SWs near onset, a fact verified by the simulation results reported in §4.7. The behaviour of these large-scale modes matches the predictions of the linear theory. Furthermore, the behaviour of the large-scale modes as predicted by the weakly nonlinear theory is apparent in numerical simulations further from threshold or with large γ values, where uniformly propagating pulses of modulation (with the predicted speed $(G_0 H)^{1/2}$) can be observed. Thus, these amplitude equations offer a guide to the behaviour of SWs away from the small-viscosity, near-onset limit.

For pure capillary waves ($G_0 = 0$), where gravity effects are negligible, the analysis for mixed capillary–gravity waves fails and we have been unable to derive consistent amplitude equations using the scaling assumptions of §4.5. The root cause of this problem is a nonlinear term in the ϕ equation at $O(\epsilon^2)$, which must be balanced by an appropriate mean mode in the expansion for ϕ and, possibly, a new timescale. However, all obvious scaling choices lead to inconsistencies in the analysis and the resolution of this problem is left as an open question.

In §4.6, a new and more mathematically satisfying approach to the weakly nonlinear

analysis is outlined, where only one small parameter is employed. This involves explicitly scaling the distance above threshold to the dissipation parameter γ such that all variables are balanced in a *distinguished limit*; it thus dispenses with the ad hoc approximations of §4.5. For both the infinite- and finite-depth problems, we have been able to derive new and interesting results. For the infinite-depth problem, the resulting amplitude equation takes a form previously proposed by Mancebo and Vega [210], comprising a Ginzburg–Landau equation augmented with new cubic and quintic terms. In previous work [210], this equation has only been derived from a generic set of amplitude equations for counter-propagating waves; this is the first derivation (that we are aware of) from first principles. For the finite-depth problem, the details of the derivation are more subtle and the resulting equations take the form of a similar Ginzburg–Landau equation to the infinite-depth problem coupled (via five terms) to a large-scale mode.

It is important to stress that the results of this chapter represent only a first step towards integrating finite depth into models of Faraday waves. It is now appreciated that a separate mean flow, driven by the viscous boundary layers, should also be incorporated into the model equations [210, 214, 215]; however, this behaviour is missing from the model considered here. The focus in this chapter has been on the change in behaviour of large-scale modes due to the constraints of finite depth, rather than refining the model of Zhang and Viñals [96] to account for experimental results in shallow layers. However, the effects of finite depth still remain an interesting question as the depth of fluid is known to have a dramatic effect on the observed pattern [108]. Experimentalists often eliminate the neutral stability of long-wavelength modes by using a fluid depth far larger than the pattern wavelength [107] or using a more viscous fluid [229]. In these cases, amplitude equations which ignore the neutral stability of a zero mode can be applied.

Conclusions

IN THIS THESIS, we have examined the role of a conservation law on a variety of pattern formation problems with a common set of symmetries, building on previous work by Couillet et al. [56], Fauve et al. [73], Riecke and coworkers [54, 154, 169], and Matthews and Cox [74, 138]. The key consequence of a conserved quantity in this setting is that large-scale modes have near-neutral stability and must be included in the asymptotic analysis of the primary instability near onset. In the absence of a conservation law, such modes (if they exist at all) are not neutrally stable and can be ‘slaved’ to the pattern modes, that is, the modes with positive growthrate. In the presence of a conservation law, these large-scale modes can strongly influence the stability behaviour of the system and lead to new long-wave instabilities which give rise to amplitude-modulated or localised patterns [74, 138].

In chapter 2, a phenomenological model of pattern formation in a vibrated granular layer, proposed by Tsimring and Aranson [6, 95], was re-examined. A previous investigation [6] had failed to account for the dynamical implications of conservation of mass due to the neglect of spatial modulation over a long scale. Taking this behaviour into account, we showed that a large-scale mode must be included in the nonlinear analysis and derived a new set of amplitude equations. In fact, these equations match those previously constructed by Cox and Matthews [138] in a different context and we have been able to apply their results in a straightforward manner. As such, we have been able to give a more complete description of the stability of stripes and squares, which shows that both patterns may suffer a modulational instability induced by the constraint of conservation of mass. Curiously, the boundaries for these two modulational instabilities of stripes and squares coincide, with the result that stripes are effectively immune to modulational instability while squares are always unstable. This coincidence is also found in the modified two-dimensional Swift–Hohenberg equation (1.5.24), and it would be interesting to examine the underlying reasons for this

degeneracy, and whether it can be avoided with a more general model. Extensive numerical simulations of the model equations have verified these results and shown the long-wave instability of squares gives rise to localised patterns; a similar instability has been observed for antisquares, although there is currently no corresponding stability analysis. It is also apparent that these modulational instabilities only influence the pattern extremely close to threshold; further from onset, the realised patterns are in good correspondence with the predictions of previously derived amplitude equations for spatially unmodulated patterns [6, 95]. More generally, our numerical investigation has revealed that the phenomenological model in question is a fascinating and unusual model of pattern formation in its own right, capable of admitting a surfeit of possible steady states, which are only made possible through proper consideration of the conservation law. A possible extension to the work of this chapter would be to augment the amplitude equations (2.2.1) with higher-order terms, so that the subcritical bifurcation present in certain parameter regimes can be studied.

The generic case of a stationary pattern-forming bifurcation with a conservation law, such as that considered in chapter 2, has been the subject of detailed previous study [74, 138], and is now relatively well understood. However, the related scenario of an oscillatory bifurcation under the influence of a conservation law is considerably more complicated and has not been analysed previously; chapter 3 details such an examination. The most commonly used amplitude equations for oscillatory pattern-forming bifurcations in the absence of a conservation law are the Ginzburg–Landau equation and its extension, the complex coupled Ginzburg–Landau equations (see §1.4). Ideally, one seeks to extend these equations to account for a neutrally stable large-scale mode by employing simple symmetry considerations and retaining only terms of the correct asymptotic order. However, through such a method, we have been unable to construct *generic* amplitude equations, because the leading-order forcing term in the large-scale mode equation cannot be balanced in an asymptotically consistent way. Instead, we have pursued an interesting but nongeneric set of amplitude equations where this troublesome term is eschewed in favour of the next forcing term compatible with the system symmetries. These amplitude equations are generic for systems where the conserved quantity is a *pseudoscalar* (such as in rotating convection and magnetoconvection), where only the gradients of the conserved quantity drive the pattern, and are also expected to be applicable to systems with a scalar conserved quantity. For both travelling and standing wave solutions to the amplitude equations, detailed stability analyses show significant modification to existing stability boundaries and reveal qualitatively new instabilities that have no analogue in the absence of a conservation law. For both forms of wave, a diverse array of stability scenarios is possible, with the

region of stability being delimited by both long- and short-wave instabilities. Generally, the conserved quantity has a destabilising effect on the solutions arising from the primary instability. Indeed, for strong coupling between the pattern and conserved modes, the stability regions for standing and travelling waves disappear altogether. Numerical simulations of the amplitude equations have revealed that unstable travelling and standing waves give way to stable, highly localised structures, either coherent, time-periodic or chaotic.

The final study of this thesis concerned examining the influence of finite depth on the quasi-potential model of Faraday waves derived by Zhang and Viñals [96]. As detailed in chapter 4, this modification facilitates the influence of a conserved quantity (in this case, the fluid volume) upon the stability of standing wave patterns, and leads to new large-scale mode behaviour. The weakly nonlinear analysis of this model is not straightforward as, within the scaling framework proposed by Zhang and Viñals [96], the linearised problem can be solved only perturbatively and involves the use of two small parameters, which leads to some ad hoc elements in the analysis. The method of Zhang and Viñals can be successfully applied to the finite-depth model for the mixed capillary–gravity wave regime, where a set of three amplitude equations can be derived. Crucially, the Ginzburg–Landau equation for the standing wave amplitude remains uncoupled from the large-scale modes, and as such, no new modulational behaviour is possible. Nevertheless, the form of these amplitude equations is instructive as they predict that the large-scale modes comprise uniformly propagating spatial profiles. Numerical simulations performed away from the near-threshold, weak-viscosity limit reveal solutions that take exactly this form, propagating with the predicted speed. For the special case of pure capillary waves, this weakly nonlinear method breaks down and we have been unable to derive a consistent set of amplitude equations for this regime. Intriguingly, numerical simulations in this regime reveal modulated standing wave patterns, where the large-scale mode is of a comparable size to the pattern mode. We have also considered an alternative weakly nonlinear analysis involving a distinguished limit of the two small parameters. This simplifies the analysis since only one small parameter (the dissipation) is required. We have successfully applied the distinguished limit of Mancebo and Vega [210] to model both the infinite-depth equations of Zhang and Viñals and their finite-depth analogues. While the interesting large-scale modulational behaviour is not present in the infinite depth problem, we have been able to re-derive a Ginzburg–Landau equation previously suggested by Mancebo and Vega [210], which accounts for the wavenumber shift induced by viscous effects. For the finite depth case, we derived a new set of coupled amplitude equations for the SW amplitude and a large-scale mean mode, involving five distinct

coupling terms.

The three pattern formation problems considered in this thesis have each demonstrated interesting behaviour, primarily due to the influence of a conserved quantity. In each case, we have seen how large-scale modes induced by the presence of a conservation law can destabilise the primary patterns, and lead to amplitude modulation and localisation. Thus, we have shown that the coupling to a slow scalar mode provides a general localisation mechanism for supercritical systems; bistability is not required.

Eigenvalue theorem

In this appendix, we prove the following theorem:

Theorem 2. *The eigenvalues of any $N \times N$ matrix*

$$\mathbf{P}_N = \begin{bmatrix} x & y & \cdots & y \\ y & x & \cdots & y \\ \vdots & \vdots & \ddots & \vdots \\ y & y & \cdots & x \end{bmatrix} \quad (\text{A.0.1})$$

are $x - y$ and $(N - 1)y + x$ which occur with multiplicities $N - 1$ and 1 , respectively.

Proof. Let us define \mathbf{O}_N to be the $N \times N$ matrix where every element is equal to 1. We can then rewrite the eigenvalue problem $\mathbf{P}_N \mathbf{u} = \lambda \mathbf{u}$ as

$$((x - y) \mathbf{I}_N + y \mathbf{O}_N) \mathbf{u} = \lambda \mathbf{u}, \quad (\text{A.0.2})$$

where \mathbf{I}_N is the $N \times N$ identity matrix. This can be then be manipulated to give another eigenvalue problem:

$$\mathbf{O}_N \mathbf{u} = \theta \mathbf{u} \quad (\text{A.0.3})$$

where

$$\theta = \frac{\lambda - x + y}{y}. \quad (\text{A.0.4})$$

Thus, we have a relationship between the eigenvalues of \mathbf{O}_N and \mathbf{P}_N . The eigenvalues of \mathbf{O}_N are given by the $N \times N$ equation

$$\begin{vmatrix} 1 - \theta & 1 & \cdots & 1 \\ 1 & 1 - \theta & \cdots & 1 \\ \vdots & \vdots & \ddots & \vdots \\ 1 & 1 & \cdots & 1 - \theta \end{vmatrix} = 0. \quad (\text{A.0.5})$$

We now define two new forms of matrix:

$$\begin{aligned} \mathbf{A}_N &= (a-1)\mathbf{I}_N + \mathbf{O}_N, \\ &= \begin{bmatrix} a & 1 & \cdots & 1 \\ 1 & a & \cdots & 1 \\ \vdots & \vdots & \ddots & \vdots \\ 1 & 1 & \cdots & a \end{bmatrix}_{N \times N} \end{aligned} \quad (\text{A.0.6})$$

and

$$\mathbf{B}_N = \begin{bmatrix} 1 & 1 & \cdots & 1 \\ 1 & a & \cdots & 1 \\ \vdots & \vdots & \ddots & \vdots \\ 1 & 1 & \cdots & a \end{bmatrix}_{N \times N}. \quad (\text{A.0.7})$$

If we consider the expansion of $|\mathbf{A}_N|$ by the first column, we find

$$|\mathbf{A}_N| = a|\mathbf{A}_{N-1}| - \sum_{i=2}^N (-1)^j \text{cofactor}(\mathbf{A}_{(i,1),N}).$$

It can then be seen that for $i > 2$, the i th cofactor can be transformed into the $(i-1)$ th by a single column-swap operation. First, an, introducing a factor of -1 . Thus, all cofactors can be transformed into $\text{cofactor}(\mathbf{A}_{(2,1),N})$ with all coefficients becoming negative. Hence, we can write

$$\begin{aligned} |\mathbf{A}_N| &= a|\mathbf{A}_{N-1}| - (N-1) \text{cofactor}(\mathbf{A}_{(2,1),N}), \\ &= a|\mathbf{A}_{N-1}| - (N-1)|\mathbf{B}_{N-1}|. \end{aligned} \quad (\text{A.0.8})$$

By a similar method, we find that

$$|\mathbf{B}_N| = |\mathbf{A}_{N-1}| - (N-1)|\mathbf{B}_{N-1}|$$

which allows the elimination of $|\mathbf{B}_{N-1}|$ from (A.0.8):

$$|\mathbf{A}_{N+1}| = (a-N)|\mathbf{A}_N| + N(a-1)|\mathbf{A}_{N-1}|. \quad (\text{A.0.9})$$

We now proceed by induction, under the hypothesis:

$$|\mathbf{A}_N| = (a+N-1)(a-1)^{N-1}, \quad \text{for } M > 1. \quad (\text{A.0.10})$$

For initialisation, consider $N = 2$:

$$|\mathbf{A}_2| = \begin{vmatrix} a & 1 \\ 1 & a \end{vmatrix} = a^2 - 1 = (a+1)(a-1), \quad (\text{A.0.11})$$

which satisfies (A.0.10). Now let us assume (A.0.10) to be true for all $2 \leq N \leq k$ and consider the case $N = k + 1$, which by (A.0.9), becomes

$$|\mathbf{A}_{k+1}| = (a - k)|\mathbf{A}_k| + k(a - 1)|\mathbf{A}_{k-1}|, \quad (\text{A.0.12})$$

and applying the inductive hypothesis gives us

$$\begin{aligned} |\mathbf{A}_{k+1}| &= (a - k)(a + k - 1)(a - 1)^{k-1} + k(a - 1)(a + k - 2)(a - 2)^{k-2}, \\ &= (a - 1)^{m-1} [(a - k)(a + k - 1) + k(a + k - 2)], \\ &= (a + k)(a - 1)^k. \end{aligned} \quad (\text{A.0.13})$$

This proves the inductive hypothesis to be true for $N \geq 2$.

Consequently, the characteristic polynomial of a matrix \mathbf{O}_N must take the form

$$(N - \theta)(-\theta)^{N-1} = 0, \quad (\text{A.0.14})$$

giving a single eigenvalue N as well as $N - 1$ zero eigenvalues. Thus, transforming back to the original problem using (A.0.4), we find the eigenvalues to (A.0.1) must be a single value $y(N - 1) + x$ together with $N - 1$ eigenvalues of the form $x - y$. \square

Simulation code

In this appendix we exhibit the basic form of the MATLAB code used to run simulations for this thesis. The basic structure of the programs is very similar: in each case a one- or two-dimensional PDE is simulated in a large domain with periodic boundary conditions using pseudo-spectral methods [142]. In general, the problems considered are stiff, with the dynamics evolving over both fast and slow timescales. As opposed to using a conventional explicit method with a very small timestep, we employ a more sophisticated method that can resolve the behaviour without resorting to tiny timesteps. For all simulation programs, time-stepping is performed by one of the exponential time-stepping methods **ETD2** or **ETD2RK** of Cox and Matthews [75] (see §2.4.1 for more details of exponential time-stepping methods).

We illustrate the general code structure used in this thesis by exhibiting the program used to simulate the phenomenological model of chapter 2:

$$\begin{aligned}\psi_t &= \gamma\psi^* - (1 - i\omega)\psi + (1 + ib)\nabla^2\psi - |\psi|^2\psi - \rho\psi, \\ \rho_t &= \beta\nabla^2\rho + \alpha\nabla \cdot (\rho\nabla|\psi|^2).\end{aligned}$$

The simulation program takes the following form (pre-defined MATLAB commands are set in a bold typeface):

```
% Set coefficients and system parameters
alpha = 1.05; beta = 0.3; rho0 = 0.3; b = 1; omega = 2.5;
h = 0.2; tMax = 10000; L = 100; N = 128; nPts = 10;

5 % Calculate critical gamma value and set supercriticality condition
gc = sqrt((omega+b*(1+rho0))^2/(1+b^2)); gamma = 1.01*gc;

% Set up spatial grid and wavenumbers
nMax = floor(tMax/h); nPlt = floor(nMax/nPts);
10 [X,Y] = meshgrid([L/N*(-N/2:N/2-1)]);
k = (2*pi/L)*[0:N/2-1 0 -N/2+1:-1]';
k2 = k.*k; k2(N/2+1) = ((N/2)*(2*pi/L))^2;
```

APPENDIX B: SIMULATION CODE

```

[kx,ky] = meshgrid(k); [k2x,k2y] = meshgrid(k2);

15 % Initial conditions
psi = zeros(N) + 1e-4*randn(N);    psiHat = fft2(psi);
rho = rho0*ones(N) + 1e-4*randn(N); rhoHat = fft2(rho);
psiHatData = zeros(N,N,nPts+1); psiHatData(:,:,1) = psiHat;
rhoHatData = zeros(N,N,nPts+1); rhoHatData(:,:,1) = rhoHat;
20 tData      = zeros(1,nPts+1);

% Compute ETD2 factors
cPsi = -1+i*omega-(1+i*b)*(k2x+k2y);
cRho = -beta*(k2x+k2y);
25 M = 32; r = exp(i*pi*((1:M)-.5)/M);
LRpsi = h*cPsi(:,:,ones(M,1)) + reshape(r(ones(N,N),:),N,N,M);
nlFacPsi = h*real(mean(((1+LRpsi).*exp(LRpsi)-1-2*LRpsi)./LRpsi.^2, 3));
nlFacPsip = h*real(mean(((1-LRpsi).*exp(LRpsi)+1+LRpsi)./LRpsi.^2, 3));
LRrho = h*cRho(:,:,ones(M,1)) + reshape(r(ones(N,N),:),N,N,M);
30 nlFacRho = h*real(mean(((1+LRrho).*exp(LRrho)-1-2*LRrho)./LRrho.^2, 3));
nlFacRhop = h*real(mean(((1-LRrho).*exp(LRrho)+1+LRrho)./LRrho.^2, 3));

% Solve PDE
for n = 1:nMax
35   T = n*h; psi = ifft2(psiHat); rho = ifft2(rhoHat);

% Nonlinear terms
modPsiSqd_x = ifft2(i*kx.*fft2(abs(psi).^2));
modPsiSqd_y = ifft2(i*ky.*fft2(abs(psi).^2));
40   nlPsi = fft2(gamma*conj(psi) - psi.*abs(psi).^2 - rho.*psi);
nlRho = alpha*(i*kx.*fft2(rho.*modPsiSqd_x)+i*ky.*fft2(rho.*modPsiSqd_y));
if n == 1 nlPsip = nlPsi; nlRhop = nlRho; end

% Stepping in time.
45   psiHat = psiHat.*exp(h*cPsi) + nlFacPsi.*nlPsi + nlFacPsip.*nlPsip;
rhoHat = rhoHat.*exp(h*cRho) + nlFacRho.*nlRho + nlFacRhop.*nlRhop;
nlPsip = nlPsi; nlRhop = nlRho;

% Storing data.
50   if mod(n,nplt) == 0
psiHatData(:,:,n/nplt+1) = psiHat;
rhoHatData(:,:,n/nplt+1) = rhoHat;
tData(n/nplt+1) = T;
end
55 end

% Convert back to physical space
psiData = ifft2(psiHatData);
rhoData = ifft2(rhoHatData);

```

This program is loosely based on the sample program p27.m from Trefethen [142], where nonlinear terms are computed pseudo-spectrally (lines 38–41), that is, they are calculated in physical space before being transformed back to spectral space. We remark further:

- For computational convenience, the conjugate term $\gamma\psi^*$ is grouped with the non-linear terms (line 40). This means that only some of the linear terms are integrated exactly; however, treating this conjugate term exactly would require the decomposition of the problem into real and imaginary parts and give rise to a nondiagonal linear problem. Although methods exist to deal with systems that have nondiagonal linear parts [75], they are computationally more expensive and more complicated to program; furthermore, the present method suffices for the problem at hand.
- The coefficients of the **ETD2** method (and other ETD methods) suffer from a cancellation error for modes with small linear growth rate and some care must be exercised in their calculation. This was first noted by Kassam and Trefethen [143] who proposed a contour integral method to evaluate the coefficients; this method is implemented in lines 25–31 to derive the coefficients `n1FacPsi`, `n1FacPsiP`, `n1FacRho` and `n1FacRhoP`.

The programs used to generate the figures of chapter 1 as well as perform simulations for chapter 3 and chapter 4 are qualitatively similar to the above program.

Eigenfunction parity in binary fluid convection

The equations for two-dimensional convection in a binary mixture at infinite Prandtl number [154] are:

$$\begin{pmatrix} -\nabla^4 & -S\partial_x & -\partial_x \\ -\mathcal{R}\partial_x & \partial_t - \nabla^2 & 0 \\ -\mathcal{R}S\partial_x & \mathcal{L}S\nabla^2 & \partial_t - \mathcal{L}\nabla^2 \end{pmatrix} \begin{pmatrix} \phi \\ \theta \\ c \end{pmatrix} = \begin{pmatrix} 0 \\ -J(\phi, \theta) \\ -J(\phi, c) \end{pmatrix}, \quad (\text{C.0.1})$$

where, for arbitrary functions f and g :

$$J(f, g) = \frac{\partial f}{\partial x} \frac{\partial g}{\partial z} - \frac{\partial g}{\partial x} \frac{\partial f}{\partial z}; \quad (\text{C.0.2})$$

ϕ is the streamfunction and θ and c denote the departures of the temperature and concentration, respectively, from their conductive profiles. The dimensionless parameter S is the separation ratio, \mathcal{R} is the Rayleigh number and \mathcal{L} is the Lewis number. We impose no-slip, impermeable boundary conditions:

$$\phi = \phi_z = 0, \quad \theta = 0, \quad (c/S - \theta)_z = 0, \quad \text{at } z = 0, 1, \quad (\text{C.0.3})$$

which are the experimentally relevant conditions. The linear stability problem for a Hopf bifurcation can be formulated by writing

$$\begin{pmatrix} \psi \\ \theta \\ c \end{pmatrix} = \begin{pmatrix} \psi_0(z) \\ \theta_0(z) \\ c_0(z) \end{pmatrix} e^{i\omega t + ikx}, \quad (\text{C.0.4})$$

where ψ_0, θ_0, c_0 are complex-valued, to yield

$$0 = -k^4 \psi_0 + Sik\theta_0 + ikc_0, \quad (\text{C.0.5a})$$

$$0 = \mathcal{R}ik\psi_0 + (i\omega + k^2)\theta_0, \quad (\text{C.0.5b})$$

$$0 = \mathcal{R}ikS\psi_0 - \mathcal{L}Sk^2\theta_0 + (i\omega + \mathcal{L}k^2)c_0. \quad (\text{C.0.5c})$$

(Note that the eigenmode for the counter-propagating mode is $e^{i\omega t - ikx}$ is $(-\psi_0, \theta_0, c_0)$). The following argument is relevant if the Lewis number is taken to be $O(1)$. Since the linear problem is invariant under $z \rightarrow 1 - z$, the reflection of the eigenfunctions (about $z = 1/2$) must also be eigenfunctions. However, since the eigenfunctions are uniquely defined up to multiplication by a constant, this implies that the eigenfunctions are either all odd or all even. Thus, the parity of the eigenfunctions for both the streamfunction and the concentration mode will be the same and, as outlined in §3.2, the coefficient of the coupling term (3.2.4) will be zero.

While we have ruled out a leading-order term of the form (3.2.4), a similar derivation to that of §3.2 reveals the coefficient of the next-order coupling term $(|\tilde{A}_1|^2 + |\tilde{A}_2|^2)_{XX}$ also to be zero. This is a consequence of the invariance of (C.0.1) to the $z \rightarrow 1 - z$ symmetry, which is not present in magnetoconvection or rotating fluid convection. Moreover, in the formulation (C.0.1) the odd parity of the Jacobian implies that there can be no non-linear contribution to the evolution of a conserved mode. This prompts the question of how a conserved mode will evolve in the binary fluid equations with the reflection symmetry in z broken.

For the experimentally more interesting case of small Lewis number, the large-scale mode arises from a different mechanism, and does not require the concentration field to be conserved [154, 175]. This type of mode is z -dependent and is an odd function of $z - 1/2$, so it has the correct parity to be excited by the Jacobian and then the generic form of the coupling holds.

Notation guide

The following table is a quick-reference guide to the notation used in each chapter.

Table D.1: Notation guide

<i>Nomenclature</i>	<i>Meaning</i>
CHAPTER 2	
f	frequency of forcing
A	amplitude of forcing
$\Gamma = 2\pi^2 f^2 A/g$	dimensionless acceleration (g is acceleration due to gravity)
$\psi(x, y, t)$	order parameter for complex amplitude of pattern (the surface deformation is given by $h = \psi \exp(i\pi ft) + \text{c.c.}$)
$\rho(x, y, t)$	order parameter for local mass of granular layer per unit area
γ	dimensionless forcing amplitude
ρ_0	initial uniform layer height
α	nonlinear coupling coefficient in evolution equation for ρ
β	diffusion coefficient in evolution equation for ρ
$\phi = \alpha\rho_0/\beta$	an important control parameter
CHAPTER 3	
A_1, A_2	amplitudes of left/right-travelling waves
C	mean mode
s	rescaled group velocity parameter
r_2	supercriticality parameter
σ	diffusion coefficient of C equation
μ	strength of coupling between mean mode and pattern modes

Table D.1: (continued)

<i>Nomenclature</i>	<i>Meaning</i>
Q	amplitude of travelling or standing wave
q	wavenumber correction
l	perturbation wavenumber
CHAPTER 4	
h	surface displacement
ϕ	velocity potential
ν	kinematic viscosity
ρ	density of fluid
Γ	surface tension
γ	dimensionless linear damping coefficient
G_0	dimensionless gravity coefficient
Γ_0	dimensionless capillary number
f	dimensionless driving amplitude
H	fluid depth

References

- [1] M.C. Cross and P.C. Hohenberg. Pattern formation outside of equilibrium. *Rev. Mod. Phys.*, 65:851–1112, 1993.
- [2] P.S. Stevens. *Patterns in nature*. Peregrine Books, 1976.
- [3] S. Nettesheim, A. von Oertzen, and H.H. Roturmund. Reaction-diffusion patterns in the catalytic cooxidation on Pt(110) - front propagation and spiral waves. *J. Phys. Chem.*, 98(12):9977–9985, 1993.
- [4] E.L. Koschmeider. Bénard convection. *Adv. Chem. Phys.*, 26:177–212, 1974.
- [5] <http://www.haverford.edu/physics-astro/Gollub/faraday/faraday2.html>.
- [6] L.S. Tsimring and I.S. Aranson. Localized and cellular patterns in a vibrated granular layer. *Phys. Rev. Lett.*, 79(2):213–216, 1997.
- [7] I.S. Aranson and L. Kramer. The world of the complex Ginzburg–Landau equation. *Rev. Mod. Phys.*, 74:99–143, 2002.
- [8] A.C. Newell, T. Passot, and J. Lega. Order parameter equations for patterns. *Annu. Rev. Fluid Mech.*, 25:399–453, 1993.
- [9] D.W. Jordan and P. Smith. *Nonlinear ordinary differential equations*. Oxford University Press, 1977.
- [10] L.D. Landau. On the problem of turbulence. In *Collected papers of L.D. Landau*. Gordon and Breach, 1944.
- [11] J.T. Stuart. On the non-linear mechanics of wave disturbances in stable and unstable parallel flows. *J. Fluid Mech.*, 9:353–370, 1960.
- [12] A.C. Newell. Envelope equations. *Lect. Appl. Math.*, 15:157–163, 1974.
- [13] A.C. Newell and J.A. Whitehead. Finite bandwidth, finite amplitude convection. *J. Fluid Mech.*, 38:279–303, 1969.

REFERENCES

- [14] L.A. Segel. Distant side-walls cause slow amplitude modulation of cellular convection. *J. Fluid Mech.*, 38:203–224, 1969.
- [15] V.L. Ginzburg and L.D. Landau. On the theory of superconductivity. *Zhurnal Eksperimentalnoi i Teoreticheskoi Fiziki*, 20:1064–1082, 1950.
- [16] P. Grindrod. *The theory and applications of reaction–diffusion equations: patterns and waves*. Oxford University Press, 1996.
- [17] E. Kreyszig. *Introductory functional analysis with applications*. John Wiley & sons, 1978.
- [18] B. Dionne, M. Silber, and A.C. Skeldon. Stability results for steady, spatially periodic planforms. *Nonlinearity*, 10:321–353, 1997.
- [19] J.H.P. Dawes, P.C. Matthews, and A.M. Rucklidge. Reducible actions of $D_4 \times T^2$: superlattice patterns and hidden symmetries. *Nonlinearity*, 16(2):615–645, 2003.
- [20] M. Golubitsky, I. Stewart, and D.G. Schaeffer. *Singularities and groups in bifurcation theory. Volume II*. Number 69 in Applied Mathematical Series. Springer-Verlag, New York, 1988.
- [21] J.T. Stuart and R.C. DiPrima. The Eckhaus and Benjamin–Feir resonance mechanisms. *Proc. R. Soc. Lond.*, 362:27–41, 1978.
- [22] I. Melbourne. Steady-state bifurcation with Euclidean symmetry. *Trans. Am. Math. Soc.*, 351:1575–603, 1999.
- [23] C. Elphick, E. Tirapegui, M. Brachet, P. Coullet, and G. Iooss. A simple global characterization for normal forms of singular vector fields. *Physica D*, 29:95–127, 1987.
- [24] W. Pesch and L. Kramer. Nonlinear analysis of spatial structures in two-dimensional anisotropic pattern forming systems. *Z. Phys. B: Condens. Matter*, 63:121–130, 1986.
- [25] L. Kramer and W. Pesch. Convection instabilities in nematic liquid-crystals. *Annu. Rev. Fluid Mech.*, 27:515–541, 1995.
- [26] I.A. Eltayeb. Hydrodynamic convection in a rapidly rotating fluid layer. *Proc. R. Soc. London, Ser. A*, 326(1565):229, 1972.
- [27] I. Melbourne and G. Schneider. Phase dynamics in the real Ginzburg–Landau equation. *Math. Nachr.*, 263–264:171–180, 2004.

REFERENCES

- [28] W. Eckhaus. *Studies in non-linear stability theory*. Number 6 in Springer tracts in natural philosophy. Springer-Verlag, Berlin, 1965.
- [29] L.S. Tuckerman and D. Barkley. Bifurcation analysis of the Eckhaus instability. *Physica D*, 46:57–86, 1990.
- [30] M.L. Lowe and J.P. Gollub. Pattern selection near the onset of convection: the Eckhaus instability. *Phys. Rev. Lett*, 55(23):2575–2579, 1985.
- [31] L. Kramer and W. Zimmerman. On the Eckhaus instability for spatially periodic patterns. *Physica D*, 16:221–232, 1985.
- [32] M.I. Tribelsky, S. Kai, and H. Yamazaki. Transitions between different stable states in one dimensional Ginzburg–Landau equation. *Prog. Theor. Phys.*, 85(5): 963–967, 1991.
- [33] R.B. Hoyle. Long wavelength instabilities of square patterns. *Physica D*, 67:198–223, 1993.
- [34] R.B. Hoyle. Nonlinear phase diffusion equations for the long-wave instabilities of hexagons. *Appl. Math. Lett.*, 8(3):81–85, 1995.
- [35] B. Janiaud, A. Pumir, D. Bensimon, V. Croquette, H. Richter, and L. Kramer. The Eckhaus instability for travelling waves. *Physica D*, 55:269–286, 1992.
- [36] A.C. Newell, C.G. Lange, and P.J. Aucoin. Random convection. *J. Fluid Mech.*, 40: 513–542, 1970.
- [37] J.M. Vega. Instability of the steady states of some Ginzburg–Landau equations with real coefficients. *Nonlinearity*, 18:1425–1441, 2005.
- [38] A. Doelman, R.A. Gardner, and C.K.R.T. Jones. Instability of quasiperiodic solutions of the Ginzburg–Landau equation. *Proc. Roy. Soc. Edinburgh Sect. A*, 125(3): 501–517, 1995.
- [39] A.C. Newell and J.A. Whitehead. Review of the finite bandwidth concept. In H. Leipholz, editor, *Proceedings of the IUTAM Conference on Instabilities in Continuous systems, Herrenalb, 1969*, page 234. Springer, Heidelberg, 1971.
- [40] K. Stewartson and J.T. Stuart. A non-linear instability theory for a wave system in plane Poiseuille flow. *J. Fluid Mech*, 48:529–545, 1971.
- [41] C.B. Ermentrout. Stable small-amplitude solutions in reaction-diffusion systems. *Quart. Appl. Math.*, 39:61–86, 1981.

REFERENCES

- [42] Y. Kuramoto. *Chemical oscillations, waves, and turbulence*, volume 19 of *Springer Series in Synergetics*. Springer-Verlag, Berlin, 1984.
- [43] B.J. Matkowsky and V. Volpert. Stability of plane wave solutions of complex Ginzburg–Landau equations. *Quart. Appl. Math.*, 51(2):265–281, June 1993.
- [44] C.G. Lange and A.C. Newell. A stability criterion for envelope equations. *SIAM J. Appl. Math.*, 27(3):441–456, November 1974.
- [45] T.B. Benjamin and J.E. Feir. The disintegration of wave trains on deep water. *J. Fluid. Mech.*, 27(3):417–430, 1967.
- [46] L. Brusch, M.G. Zimmermann, M. van Hecke, M. Bär, and A. Torcini. Modulated amplitude waves and the transition from phase to defect chaos. *Phys. Rev. Lett.*, 85(1):86–89, 2000.
- [47] Y. Lan, N. Garnier, and Cvitanović. Stationary modulated-amplitude waves in the 1D complex Ginzburg–Landau equation. *Physica D*, 188(3-4):193–212, 2004.
- [48] B.I. Shraiman, A. Pumir, W. van Saarloos, P.C. Hohenberg, H. Chaté, and M. Holen. Spatiotemporal chaos in the one-dimensional complex Ginzburg–Landau equation. *Physica D*, 57:241–248, 1992.
- [49] Y. Kuramoto and T. Tsuzuki. Persistent propagation of concentration waves in dissipative media far from thermal equilibrium. *Prog. Theor. Phys.*, 55:356–369, 1976.
- [50] H. Chaté. Spatiotemporal intermittency regimes of the one-dimensional Ginzburg–Landau equation. *Nonlinearity*, 7:185–204, 1994.
- [51] K. Nozaki and N. Bekki. Pattern selection and spatiotemporal transition to chaos in the Ginzburg–Landau equation. *Phys. Rev. Lett.*, 51(24):2171–2174, 1983.
- [52] W. van Saarloos and P.C. Hohenberg. Fronts, pulses, sources and sinks in generalized complex Ginzburg–Landau equations. *Physica D*, 56:303–367, 1992.
- [53] H. Sakaguchi. Phase dynamics and the coupled complex Ginzburg–Landau equations. *Prog. Theor. Phys.*, 93(3):491–502, 1995.
- [54] H. Riecke and L. Kramer. The stability of standing waves with small group velocity. *Physica D*, 137:124–142, 2000.
- [55] M. van Hecke, C. Storm, and W. van Saarloos. Sources, sinks and wavenumber selection in coupled CGL equations and experimental implications for counter-propagating wave systems. *Physica D*, 134:1–47, 1999.

REFERENCES

- [56] P. Couillet, S. Fauve, and E. Tirapegui. Large-scale instability of nonlinear standing waves. *J. Physique Lett.*, 46(17):L-787–L-791, 1985.
- [57] H. Sakaguchi. Localized solutions to the coupled complex Ginzburg–Landau equations. *Prog. Theor. Phys.*, 95(4):823–827, 1996.
- [58] H. Sakaguchi. Travelling wave-standing wave transition in the coupled complex Ginzburg–Landau equations. *Phys. Scrip.*, T67:148–1996, 1996.
- [59] M.C. Cross. Structure of nonlinear travelling-wave states in finite geometries. *Phys. Rev. A*, 38(7):3593–3600, 1988.
- [60] J. Fineberg, E. Moses, and V. Steinberg. Spatially and temporally modulated traveling-wave patterns in convecting binary mixtures. *Phys. Rev. Lett.*, 61:838–841, 1988.
- [61] C.M. Surko and P. Kolodner. Oscillatory traveling-wave convection in a finite container. *Phys. Lett.*, 58:2055–2058, 1987.
- [62] H. Riecke and G.D. Granzow. Localization of waves without bistability: worms in nematic electroconvection. *Phys. Rev. Lett.*, 81(2):333–336, 1998.
- [63] A. Amengual, D. Walgraef, M. San Miguel, and E. Hernández-García. Wave-unlocking transition in resonantly coupled complex Ginzburg–Landau equations. *Phys. Rev. Lett.*, 76(11):1956–1959, 1996.
- [64] A. Amengual, E. Hernández-García, R. Montagne, and M. San Miguel. Synchronization of spatiotemporal chaos: the regime of coupled spatiotemporal intermittency. *Phys. Rev. Lett.*, 78(23):4379–4382, 1997.
- [65] B.A. Malomed. Domain wall between traveling waves. *Phys. Rev. E*, 50(5):R3310–R3313, 1994.
- [66] R. Montagne and Hernández-García. Localized structures in coupled Ginzburg–Landau equations. *Phys. Lett. A*, 273:239–244, 2000.
- [67] R.J. Deissler. Interaction of two-dimensional localized solutions near a weakly nonlinear inverted bifurcation. *Phys. Rev. A*, 44(6):R3411–R3414, 1991.
- [68] L. Gil. Vector order parameter for an unpolarized laser and its vectorial topological defects. *Phys. Rev. Lett.*, 70(2):162–165, 1993.
- [69] E. Knobloch and J. De Luca. Amplitude equations for travelling wave convection. *Nonlinearity*, 3:975–980, 1990.

REFERENCES

- [70] J.M. Vega. On the amplitude equations arising at the onset of the oscillatory instability in pattern formation. *SIAM J. Math. Anal.*, 24(3):603–617, 1993.
- [71] E. Knobloch. Nonlocal amplitude equations. In S. Kai, editor, *Pattern formation in complex dissipative systems*, volume 65, pages 263–274, Singapore, 1992. World Scientific.
- [72] E. Knobloch. Remarks on the use and misuse of the Ginzburg–Landau equation. In A. Doelman and A. van Harten, editors, *Nonlinear dynamics and pattern formation in the natural environment*, volume 335 of *Pitman Research Notes in Mathematics*, pages 130–146. Longman, Harlow, UK, 1995.
- [73] S. Fauve, S. Douady, and C. Laroche. Collective behaviours of granular masses under vertical vibrations. *J. Phys. C3*, 50:187–191, 1989.
- [74] P.C. Matthews and S.M. Cox. Pattern formation with a conservation law. *Nonlinearity*, 13:1293–1320, 2000.
- [75] S.M. Cox and P.C. Matthews. Instability and localisation of patterns due to a conserved quantity. *Physica D*, 175:196–219, 2003.
- [76] P. Coulet and S. Fauve. Propagative phase dynamics for systems with Galilean invariance. *Phys. Rev. Lett.*, 55(26):2857–2859, 1985.
- [77] B.A. Malomed. Patterns produced by a short-wave instability in the presence of a zero mode. *Phys. Rev. A*, 45(2):1009–1017, 1992.
- [78] M.L. Tribelsky and K. Tsuboi. New scenario for transition to turbulence? *Phys. Rev. Lett.*, 76(10):1631–1634, 1996.
- [79] M.L. Tribelsky and M.G. Velarde. Short-wavelength instability in systems with slow long-wavelength dynamics. *Phys. Rev. E*, 54(5):4973–4981, 1996.
- [80] P.C. Matthews and S.M. Cox. One-dimensional pattern formation with Galilean invariance near a stationary bifurcation. *Phys. Rev. E*, 62(2):R1473–R1476, August 2000.
- [81] D.M. Winterbottom, P.C. Matthews, and S.M. Cox. Oscillatory pattern formation with a conserved quantity. *Nonlinearity*, 13:1293–1320, 2005.
- [82] P. Coulet and G. Iooss. Instability of one-dimensional cellular patterns. *Phys. Rev. Lett.*, 64(866–869), 1990.

REFERENCES

- [83] N.L. Komarova and A.C. Newell. Nonlinear dynamics of sand banks and sand waves. *J. Fluid Mech.*, 415:285–321, 2000.
- [84] S.M. Cox. The envelope of a one-dimensional pattern in the presence of a conserved quantity. *Phys. Lett. A*, 333:91–101, 2004.
- [85] M.R.E. Proctor. Finite amplitude behaviour of the Matthews–Cox instability. *Phys. Lett. A*, 292:181–187, 2001.
- [86] J. Norbury, J. Wei, and M. Winter. Existence and stability of singular patterns in a Ginzburg–Landau equation coupled with a mean field. *Nonlinearity*, 15:2077–2095, 2002.
- [87] F.H. Busse and J.A. Whitehead. Instabilities of convection rolls in a high Prandtl number fluid. *J. Fluid Mech.*, 47(2):305–320, 1971.
- [88] F.H. Busse and R.M. Clever. Instabilities of convection rolls in a fluid of moderate Prandtl number. *J. Fluid Mech.*, 91:319–335, 1979.
- [89] F.H. Busse. The oscillatory instability of convection rolls in a low Prandtl number fluid. *J. Fluid Mech.*, 52:97–112, 1972.
- [90] B. Echebarria and C. Pérez-García. Phase instabilities in hexagonal patterns. *Europhys. Lett.*, 43:35–40, 1998.
- [91] S.M. Cox and P.C. Matthews. New instabilities in two-dimensional rotating convection and magnetoconvection. *Physica D*, 129(3):210–229, 2001.
- [92] S.M. Cox, P.C. Matthews, and S.L. Pollicott. Swift–Hohenberg model for magnetoconvection. *Phys. Rev. E*, 69(066314), 2004.
- [93] A.A. Golovin, B.J. Matkowsky, A. Bayliss, and A.A. Nepomnyashchy. Coupled KS–CGL and coupled Burgers–CGL equations for flames governed by a sequential reaction. *Physica D*, 129:253–298, 1999.
- [94] F.J. Mancebo and J.M. Vega. Viscous Faraday waves in 2D large aspect ratio containers. *J. Fluid Mech., under consideration*, 2005.
- [95] I.S. Aranson and L.S. Tsimring. Formation of periodic and localized patterns in an oscillating granular layer. *Physica A*, 249:103–110, 1998.
- [96] W. Zhang and J. Viñals. Pattern formation in weakly damped parametric surface waves. *J. Fluid Mech.*, 336:301–330, 1997.

REFERENCES

- [97] H.M. Jaeger, S.R. Nagel, and R.P. Behringer. Granular solids, liquids and gases. *Rev. Mod. Phys.*, 68(4):1259–1273, 1996.
- [98] J. Rajchenbach. Granular flows. *Adv. Phys.*, 49(2):229–256, 2000.
- [99] L.P. Kadanoff. Built upon sand: theoretical ideas inspired by granular flows. *Rev. Mod. Phys.*, 71(1):435–444, 1999.
- [100] I.S. Aranson and L.S. Tsimring. Patterns and collective behaviour in granular media: theoretical concepts. *Rev. Mod. Phys.*, In press, 2005.
- [101] P.B. Umbanhowar and H.L. Swinney. Wavelength scaling and square/stripe and grain mobility transitions in vertically oscillated granular layers. *Physica A*, 288: 344–362, 2000.
- [102] P. Melby, F. Vega Reyes, A. Prevost, R. Robertson, P. Kumar, D.A. Egolf, and J.S. Urbach. The dynamics of thin vibrated granular layers. *J. Phys. Condens. Matter*, 17:S2689–S2704, 2005.
- [103] F. Melo, P. Umbanhowar, and H.L. Swinney. Transition to parametric wave patterns in a vertically oscillated granular layer. *Phys. Rev. Lett.*, 72(1):172–175, 1994.
- [104] F. Melo, P.B. Umbanhowar, and H.L. Swinney. Hexagons, kinks and disorder in oscillated granular layers. *Phys. Rev. Lett.*, 75(21):3838–3841, 1995.
- [105] T.H. Metcalf, J.B. Knight, and H.M. Jaeger. Standing wave patterns in shallow beds of vibrated granular material. *Physica A*, 236:202–210, 1997.
- [106] P. Umbanhowar, F. Melo, and H. Swinney. Localized excitations in a vertically vibrated granular layer. *Nature*, 382:793–796, 1996.
- [107] W.S. Edwards and S. Fauve. Patterns and quasi-patterns in the Faraday experiment. *J. Fluid Mech.*, 278:123–148, 1994.
- [108] M-T. Westra, D.J. Binks, and W. van de Water. Patterns of Faraday waves. *J. Fluid Mech.*, 496:1–32, 2003.
- [109] A. Kudrolli and J. Gollub. Patterns and spatiotemporal chaos in parametrically forced surface waves: a systematic survey at large aspect ratio. *Physica D*, 97: 133–154, 1996.
- [110] E.F.F. Chladni. *Entdeckungen im Reich des Klanges*. 1787.
- [111] M. Faraday. On the forms and states assumed by fluids in contact with vibrating elastic surfaces. *Phil. Trans. Roy. Soc. London*, 121:319–340, 1831.

REFERENCES

- [112] S. Douady, S. Fauve, and C. Laroche. Subharmonic instabilities and defects in a granular layer under vertical vibrations. *Europhys. Lett.*, 8(7):621–627, 1989.
- [113] <http://chaos.ph.utexas.edu/granular/granular.html>, .
- [114] <http://denali.phys.uniroma1.it/~puglisi/thesis/node12.html>.
- [115] H.K. Pak, E. van Doorn, and R.P. Behringer. Effects of ambient gases on granular materials under vertical vibration. *Phys. Rev. Lett.*, 74(23):4643–4646, 1995.
- [116] A. Garcimartín, D. Maza, J.L. Ilquimiche, and I. Zuriguel. Convective motion in a vibrated granular layer. *Phys. Rev. E*, 3(1), 2002.
- [117] J.R. de Bruyn, M.D. Bizon, M.C. Shattuck, D. Goldman, J.B. Swift, and H.L. Swinney. Continuum-type stability balloon in oscillated granular layers. *Phys. Rev. Lett.*, 81(7):1421–1424, 1998.
- [118] <http://super.phys.northwestern.edu/~pbu/>, .
- [119] C. Bizon, M.D. Shattuck, J.B. Swift, W.D. McCormick, and H.L. Swinney. Patterns in 3D vertically oscillated granular layers: simulation and experiment. *Phys. Rev. Lett.*, 80(1):57–60, 1998.
- [120] I.S. Aranson, D. Blair, W.K. Kwok, G. Karapetrov, U. Welp, G.W. Crabtree, and V.M. Vinokur. Controlled dynamics of interfaces in a vibrated granular layer. *Phys. Rev. Lett.*, 82(4):731–734, 1999.
- [121] S.J. Moon, M.D. Shattuck, C. Bizon, D.I. Goldman, J.B. Swift, and H.L. Swinney. Phase bubbles and spatiotemporal chaos in granular patterns. *Phys. Rev. E*, 65 (011301), 2001.
- [122] O. Liouvashevski, Y. Hamiel, A. Agnon, Z. Reches, and J. Fineberg. Oscillons and propagating solitary waves in a vertically vibrated colloidal suspension. *Phys. Rev. Lett.*, 83(16):3190–3193, 1999.
- [123] T. Shinbrot. Competition between randomizing impacts and inelastic collisions in granular pattern formation. *Nature*, 389:574–576, 1997.
- [124] D.H. Rothman. Oscillons, spiral waves, and stripes in a model of vibrated sand. *Phys. Rev. E*, 57(2):R1239–R1242, 1998.
- [125] E. Cerda, F. Melo, and S. Rica. Model for subharmonic waves in granular materials. *Phys. Rev. Lett.*, 79(23):4570–4573, 1997.

REFERENCES

- [126] K.M. Aoki and T. Akiyama. Spontaneous wave pattern formation in vibrated granular materials. *Phys. Rev. Lett.*, 77(20):4166–4168, 1996.
- [127] J. Bougie, J. Kreft, J.B. Swift, and H.L. Swinney. Onset of patterns in an oscillated granular layer: continuum and molecular dynamics simulations. *Phys. Rev. E*, 71(2), 2005.
- [128] C. Bizon, M.D. Shattuck, J.B. Swift, W.D. McCormick, and H.L. Swinney. Computational test of kinetic theory of granular media. *J. Stat. Phys.*, 274(1–2):158–170, 1998.
- [129] S.C. Venkataramani and E. Ott. Spatiotemporal bifurcation phenomena with temporal period doubling. *Phys. Rev. Lett.*, 80(16):3495–3498, 1998.
- [130] S.C. Venkataramani and E. Ott. Pattern selection in extended periodically forced systems: a continuum coupled map approach. *Phys. Rev. E*, 63(4), 2001.
- [131] S-O. Jeong, T-W. Ko, and H-T. Moon. Oscillons, kinks and patterns in a model for a periodically forced medium. *Physica D*, 164:71–84, 2002.
- [132] S-O. Jeong, H-T. Moon, and T-W. Ko. Nearest pattern interaction and global pattern formation. *Phys. Rev. E*, 62(6):7778–7780, 2000.
- [133] R. Deng and C-H. Wang. Instabilities of granular material undergoing vertical vibrations: a uniformly driven layer. *J. Fluid Mech.*, 492:381–410, 2003.
- [134] J. Eggers and H. Riecke. Continuum description of vibrated sand. *Phys. Rev. E*, 59(4):4476–4483, 1999.
- [135] H-K. Park and H-T. Moon. Square to stripe transition and superlattice patterns in vertically oscillated granular layers. *Phys. Rev. E*, 65:art. no. 051310, 2002.
- [136] J.D. Crawford. $D_4 \dot{+} T^2$ mode interactions and hidden rotational symmetry. *Nonlinearity*, 7:697–739, 1994.
- [137] I.S. Aranson, L.S. Tsimring, and V.M. Vinokur. Hexagons and interfaces in a vibrated granular layer. *Phys. Rev. E*, 59(2):R1327–R1330, 1999.
- [138] S.M. Cox and P.C. Matthews. Exponential time differencing for stiff systems. *J. Comp. Phys.*, 176:430–455, 2002.
- [139] W. Zhang and J. Viñals. Secondary instabilities and spatiotemporal chaos in parametric surface waves. *Phys. Rev. Lett.*, 74(5):690–693, 1995.

REFERENCES

- [140] S.V. Kiyashko, L.N. Korzinov, M.I. Rabinovich, and L.S. Tsimring. Rotating spirals in a Faraday experiment. *Phys. Rev. E*, 54(5):5037–5040, 1996.
- [141] D. Blair, I.S. Aranson, G.W. Crabtree, V. Vinokur, L.S. Tsimring, and C. Josserand. Patterns in thin vibrated granular layers: interfaces, hexagons and superoscillations. *Phys. Rev. E*, 61(5):5600–5610, 2000.
- [142] L.N. Trefethen. *Spectral methods in Matlab*. Soc. for Industr. & Appl. Math., Philadelphia, 2000.
- [143] A.K. Kassam and L.N. Trefethen. Fourth-order time-stepping for stiff PDEs. *SIAM J. Sci. Comp.*, 26(4):1214–1233, 2005.
- [144] U. Bisang and G. Ahlers. Bifurcation to worms in electroconvection. *Phys. Rev. E*, 60(4):3910–3918, 1999.
- [145] H. Herrero and H. Riecke. Front structures in a real Ginzburg–Landau equation coupled to a mean field. *Int. J. Bifurcat. Chaos*, 4(5):1343–1346, 1994.
- [146] C. Crawford and H. Riecke. Oscillon-type structures and their interaction in a Swift–Hohenberg model. *Physica D*, 129:83–92, 1999.
- [147] H. Herrero and H. Riecke. Bound pairs of fronts in a real Ginzburg–Landau equation coupled to a mean field. *Physica D*, 85:79–92, 1995.
- [148] P.C. Matthews and A.M. Rucklidge. Travelling and standing waves in magnetoconvection. *Proc. R. Soc. Lond. A*, 441:649–658, 1993.
- [149] P. Kolodner. Stable, unstable, and defected confined states of traveling-wave convection. *Nonlinearity*, 50:2731–2755, 1990.
- [150] F. Charru and P. Barthelet. Secondary instabilities of interfacial waves due to coupling with a long wave mode in a two-layer Couette flow. *Physica D*, 125:311–324, 1999.
- [151] S. Fauve. *Instabilities and nonequilibrium structures*, pages 63–88. Dordrecht, Reidel, 1987.
- [152] P. Barthelet and F. Charru. Benjamin–Feir and Eckhaus instabilities with Galilean invariance: the case of interfacial waves in viscous shear flows. *Eur. J. Mech. B*, 17(1):1–18, 1998.
- [153] N.J. Balmforth and A. Casti. Convection in a slowly diffusing, weakly stratified salt field. *Phys. Lett. A*, 238:34–42, 1998.

REFERENCES

- [154] H. Riecke. Ginzburg–Landau equation coupled to a concentration field in binary-mixture convection. *Physica D*, 61:253–259, 1992.
- [155] A. Doelman, G. Hek, and N. Valkhoff. Stabilization by slow diffusion in a real Ginzburg–Landau equation. *J. Nonl. Sc.*, 14(3):237–278, 2004.
- [156] H. Herrero and H. Riecke. Holes and chaotic pulses of traveling waves coupled to a long-wave mode. *Phys. Lett. A*, 235:493–498, 1997.
- [157] M. Ipsen and P.G. Sørensen. Finite wavelength instabilities in a slow mode coupled complex Ginzburg–Landau equation. *Phys. Rev. Lett.*, 84(11):2389–2392, 2000.
- [158] H. Sakaguchi. Phase dynamics and localized solutions to the Ginzburg–Landau type amplitude equations. *Prog. Theor. Phys.*, 89(6):1123–1146, 1993.
- [159] D. Walgraef. Pattern selection and the effect of group velocity on interacting oscillatory and stationary instabilities. *Phys. Rev. E*, 55(6):6887–6897, 1997.
- [160] J.J. Niemala, G. Ahlers, and D.S. Cannell. Localized traveling-wave states in binary-fluid convection. *Phys. Rev. Lett.*, 64(12):1365–1368, 1990.
- [161] P. Kolodner. Drifting pulses of traveling-wave convection. *Phys. Rev. Lett.*, 66(9):1165–1168, 1991.
- [162] W. Barten, M. Lücke, M. Kamps, and R. Schmitz. Convection in binary fluid mixtures II. Localized traveling waves. *Phys. Rev. E*, 51(6):5662–5681, 1995.
- [163] S. Koga and Y. Kuramoto. Localized patterns in reaction-diffusion systems. *Prog. Theor. Phys.*, 63(1):106–121, 1980.
- [164] M. Dennin, G. Ahlers, and D.S. Cannell. Chaotic localized states near the onset of electroconvection. *Phys. Rev. Lett.*, 77(12):2475–2478, 1996.
- [165] M. Dennin, G. Ahlers, and D.S. Cannell. Spatiotemporal chaos in electroconvection. *Science*, 272(5260):388–390, 1996.
- [166] M. Dennin, D.S. Cannell, and G. Ahlers. Patterns of electroconvection in a nematic liquid crystal. *Phys. Rev. E*, 57(1):638–649, 1998.
- [167] K. Lerman, E. Bodenschatz, and D.S. Cannell. Transient localized states in 2D binary-liquid convection. *Phys. Rev. Lett.*, 70(23):3572–3575, 1993.
- [168] L. Hocking and K. Stewartson. Nonlinear instability burst in plane parallel flow. *J. Fluid Mech.*, 51:705, 1972.

REFERENCES

- [169] H. Riecke. Localized structures in pattern-forming systems. In *Pattern formation in continuous and coupled systems*, volume 115 of *IMA Vol. Math. Appl.*, pages 215–229. Springer, New York, 1999.
- [170] H. Riecke. Solitary waves under the influence of a long-wave mode. *Physica D*, 92:69–94, 1996.
- [171] A. Roxin and H. Riecke. Destabilisation and localisation of traveling waves by an advected field. *Physica D*, 156:19–38, 2001.
- [172] M. Iima and Y. Nishiura. Collisions of localized traveling-wave convection cells in binary fluid. In *GAKUTO International Series, Mathematical Sciences and Applications*, 2005 (submitted).
- [173] G.D. Granzow and H. Riecke. Phase diffusion in localized spatiotemporal amplitude chaos. *Phys. Rev. Lett.*, 77(12):2451–2454, 1996.
- [174] W. Schopf and Zimmermann. W. Convection in binary fluids: amplitude equations, codimension-2 bifurcation and thermal fluctuations. *Phys. Rev. E*, 47(3):1739–1764, 1993.
- [175] H. Riecke. Self-trapping of traveling-wave pulses in binary mixture convection. *Phys. Rev. Lett.*, 68(3):301–304, 1992.
- [176] C. Martel and J. Vega. Finite size effects near the onset of the oscillatory instability. *Nonlinearity*, 9:1129–1171, 1996.
- [177] C. Martel and J. Vega. Dynamics of a hyperbolic system that applies at the onset of the oscillatory instability. *Nonlinearity*, 11:105–142, 1998.
- [178] R. Montagne, E. Hernández-García, and M. San Miguel. Winding number instability in the phase-turbulence regime of the phase-turbulence regime of the complex Ginzburg–Landau equation. *Phys. Rev. Lett.*, 77(2):267–270, 1996.
- [179] H. Riecke. Personal communication, 2005.
- [180] J. Miles and D. Henderson. Parametrically forced surface waves. *Annu. Rev. Fluid. Mech.*, 22:143–165, 1990.
- [181] B. Christiansen, P. Alstrøm, and M.T. Levinsen. Ordered capillary-wave states: quasicrystals, hexagons, and radial waves. *Phys. Rev. E*, 68(14):2157–2160, 1992.
- [182] N.B. Tufillaro, R. Ramshankar, and J.P. Gollub. Order-disorder transition in capillary ripples. *Phys. Rev. E*, 62(4):422–425, 1989.

REFERENCES

- [183] D. Binks and W. Water. Nonlinear pattern formation in Faraday waves. *Phys. Rev. E*, 78:4043, 1997.
- [184] B. Christiansen, P. Alstrøm, and M.T. Levinsen. Dissipative and ordering in capillary waves at high aspect ratios. *J. Fluid Mech.*, 291:323–, 1995.
- [185] O. Liouvashevski, H. Arbell, and J. Fineberg. Dissipative solitary states in driven surface waves. *Phys. Rev. Lett.*, 76:3969, 1996.
- [186] J. Fineberg and O. Liouvashevski. Propagating solitary states in highly dissipative driven fluids. *Physica A*, 249:10–17, 1998.
- [187] L. Daudet, V. Ego, S. Manneville, and J. Bechhoefer. Secondary instabilities of surface-waves on viscous fluids in the Faraday instability. *Europhys. Lett.*, 32:313–318, 1995.
- [188] A.B. Ezerskii, Korotin. P.I., and M.I. Rabinovich. Random self-modulation of two-dimensional structures on a liquid surface during parametric-excitation. *Sov. Phys. JETP*, 41:157–160, 1986.
- [189] <http://www.physics.utoronto.ca/nonlinear/faraday.html>.
- [190] <http://www.haverford.edu/physics-astro/Gollub/lab.html>.
- [191] A. Kudrolli, B. Pier, and J.P. Gollub. Superlattice patterns in surface waves. *Physica D*, 123:989–111, 1998.
- [192] H. Arbell and J. Fineberg. Spatial and temporal dynamics of two interacting modes in parametrically driven surface waves. *Phys. Rev. Lett.*, 81(20):4384–4387, 1998.
- [193] H. Arbell and J. Fineberg. Temporally harmonic oscillons in Newtonian fluids. *Phys. Rev. Lett.*, 85(4):756–759, 2000.
- [194] H. Arbell and J. Fineberg. Pattern formation in two-frequency forced parametric waves. *Phys. Rev. E*, 65:036224, 2002.
- [195] W. Zhang and J. Viñals. Square patterns and quasipatterns in weakly damped Faraday waves. *Phys. Rev. E*, 53(5):R4283–R4286, 1996.
- [196] J.W.S. Lord Rayleigh. On the crispations of fluid resting upon a vibrating support. *Phil. Mag.*, 16:50–58, 1883.
- [197] K. Kumar and L.S. Tuckerman. Parametric instability of the interface between two fluids. *J. Fluid Mech.*, 279:49–68, 1994.

REFERENCES

- [198] T. Benjamin and F. Ursell. The stability of the plane surface of a liquid in vertical periodic motion. *Proc. R. Soc. Lond.*, 225:505–515, 1954.
- [199] J.R. Ockendon and H. Ockendon. Resonant surface waves. *J. Fluid Mech.*, 59(39), 1973.
- [200] J. Bechhoefer, V. Ego, S. Manneville, and B. Johnson. An experimental study of the onset of parametrically pumped surface waves in viscous fluids. *J. Fluid Mech.*, 288:351–381, 1995.
- [201] O. Lioubashevski, J. Fineberg, and L. Tuckerman. Scaling of the transition to parametrically driven surface waves in highly dissipative systems. *Phys. Rev. E*, 55:R3832–R3835, 1997.
- [202] S. Ubal, M.D. Giavedoni, and F.A. Saita. A numerical analysis of the influence of the liquid depth on two-dimensional Faraday waves. *Phys. Fluids*, 15(10):3099–3113, 2003.
- [203] F.J. Mancebo and J.M. Vega. Faraday instability threshold in large-aspect-ratio containers. *J. Fluid Mech.*, 467:307–330, 2002.
- [204] S.T. Milner. Square patterns and secondary instabilities in driven capillary waves. *J. Fluid Mech.*, 225:81–100, 1991.
- [205] P. Chen and J. Viñals. Amplitude equation and pattern selection in Faraday waves. *Phys. Rev. E*, 60(1):559–570, 1999.
- [206] M. Umeki. Pattern selection in Faraday waves. *J. Phys. Soc. Jpn.*, 65:2072–, 1996.
- [207] K. Yoshimatsu and M. Funakoshi. Primary patterns in Faraday surface waves at high aspect ratio. *J. Phys. Soc. Jpn.*, 67:451, 1998.
- [208] J. Miles. Nonlinear Faraday resonance. *J. Fluid Mech.*, 146:285–302, 1984.
- [209] J. Miles. On Faraday waves. *J. Fluid Mech.*, 248:671–683, 1993.
- [210] F.J. Mancebo and J.M. Vega. Standing wave description of nearly conservative parametrically driven waves in extended systems. *Physica D*, 197:346–363, 2004.
- [211] W. Zhang and J. Viñals. Pattern formation in weakly damped parametric surface waves driven by two frequency components. *J. Fluid Mech.*, 341:225–244, 1997.
- [212] J.M. Vega, E. Knobloch, and C. Martel. Nearly inviscid Faraday waves in annular containers of moderately large aspect ratio. *Physica D*, 154:313–336, 2001.

REFERENCES

- [213] S. Douady, S. Fauve, and O. Thual. Oscillatory phase modulation of parametrically forced surface waves. *Europhys. Lett.*, 10:309–315, 1989.
- [214] E. Martín, C. Martel, and J.M. Vega. Drift instability of standing Faraday waves. *J. Fluid Mech.*, 467:57–79, 2002.
- [215] E. Martín, C. Martel, and J.M. Vega. Mean flow effects in the Faraday instability. *Int. J. Mod. Phys.*, 17(22,23&24):4278–4283, 2003.
- [216] M. Higuera, J.M. Vega, and E. Knobloch. Coupled amplitude-mean flow equations for nearly inviscid Faraday waves in moderate aspect ratio containers. *J. Nonlinear. Sci.*, 12:505–551, 2002.
- [217] V. Lapuerta, C. Martel, and J.M. Vega. Weakly nonlinear Faraday waves in 2D large aspect ratio annuli. *Physica D*, 173:178–203, 2002.
- [218] W. Zhang. *Pattern formation in weakly damped parametric surface waves*. PhD thesis, Florida State University, 1994.
- [219] T.S. Lundgren and N.N. Mansour. Oscillations of drops in zero gravity with weak viscous effects. *J. Fluid Mech.*, 194:479–510, 1988.
- [220] K.D. Ruvinsky, F.I. Feldstein, and G.I. Freidman. Numerical simulations of the quasi-stationary stage of ripple excitation by steep gravity capillary waves. *J. Fluid Mech.*, 230(339–353), 1991.
- [221] W. Zhang and J. Viñals. Numerical study of pattern formation in weakly damped parametric surface waves. *Physica D*, 116:225–243, 1998.
- [222] A. Catllà, J. Porter, and M. Silber. A weakly nonlinear analysis of impulsively forced Faraday waves. *In press*, 2005.
- [223] J. Bechhoefer and B. Johnson. A simple model for Faraday waves. *Amer. J. of Phys.*, 64:1482–1488, 1996.
- [224] M. Silber, C. Topaz, and A.C. Skeldon. Two-frequency forced Faraday waves: weakly damped modes and pattern selection. *Physica D*, 143:205–225, 2000.
- [225] C.M. Topaz and M. Silber. Resonances and superlattice pattern stabilization in two-frequency forced Faraday waves. *Physica D*, 172:1–29, 2002.
- [226] J.M. Vega, S. Rüdiger, and J. Viñals. A phenomenological model of weakly damped Faraday waves and the associated mean flow. *Phys. Rev. E*, 70, 2004.

REFERENCES

- [227] W. Craig and C. Sulem. Numerical simulation of gravity waves. *J. Comp. Phys.*, 108:73–83, 1993.
- [228] P. Guyenne and D.P. Nicholls. Numerical simulation of solitary waves on plane slopes. *Math. Comput. Simulat.*, 69(3–4):269–281, 2005.
- [229] A.C. Skeldon and G. Guidoboni. Pattern selection for Faraday waves in an incompressible viscous fluid. *In press*, 2005.